Spacecraft Charge Neutralization During Active Electron Emission

by

Grant Camden Miars

A dissertation submitted in partial fulfillment
of the requirements for the degree of
Doctor of Philosophy
(Electrical Engineering)
in The University of Michigan
2020

Doctoral Committee:

Professor Brian E. Gilchrist, Chair
Doctor Gian Luca Delzanno
Professor John Foster
Professor Mark Kushner

Grant Camden Miars

gmiars@umich.edu

ORCID iD: 0000-0003-1871-6675

For my grandpa Cam, who introduced me to a world unseen.

ACKNOWLEDGEMENTS

It takes a village to raise a child. I've always liked that phrase, and it certainly feels true in this moment. Perhaps it would be more accurate in this case to say it takes a village to recognize a lost child and guide them down the path to academic and professional self-actualization. To obtain a PhD was never the plan. It was a dream too big to dream. But here we stand. I am eternally grateful to my village and those who helped me "raise" this dissertation.

I must first and foremost thank my advisor, Professor Brian Gilchrist, without whom I would almost certainly not be writing this. Several years ago, Brian agreed to write a recommendation letter for my PhD applications. To this day, I am convinced I was only accepted because he took a chance on a candidate with more hours washing dishes than working in a laboratory. Since then, Brian has been a constant source of opportunity, understanding, and inspiration. While I may never understand the supernatural force that drives Brian to work as hard as he does for all of us, it inspires me everyday to be a better person and more effective researcher.

I am also very pleased to thank my all-star committee members, each of whom have taught me an immense amount over my graduate career. Professor Mark Kushner was the first to introduce to me to plasmas. His deep understanding, innate curiosity, and interdisciplinary relationships have contributed significantly to my knowledge of the plasma field. Professor John Foster was the first to introduce me to plasma experiments. His passion and perspective have often reassured me that I am in the right place and the future is bright. Doctor Gian Luca Delzanno has been one of my

closest collaborators during the work presented in this dissertation. His extraordinary plasma knowledge and commitment to quality has helped teach me how to approach plasma research and professional work moving forward.

I would be remiss to continue without thanking my partner in crime, Omar Leon. Omar and I started our journeys the same year and were the only two PhD students in our research group for most of our time at Michigan. We learned the ropes together and spent many days bouncing ideas off each other. Much of the work addressed in this dissertation was done with Omar at my side and I can only hope that the "Gromar" labels we leave behind confuse new lab students for years to come.

A host of different laboratories at the University of Michigan made graduate life immensely more bearable and taught me quite a bit. Much of my research was performed at the Plasmadynamic and Electric Propulsion Laboratory (PEPL), which I consider my research home. At PEPL I was lucky enough to work with Scott Hall, Tim Collard, Ethan Dale, Sarah Cusson, Marcel Georgin, Ben Wachs, Quentin Millette, Eric Viges, JP Sheehan, Ben Jorns, and others. A special thank you to Iverson Bell, for blazing many trails Omar and I would later follow. His fantastic advice was exactly what a green PhD candidate needed to hear. I would also like to thank all the MiTEE satellite team members I have had the pleasure of working with over the years, especially the plasma subteam. I learned a lot about the satellite design process from MiTEE and am endlessly impressed by the students it attracts. The Space Physics Research Laboratory (SPRL) also deserves recognition for its support of MiTEE and the wealth of experience it offered across several space projects. Another great community was found in the Michigan Institute for Plasma Science and Engineering (MIPSE). In fact, MIPSE sparked my interest in plasma science via a particularly colorful flyer spotted on campus many years ago. The Radiation Laboratory was also kind enough to take me in and help me through the challenging classwork early in my graduate career.

I would also like to express my gratitude to the space community at large. Collaborators at LANL and the Space Science Institute (SSI) such as Joe Borovsky, Reiner Freidel, Eric Dors, and Federico Lucco Castello played a big part in shaping my graduate school experience and involvement with the CONNEX mission concept. Professor John Williams, the Colorado State University Electric Propulsion and Plasma Engineering Laboratory (CEPPE), and the Farnells of Plasma Controls were an endless source of knowledge and enabled my experiments by providing several plasma sources. The spacecraft charging community has also been very welcoming and deserves enormous credit for the work that they do. In particular, I would like to thank Linda Krause, Jesse McTernan, Sven Bilen, Dale Ferguson, David Cooke, Dan Goebel, and Ira Katz.

Any quality found in this dissertation is in large part thanks to my two teams of generous editors. Thank you to Mara Darian, Lindsay Miars, Alex Schelb, Dean Miars, Christine Miars, Marissa Miars, John Lavoie-Mayer, Karon Miars, Ron Baker, and Talin Darian for your text and grammar edits. Thank you also to Iverson Bell, Sven Bilen, Federico Lucco Castello, Brian Gilchrist, Omar Leon, Joe Borovsky, John Williams, and David Cooke for your technical edits.

I received financial support from a few different sources during my graduate career, however the biggest support undoubtedly came from Los Alamos National Laboratory (LANL). Support came specifically from the LANL Directed Research and Development (LDRD) program under project 20170423ER and the LANL Center for Space and Earth Science as part of the project titled: Validation of Electron Beam Emission Mediated by a Plasma Contactor. Additional support came from the Michigan Institute for Plasma Science and Engineering and the University of Michigan's Horace H. Rackham School of Graduate Studies. I would not have been able to complete my PhD research without this critical support.

I would also not be here without the incredible effort and sacrifices made by my

parents and the support of my family. Thank you to my mother for instilling the importance of education, empathy, and perseverance in me. Thank you to my father for being my rock, gifting me an interest in science, and teaching me the importance of humor. Thank you to my grandpa Cam, the self-taught electrical engineer who was making electron beams work over 60 years ago. It seems wandering into your basement workshop all those years ago may have had an impact. Thank you to my sisters, Lindsay and Marissa. I can't put all the ways your lives have changed mine into words. All that comes to mind is: we did it and thank you. I feel extraordinarily lucky to be blessed with the family I have and will never be able to repay them in full. Thank you for supporting me in everything I do.

Thank you to my friends. I think it's fair to say that you kept me sane over the past six years. Thank you for reminding me who I am, what life is about, and what work-life balance is. Special shout out to John Lavoie-Mayer, Alex Schelb, Ray Mahaffy, TEAM, the OX House, the game night regulars, the IM squads, and my Washington family. Thank you for putting up with my nonsense.

Speaking of putting up with my nonsense, approximately one million thank yous to my adventure buddy Talin. Your unwavering support has gotten me through innumerable hard times, and this is certainly no exception. I look forward to being with you always and you remind me what things in life are worth fighting for. Your work ethic, kindness, and generosity have amazed me over and over again. Thank you for somehow making me a stronger, better, more whole person all at once. Whether we're working or exploring, I know one thing is for sure: we have to go further!

GCM

Ann Arbor, MI

2020

TABLE OF CONTENTS

LIST OF FIGURES

Figure

LIST OF TABLES

LIST OF APPENDICES

Appendix

ABSTRACT

Active (i.e. deliberate) electron emission in space is a powerful scientific technique that often proves problematic due to the spacecraft charging it induces. Indeed, effective spacecraft neutralization during active electron emission in low density space plasmas continues to be a challenge. A charge control technique was recently identified through particle-in-cell (PIC) simulations which promises to deliver this critical capability. The technique is termed the ion emission model and uses ion emission from the surface of a dense, quasi-neutral contactor plasma across a plasma sheath (double layer). This ion emission is shown to balance the electron emission current from the spacecraft without inducing significant spacecraft charging. Before conducting in-space demonstration experiments to validate PIC results, ground-based plasma chamber experiments were needed to help with early validation.

This dissertation focuses on Earth-based plasma experiments conducted in a vacuum chamber to validate the ion emission model. These experiments are divided into four experimental campaigns which addressed distinct aspects of the "spacecraft"-plasma system. The campaigns examined: 1) the initial, transient "spacecraft" potential and plasma response to simulated electron beam emission, 2) the steady state plasma response to simulated electron beam emission, 3) the spatial ion emission current (and nearby plasma parameters which define it), and 4) how the peak spacecraft potential during simulated electron emission scales with electron emission current, emitted plasma current, and ion mass. The results from these experiments support the ion emission model and add to the physical understanding of ion emission as it may occur in tenuous space plasmas.

Contributions of this work include:

1. Demonstration of "spacecraft" neutralization during simulated electron emission. The "spacecraft" potential and bulk plasma potential were found to react

in unison. The "spacecraft" potential was found to reach equilibrium tens of seconds into electron "beam" emission.

2. A measured plasma response to changes in hollow cathode source potential relative to chamber ground. Langmuir probe measurements of the bulk plasma potential, floating potential, electron temperature, electron density, and ion density are presented for two plasma source potentials. The plasma potential was found to stay within a few electron temperatures of the source potential. The electron temperature was found to increase for higher source potentials. Charged particles were found to concentrate near the plasma source for higher source potentials, while the bulk plasma remained quasi-neutral outside of the chamber wall's plasma sheath.

3. Direct experimental validation of the semi-analytical ion emission model. Plasma measurements of the ion emission region near the chamber wall are presented via Langmuir probe, retarding potential analyzer (RPA), and emissive probe measurements of the bulk electron temperature, ion energy distribution function (IEDF), and spatial plasma potential. These measurements were used as inputs to the ion emission model and an analytical space-charge limit (SCL) expression. The ion emission model and SCL emission current predictions were compared to the measured emission currents and both were found to agree within 50%.

4. A parametric analysis of physical properties that affect ion emission from a quasi-neutral plasma. The "spacecraft" potential scaling with simulated electron emission current was found to follow an exponential function which is likely defined by the electron temperature. The peak "spacecraft" potential during electron emission was found to decrease for both lower simulated electron emission current and ion mass.

CHAPTER I

Introduction

1.1 Problem Statement

The active, or deliberate, emission of electrons from spacecraft surfaces is a powerful scientific technique that has been used since the late 1960s [1, 2]. Electron beams have been used during space environment studies in order to produce artificial aurora, measure ambient magnetic field gradients over large distances, and neutralize the spacecraft charge (allowing unperturbed measurements of ambient charged particles) [3–5]. They have also been used for answering fundamental plasma physics questions, such as the nature of wave-particle interactions or how kinetic beam energy feeds into plasma waves and instabilities [6]. Most electron beam missions have taken place in relatively dense plasmas where emitted electron current can be balanced by electron current collection from a dense plasma with only minor changes to the spacecraft potential. Electron emission attempts in more tenuous plasmas have been known to encounter serious difficulties associated with spacecraft charging. For example, when a 6 mA electron beam was last emitted in the low plasma density environment of the Earth's magnetosphere, the spacecraft charged so positive that the beam returned and caused three distinct payload failures [7].

There have been no successful, published electron emission demonstrations exceeding 1 mA in tenuous space plasmas (with densities below 10 cm^3) to date, despite

attempts made by the SCATHA experiment in 1979 [7]. However, that does not mean that the capability is not required. Even prior to the SCATHA experiment, a mission concept featuring the emission of a high power (> 1 kW) electron beam from the magnetosphere was already considered to understand what magnetospheric processes drive the aurora [8]. This mission concept calls for connecting the spacecraft's position in the magnetosphere to its magnetic footpoint in the ionosphere by firing a high power electron beam along the local magnetic field and detecting its impact in the Earth's upper atmosphere [8]. This mission concept sat idle for decades after the severe spacecraft charging issues encountered on SCATHA. However, renewed research in electron-emitting spacecraft neutralization (including the work presented in this dissertation) has resurrected this mission concept in the form of the Magnetosphere-Ionosphere Connections Explorer (CONNEX) mission [8–10]. There has also been increased interest in using electron beams to flush the Earth's radiation belts of energetic, man-made charged particles using beam-induced plasma waves should the need arise [10, 11]. The demand for spacecraft charging mitigation of high-power electron beams led to its inclusion in the latest decadal survey for space physics [12, 13].

Numerical and theoretical research has been ongoing at Los Alamos National Laboratory (LANL) in response to this demand [14–17]. This research has revealed a promising neutralization technique that relies on ion emission from the surface of a quasi-neutral plasma. Experimental validation is required to apply the results of this research to real space missions. In response to this, LANL has partnered with the University of Michigan to complete a series of experimental plasma campaigns. The results of these experimental plasma campaigns are the topic of this dissertation.

1.2 Objectives and Contribution

The first objective of this work is to validate the numerical and theoretical spacecraft neutralization research performed at LANL. The second objective is to determine

and characterize what physical processes may be missing from the developed models. The third objective is to demonstrate ion emission and "spacecraft" neutralization in a laboratory setting. Finally, the experiments described have scientific merit in their own right: they reveal and expand upon fundamental plasma concepts in ways that are applicable across disciplines.

Contributions of this work include:

1. (Chapter 4) A laboratory demonstration of an isolated plasma-emitter (or "spacecraft") achieving potential equilibrium while removing a constant electron current using a power supply (to mimic "electron beam" emission). Additionally, "spacecraft" potential and bulk plasma potential measurements when an "electron beam" is first emitted show that the "spacecraft" potential reaches equilibrium in a few tens of seconds. Further, electron and ion saturation current measurements dispersed throughout the vacuum chamber provide insight into plasma density and current transients during the "spacecraft" neutralization process.

2. (Chapter 5) A measured plasma response to changes in source potential. Plasma potential, floating potential, electron temperature, electron density, and ion density contours are presented for two plasma source potentials. These contours illustrate how the bulk, quasi-neutral plasma responds to steady state electron emission for comparison with numerical predictions. This result is applicable for general plasma science purposes.

3. (Chapter 6) Direct experimental validation of a semi-analytical ion emission model based on space-charge limited (SCL) ion emission from a positively biased quasi-neutral plasma [16]. Detailed measurements of the ion emission region are presented. These measurements were used as inputs to the ion emission model. Model predictions were compared to measured emission currents and found to

be in good agreement, paving the way for future model use.

4. (Chapter 7) A parametric analysis of physical properties that affect ion emission from a quasi-neutral plasma. An array of ion masses, neutral gas flow rates, and keeper currents were tested to assess their impact on "spacecraft" potential during electron emission. A statistical analysis reveals scaling laws and correlated parameters that must be considered when designing in-space systems. These scaling laws are also compared to numerical predictions.

1.3 Organization

Chapter 2 introduces the basic concepts used in the remainder of this work. Plasma science and spacecraft charging fundamentals are presented in a descriptive and intuitive manner with references to more rigorous source material. A brief history of spacecraft charging and electron-emitting space experiments is provided to motivate and contextualize the work presented. Chapter 3 summarizes the numerical and analytical research relevant to the ion emission model. Chapter 4 presents transient experiments that characterize the spacecraft potential and plasma response to "electron beam" emission. Chapter 5 describes the steady state plasma response to "spacecraft" potential changes (such as those induced by electron emission). Chapter 6 presents detailed measurements in the ion emission region near the chamber wall. This chapter also inputs these measurements into the ion emission model and space-charge limit for validation purposes. Chapter 7 presents the results of a parametric trade study. This experimental study identifies parameters and scaling laws related to ion emission. Chapter 8 draws conclusions and outlines future work.

CHAPTER II

Background and Motivation

2.1 Plasma Fundamentals

2.1.1 Motivation

Excess electrical charge accumulation and distribution on a spacecraft often varies in response to a variety of physical processes. The accumulation of this excess charge is known as spacecraft charging (as is the field which studies it). To understand which physical processes dominate spacecraft charging behavior, we must first understand some aspects of its physical configuration. Aspects that contribute to spacecraft charging can be categorized as internal (spacecraft) sources and external (environmental) sources. The interplay of these two sources determines a spacecraft's charge distribution. Internal sources of spacecraft charging are driven by decisions made by the spacecraft design team. Some concepts relevant to internal charging sources are described in this chapter, but it is not meant to be an exhaustive list. As the chapter will also show, many considerations arise when accounting for external sources of spacecraft charging. Two major sources from the ambient environment are ambient particles and electromagnetic fields acting upon the spacecraft body. These two sources can be subdivided into numerous subfields. One such subfield relates to the subject of charged particles which strike the spacecraft surface. Because these parti-

cles often deposit charge on the surface they strike, this is a particularly important spacecraft charging subfield. The ubiquitous presence of charged particles in space thus necessitates an examination of their properties and behavior in order to understand spacecraft charging at a fundamental level. In the work which follows, we will discuss critical aspects of these charged particles, or "plasma."

2.1.2 Plasma Definition

In general terms, a plasma is a collection of unbound charged particles. There are three requirements for this collection to be defined as a plasma. These requirements are summarized below in plain English and mathematically.

1. Quasi-neutrality: A plasma is approximately neutral in terms of overall charge density. A plasma may be non-neutral over very small scale lengths or in perturbed regions, but must have approximately zero charge throughout most of its volume. For plasmas dominated by singly charged ions and electrons, this requirement simplifies to equal ion and electron densities (n_i and n_e respectively) in unperturbed regions. This approximate equality is given explicitly in Equation (2.1). Quasi-neutrality differentiates plasmas from collections of charges of a single polarity and allows the second requirement to be satisfied.

$$n_i \approx n_e \quad m^{-3} \tag{2.1}$$

2. Collective or group behavior: There must be a sufficient number of charged particles present for plasma behavior to be dominated by inter-particle electromagnetic forces. Two example requirements to ensure collective behavior are provided in Equations (2.2) and (2.3). In these equations, N_D is the Debye number (or plasma parameter) and represents the number of charged particles

present in a sphere with a radius of one Debye length (λ_D). Equation (2.2) ensures there are enough plasma particles to have a strong effect on each other and act as a group. D of Equation (2.3) is the characteristic length of a plasma-confining volume. If the requirement defined in Equation (2.3) is not met, the plasma is confined to such a small space that it can be non-neutral throughout its volume. The Debye length will be discussed in more detail later in this chapter.

$$N_D = \frac{4\pi}{3} n_e {\lambda_D}^3 >> 1 \tag{2.2}$$

$$\lambda_D << D \quad m \tag{2.3}$$

3. Dominated by electric and magnetic forces: Electric and magnetic forces must play a major role in plasma behavior for the first two requirements to be met. Collisions are one of the main ways that electric and magnetic plasma phenomena are disrupted, as they can redirect and redistribute particle velocity vectors probabilistically. Equation (2.4) defines one important condition for this requirement to be met, namely that the plasma frequency (f_p) is much greater than any plasma collision frequency (f_c). Collisional processes will be treated in more detail later in this chapter.

$$f_p >> f_c \quad Hz \tag{2.4}$$

2.1.3 Plasma Composition

Plasma is often referred to as the fourth state of matter and the most common form of visible matter in the universe. Indeed, plasma fills both the immense "void" of space and the stars that light it. A wide array of plasma compositions have been observed in space and laboratory experiments, but they can be grouped according to the three common properties defined in the preceding section. This broad plasma definition leaves room for a huge range of other physical properties. Other important physical properties for the purposes of this dissertation are listed in Table 2.1. Representative values from three relevant plasma environments are also provided in Table 2.1. Specifically, plasma properties typical of the laboratory experiments in this dissertation, low earth orbit (LEO), and geostationary orbit (GEO) are listed. For completeness, we will also state that the ion energy distribution functions of LEO and GEO are typically Maxwellian, but appear to be drifting Maxwellian before correcting for the satellite's orbital velocity. Orbital velocities typical of LEO and GEO are ≈7.7 km/s and ≈3.1 km/s respectively. Relevant plasma properties are listed where used for the remainder of this dissertation. It is worth noting that a Maxwellian or drifting Maxwellian energy distribution function is assumed for ion and electrons consistently throughout this work. This a commonly observed plasma energy distribution function that develops when a gas reaches collisional equilibrium via repetitious elastic collisions [18].

2.1.4 Collisional Processes

Particle collisions often play an integral role in defining plasma behavior and extraordinary progress has been made in identifying, measuring, and modeling particle collision types [22, 23]. One particularly useful tool that utilizes this research is the global plasma model. Global plasma models approximate an entire plasma discharge by neglecting spatial derivatives in order to enhance computational efficiency [24].

Plasma Property	Laboratory	LEO	GEO
Ion density [m^{-3}]	10^{13}	10^{11}	10^{6}
Ion mass [kg]	$2.2x10^{-25}$	$2.7x10^{-26}$	$1.7x10^{-27}$
Ion charge [C]	$1.6x10^{-19}$	$1.6x10^{-19}$	$1.6x10^{-19}$
Ion energy distribution function	Drifting Max.	Maxwellian	Maxwellian
Ion temperature [eV]	0.15	0.1	3,000
Ion drift velocity [km/s]	4	0	0
Electron density [m^{-3}]	10^{13}	10^{11}	10^{7}
Electron mass [kg]	$9.11x10^{-31}$	$9.11x10^{-31}$	$9.11x10^{-31}$
Electron charge [C]	$-1.6x10^{-19}$	$-1.6x10^{-19}$	$-1.6x10^{-19}$
Electron energy distribution function	Maxwellian	Maxwellian	Maxwellian
Electron temperature [eV]	2	0.2	3,000

Table 2.1: A summary of relevant plasma properties along with values typical of the laboratory experiments in this dissertation, low earth orbit (LEO), and geostationary orbit (GEO) [19–21].

These models predict energy distribution and species evolution by accounting for collisions using their respective rate coefficients and the state of the plasma discharge [24, 25]. Despite their importance, particle collisions increased plasma complexity significantly by disrupting phenomena defined by electric and magnetic forces. It is common to label plasmas in which these phenomena occur uninhibited by collisions as "collisionless". The collisionless plasma assumption is common for space applications, as the ambient neutral gas density (and/or plasma density) in space is quite low compared to Earth-based plasmas.

2.1.5 Plasma Frequency

The electron plasma frequency is often considered the fundamental time scale of collective plasma behavior. More concretely, it is the electron oscillation frequency in response to charge separation within a plasma volume. The plasma frequency can be derived by assuming two "slabs" of opposite charge separated by some distance. Using the electric field between the two slabs and allowing them to move in response

to this field yields an oscillatory solution. The corresponding plasma frequency (in Hz) is defined in Equation (2.5), where e is the elementary charge, m_e is the electron mass, and ϵ_0 is the permittivity of free space. The plasma frequency tends to be quite high such that plasmas respond rapidly to changing environments. For example, the laboratory plasma defined in Table 2.1 has a plasma frequency of 28 MHz, whereas the LEO plasma has a plasma frequency of 2.8 MHz. The plasma frequency also has important implications for electromagnetic radiation propagation. Incident electromagnetic (EM) waves with frequencies lower than the plasma frequency are reflected and those with higher frequencies are transmitted.

$$f_p = \frac{1}{2\pi}\sqrt{\frac{n_e e^2}{m_e \epsilon_0}} \quad Hz \tag{2.5}$$

2.1.6 Ambipolar Diffusion

Plasma thermal velocities scale inversely with the square root of particle mass. Because of this, electron thermal velocities are at least 43 times that of ions with the same temperature. This thermal velocity difference favors electrons rapidly diffusing from a plasma volume before the slower ions have had a chance to react. However, we also know that plasmas are dominated by electric forces, magnetic forces, and collective behavior. In this case, charge separation rapidly establishes an electric field which slows electron expansion and accelerates ion expansion such that the two diffuse at the same rate. This phenomenon is known as ambipolar diffusion. Simplified expressions for the ambipolar diffusion coefficient and ambipolar electric field are provided in Equations (2.6) and (2.7), respectively by neglecting the ion contribution in favor of the (typically) much larger electron contribution. D_a is the ambipolar diffusion coefficient, T_e is the electron temperature, T_i is the ion temperature, and D_i is the ion diffusion coefficient in Equation (2.6). E_a is the ambipolar electric field, D_e

is the electron diffusion coefficient, μ_e is the electron mobility, and n_e is the electron density in Equation (2.7). A complete derivation of the ambipolar diffusion coefficient and electric field may be found in [26].

$$D_a \approx \left(1 + \frac{T_e}{T_i}\right) D_i \quad m^2/s \tag{2.6}$$

$$E_a \approx -\frac{D_e}{\mu_e} \frac{\nabla n_e}{n_e} \quad V/m \tag{2.7}$$

2.1.7 Debye Screening and Sheath Formation

A plasma's collective behavior acts to shield potential disturbances in a process known as Debye screening. This process can be understood via the example of a negatively biased conductor placed in a quasi-neutral Maxwellian plasma. Electrostatic electric fields will quickly repel plasma electrons in the vicinity of the conductor and, conversely, positive ions will be attracted to its surface. This process reaches equilibrium when the charge disturbance introduced by the negative conductor is completely canceled out by the ion-dominated space charge surrounding it. The characteristic distance over which plasma quasi-neutrality is disturbed in order to shield out this disturbance is known as the Debye length (λ_D). The most commonly used approximation for the Debye length is provided in Equation (2.8) using standard notation by neglecting the ion contribution in favor of the (typically) much larger electron contribution. A complete derivation of this expression can be found in [27].

$$\lambda_D \approx \sqrt{\frac{\epsilon_0 k_B T_e}{n_e e^2}} \quad m \tag{2.8}$$

The region of perturbed space charge surrounding a potential disturbance (such as a biased conductor) is known as the plasma sheath. Different sheath types form based on the potential of the disturbing object and the plasma composition. Two of the most common types of DC, collisionless sheaths are known as the Debye sheath and Child-Langmuir sheath. The Debye sheath forms for low sheath potentials and the Child-Langmuir sheath forms for high sheath potentials. For the purposes of this dissertation, the Debye sheath forms for sheath potentials less than about 5 electron or ion temperatures (depending on the sheath potential polarity) such that particles of the opposite charge are still able to reach the conducting surface. These charged particles help neutralize the space charge surrounding the conductor and establish a radial electrostatic potential profile defined by Equation (2.9). Equation (2.9) uses $\phi(r)$ for the local electrostatic potential, q for the test particle charge, r for the position (radius) relative to the conducting surface, and standard definitions for all other variables. Example density and potential profiles for the Debye sheath are shown in Figure 2.1 [28, 29].

A classical Child-Langmuir sheath forms when the sheath potential is high enough that very few repelled particles can reach the screened object. When this occurs, a net space-charge (and associated potential barrier) in the vicinity of the charged conductor is established, which prevents further particles of the same charge from entering. This type of sheath is space-charge limited, meaning that the current to the screened conductor is limited by a space-charge layer as defined in Equation (2.10) for planar geometries. Equation (2.10) uses J_{SCL} for the space-charge limited current density, m_α for the relevant particle mass, V for the voltage across the space-charge layer, and d for the sheath thickness. A complete derivation of Equations (2.9) and (2.10) can be found in [27].

$$\phi = \frac{q}{4\pi\epsilon_0 r} exp\left(-\frac{r}{\lambda_D}\right) \quad V \tag{2.9}$$

$$J_{SCL} = \frac{4\epsilon_0}{9}\sqrt{\frac{2q}{m_\alpha}}\left(\frac{V^{\frac{3}{2}}}{d^2}\right) \quad A/m^2 \tag{2.10}$$

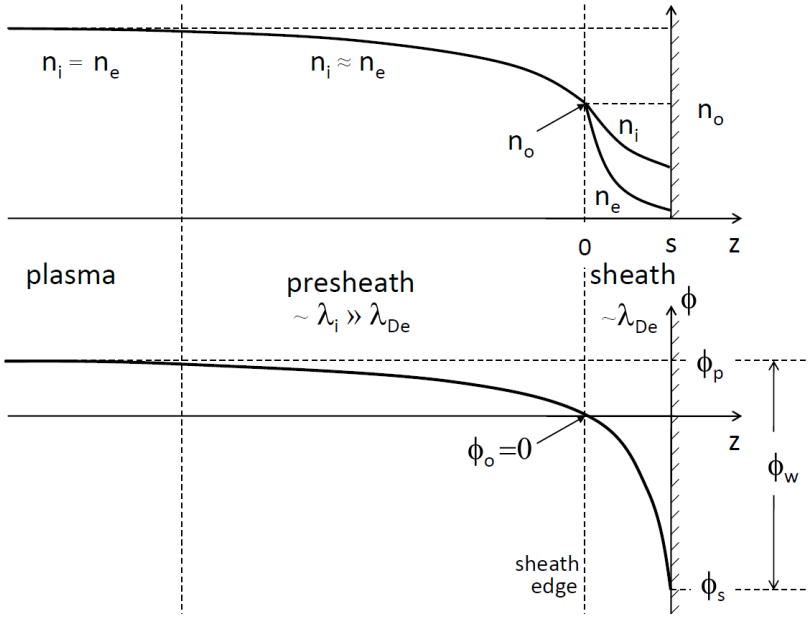

Figure 2.1: Example Debye sheath density and potential profiles showing the sheath, presheath, and plasma regions [28, 29].

Figure 2.1 pictures a large region between the sheath and quasi-neutral plasma known as the presheath. This quasi-neutral region is required to form a stable plasma sheath. The presheath accelerates cold ions to what's known as the Bohm velocity in order to produce a monotonic sheath potential profile with $n_i > n_e$ at all locations. The Bohm velocity is given by equation (2.11), in which v_B is the Bohm velocity, k_B is Boltzmann's constant and m_i is the ion mass. A full treatment of the Bohm velocity may be found in [27].

$$v_B = \sqrt{k_B T_e / m_i} \quad m/s \tag{2.11}$$

2.1.8 Magnetic Field Effects

Magnetic forces play a defining role in many different plasmas. As a starting point in the treatment of magnetic field effects, one can envision a single charged particle in a background magnetic field of constant magnitude and direction. The motion of such a particle is subject to the Lorentz force ($F_{Lorentz}$ in Equation (2.12)) according to the particle charge (q), velocity vector ($\mathbf{v}$), and background magnetic field ($\mathbf{B}$). Equation (2.12) states that the Lorentz force will always be perpendicular to both the particle velocity and background magnetic field, meaning the initial particle velocity along the magnetic field will not change. In addition, this constant force will result in an orbit circling the ambient B-field vector. By setting the centripetal force equal to the Lorentz force, we can solve for the radius of this orbit. This gyroradius (or Larmor radius) can be calculated using Equation (2.13) for nonrelativistic cases, for which r_g is the gyroradius, v_{perp} is the velocity component perpendicular to the magnetic field, and m_α is the particle mass. From here, it is straightforward to calculate the frequency at which the charged particle orbits the magnetic field vector. This gyrofrequency (f_g) can be calculated according to Equation (2.14).

$$F_{Lorentz} = q\,(\mathbf{v} \times \mathbf{B}) \quad N \tag{2.12}$$

$$r_g = \frac{m_\alpha v_{perp}}{qB} \quad m \tag{2.13}$$

$$f_g = \frac{qB}{2\pi m_\alpha} \quad Hz \tag{2.14}$$

Charged particle gyromotion effectively traps plasma particles along magnetic field lines, but the gyroradius dependence on mass leads to it impacting electron and ion populations differently. There are also a host of other plasma magnetic field effects which have been discovered and characterized over the years. These effects will not be treated by plasma diagnostic analysis techniques and most numerical models used in this dissertation as the experimental plasma was "non-magnetized." We say that the plasma is non-magnetized when the electron and ion gyroradii are both larger than the plasma Debye length in this context. An electron gyroradius representative of the experimental plasmas in this dissertation can be calculated using Equation (2.13). We do so by assuming an electron energy equal to the average experimental electron temperature (2 eV) entirely perpendicular to the local magnetic field ($v_{perp} = 8.4\text{x}10^5$ m/s) and a field strength at the Earth's surface of 0.5 G (50 μT). The resulting electron gyroradius of 9.5 cm is both larger than experimental Debye lengths and much smaller than the corresponding ion gyroradius. In reality, electron velocities typically followed an isotropic, Maxwellian (or Druyvestyn) distribution relative to the ambient magnetic field (see Chapter 5), leading to a continuum of v_{perp} over small values. The local magnetic field strength was also reduced significantly in comparison to its general surface magnitude of $\sim$0.5 G ($\sim$50 μT) by the stainless steel vacuum chamber walls. For example, the ambient magnetic field in the Large Vacuum Test Facility used in Chapters 4 and 5 actually has a magnitude of $\sim$9 μT [30]. There are other requirements used to define a plasma as non-magnetized, but the definition used here is considered conservative. Anticipating magnetic field effects in the unbounded domain of space is done elsewhere using numerical modeling and upcoming scaled

magnetic field chamber experiments (see Chapter 8).

2.2 Spacecraft Charging Fundamentals

2.2.1 Surface Charging

2.2.1.1 Current Balance Formulation

Surface charging, also known as frame or absolute charging, treats the spacecraft common potential with respect to the ambient plasma potential. Because spacecraft surfaces vary considerably, the entire surface is not necessarily at the spacecraft common potential. Nevertheless, the current balance formulation presented below is applicable to any isolated conductor and can be used to treat individual structures on the spacecraft surface. In addition, it is best practice to make the entire spacecraft surface conductive (often via coatings such as Indium Tin Oxide (ITO)). This is essentially why surface, frame, and absolute charging are used interchangeably. The metallic spacecraft frame and spacecraft common are typically defined by currents to the spacecraft surface and so we will treat the entire spacecraft surface as conducting.

A summary of all the major currents to a spacecraft surface are provided in Equation (2.15) [31]. I_{Total} is the total current, I_E is the electron current incident on the spacecraft surface, I_I is the ion current incident on the spacecraft surface, I_{SE} is the secondary electron current due to I_E, I_{SI} is the secondary electron current due to I_I, I_{BSE} is the backscattered electron current due to I_E, I_{PH} is the photoelectron current, I_{Active} is the current contribution of any active sources such as particle beams and plasma contactors, and V_{SC} is the spacecraft potential in Equation (2.15). A simple extension of Kirchhoff's Current Law (KCL) allows us to set Equation (2.15) to zero for equilibrium (constant potential) charging conditions. Equilibrium charging conditions are typically assumed, as the small capacitances associated with isolated spacecraft and short plasma current time scales often cause spacecraft po-

tential changes to occur more rapidly than environmental changes. A more complete treatment using numerical tools or circuit modeling is typically required if dV/dt is the metric of interest.

$$I_{Total} = I_E(V_{SC}) - [I_I(V_{SC}) + I_{SE}(V_{SC}) + I_{SI}(V_{SC}) + I_{BSE}(V_{SC}) + I_{PH}(V_{SC}) + I_{Active}(V_{SC})] \quad (2.15)$$

Solving Equation (2.15) by setting it equal to zero yields an equilibrium spacecraft potential but also requires all listed current values as a function of spacecraft potential. Most current terms are based on different physical phenomena and so draw from different physical disciplines. In the sections that follow, we provide a brief summary of how current terms are estimated and references to additional information. Before doing so, we would like to reiterate that the current balance formulation is most applicable for conducting spacecraft in cold, equilibrium plasmas (such as those found in LEO) and is by no means comprehensive. Modern spacecraft charging simulation tools such as NASCAP, MUSKAT, and SPIS are often required for missions with more stringent charging requirements.

2.2.1.2 Current Collection Theories

The foundational theory in current collection was originally laid out in the context of a conducting probe by Langmuir and Mott-Smith in 1926 [32]. The geometric shapes that were solved analytically include an infinite plane, an infinite cylinder, and a sphere - each in a non-magnetized, Maxwellian plasma. These results have since been generalized to also include Kappa, Cairns, and Kappa-Cairns distributions [33]. The validity of assuming infinite probe geometries, a non-magnetized plasma, or a Maxwellian plasma varies considerably with the spacecraft design and space plasma

in which it is immersed, but these assumptions are typically acceptable when developing first order approximations for LEO. Assumptions about the electrostatic potential near the conducting body are also necessary, as calculating the potential structure *ab initio* requires solving Vlasov's equation and Poisson's equation [34]. One required assumption is that the sheath potential structure must be monotonic to use these theories. Equation (2.16) gives the collected current of repelled particles for spherical, cylindrical, and planar geometries. Equation (2.17) gives the collected current of attracted particles to a sphere. Equivalent expressions for cylindrical and planar geometries are also available, but omitted here for the sake of brevity. These expressions were first developed by Langmuir and Mott-smith, while a more modern derivation is performed by Conde [32, 35]. A summary of the variables and nomenclature used in these expressions is provided in Table 2.2 and α is used to differentiate between ion and electron species.

Symbol	Definition
q	Particle charge
n	Ambient plasma density
A	Spacecraft surface area
k_B	Boltzmann's constant
T	Particle temperature
m	Particle mass
V_{SC}	Spacecraft potential
V_P	Ambient plasma potential
R_{Sheath}	Spacecraft sheath radius
R_{SC}	Spherical spacecraft radius

Table 2.2: Collected current nomenclature summary.

$$I_{Repelled} = \frac{q_\alpha n_{\alpha,0} A_{SC}}{4} \sqrt{\frac{8 k_B T_\alpha}{\pi m_\alpha}} exp\left(\frac{q_\alpha (V_{SC} - V_P)}{k_B T_\alpha}\right) \tag{2.16}$$

$$I_{Attracted,Sphere} = \frac{q_\alpha n_{\alpha,0} A_{SC}}{4}\sqrt{\frac{8k_B T_\alpha}{\pi m_\alpha}}\frac{{R_{Sheath}}^2}{{R_{SC}}^2} \left[1 - \left(1 - \frac{{R_{SC}}^2}{{R_{Sheath}}^2}\right) exp\left(-\frac{{R_{SC}}^2}{{R_{Sheath}}^2 - {R_{SC}}^2}\frac{|q_\alpha(V_{SC} - V_P)|}{k_B T_\alpha}\right)\right] \quad (2.17)$$

The repelled particle current in Equation (2.16) is straightforward to calculate and requires no further simplification. However, the attracted current in Equation (2.17) relies on the unknown parameter of R_{Sheath}. One assumption that is often used to eliminate R_{Sheath} is that the sheath is either very thick or very thin compared to the spacecraft dimensions. The validity of these assumptions depends entirely on the spacecraft size (R_{SC}) compared to the ambient plasma Debye length (λ_D), as the sheath thickness is approximately a few Debye lengths. For the thin sheath approximation, $R_{SC} >> \lambda_D$. In this case, the sheath is so thin that no escape is possible (except via reflection) and we say that any particle that enters the spacecraft sheath with sufficient energy will be collected. For the thick sheath approximation ($R_{SC} << \lambda_D$), we can imagine that particles may enter and exit the sheath without striking the spacecraft surface due to their initial angular momentum. Equation (2.17) is approximately equal to Equation (2.18) using the thin sheath approximation and approximately equal to Equation (2.19) using the thick sheath approximation [35].

$$I_{Attracted,ThinSheath,Sphere} \approx I_{sat,\alpha} = \frac{q_\alpha n_{\alpha,0} A_{SC}}{4}\sqrt{\frac{8k_B T_\alpha}{\pi m_\alpha}} \quad (2.18)$$

$$I_{Attracted,ThickSheath,Sphere} \approx I_{sat,\alpha}\left(1+\frac{|q_\alpha(V_{SC}-V_P)|}{k_BT_\alpha}\right)$$
$$= \frac{q_\alpha n_{\alpha,0}A_{SC}}{4}\sqrt{\frac{8k_BT_\alpha}{\pi m_\alpha}}\left(1+\frac{|q_\alpha(V_{SC}-V_P)|}{k_BT_\alpha}\right) \quad (2.19)$$

Equations (2.16), (2.18), and (2.19) can typically be used as first order approximations for $I_E(V_{SC})$ and $I_I(V_{SC})$. Figure 2.2 shows a I-V curve reporting the sum of ion and electron currents to spherical and cylindrical conducting probes in a Maxwellian plasma using these approximations [35]. The current to a planar (or flat) probe overlaps with those shown in Figure 2.2 between the floating and plasma potentials and is constant (flat) outside of this region [35]. Equation (2.16) is fairly simple and generally accepted for repelled particles in a Maxwellian plasma. However, Equations (2.18) and (2.19) are subject to a number of qualifications and are often found inadequate. Equation (2.18) is problematic as it does not account for sheath expansion when the spacecraft potential deviates from the plasma potential. In addition, most space plasmas studied thus far have Debye lengths too large ($>$ 1 cm) to reliably use the thin sheath approximation. Equation (2.19) is derived using Orbit-Motion-Limited theory and does not solve Poisson's equation, account for the space-charge of each particle, or include trapped particle trajectories [32, 36]. These limitations have led to a multitude of corrections, extensions, and more complete theories [36–38]. The thin- and thick-sheath approximations also leave an analytical gap for conditions in which $R_{SC} \approx \lambda_D$. Numerical tools are often the best solution for spacecraft operating under such conditions.

2.2.1.3 Secondary and Backscattered Particles

Secondary and backscattered currents are both caused by incident charged particles striking the spacecraft surface. Secondaries are emitted when a charged particle

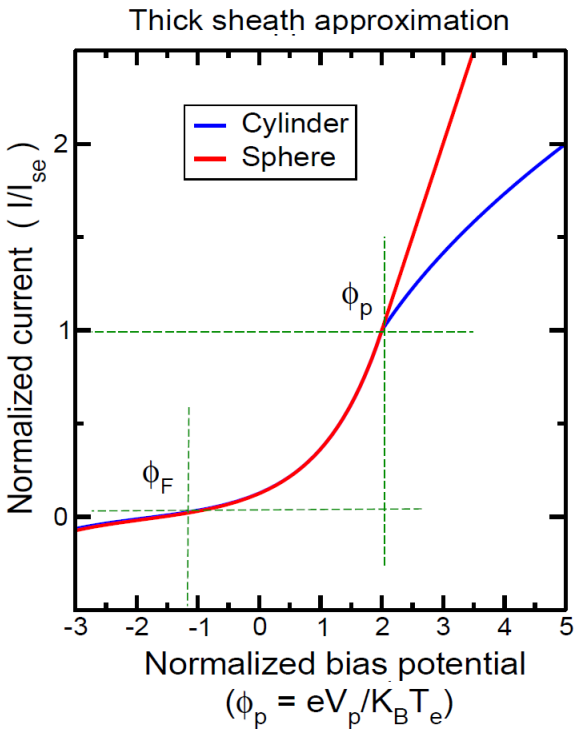

Figure 2.2: An example, normalized I-V curve showing the total current collection to a cylinder and sphere using the thick sheath approximation. The plasma and floating potentials are marked at the intersection of green dashed lines. The current grows roughly exponentially between these two potentials, as the collection current is dominated by repelled electrons [35].

approaches a surface with sufficient energy (typically $>$ 10 eV) and interacts with subatomic charged particles composing the surface lattice atoms [39]. These processes sometimes give neighboring charges the energy required to escape from the material surface. At high incident charged particle energies, the secondary emission process is limited by the particle embedding itself deep within the material. At low incident charged particle energies, secondary emission is rare as there is insufficient energy to knock out neighboring charges and particle reflection is more common. It is also worth noting the possibility for an incident particle to trigger the emission of multiple secondaries such that the secondary yield is greater than one. In contrast, the backscattering process deals with the fraction of particles that strike the surface and are backscattered rather than depositing their charge. This process typically oc-

curs when an electron is incident near a surface ion site such that it is attracted and redirected away by the nearby positive nucleus [39]. Backscattering increases with incident particle energy, as this also increases the particle's angular momentum.

Secondary and backscattered currents can be thought of as multipliers to the collected current term and represented using the coefficients δ and η, respectively in Equation (2.15). The coefficients represent the average number of secondary or backscattered particles that leave the surface for each incident (primary) particle. This coefficient representation allows the $I_{SE}(V_{SC})$, $I_{SI}(V_{SC})$, and $I_{BSE}(V_{SC})$ terms of Equation (2.15) to be replaced using $I_E(V_{SC})$, $I_I(V_{SC})$, δ, and η. Equation (2.20) demonstrates one such current term replacement using the coefficient representation, where $\delta_{E,E}$ and $\delta_{E,I}$ are the average number of secondary electrons emitted per incident electron and ion respectively, K_i is the incident particle kinetic energy, and θ_i is the incident particle angle. An example of how these coefficients vary with incident energy is provided in Figure 2.3.

$$I_{SE}(V_{SC}) = \delta_{E,E}(K_i, \theta_i) I_E(V_{SC}) + \delta_{E,I}(K_i, \theta_i) I_I(V_{SC}) \tag{2.20}$$

The secondary particle emission and backscattering processes are also heavily dependent on surface material properties. Unfortunately, this is an area of spacecraft charging that is notoriously incomplete and time consuming to advance. To illustrate this point, consider the basic physical parameters that affect secondary particle emission and backscattering. The angle of incidence, particle energy (which itself depends on the spacecraft potential), and a secondary or backscattering coefficient that accounts for both of these effects are all required for each individual particle type and surface prior to constructing a model that properly assigns an average coefficient to an assembly of collected particles [39]. To complicate matters, material properties that

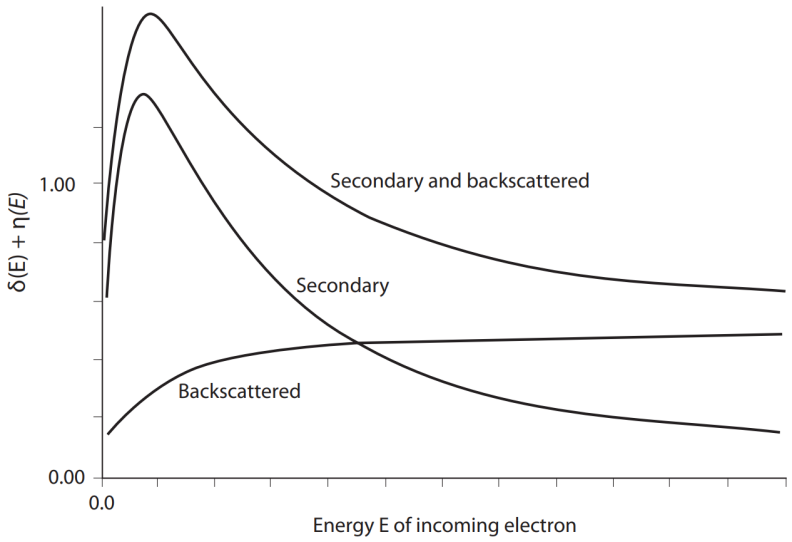

Figure 2.3: Example secondary and backscattering electron coefficients over incident electron energy [39].

have been studied in Earth-based vacuum chambers are found to change significantly in space due to radiation exposure, surface sputtering, and surface deposition [40, 41]. Simplifying assumptions are necessary due to these complications. One frequent assumption is that the contribution of secondary and backscattered ions is negligible [31]. This assumption allows us to eliminate $I_{SI}(V_{SC})$ from Equation (2.15), leaving $I_{SE}(V_{SC})$ and $I_{BSE}(V_{SC})$. These two currents may be estimated using the procedures and practices outlined by Sternglass and others [42–45].

2.2.1.4 Photoelectron Emission

The photoelectric effect in space also contributes to the net electron current leaving the spacecraft surface due to solar irradiance. In fact, the average photoemission current for normally incident sunlight in Earth orbit ($\sim$2 nA/cm^2) often dominates the other environmental current sources in Equation (2.15) [46, 47]. This large electron emission current forces most sunlit spacecraft to a potential positive with respect to the ambient plasma. Emitted photoelectron energy distributions may be approximated using a directed Maxwellian modified using Lambert's cosine law with a char-

acteristic energy in the range of 1 - 2 eV [48–50]. Thus, if the spacecraft potential is higher than a few volts positive with respect to the ambient plasma, photoelectrons will have insufficient energy to escape the spacecraft sheath and be recollected to the surface. This sharp gradient in $I_{PH}(V_{SC})$ just above the plasma potential limits spacecraft charging due to photoelectron emission to just a few volts positive. It is worth remembering that photoemission only occurs on sunlit surfaces and there is a strong angular dependence. Because of this, there may be large potential differences between sunlit and shaded spacecraft surfaces if they are not in electrical contact. This scenario is one example of what is known as differential charging.

2.2.1.5 Surface Charging Concerns

Surface charging in and of itself is typically not dangerous to spacecraft systems. Using proper practices to limit differential and internal charging allows geosynchronous spacecraft to safely operate with a spacecraft common potential thousands of volts below that of the ambient plasma [51]. One of the concerns introduced by surface charging is surface degradation via sputtering and material deposition [31]. Other concerns include potential arcs to the ambient environment and interference with space plasma measurements [31]. Surface charging can interfere with space plasma measurements by altering the energy and velocity vector of charged plasma particles. While the energy shift can be removed if contemporaneous spacecraft potential data are available, velocity vector correction requires an accurate model of the sheath potential structure surrounding the spacecraft (which is typically not possible). Ambient plasma measurements can also be contaminated by the presence of secondaries, backscattered electrons, and photoelectrons coming off the spacecraft surface.

2.2.2 Differential Charging

We previously described how one can determine a conductor's equilibrium potential using the current balance formulation. We specifically considered a spacecraft whose surface is entirely conductive; however, real world systems do not necessarily have all internal conductors and surfaces in electrical contact. Instead, each isolated component has its own respective current balance and charges to a different potential. This process is known as differential charging, a fairly straightforward concept which can be very difficult to control in practice.

Differential charging can lead to unanticipated electric fields and dangerous discharges or arcs between spacecraft components. Electrostatic discharges (ESDs), arcs, flashovers, etc. occur when a non-conductive medium breaks down under the influence of a strong electric field and suddenly becomes conductive [31]. The resulting current surge and its associated electromagnetic interference (EMI) has been shown to couple into nearby spacecraft systems. The end result is a wide array of system anomalies, from switch and logic latch ups, to telemetry interruption, to complete spacecraft loss [52, 53]. Formal guidelines were established in the 1980s to prevent differential charging. These guidelines recommend directly grounding systems to the spacecraft frame, using proper cable shielding, making the spacecraft surfaces conducting, and electrically isolating sensitive systems whenever possible [52, 54]. These measures have been largely successful in reducing the number of spacecraft anomalies induced by differential charging.

2.2.3 Internal Charging

Internal charging (also known as deep dielectric charging) is not altogether different from differential charging. Both forms of charging cause the breakdown of a nonconductive medium using an electric field. The defining characteristic of internal charging is that it takes place inside of an insulating material (which is often a di-

electric). High energy charged particles (> 1 MeV) are known to penetrate materials and stop at a depth determined by their initial kinetic energy and angle of incidence [55, 56]. Both protons and electrons penetrate aluminum at least 10 μm when their energy exceeds 1 MeV, as seen on the plot of penetration depth in Figure 2.4 [57]. Space plasma environments such as those at geosynchronous orbit feature particles exceeding this energy during geomagnetic substorms [56]. One can calculate the total fluence of energetic particles deposited in a dielectric layer during a substorm by multiplying the high energy flux by the substorm's duration. By accounting for the charge leak rate introduced by dielectric conductance, one can calculate the dielectric's internal electric field strength due to deposited charge separation. If the internal field exceeds the dielectric breakdown strength (typically $10^6 - 10^8$ V/m), an ESD will occur [56]. These ESDs have effects similar to those caused by differential charging, with the additional complication of being near critical internal components such as logic processors. Recent years have seen the recognition that internal ESDs occur far more frequently than originally thought (as will be discussed in Section 2.3) [58]. These revelations prompted the development of a comprehensive NASA handbook addressing internal charging which was originally released in 1999 [55, 59]. Numerical internal charging tools have also been developed in the form of the Fluence Model for Internal Charging (FLUMIC), Space Environment Information System (SPENVIS), the Dielectric Internal Charging Threat Assessment Tool (DICTAT), and others [60].

2.2.4 Charging Induced Anomalies

The spacecraft charging categories summarized in the preceding sections represent some of the gravest dangers to spacecraft during their operational lifetime. To understand the magnitude of this danger, we turn to publicly available data on satellite anomalies (a catch-all term used for unanticipated problems encountered in orbit). The dataset presented here was assembled using multiple anomaly databases and a

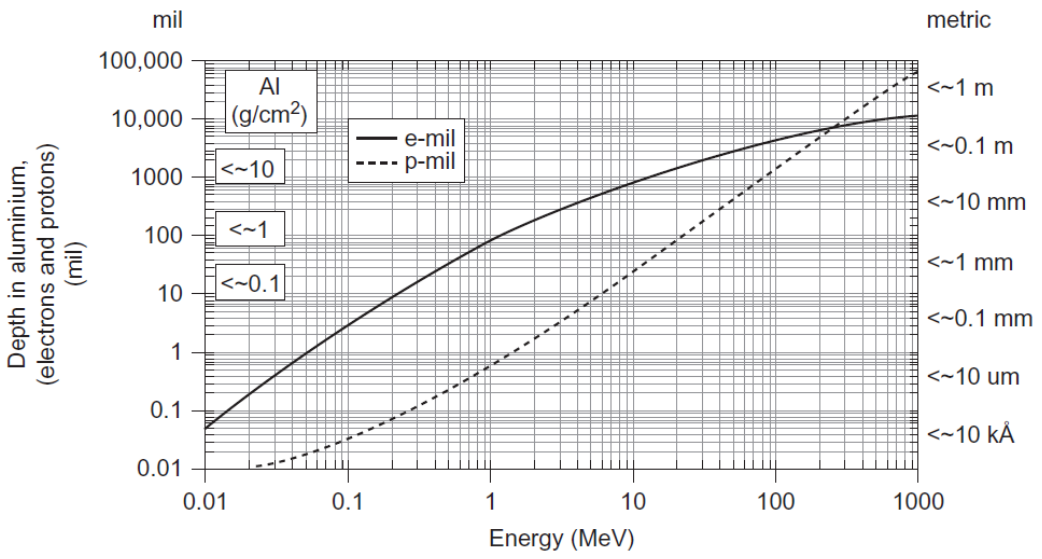

Figure 2.4: Proton and electron penetration depth in aluminum for a range of incident energies [57].

direct survey of relevant professionals across the space industry in the late 1990s [61]. 326 "Space Environment Impact Forms" were completed and 299 (92%) of these identified anomalies were attributed to the space environment [61]. Table 2.3 summarizes the 299 environmental anomalies by diagnosis type (or cause) and indicates that a full 54% were caused by ESDs tied to spacecraft charging [61]. In addition, this study identified 5 specific missions lost or terminated entirely due to electrostatic discharges prior to 1998 [61].

This particular dataset of 326 anomalies represented one of the more complete references on spacecraft anomalies. In reality, the vast majority of anomalies remain unknown to the public. There are many reasons for this secrecy, and they are often tied to protecting technical designs or spacecraft insurance claims [61, 62]. A 2014 report sponsored by the Defense Advanced Research Projects Agency (DARPA) advocates strongly for a central database to help bring the private world of spacecraft anomalies to light [62]. This report suggests that anomalies tied to spacecraft charging remain an important issue to this day. Further evidence of the ongoing dangers presented by spacecraft charging can be found in the anomaly studies of the last 10

years [63–66].

Diagnosis	Number of Forms
ESD - Internal Charging	74
ESD - Surface Charging	59
ESD - Uncategorized	28
Surface Charging	1
Total ESD and Charging	**162**
SEU - Cosmic Ray	15
SEU - Solar Particle Event	9
SEU - South Atlantic Anomaly	20
SEU - Uncategorized	41
Total SEU	**85**
Total Radiation Damage	**16**
Total Miscellaneous	**36**

Table 2.3: A survey of spacecraft anomalies caused by the space environment completed in 1998 [61].

2.3 A Brief History of Spacecraft Charging

The history of spacecraft charging research is as old as spaceflight itself. Indeed, much of the fundamental theory supporting the spacecraft charging field was developed prior to spaceflight for plasma probes [32]. A seminal review of spacecraft charging research published by Hank Garrett breaks its history prior to 1981 into four periods [31]. The first period was prior to 1957 when very little *in-situ* data were available. These early studies were focused on predicting the potential of interstellar dust grains and sub-orbital rockets [67, 68].

The second period began around the launch of Sputnik 3 in 1958, which made the first satellite potential measurements. Much of the foundational spacecraft charging work began during this period. Spacecraft sheaths, photoemission, the impact of satellite velocity, induced electric fields, and charged particle emission were first treated during this period and some success was found in predicting early satellite potential measurements [31, 69, 70]. The second period of spacecraft charging concludes

with the Chopra review paper of 1961 [71].

The third period occurred approximately between 1961 and 1965. It is during this period that the first accurate spacecraft potential measurements were obtained between 425 km and 2300 km above Earth [72]. Self-consistent solutions to Vlasov's and Poisson's equations were first used during this period, introducing particle trajectory tracking in the vicinity of the spacecraft [73, 74]. Realistic estimates of secondary electron emission, photoelectron currents, and drifting ion currents were also realized during this period. The third period of spacecraft charging ended in 1965 with the publication of the first book and thesis directly concerned with spacecraft charging [75, 76].

The fourth period began around 1965. It is defined by increasingly sophisticated surface charging models and a wealth of new *in-situ* spacecraft potential and plasma environment measurements, particularly in low Earth orbit (LEO) [77]. It is during this period that kilovolt potentials were first observed at geosynchronous orbit [78–80]. The Applied Technology Technology Satellites 5 and 6 (ATS-5 and ATS-6) were launched into geosynchronous orbit in 1969 and 1974 respectively [80]. Both satellites featured plasma detectors, ion thrusters, and normally observed spacecraft potentials of -1 to -10 kV in eclipse [80]. One major difference between these sequential missions is that ATS-5 used a hot filament electron emitter to neutralize the ion thruster beam while ATS-6 used a hollow cathode (plasma emitter) [80]. Plasma emission was found to be a much more effective neutralizer, as it forced the spacecraft potential closer to zero and resolved the differential charging issues encountered during active electron emission on ATS-5 [80]. The Spacecraft Charging at High Altitudes (SCATHA or P78-2) spacecraft was also hugely influential during this period. SCATHA featured instrumentation similar to ATS-6 with the notable addition of a dedicated electron beam [80]. The effects of varying electron emission current and electron beam return were both observed on SCATHA [80, 81]. The end of the fourth period of spacecraft

charging research coincides roughly with Garrett's review paper in 1981 [31]. These developments culminated in spacecraft design guideline and requirement documents that are still in use to this day [52, 54].

The fifth period of spacecraft charging is summarized via a review paper in 2000 [77]. The broader community rightfully recognized surface charging as a serious operational threat and official guidelines began to bear fruit during this period [77]. One major outcome of the Combined Release and Radiation Effects Satellite (CRRES) mission in 1990-1991 was the discovery that internal (deep dielectric) charging is a much more frequent and dangerous process than previously thought. Over 4,000 internal electrical discharges were recorded during the 14-month lifespan of that mission [58]. The lessons learned from the CRRES mission contributed significantly to the release of a NASA handbook specifically addressing internal charging in 1998 [55].

The fifth period also featured novel technology missions which made use of high-voltage and complex space structures such as the electrodynamic tether [77]. Two example electrodynamic tether shuttle missions from this period include the Tethered Satellite System 1 Reflight (TSS-1R) and Plasma Motor Generator (PMG). The TSS-1R mission deployed a large spherical conductor over 19 km from the space shuttle in order to understand its current collection behavior and test the gravity-gradient stabilization of a long, two-body system [82]. This ambitious mission demonstrated electron collection 2-3 times larger than predicted despite a premature tether break [82]. The PMG mission used a 500 m tether and had similar goals to TSS-1R, with the notable addition that plasma emission (via plasma contactor) was successfully used to enhance current to the tether end bodies [83, 84]. These complex structures pushed the limits of existing analytical theories and a budding ecosystem of computer simulations.

If one were to define a sixth period of spacecraft charging covering the last 20 years, it would be one marked by steady growth and practicality for large spacecraft

and a new frontier for small spacecraft. Charging simulation software has gained widespread traction internationally in the form of the NASA/Air Force Spacecraft Charging Analyzer Program (NASCAP), the Multi-Utility Spacecraft Charging Analysis Tool (MUSCAT), the Spacecraft Plasma Interaction Software (SPIS), and others. Several instructive documents have been compiled in this period to solidify and spread knowledge on the spacecraft charging field [19, 57]. These advances have supported some of the most rigorous spacecraft charging analyses to date for Juno and the Van Allen Probes as they explore the extreme environments of the Jovian magnetosphere and the Earth's radiation belts respectively [85–87]. Studies into the cause of extreme charging at GEO during this period also supported the JUNO and Van Allen Probe missions [51, 63].

The ongoing operation of the International Space Station (ISS) is another major achievement in the world of spacecraft charging over the past two decades. Understanding and accounting for the charging induced by 2,500 m^2 of 160 V solar arrays on the ISS led to new procedures which prevent high voltage solar array arcing [64, 88–90]. The ISS solar arrays also represented a very real shock hazard to astronauts during extravehicular activities (EVAs). The solar arrays were originally predicted to drive the spacecraft potential below -140 V while spacesuit materials were found to arc at voltages as small as +/- 70 V [88]. This discovery led to a spacecraft potential diagnostic being quickly integrated on the station and the standard operation of two neutralizing plasma contactor units (PCUs) during EVAs [88]. Thankfully the ISS was equipped with these plasma-emitting spacecraft neutralizers since its inception [91, 92]. Spacecraft neutralization using plasma emission will be discussed further in Section 2.5.2.

Spacecraft have been miniaturized as never before in this sixth period of spacecraft charging with the advent and growing popularity of the CubeSat standard [93]. The small form factor of this new spacecraft class (composed of 10 cm cubes) exposes

CubeSats to the space environment more than larger, traditional spacecraft. This exposure makes CubeSats and other small spacecraft more susceptible to spacecraft charging [94]. Their low cost and general accessibility often leads to less rigorous spacecraft charging analyses as well [94]. Numerical tools such as the Probe Spacecraft Interaction Code for Low Earth Orbit (PSIC-LEO) and dedicated testing facilities such as those at NASA Marshall Space Flight Center are actively making spacecraft charging tools more accessible to users of this new spacecraft class [95–97]. In the present year of 2020, we look forward to a future of spacecraft charging developments that will enable new missions benefitting mankind.

2.4 A Brief History of Electron Emitting Space Experiments

The history of electron beam experiments in space begins with the theory work of Lee Parker and Brian Murphy. The Parker-Murphy model of 1967 predicts the potential of electron-emitting satellites in a collisionless, magnetized plasma assuming the conservation of angular momentum and is still used to this day [98]. This theoretical work paved the way for missions such as the ATS-5 and the Artificial Aurora Experiment of 1969 [1, 80]. The ATS-5 and SCATHA technology demonstration missions both used active electron emission to advance the field of spacecraft charging as described in the preceding section. POLAR-5 (1976), MAIMIK (1985), CHARGE-2 (1985), and CHARGE-2B (1992) were other technology demonstration missions which also studied plasma wave generation by electron beam injection [99–104].

Many missions used electron accelerators to explore fundamental plasma problems and critical aspects of the space plasma environment in brand new ways [104]. Topics of particular interest were beam-plasma interactions (especially what is known as the beam-plasma discharge), artificial aurora generation, geomagnetic particle mirroring, and induced plasma waves [104]. The excitement and flurry of activity during this experimental heyday are well captured in a 1985 review paper and summary book

released in 1982 [103, 104]. A few notable science missions include the ECHO experiment series (1970-1988), the Artificial Radiation and Aurora between Kerguelen and the Soviet Union (ARAKS, 1975), and Spacelab 2 (1985) [103–106]. ARAKS and the ECHO experiments observed geomagnetic particle mirroring and conjugate magnetic field points starting from the ionosphere/plasmasphere and validated contemporary magnetic field models [103, 105]. The Spacelab 2 electron beam generated Whistler waves detected 216 m away along the local magnetic field line using direct current (DC) electron beam emission from the space shuttle bay [106].

The number of electron-emitting missions decreased markedly after the CHARGE-2B suborbital rocket launch and TSS-1 shuttle mission of 1992 [107]. Recent, dedicated scientific missions have largely focused on the same questions as before [108]. However, there have also been notable new applications for electron emitting technologies. For example, electron emission research supported the surge of tethered space missions in the 1990s [107]. Active electron emission is somewhat uncommon today and often done using specialized, niche hardware. The e-beam thermionic cathode is designed for efficiency and low-power ($\sim$0.1 W) operation. This cathode has been included on small satellites with limited power budgets such as the SENSE satellites and MiTEE-1 [109, 110]. The Electron Drift Instrument (EDI) fires two low-current electron beams perpendicular to the background magnetic field and observes their return to the spacecraft via magnetic gyration. EDI is able to determine local electric fields, magnetic field gradients, and magnetic field strength using this arrangement [4]. A relativistic ($\sim$1 MeV) electron beam is even under development for space applications [111]. Electron-emitting space experiments actively being pursued include MiTEE-1, MiTEE-2, Beam-PIE, B-SPICE, and CONNEX [8, 10, 110, 112].

2.5 Modern Spacecraft Charge Control

2.5.1 Introduction

In this section we focus on active charge control techniques used to modify the spacecraft frame potential (or spacecraft common). Active charge control techniques, as the name suggests, require specific spacecraft subsystems, power, and control. These techniques can be used to directly alter the spacecraft current balance of Equation (2.15) in order to achieve the desired V_{SC}. In contrast to active charge control, there are numerous passive charge control techniques that limit spacecraft charging effects without any power or control required. One such technique is coating the spacecraft surface to alter material properties such as conductance, secondary electron yield, or photoelectric work function. One recent example of spacecraft using this technique to limit differential charging in an extreme environment are the Radiation Belt Storm Probes (RBSP, also known as the Van Allen Probes) [87]. Numerous other passive control techniques have proven to be quite effective at limiting differential and internal charging. A detailed description of these techniques is not required for the purposes of this dissertation, but recommended practices can be found in the relevant NASA charging handbooks [52, 55, 59].

2.5.2 Active Charge Control Techniques

2.5.2.1 Ion Emission

Ion current emission is a straightforward and direct way to alter V_{SC} by setting $I_{Active}(V_{SC})$ of Equation 2.15 to a constant, negative value. In general, ion emission drives the spacecraft potential down by removing positive charge from the spacecraft. Emitted ion populations are characterized by their current, kinetic energy, charge, and mass. These values are often constant for simplicity, but this is by no means a requirement. Ion emission current and energy are two particularly important param-

eters as the first drives changes in the spacecraft potential and the second defines the potential at which emitted ions will be electrostatically pulled back to the spacecraft surface. Indeed, one of the major practical considerations when using an ion emission technique are ion trajectories relative to the spacecraft structure. Ions are often emitted in a divergent cone and ion impingement on spacecraft surfaces can instigate a host of negative side effects from surface sputtering to an increase in the spacecraft's angular momentum [113].

Two of the most common types of ion emitting device are plasma-based ion sources and liquid metal ion sources (LMIS). Plasma-based ion sources include the Kaufman source, multipole or magnetic cusp source, bucket source, and RF source. All of these devices generate quasi-neutral plasmas in an enclosed volume by ionizing a neutral gas expellant. The use of biased screen grids over part of the enclosing surface allows for the selective emission of positive plasma particles and the retention of negative particles. This class of ion source has a significant amount of spaceflight heritage as they are often used for spacecraft propulsion purposes as ion thrusters [27]. In fact, seminal spacecraft charging missions such as ATS-5, ATS-6, and SCATHA used their ion thrusters as an ion beam by simply turning off the beam neutralizer [114, 115]. A graphical representation of a plasma ion source is shown in Figure 2.5 (a) [116].

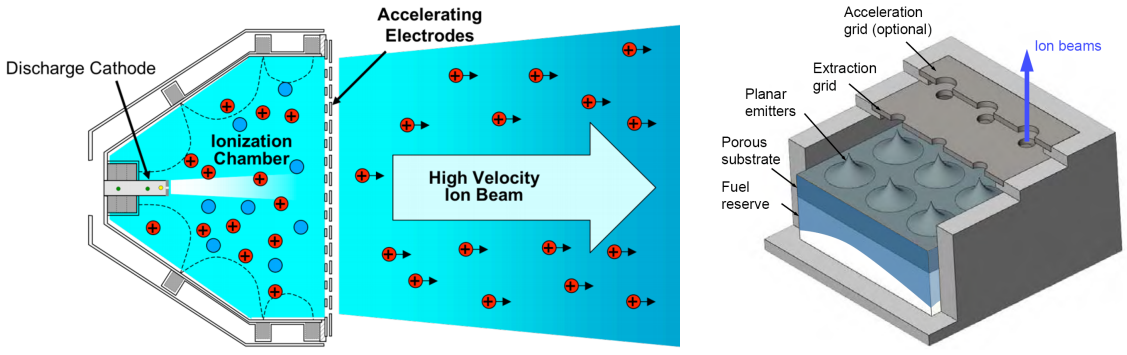

(a) (b)

Figure 2.5: Ion sources used for spacecraft charging purposes include (a) plasma-based ion sources and (b) liquid metal ion sources [116, 117].

Liquid metal ion sources (LMIS) apply electric fields to sharp points coated in a low volatility metallic liquid [118]. Under the influence of a sufficiently strong electric field, field ion evaporation extracts ions directly from the metallic liquid at the tip of a Taylor cone [118, 119]. Space-based LMIS are a fairly new technology in comparison to plasma ion sources, with their own inherent advantages and disadvantages. LMIS are small and low power in comparison to plasma ion sources. LMIS can also be operated at low ion beam energies and do not require compressed gas storage and management systems. However, LMIS are also low current ($\sim$20 μA), must heat the metal expellant in order to make it liquid, and have yet to address important lifetime and surface contamination questions [120, 121]. One technique used to scale up LMIS emission current and reduce the metal expellant heating restriction is using an array of emitting points in one common liquid metal reservoir. An example of this configuration is provided in Figure 2.5 (b) [117]. Two notable missions which made use of LMIS for spacecraft charging purposes are the Geotail and Magnetospheric Multiscale (MMS) missions [120, 121].

2.5.2.2 Electron Emission

Many of the considerations relevant to spacecraft charge control using ion emission also apply to electron emission. The emission of a pure electron current is a direct way to alter V_{SC} by setting $I_{Active}(V_{SC})$ to a non-negligible, positive value. In general, electron emission increases the spacecraft potential by removing negative charge from the spacecraft and emitted electron populations are characterized by their current and kinetic energy. Electron emission current and energy are often constants due to the prevalence of DC electron sources, but radiofrequency (RF) or alternating current (AC) electron sources are also used. Electron emission current and energy are particularly important parameters with respect to spacecraft charging as the current drives changes in V_{SC} and the energy defines the spacecraft potential at

which electrons will return to the spacecraft. One other practical consideration when actively emitting electrons is accounting for their trajectories in the vicinity of the spacecraft. Electron impingement on spacecraft surfaces can cause side effects ranging from differential charging to spacecraft sheath ionization.

By far the most common type of electron emitting device is the thermionic electron source. Thermionic sources "boil" electrons off a material that has been heated to a very high temperature. High temperatures are typically achieved via Joule heating by passing an electrical current through the cathode. The thermionic current emitted from a hot cathode is a function of the cathode temperature and work function as defined by the Richardson-Dushman equation (Equation 2.21) [122]. $J_{Emission}$ is the thermionic emission current density, A is Richardson's constant, T is the cathode temperature (in K), W is the cathode work function, and k_B is Boltzmann's constant in Equation 2.21. Accelerating electric fields are often used in the vicinity of thermionic cathodes to overcome space-charge current limitations, direct electron emission, and increase electron energy. A simplified example of one such system is shown in Figure 2.6 (a) as configured for the MiTEE-1 spacecraft [110]. A thermionic electron source was used on most historical missions featuring active electron emission for spacecraft charging purposes. For example, hot filament sources were used on the ATS-5 and SCATHA missions [114, 123].

$$J_{Emission} = AT^2 exp\left(-\frac{W}{k_B T}\right) \tag{2.21}$$

One alternative to thermionic sources are field effect electron sources, which make use of electric fields in order to extract electrons from a solid via quantum tunneling [125]. The current produced by this tunneling process depends upon a host of system parameters and is summarized by the Fowler-Nordheim equation [125]. The design

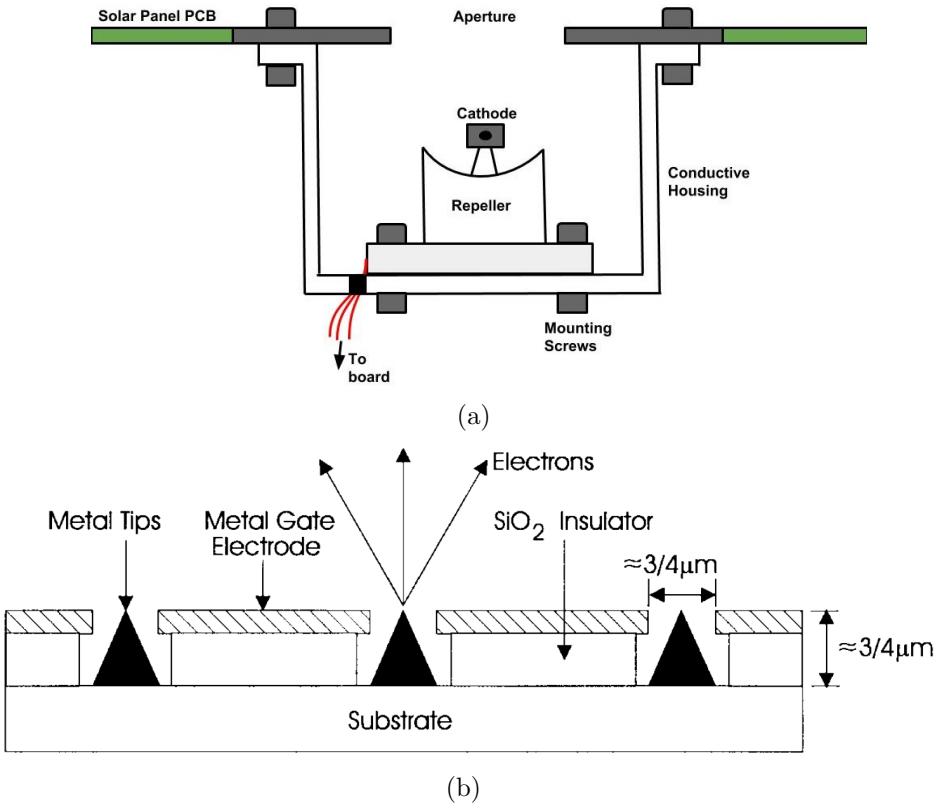

Figure 2.6: Electron sources used for spacecraft charging purposes include (a) thermionic sources and (b) field effect sources [124].

most optimized for space applications consists of an array of cold, Spindt points arranged so that the electron-emitting points are aligned with the center of accelerating grid apertures [126]. This particular arrangement is known as a field emitter array (FEA) and has been shown to increase electron emission current density and reduce system power requirements [126]. An example FEA is shown graphically in Figure 2.6 (b) [124]. Field effect emission is much more energy efficient than the more traditional thermionic emission. However, field emission sources suffer from low current densities and lifetime concerns associated with the degradation of its small scale structures [126]. Because of these drawbacks, the FEA has seen relatively little use for spacecraft charging purposes thus far.

2.5.2.3 Plasma Emission

While pure ion or electron emission allows for direct modification of the current balance in Equation 2.15, the emission of a cold, quasi-neutral plasma has proven to be preferable for spacecraft charge neutralization in almost all cases. Essentially, this is because of the flexibility provided by plasma emission compared to other active techniques. Plasma emission allows $I_{Active}(V_{SC})$ to be either positive or negative. Plasma emission can also be engineered to dominate the other current terms in Equation 2.15, solving the equation such that V_{SC} is within a few volts of the ambient plasma potential ($\sim$0 V). The current contribution due to plasma emission is also not strictly limited to charge emission. Plasma emission enables enhanced current collection from the ambient plasma by expanding the spacecraft's effective collection area, thereby forming a conductive "bridge" or "contactor" to the ambient plasma [84, 127, 128]. Plasma emission also remedies differential surface charging, unlike ion and electron emission which typically exacerbate it [123, 129]. The presence of a dense, low energy plasma population allows for particles to flow to differentially charged spacecraft surfaces so that an approximately equipotential structure is achieved. For these reasons, plasma emission is considered the gold standard in active spacecraft charge control and has been used on hundreds of satellites and the ISS [27, 130].

Plasma sources, or plasma contactors, come in a variety of forms. While there is a long list of different methods to generate and emit a plasma, the most commonly used device for space applications is some variant of the hollow cathode. A graphical representation of a space-based hollow cathode is provided in Figure 2.7 for reference. Hollow cathodes produce plasma primarily through impact ionization as electrons are accelerated between cathode and keeper electrodes in a volume filled with neutral gas. These electrons can stem either from previous impact ionization events (as in a steady state glow discharge) or from thermionic emission off a hot cathode insert. A low work function, thermionic insert is used to produce primary electrons that initiate plasma

emission. Therefore, insert heating is required to initiate plasma emission. Two common heating mechanisms are Joule heating (using a "heater" wire close to the insert) and sustained, high voltage arcing between the cathode and keeper electrodes [27, 131]. Additional ionization stages and confining magnetic fields can also be added to optimize the cathode's ionization efficiency and expellant utilization.

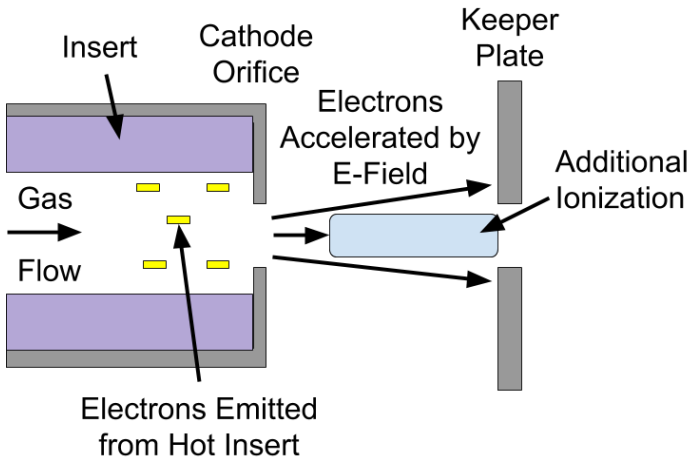

Figure 2.7: A graphical representation of a space-based hollow cathode.

2.5.2.4 Alternate Active Techniques

There are a few less common active charge control techniques that deserve mentioning besides direct charged particle emission. Current collection to the spacecraft can be altered by actively biasing an exposed surface relative to spacecraft common. For example, consider a conducting sphere that can be actively biased in the ambient plasma far from the spacecraft. Applying a positive bias to this sphere will cause it to collect net electron current which ultimately is accumulated by spacecraft common. Thus, biasing this sphere positive will cause spacecraft common potential to decrease. The opposite relationship also holds true for ions (although the collected current magnitude is significantly lower). The large number of active bias configurations make it a flexible option when active charged particle emission is not possible, such as on spacecraft measuring low energy ion populations. It has also been suggested that ul-

traviolet LED light be directed at spacecraft surfaces in order to neutralize negative charging via forced photoelectron emission. This technique could be easily controlled and used to prevent charging in eclipse, but a mission demonstrating this technique has yet to be flown.

2.6 Modern Charge Control Limitations

2.6.1 Size, Weight, and Power

The acronym SWaP is often used in the space engineering world. Component size, weight, and power (SWaP) are of paramount importance during the design (and costing) process and is often the reason why certain systems are selected over others. Passive charge control techniques such as coating the spacecraft surface are fairly low SwaP and low complexity. This is one major reason why they have been so widely adopted in comparison to active charge control techniques. Active charge control techniques are fairly high SwaP as they involve machined, metallic structures that must be mounted on the exterior of the spacecraft. The acceleration of charged particles and heating of thermionic materials also means these techniques demand more power than many small satellites can afford to spare. Finally, any device that emits ions requires some sort of expellant storage and feed system. The storage of compressed gas on a spacecraft sometimes requires special launch approval to ensure tank rupture is not a concern. Reducing charge control SWaP and complexity would lead to higher adoption rates and/or increased capabilities.

2.6.2 Charge Monitoring

One of the largest limitations on effective spacecraft charge control is a distinct lack of charge monitoring. In fact, most spacecraft do not feature any form of spacecraft charge monitoring. The primary reason for this is that most missions meet their re-

quirements without active charge control using modern practices. A charge monitor is often not worth its innate cost/complexity if there is no active charge control in place to make use of the information. Spacecraft potential monitors must be placed so that they are exposed to the ambient plasma in order to estimate its potential. These monitors typically require a custom design to suit the mission, precision machining and assembly, and dedicated electrical hardware. The list of spacecraft potential monitors includes Langmuir probes, electrostatic analyzers (ESAs), retarding potential analyzers (RPAs), and surface potential monitors [19]. Differential and internal charging monitors are similar in that they measure either local electric fields (sometimes via local potential measurements) or electrostatic discharges. Both measurements are fairly straightforward in comparison to spacecraft potential monitors, but their localized nature requires that monitors be distributed throughout the spacecraft (or at least in locations where differential charging may occur). Example monitors which fit this mold are internal discharge and surface potential monitors [58, 132, 133].

There are also charge monitoring requirements that cannot be achieved using existing technologies. Monitor data typically must be downlinked and analyzed using the esoteric plasma theories relevant to spacecraft charging in order to produce an actionable data product. This restriction precludes making critical decisions on-orbit in order to prevent damage associated with rapid spacecraft charging. In addition, the ability to measure rapid spacecraft charging (high dV/dt events) is limited by current spacecraft potential monitors. For example, spacecraft potential monitors rely on sampling the ambient plasma to calculate the spacecraft potential. A monitor's capacitance must be filled by current from the ambient plasma prior to making reliable voltage and current measurements [134]. Thus, events that trigger rapid spacecraft charging cannot be properly monitored in tenuous space plasmas. Particle beam emission (such as what is proposed for the CONNEX mission) and solar array unshunts/disconnects (such as those performed on the ISS) are two examples

that are not always resolved sufficiently using existing spacecraft potential monitors [14, 135]. Clearly modern charge control options suffer thanks to the cost, complexity, and limitations of the spacecraft charge monitoring that informs them.

2.6.3 Untested Configurations

New and postulated charge control techniques that would benefit from renewed research are introduced in this chapter. Because spacecraft charge control is often considered a support activity or engineering problem, innovation has slowed significantly since the dedicated missions and handbooks of the previous century. In reality, there remain critical capabilities beyond our reach due to spacecraft charging effects and untested charge control schemes that promise to resolve the issue. One example capability currently beyond our reach is the emission of a high current electron beam in tenuous space plasmas. The last time this was attempted in the magnetosphere (on the SCATHA mission in 1979), the spacecraft charged so positive that the beam returned to the spacecraft and caused three distinct payload failures [7]. The work presented in this dissertation aims to enable high current electron beam emission in tenuous space plasmas by experimentally validating a novel charge control scheme on the ground. It is our hope that other untested configurations be validated such that spacecraft charging does not impede the advance of space science.

CHAPTER III

A Novel Spacecraft Charge Neutralization Method: The Ion Emission Technique

3.1 Motivation

Dangerously high spacecraft potentials have been experienced by active missions emitting electron beams without a charge mitigation scheme [129, 136]. Previous missions falling into this category sometimes report induced spacecraft potentials exceeding hundreds, or even thousands of volts depending on their respective beam current and energy [129, 136]. When the positive spacecraft potential reaches the electron beam energy during active emission, the beam must return to the spacecraft as the electrons are pulled back electrostatically [7, 81]. Beam return is highly undesirable in most scenarios as it prevents beam escape and the returning electrons have been shown to damage spacecraft systems [7, 81]. For example, emission of a 6 mA, 3 keV electron beam on the P78-2 (SCATHA) satellite at an altitude exceeding 28,000 km (where the electron density was estimated to be less than 10 cm^{-3}) caused three distinct payload failures and created a transient problem in the satellite telemetry system [7]. Applying Gauss's law shows that a 1-meter radius spacecraft emitting the SCATHA electron beam would experience beam return in just 56 μs when ignoring current collection from the ambient plasma (which for SCATHA was quite small

compared to the electron beam current). A spacecraft charge mitigation scheme has proven critical for scenarios in which the electron beam current exceeds the thermal electron current from the ambient plasma. We will refer to electron beams capable of exceeding the local plasma thermal electron current as "high-current".

One proposed mission concept, known as the Magnetosphere-Ionosphere Connections Explorer (CONNEX), uses high-current electron beams to trace magnetic field lines from the magnetosphere down into Earth's upper atmosphere/lower ionosphere [8, 9, 12]. In doing so, CONNEX promises to connect distant regions of near-Earth space via the electron beam and establish causality between magnetospheric and ionospheric phenonmena [8, 9, 12]. This connection would allow space scientists to answer important, fundamental questions on magnetosphere-ionosphere coupling for the first time [8, 9, 12]. The potential impact of such a mission is significant enough that spacecraft charging mitigation of high-power electron beams is listed as an outstanding technology problem in the National Research Council's 2012 decadal survey for space physics [12, 13].

While the simultaneous emission of a high-current ion beam may seem the most straightforward mitigation strategy, the need to precisely balance independent ion and electron beam currents and all their induced effects make implementing this strategy challenging at best [14, 129, 137, 138]. As a simple example, consider balancing the SCATHA electron beam with an equivalent ion beam current whose current differs by just 1% (60 μA). Applying Gauss's law shows that a 1-meter radius spacecraft emitting these beams would still experience beam return in just 5.6 ms when ignoring current collection from the ambient plasma.

Another potential spacecraft charging mitigation scheme involves the emission of a quasi-neutral plasma. Plasma emitting devices (such as the hollow cathode or more generally, a plasma contactor) have been shown to mitigate positive spacecraft charging during electron beam emission exceeding 0.8 A in LEO [139]. As a result of

the higher plasma density in LEO (which typically exceeds 10^4 cm^{-3}), it is possible for a plasma contactor to balance the electron beam current by acting primarily as an ion emitter, an electron collector, or both [140]. The two most extreme cases, in which the contactor (emitted) plasma acts exclusively as an ion emitter or exclusively as an electron collector, are shown graphically in Figure 3.1. Ground-based studies suggest that both processes occur in LEO as positive and negative charges counter flow through a double layer separating the dense contactor plasma from the less dense ambient plasma [127]. Space and ground based studies of this system indicate that the electron collection process in LEO likely benefits from plasma turbulence or some other form of anomalous resistivity to enhance electron current collection across the Earth's magnetic field [84, 128]. These studies are critical to understanding the plasma contactor neutralization process in the high-density plasma environment of LEO.

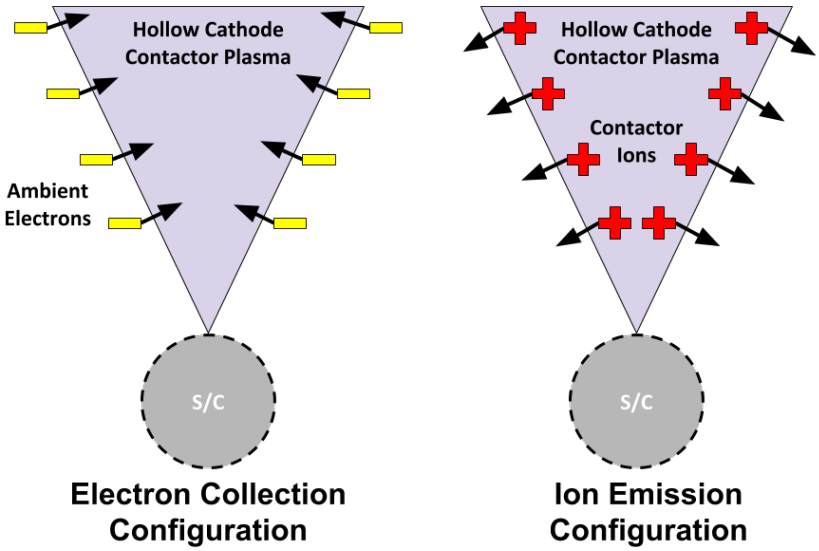

Figure 3.1: Fundamental contactor plasma current flow configurations for positively charged spacecraft.

The regime (electron collection or ion emission) in which the plasma contactor operates most effectively and to what extent spacecraft charging neutralization can be achieved remains an important open question. The plasma contactor regime depen-

dence on electron beam current, spacecraft size, and ambient plasma conditions are of particular interest. For example, the ion emission regime is the only viable charge mitigation scheme in tenuous space plasmas. There is experimental evidence that plasma emission can mitigate positive spacecraft charging in more tenuous plasma environments. Two early missions which first reported this capability were the ATS-5 and ATS-6 missions operating in geosynchronous orbit [80]. Recent work has also reported on the neutralizing effect of plasmas generated during hypervelocity dust impact in tenuous plasmas [141, 142]. However, contactor plasma physics from an electron beam emitting spacecraft in a tenuous space plasma has never been studied with space experiments. Whether the contactor would operate successfully in this regime has remained an open question that demanded further study.

In this chapter, we summarize extensive numerical modeling efforts led by Los Alamos National Laboratory which attempt to answer the open questions posed above. These efforts were initially undertaken to identify an effective and reliable neutralization scheme for the CONNEX mission and henceforth enable high-current electron beam emission in tenuous space plasmas. The Curvilinear Particle-in-Cell (CPIC) tool is described first and the predicted results using various charge control methods reviewed. A physical understanding known as the ion emission model came from this work and was later formalized into a semi-analytical numerical model with notable advantages in run time, accessibility, and applicable regimes. The spherical form of this model is derived, and its results are compared to what was found using CPIC. Successful comparisons between these two tools motivate the experimental validation campaigns treated subsequently in this work.

3.2 Curvilinear Particle-in-Cell (CPIC) Ion Emission Simulations

3.2.1 CPIC Description

The CPIC code is based on the kinetic Particle-In-Cell (PIC) method which is frequently used for plasma simulation and was originally developed in the mid-1950s [143–146]. The PIC method tracks individual particles in Langrangian coordinates by storing each individual particle's position, velocity, mass, and charge. These simulated particles are typically used to represent an ensemble of many real-world particles (portions of phase-space) in the physical plasma system in order to make simulation run times manageable. Super-particles (or macroparticles) such as these must have the same charge to mass ratio as the physical particles they represent. To determine how particle position and velocities evolve in time, plasma moments such as the local particle and current densities are calculated at each physical location (in Eulerian coordinates) by summing up individual particle contributions in each cell. These plasma moments are then converted to force fields using Maxwell's equations. The resulting force fields are used to modify the particle position and velocity according to the Vlasov equation [147, 148]. The Vlasov equation (Equation (3.1)) describes how particle distribution functions change in time (the first term) according to their motion (the second term) and the forces acting on them (the third term). f is the particle distribution function, α is the particle species, v is the velocity vector, q is the particle charge, m is the particle mass, E is the electric field, and B is the magnetic field in Equation (3.1). A summary of the general PIC procedure for each individual time step is provided in Figure 3.2 for reference.

$$\frac{\partial f_\alpha}{\partial t} + \mathbf{v} \cdot \nabla f_\alpha + \frac{q_\alpha}{m_\alpha}(\mathbf{E} + \mathbf{v} \times \mathbf{B}) \cdot \nabla_v f_\alpha = 0 \tag{3.1}$$

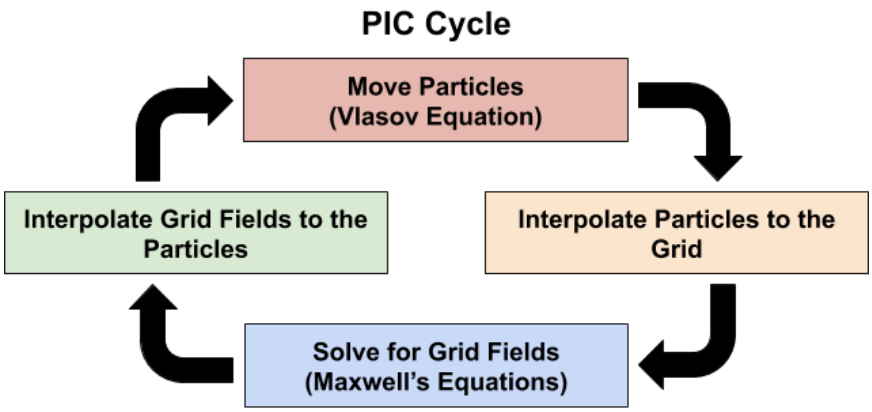

Figure 3.2: The basic procedural cycle completed during each time step of the PIC method.

The CPIC tool was developed around 2013 for the purpose of plasma-material interaction studies at Los Alamos National Laboratory [147]. This electrostatic code was designed to improve upon standard PIC codes in order to properly treat multiscale plasma problems such as the interaction of complex objects that are very large or small compared to local plasma scale lengths. In order to accomplish this, CPIC uses non-uniform, adaptive, curvilinear grids in the physical space and maps them onto a uniform, Cartesian logic space using a coordinate transform. This allows small, curved objects to be treated directly rather than approximated by small cubes which conform to the uniform, Cartesian grids used by traditional PIC codes [143]. Multi-block structured meshes and grid adaptability also increase the code's performance by reducing its run time. Plasma-material interaction problems typically feature dramatically different physical scale lengths in different parts on the simulated domain which must be properly resolved by the local grid spacing. Uniform grid spacing requires that the minimum local grid spacing be used throughout the entire domain, often leading to a massive number of simulated cells (and a proportionately long run-time) or a restricted domain. The adaptive grids used in CPIC improve code performance significantly by reducing the number of cells, however this is far from the only feature which makes CPIC robust, efficient, and scalable. These additional

features and various supporting benchmark work can be found in [147]. An example CPIC simulation featuring the electrostatic potential near a meshed object resembling a Van Allen Probe spacecraft is provided in Figure 3.3. This figure clearly shows curved cells geometries with better spatial resolution in areas of interest and/or rapid change.

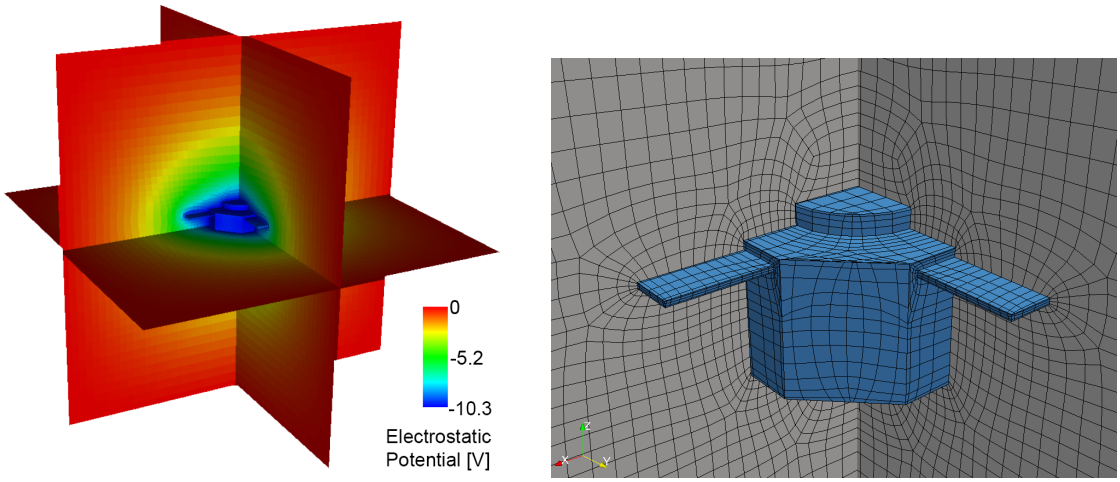

(a) (b)

Figure 3.3: The electrostatic potential around the Van Allen Probe spacecraft arising from a 5 eV Maxwellian plasma distribution (a). The curvilinear multi-block mesh conforming to the surface of the Van Allen Probe spacecraft is also shown (b).

3.2.2 Simulated Electron Beam Emission in the Magnetosphere

CPIC simulations were performed to determine whether electron beam emission is possible in tenuous space plasmas in spite of the expected spacecraft charging. A 2.35 meter radius spherical spacecraft was placed at the center of a 118 meter simulation. A constant current, 11 mA beam of electrons with an energy of 2 keV was emitted from a 1 m^2 injection area on the spacecraft surface. The charge of this beam was accumulated on the spacecraft. The spacecraft potential was found to increase linearly until surpassing the electron beam energy, when beam return was observed. In a system such as this, the spacecraft essentially acts as an isolated

capacitor charged by a constant current and its potential increases linearly in time. This simple relation is shown in Equation (3.2) below, in which V_{SC}, Q_{SC}, and C_{SC} are the spacecraft voltage, net charge, and capacitance respectively and I_{beam} is the electron beam current. The potential levels off when the positive spacecraft potential surpasses the electron beam energy as the beam is electrostatically pulled back to the spacecraft rather than leaving the system entirely. For the parameters studied using CPIC, beam return occurred in under 60 μs after the electron beam had traveled only 1.4 km [15]. The beam return process is observed in CPIC using beam density contours at different points in time after beam ignition in Figure 3.4. The simulation input parameters used to produce Figure 3.4 are summarized in Table 3.1.

$$V_{SC} = \frac{Q_{SC}}{C_{SC}} \implies \frac{\partial V_{SC}}{\partial t} = \frac{\partial Q_{SC}}{\partial t \times C_{SC}} \approx \frac{I_{beam}}{C_{SC}} \tag{3.2}$$

Simulation Parameter	Value
Spacecraft Radius	2.35 m
Simulation Domain Radius	118 m
Ambient Magnetic Field	100 nT
Electron Beam Current	11 mA
Electron Beam Energy	2 keV
Electron Beam Injection Area	1 m^2

Table 3.1: CPIC simulation parameters used in Figure 3.4.

3.2.3 Simulated Spacecraft Charging Control Methods

The emission of an ion beam and a plasma contactor were both explored with CPIC as promising charge neutralization techniques to prevent electron beam return. However, space charge limitations were immediately an issue when attempting to emit large currents with an ion beam. As discussed in Chapter 2, a flux of charged particles can accumulate in a finite volume such that they enhance the local potential (accord-

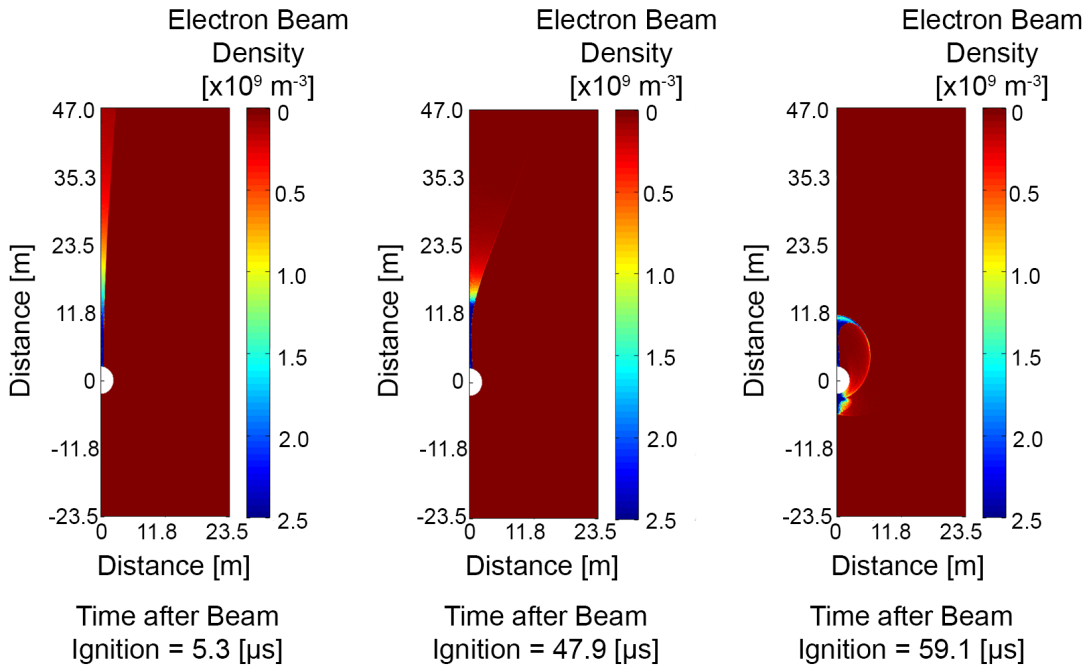

Figure 3.4: CPIC electron beam densities at different points in time after beam ignition in which total beam return is ultimately achieved and clearly visible [15].

ing to Poisson's equation). This local potential barrier can prevent further particles from entering the volume, effectively limiting the particle flux to what's known as the space-charge-limit. These effects can be summarized for cold, isotropic particles in planar geometries using the Child-Langmuir law summarized below in Equation (3.3) [149]. In Equation (3.3), J_{SCL} is the space-charge-limited current density, ϵ_0 is the permittivity of free space, q_α is the particle charge, m_α is the particle mass, V_a is the voltage applied between planar surfaces, and d is the physical separation between the two planes. Examination of Equation (3.3) reveals that the space-charge-limited (SCL) current scales inversely with the square root of the particle mass. Because the lightest ion (H^+) is 1836 times more massive than an electron, the SCL current for ions is at most 2.3% that of electrons for a comparable system. While an ion beam system with enough energy (V_a) and surface area could be designed to match the associated electron beam current. The practical difficulties of precisely balancing and

syncing these two beams over the lifetime of a mission creates a substantial risk not tolerable for many mission classes.

$$J_{SCL} = \frac{4\epsilon_0}{9}\sqrt{\frac{2q_\alpha}{m_\alpha}}\frac{V_a^{3/2}}{d^2} \quad A/m^2 \tag{3.3}$$

Plasma contactor operation during electron beam emission was another charge control method tested using CPIC [14]. Two main configurations were tested. In the "electron collection" configuration, the contactor current (plasma current generated by the plasma contactor) was lower than the electron beam current. In such a configuration, the electron beam current must be balanced by significant electron collection from the ambient plasma. This is essentially a test of whether the configuration on the left side of Figure 3.1 is sufficient to neutralize a magnetospheric spacecraft with significant electron emission (such as for the proposed CONNEX mission). If the contactor plasma fails to direct enough ambient electrons to the spacecraft surface, then beam return will occur in short order. To summarize the CPIC results: beam return does occur for this configuration as insufficient electron current is drawn from the ambient plasma [14].

The "ion emission" configuration was also tested directly via CPIC simulation [14, 15]. In this configuration, ions are emitted from the surface of the contactor plasma across a double layer in order to balance the electron beam current (see the right side of Figure 3.1). This configuration was tested numerically by setting the contactor current to greater than the electron beam current. In theory, this inequality should enable neutralization when solely emitting ions produced by the plasma contactor such that no return current (electron collection) is required from the ambient plasma. The CPIC results indicate that this is indeed the case. The simulated spacecraft potential is shown to peak well before reaching the electron

beam energy in this configuration, enabling electron beam escape in perpetuity with minimal electron energy loss.

3.2.4 Ion Emission Concept of Operation

CPIC studies of the ion emission configuration ultimately led to an improved understanding of the dominant physical processes at play. The contactor plasma potential was observed to remain relatively close to the spacecraft potential [15]. This makes sense as the plasma is conductive and most of the contactor plasma is observed to be quasi-neutral. The potential drop from the spacecraft surface to the edge of the contactor plasma is on the order of a few electron temperatures [15]. This is not all that surprising given how rapidly a Maxwellian electron energy distribution function drops off for energies above a few electron temperatures. The distribution is such that almost no electrons could reach the edge of the quasi-neutral plasma if the potential drop was 10 times the electron temperature, for example. As mentioned previously, the contactor plasma is mostly quasi-neutral. However, the plasma potential and local electron density is shown to drop dramatically at the contactor plasma edge [14, 15]. The ion density is observed to drop less dramatically in this region, producing a non-neutral, ion-rich region (see Figure 3.5 and its respective simulation parameters in Table 3.2) [14]. The dramatic potential change and presence of just one charge species in this region closely resembles the assumptions used to derive the SCL (Child-Langmuir) law in Equation (3.3). Based on these observations, it was understood that ion emission from the quasi-neutral contactor plasma is space-charge limited. This basic understanding would ultimately be used to develop a semi-analytical model which approximates CPIC results.

Simulation Parameter	Value
Spacecraft Radius	2.35 m
Simulation Domain Radius	118 m
Ambient Magnetic Field	100 nT
Ambient Plasma Ion Mass	1.7×10^{-27} kg
Ambient Plasma Density	10^{6} m^{-3}
Ambient Plasma Ion Temperature	1 keV
Ambient Plasma Electron Temperature	1 keV
Electron Beam Current	11 mA
Electron Beam Energy	Beam Trajectories Not Simulated
Electron Beam Injection Area	1 m^2
Contactor Plasma Ion Mass	1.7×10^{-27} kg
Contactor Current	22 mA
Contactor Plasma Density	10^{12} m^{-3}
Contactor Ion Temperature	10 eV
Contactor Electron Temperature	10 eV
Contactor Ion Drift Velocity	130 km/s
Contactor Expansion Time	36 μs

Table 3.2: CPIC simulation parameters used in Figure 3.5.

3.3 The Semi-Analytical Ion Emission Model

3.3.1 Motivation

A variety of semi-analytical, physics-based models were developed for three primary purposes. The first purpose was to corroborate CPIC simulation results and the physical processes underlying ion emission (at least for simple geometries). The second was to validate a tool that could produce results similar to CPIC on a personal laptop without the need for expensive super computer access. The final purpose was to generate predictions for regimes normally not accessible to PIC simulations. Of the models developed, the most complete one-dimensional (1D), spherical model produced the best agreement with CPIC simulations (as will be discussed later). This specific model (and its planar counterpart introduced in Chapter 6) will henceforth be termed the ion emission model.

A good physical understanding is required to develop an efficient, representative

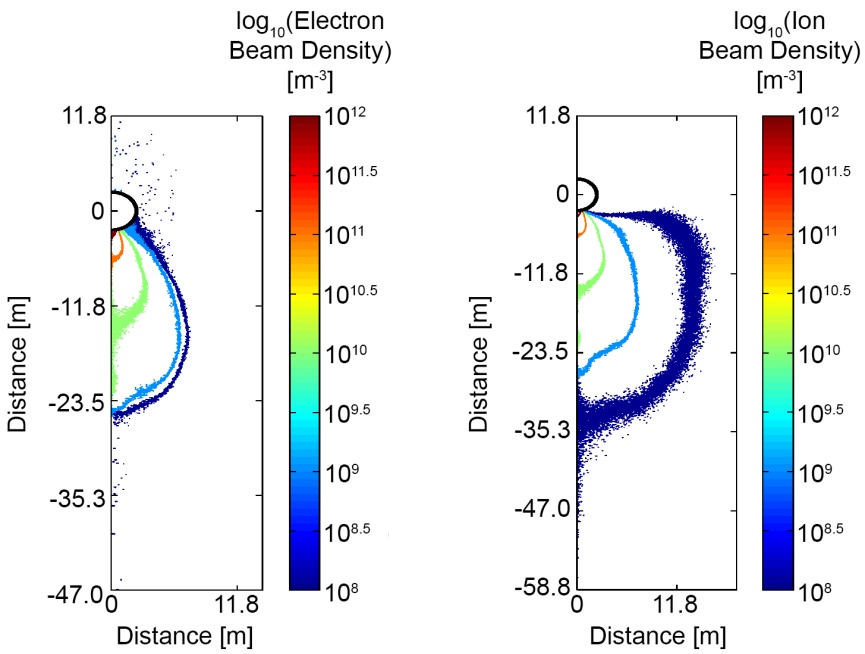

Figure 3.5: CPIC contactor plasma electron and ion densities 120 μs after electron beam ignition in the ion emission configuration. Density contours are roughly co-located (signifying equal charged particle densities and quasi-neutrality) except for the low density (dark blue) contour at the plasma edge [14].

model. Going through the process of improving agreement between the CPIC code and semi-analytical ion emission model aided our physical understanding immensely. Improved understanding allows for more assumptions to be used while maintaining accuracy, thereby improving code efficiency and run times for CPIC and the ion emission model. The practical consideration of run time is a major advantage that the semi-analytical model has when compared to CPIC. In addition, the already restrictive run time scales up significantly with the simulation domain dimensions using CPIC. One other notable limitation associated with CPIC is that it requires a finite simulation domain, whereas in space the assumption of no definite boundary which limits the contactor plasma's expansion is a good one. A semi-analytical model, on the other hand, allows the outer model boundary to be placed at infinity in a configuration more representative of space. The final assumptions going into the

most accurate spherical representation of what we call the ion emission model and a comparison with CPIC are treated below.

3.3.2 Model Assumptions and Inputs

The CPIC simulation domain was split into five well-defined regions which compose the semi-analytical model. These regions include the spacecraft, quasi-neutral plasma, ion-rich plasma, and vacuum when moving out from the simulation center. It is also possible to include a grounded outer domain boundary beyond the vacuum region when comparing laboratory experiments with CPIC simulations. The boundaries of these regions are defined by the radii r_1, r_{qn}, r_i, and r_2 when moving out from the simulation center. These plasma regions and bounding radii are shown graphically in Figure 3.6. Additional assumptions used in the development of the 1D, spherical ion emission model are enumerated below. These assumptions are treated in more detail in [16].

1. The system is spherically symmetric. This is one notable deviation from a "real world" system as it means plasma is emitted evenly from the entire spacecraft surface.

2. The electron beam energy is large enough that it (and its associated charge) leaves the system instantaneously.

3. The contactor current equals the electron beam current ($I_{contactor} = I_{beam}$), a minimum $I_{contactor}$ value for the plasma contactor to neutralize electron beam-induced spacecraft charging.

4. The model is electrostatic.

5. The system evolves on slow, ion time scales.

6. The contactor emits a constant ion current for positive spacecraft potentials.

7. The contactor ions are cold with finite drift velocity at injection.

8. There is no potential drop across the quasi-neutral region. This assumption implies the spacecraft potential is equal to the potential at r_{qn}.

9. There is vacuum beyond the ion front.

10. The outer model boundary at r_2 is grounded (0 V).

11. The plasma is quasi-neutral ($n_e = n_i$) for $r \leq r_{qn}$.

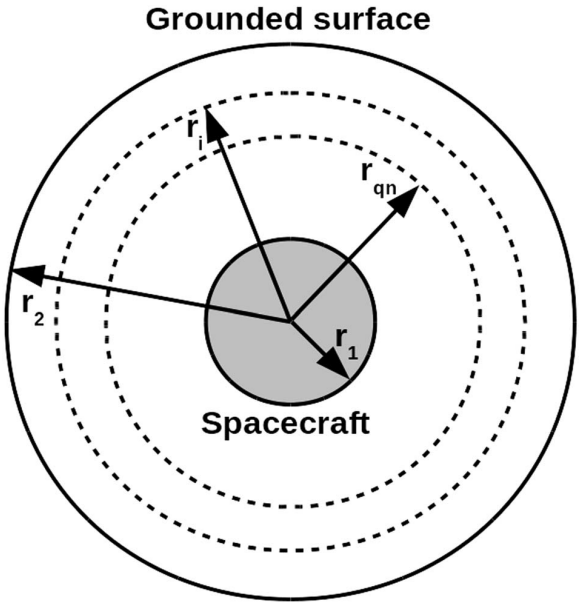

Figure 3.6: A graphical representation of the plasma regions and radii used in the spherical ion emission model [16].

Many of the spherical ion emission model inputs are the same as those required by CPIC. The beam current, spacecraft radius, and outer domain radius are three required system inputs. The required plasma parameters include the injected ion contactor current, electron contactor current, ion temperature, ion drift energy, and electron temperature. The quasi-neutral contactor plasma geometry is also required as it defines the surface area from which ions are emitted. The primary model treated here uses a static, quasi-neutral plasma boundary which must be input from some

other source (such as a previous CPIC simulation). Using these inputs and the assumptions above, we may derive a spherical, semi-analytical model to predict in-space system behavior.

Simpler models were developed in addition to the full semi-analytical model treated specifically in this chapter [16]. These simplified models are not as accurate as the full model, but may be sufficient for some applications and require fewer inputs. A full derivation of the simplest analytical model (with the fewest required inputs) is provided in Appendix A. This very simple model tracks the spacecraft potential and contactor plasma radius in time by treating the contactor plasma as part of an expanding spherical capacitor. This capacitor model does not require a model boundary or initial contactor plasma conditions like the 1D, spherical ion emission model.

3.3.3 Spherical Ion Emission Model Derivation

We begin our derivation by defining the unspecified system radii/boundaries. r_{qn} does not change after a short transient period triggered by beam turn on in the CPIC simulations when the beam current equals the contactor current. Because of this we can set r_{qn} to a constant value. The evolution of the ion front position, r_i, can be estimated starting from the simple equation of motion (Equation (3.4)). The variables used in Equation (3.4) and all subsequent ones related to the ion emission model are normalized according to Tables 3.3 and 3.4 [16]. Nomenclature and parameter definition for the ion emission model are also summarized in Table 3.5 for simplicity. For a more complete treatment of the spherical model derivation, see [16]. To calculate the electric field at the ion front in Equation (3.4), we turn to Gauss's law in Equation (3.5). For the critical estimation of the charge enclosed by r_i, we simply add the initial system charge (which is typically input using results from a comparable CPIC simulation) to the charge removed by the electron beam in Equation (3.6). Combining Equations (3.4), (3.5), and (3.6) directly leads to Equation (3.7). Equation (3.7)

defines the evolution of the ion front in time according to known model parameters.

Symbol	Definition	Value	Unit
e	Elementary charge	1.6×10^{-19}	As
k_B	Boltzmann constant	1.38×10^{-23}	m^2kg/Ks^2
m_e	Electron mass	9.11×10^{-31}	kg
ϵ_0	Vacuum permittivity	8.85×10^{-12}	A^2s^4/kgm^3
T_{ref}	Reference temperature	User Input	K
n_{ref}	Reference density	User Input	m^{-3}
$v_{th,ref}$	Reference thermal velocity	$\sqrt{k_B T_{ref}/m_e}$	m/s
λ_{ref}	Reference Debye length	$\sqrt{\epsilon_0 k_B T_{ref}/e^2 n_{ref}}$	m
$\omega_{p,ref}$	Reference plasma frequency	$\sqrt{e^2 n_{ref}/m_e \epsilon_0}$	rad/s

Table 3.3: A summary of normalizing values used by the ion emission model.

General Symbol	Definition	Normalization
T	Temperature	T/T_{ref}
n	Density	n/n_{ref}
x/r	Length/radius	x/λ_{ref}
v	Velocity	$v/v_{th,ref}$
τ	Time	$\tau\omega_{p,ref}$
ψ	Electrostatic potential	$e\phi/k_B T_{ref}$
I	Current	$I/en_{ref}v_{th,ref}\lambda_{ref}^2$
Q	Charge	$Q/en_{ref}\lambda_{ref}^3$

Table 3.4: Ion emission model normalization summary.

$$\frac{\partial^2 r_i}{\partial \tau^2} = \frac{m_e}{m_i} E(r_i) \tag{3.4}$$

$$E(r_i) = \frac{Q}{4\pi r_i^2} \tag{3.5}$$

$$Q = Q_0 + I_{beam}\tau \tag{3.6}$$

Symbol	Definition
r_{qn}	Normalized quasi-neutral radius
r_i	Normalized ion front radius
τ	Normalized time
m_e	Normalized electron mass
m_i	Normalized ion mass
E	Normalized electric field
Q	Normalized charge enclosed by $r = r_i$
Q_0	Initial normalized charge enclosed by $r = r_i$
I_{beam}	Normalized electron beam current
$I_{contactor}$	Normalized contactor (plasma) current
r_2	Normalized model domain radius
ψ	Normalized electrostatic potential
n_e	Normalized electron density
n_i	Normalized ion density
v_d	Normalized ion drift velocity
K_i	Normalized ion drift energy
J_e	Normalized electron current density
$v_{th,e}$	Normalized electron thermal velocity
T_e	Normalized electron temperature
z	Current radius as normalized by the radius of the quasi-neutral boundary
I_i	Normalized ion current (contactor current)

Table 3.5: Ion emission model nomenclature summary.

$$\frac{\partial^2 r_i}{\partial \tau^2} = \frac{m_e}{m_i} \frac{Q_0 + I_{beam}\tau}{4\pi r_i^2} \tag{3.7}$$

The ion emission model also calculates the electrostatic potential in the simulation domain. Assumption 9 allows the potential at the ion front, r_i, to be calculated using vacuum capacitance as shown in Equations (3.8) and (3.9). The potential beyond this ion front is the solved problem of a vacuum potential distribution between two concentric spherical conductors. However, this potential distribution is not required for the model as it is located in the region ions expand/accelerate into after being emitted. Assumption 8 allows the quasi-neutral plasma potential to be neglected for simplicity such that only the potential at the quasi-neutral boundary, r_{qn}, is required. The potential at the quasi-neutral boundary (and spacecraft potential) is obtained implicitly from the solution of a nonlinear Poisson equation in the ion-rich region according to Equation (3.10). Equation (3.10) requires both electron and ion densities in addition to two boundary conditions. The boundary conditions used correspond to assumptions 6 and 9, which effectively set the electric field at the quasi-neutral boundary to zero and define the potential at the ion front.

$$C = \frac{4\pi r_2 r_i}{r_2 - r_i} \tag{3.8}$$

$$\psi_i = \frac{Q}{C} = \frac{(Q_0 + I_{beam}\tau)(r_2 - r_i)}{4\pi r_2 r_i} \tag{3.9}$$

$$\frac{1}{r^2}\frac{\partial}{\partial r}\left(r^2\frac{\partial \psi}{\partial r}\right) = n_e - n_i \tag{3.10}$$

The electrostatic potential profile in the ion-rich region depends on local particle densities. The ion density can be calculated by assuming cold, drifting ions according to assumption 7. Combining the ion continuity and momentum equations using this assumption results in Equation (3.11). The electron density is calculated assuming a Maxwellian distribution and applying the kinetic theory derived by Delzanno and Tang in the OML approximation [37]. Equations (3.12) and (3.13) summarize the local electron density for two potential regimes. We note that J_e is one remaining unknown found in Equations (3.12) and (3.13). To calculate J_e, we impose quasi-neutrality ($n_e = n_i$) at r_{qn} in order to arrive at Equation (3.14) for the electron current density. The dimensions and potentials within each defined region shown in Figure 3.6 are determined using the assumptions described above in conjunction with Equations (3.7), (3.9), (3.10), (3.11), (3.12), (3.13), and (3.14). This model also computes the electron and ion density profiles in the ion-rich region where ion emission occurs as a byproduct of solving Poisson's equation.

$$n_i = \frac{I_{beam}}{4\pi v_d r^2}\left[1 + \frac{\psi_{SC} - \psi}{K_i}\right]^{-\frac{1}{2}} \tag{3.11}$$

$$n_e = \sqrt{\frac{\pi}{2}}\frac{J_e}{v_{th,e}} exp(\frac{\psi - \psi_{SC}}{T_e})\times$$
$$\left[1 + erf\sqrt{\frac{\psi}{T_e}} - \frac{2}{\sqrt{\pi}}\sqrt{\frac{\psi}{T_e}}exp\left(-\frac{\psi}{T_e}\right) - \frac{\sqrt{z^2-1}}{z}exp\left(\frac{\psi - \psi_{SC}}{T_e(z^2-1)}\right)\right] \quad if \quad \psi(z) \leq \frac{\psi_{SC}}{z^2} \tag{3.12}$$

$$n_e = \sqrt{\frac{\pi}{2}}\frac{J_e}{v_{th,e}} exp(\frac{\psi - \psi_{SC}}{T_e}) \times$$
$$\left[1 + erf\sqrt{\frac{\psi}{T_e}} - \frac{2}{\sqrt{\pi}}\left(\sqrt{\frac{1}{T_e}\left(\psi - \frac{\psi_{SC}}{z^2}\right)} - \sqrt{\frac{\psi}{T_e}}\right) exp\left(-\frac{\psi}{T_e}\right)\right.$$
$$\left. - \frac{\sqrt{z^2-1}}{z} exp\left(\frac{\psi - \psi_{SC}}{T_e(z^2-1)}\right)\left(1 + erf\sqrt{\frac{1}{T_e}\frac{z^2\psi - \psi_{SC}}{z^2-1}}\right)\right] \quad if \quad \psi(z) \geq \frac{\psi_{SC}}{z^2} \tag{3.13}$$

$$J_e = \frac{I_i}{4\pi r_{qn}^2}\frac{v_{th,e}}{v_d}\sqrt{\frac{2}{\pi}}\left[1 + erf\sqrt{\frac{\psi_{SC}}{T_e}} - \frac{2}{\sqrt{\pi}}\sqrt{\frac{\psi_{SC}}{T_e}} exp\left(\frac{\psi_{SC}}{T_e}\right)\right]^{-1} \tag{3.14}$$

3.4 A Comparison of Model and CPIC Results

A direct comparison of ion emission model and CPIC predictions was performed using the inputs listed in Table 3.6 and the results for this test case will be summarized here [16] . Figure 3.7 presents the time evolution of the ion front potential, ψ_i, and the ion front position, r_i, over time. In this figure (and the two to follow) the "Base Model" is the same spherical, semi-analytical ion emission model which we have treated in this chapter. Figure 3.7 shows that the ion front is well characterized using the ion emission model (its potential and position are within a few percent of what is observed using CPIC). Figure 3.8 presents the equilibrium (long term) potential and charged particle density profiles in space. These profiles were taken at the end of the simulation, after the ion front had reached the grounded simulation boundary. The agreement here is very strong once again (within a few percent) with the exception of some statistical noise introduced by the finite number of CPIC macroparticles. It is worth noting that spatial density and potential profile agreement is degraded for times immediately following beam ignition, however this discrepancy appears to

have little impact on the agreement in Figure 3.7 or the spacecraft potential shown in Figure 3.9 [16]. The spacecraft potential agreement is also very good, and the two predictions fall within a narrow range throughout the simulation duration.

Simulation Parameter	Value
Spacecraft Radius	1 m
Simulation Domain Radius	100 m
Ambient Magnetic Field	0 nT
Electron Beam Current	1 mA
Electron Beam Energy	Beam Trajectories Not Simulated
Contactor Plasma Ion Mass	6.7×10^{-27} kg
Contactor Electron Current	7.2 mA
Contactor Ion Current	1 mA
Contactor Ion Temperature	0.5 eV
Contactor Electron Temperature	2.3 eV
Contactor Ion Drift Velocity	35 km/s
Initial Contactor Expansion Time	0.3 ms
Initial Quasi-neutral Radius	8.7 m
Initial Ion Front Radius	17 m
Initial Ion Front Velocity	64 km/s
Initial Spacecraft Charge	1.8×10^{-8} C

Table 3.6: Input parameters used for a direct comparison between the ion emission model and CPIC simulation in Figures 3.7 - 3.9.

3.5 The Need for Experimental Validation

The simulated results discussed here suggest that charge mitigation using a contactor plasma is possible even in the absence of an ambient plasma at charging levels well below those expected without spacecraft-charging mitigation [14, 15]. Specifically, CPIC simulations demonstrate space-charge limited ion emission from the surface of a quasi-neutral contactor plasma that can balance electron beam emission so long as the contactor current equals or exceeds the electron beam current [14, 15]. The semi-analytical ion emission model matched CPIC simulation results within a few percent and even predicted effective spacecraft neutralization in an unbounded

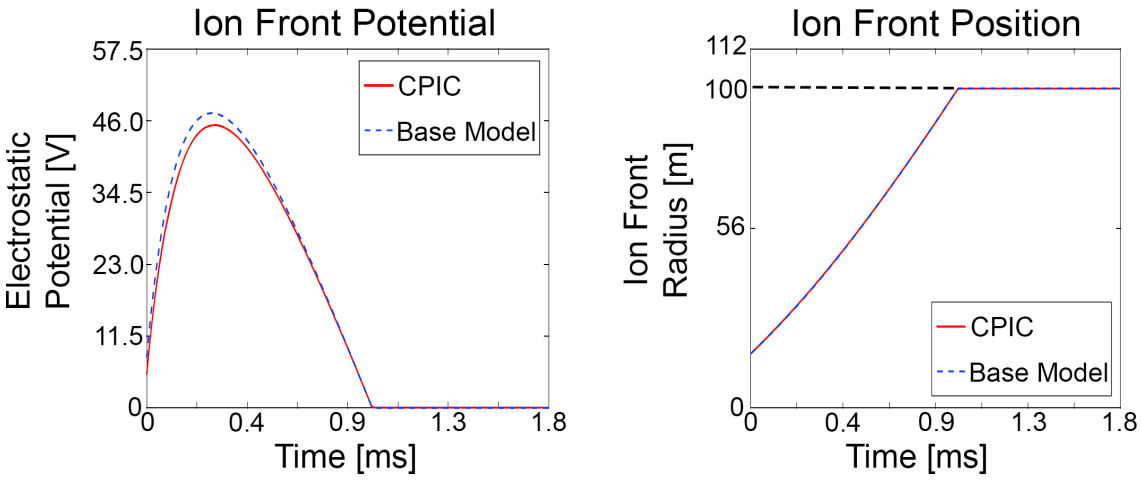

(a) (b)

Figure 3.7: The simulated ion front potential (a) and position (b) after electron beam ignition according to CPIC and the ion emission model (denoted the Base Model) [16]. Beam emission begins at Time = 0.

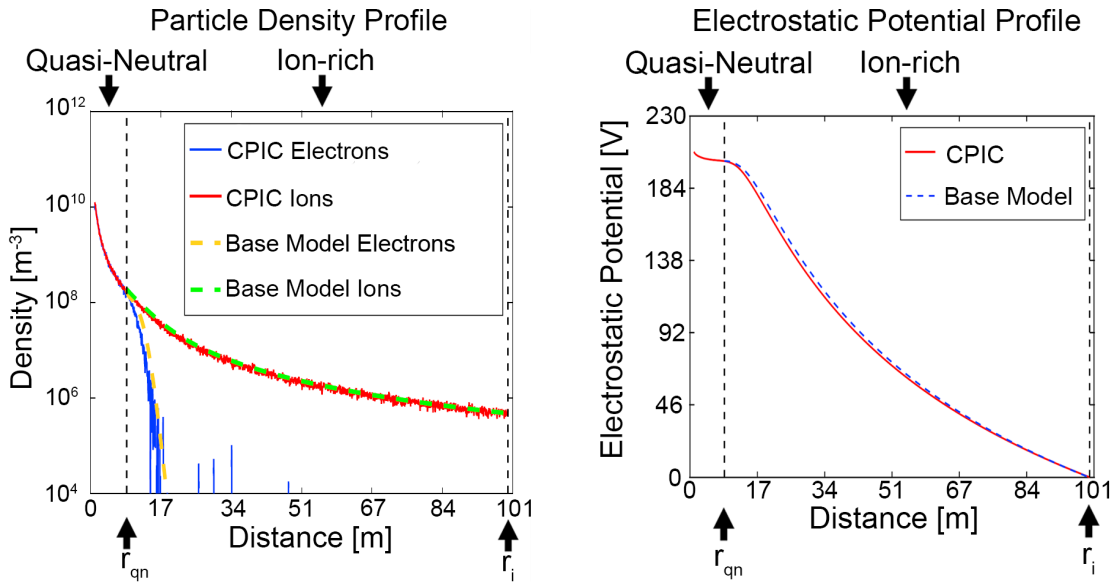

(a) (b)

Figure 3.8: The simulated equilibrium (long term) ion and electron densities (a) and electrostatic potential (b) when emitting an electron beam according to CPIC and the ion emission model (denoted the Base Model) [16]. The vertical dashed lines denote the edge of the quasi-neutral plasma and the ion front. These profiles are taken 1.8 ms after beam ignition.

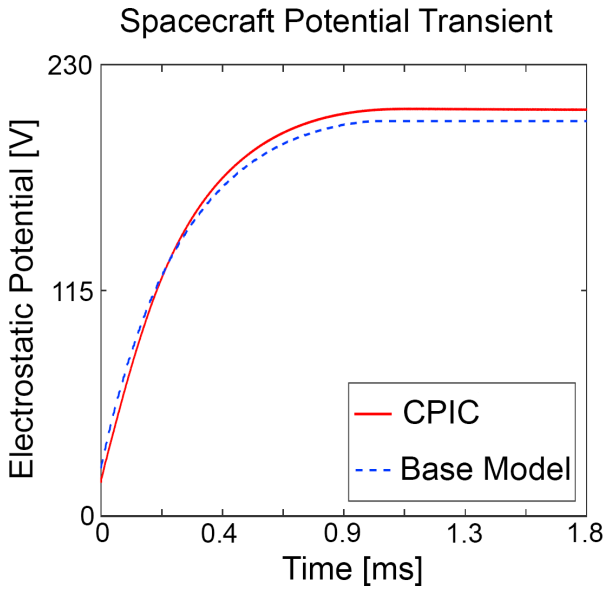

Figure 3.9: The simulated spacecraft potential after electron beam ignition according to CPIC and the ion emission model (denoted the Base Model) [16]. Beam emission begins at Time = 0.

domain (as one would expect in space) [16]. In total, CPIC simulation and ion emission model results suggest that using a hollow cathode plasma contactor is a viable strategy to achieve spacecraft charging neutralization during high-current electron beam experiments in tenuous plasmas.

While encouraging, these results should not be trusted blindly when proposing to use the ion emission technique in space. Instead, the necessary assumptions and model inputs which go into novel numerical simulations such as these should be vetted using repeatable physical experiments. By carefully scaling and designing experiments in an Earth-based vacuum chamber, we can capture many of the key scaling parameters and physical processes which are expected of a realistic space experiment. Numerical tools may then be applied directly to these experimental results. Discrepancies between numerical prediction and experimental results may be analyzed to identify opportunities for numerical tool improvement. Agreement between the two data sets indicates that the numerical tools accurately capture the real-world system and can subsequently be used for in-space prediction more reliably.

In the remainder of this work, we focus on experimental campaigns which validate the discussed numerical models and unravel the physical processes underlying net ion current emission from a quasi-neutral plasma.

CHAPTER IV

Ion Emission Validation I: Transient Response to Electron Beam Emission

4.1 Motivation

Validating the predictive capability of CPIC simulations and the ion emission model using ground based plasma chamber experiments is a critical step in identifying a spacecraft charge neutralization method during electron beam emission in space. The first step in this process is a qualitative validation of the predicted spacecraft potential response to electron beam ignition. This step indicates whether spacecraft neutralization is even possible in an earth-based vacuum chamber using a plasma contactor with contactor current roughly equal to the electron beam current. In this chapter, we will quickly summarize the predicted spacecraft and plasma potential responses relevant to sudden electron beam ignition while operating a hollow cathode plasma contactor. Next, we will describe experiments designed to observe these same transient responses in an earth-based vacuum chamber. Finally, we will compare the results of these experiments to the predicted response in space and discuss any discrepancies.

The spacecraft potential response to electron beam ignition as predicted by CPIC and the ion emission (base) model is shown in Figure 3.9 using the input parameters

listed in Table 3.6. These simulations correspond to the standard case where $I_{beam} = I_{contactor}$ as described in Chapter 3. The spacecraft potential is shown to increase approximately linearly when the beam is first fired and eventually asymptotes to a constant value due to the effects of a finite boundary. Example plasma potential profiles for an expanding contactor plasma are shown in Figure 4.1 both before and during electron beam emission using the input parameters in Table 3.6. The CPIC and model predictions show that the entire contactor plasma potential increases in unison with the spacecraft potential when an electron beam is emitted. Ion and electron density profiles are presented in Figure 4.2 (again, using the parameters listed in Table 3.6). In this plot we can see that the ion density profile continues to expand when the electron beam is fired without significant changes. In comparison, the electron density suddenly decreases much more rapidly than the ion density in regions far from the simulated spacecraft (which is situated at $r = 0$) when the beam is fired.

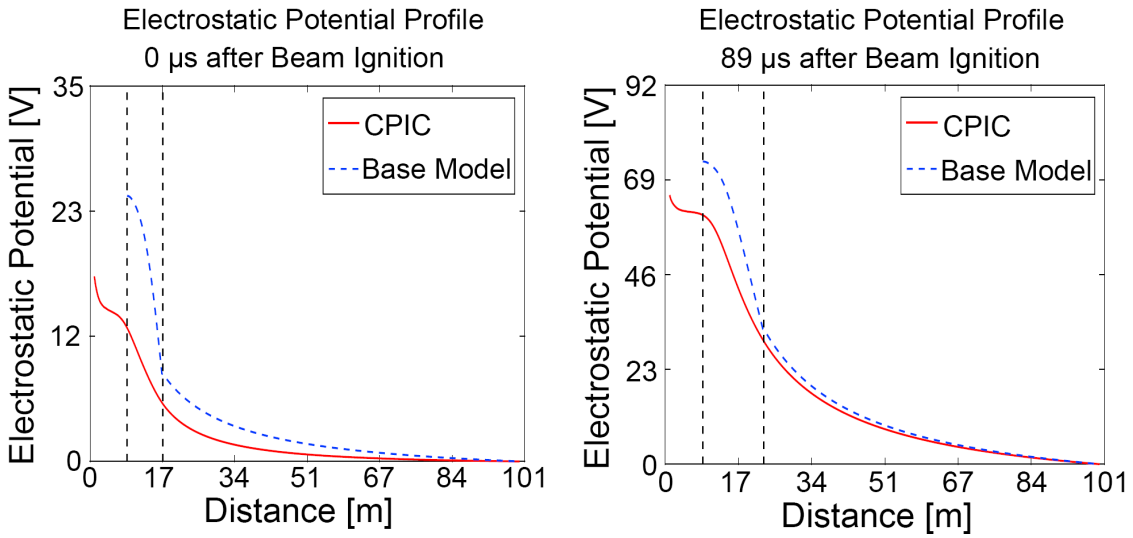

(a) (b)

Figure 4.1: Plasma potential surrounding a simulated spacecraft according to CPIC and the ion emission model (denoted the Base Model) using the same conditions 0 μs (a) and 89 μs (b) after beam ignition [16].

The results described above are precisely the focus of the experimental campaign

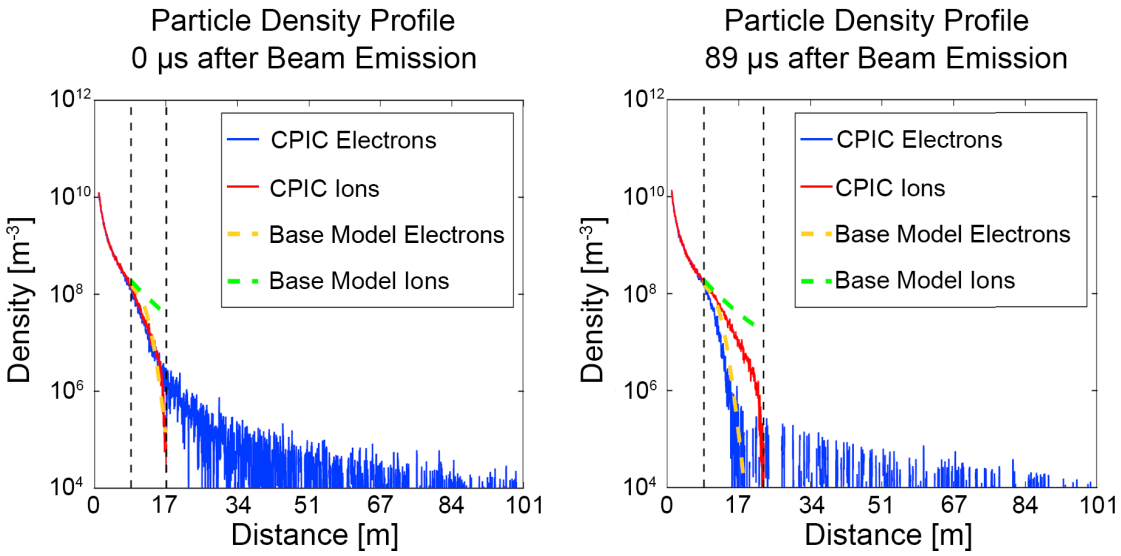

(a) (b)

Figure 4.2: Ion and electron densities surrounding a simulated spacecraft according to CPIC and the ion emission model (denoted the Base Model) using the same conditions 0 μs (a) and 89 μs (b) after beam ignition [16].

described below. Experimental "spacecraft" (S/C) and plasma potentials are tracked simultaneously during the ignition of a constant current power supply (which effectively acts as a constant current electron beam). Langmuir probes (LPs) biased in the ion and electron saturation regimes are also used to get an idea of changes to ion and electron densities in various locations surrounding the hollow cathode. The general trends observed during these experiments are compared to predicted trends in a qualitative manner (as the two system parameters are somewhat different) and any additional observations of note are addressed.

4.2 Experimental Setup

4.2.1 Simulating a Plasma Contactor and Electron Beam Emitting "Spacecraft"

In order to mimic simulations and in-space conditions for a representative "spacecraft" (S/C), we must electrically isolate it from conducting surfaces in contact with

Earth ground. This was accomplished by placing all hollow cathode components on top of a conducting steel platform. The platform was separated from the steel chamber via four 6" ceramic standoff insulators (see Figure 4.3). High voltage ceramic feedthroughs, coaxial and twisted pair cable arrangements, and woven metal shielding sleeves were used when possible. The hollow cathode was biased positive with respect to the grounded, conductive chamber walls to mimic the equivalent space system's response to electron beam emission according to the circuit diagram in Figure 4.4. A high voltage (20 kV) power supply was used to simulate the electron beam for this set of experiments. It is used in both constant current and constant voltage mode to control the S/C potential. The potential established using this power supply can also be thought of as the equivalent of a spacecraft potential with respect to the ambient space plasma, as hollow cathodes are typically tied to spacecraft common (the spacecraft frame potential). For transient testing in which the "beam" is fired, the power supply is simply switched on and off in constant current mode. The power supply's voltage and current are independently verified and recorded using an oscilloscope. The "electron beam" current is converted to a voltage using a simple, in-series, 1 Ohm resistor voltage drop. The assembled system was designed and tested with the capability to bias the S/C in excess of 1 kV with respect to the chamber ground without breakdown in air. See Figure 4.4 for the complete isolation circuit.

An open keeper, LaB_6 hollow cathode with a 1/8" orifice diameter was used to produce a steady state plasma representative of a space-based contactor plasma. The design is a variant of the cathodes used in electric propulsion devices and is shown operating in Figure 4.3. The cathode was operated using a 7 sccm flow of neutral Xenon expellant and a keeper (discharge) current of 5 A, which resulted in a keeper (discharge) voltage of 26.6 – 28.1V. The hollow cathode was operated in the "diode mode" configuration. In the diode mode, a steady state plasma discharge is maintained by forcing a constant, ionizing current to flow between the cathode

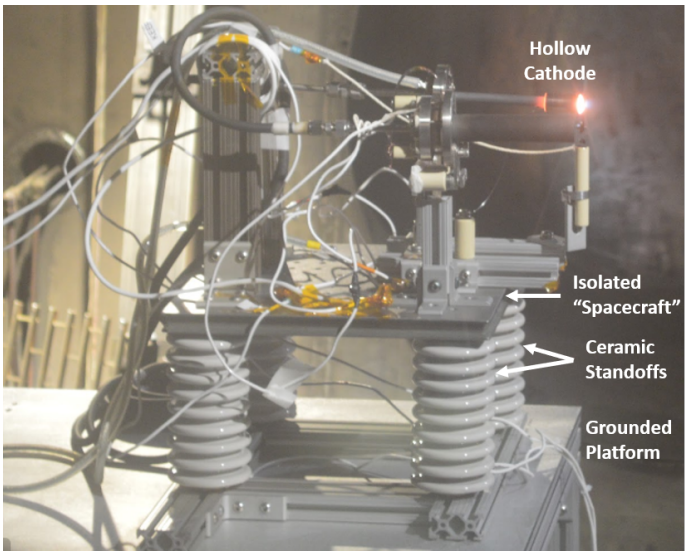

Figure 4.3: Simulated "spacecraft" during hollow cathode operation.

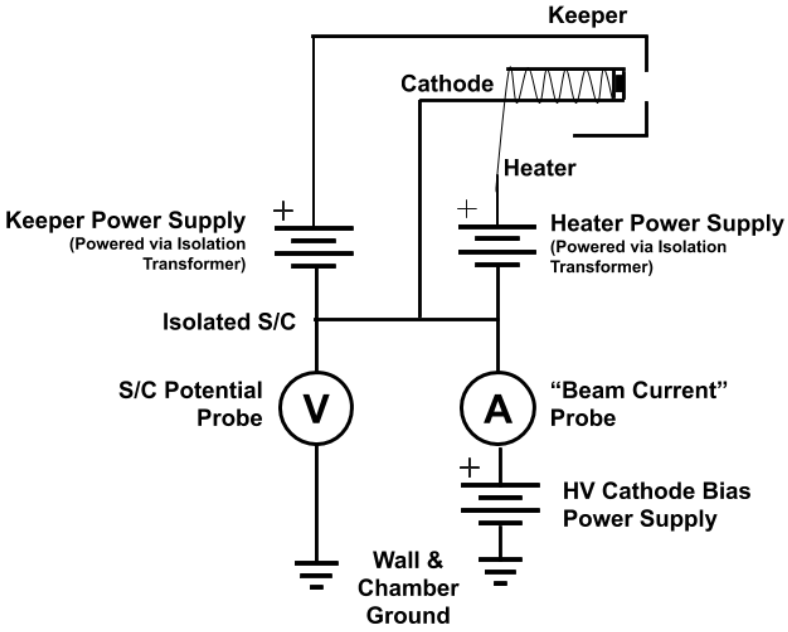

Figure 4.4: "Spacecraft" isolation and hollow cathode plasma contactor power circuit.

and keeper electrodes. The diode mode was used as it best represents the expected in-space use case during electron beam emission (when the spacecraft is positive and the hollow cathode acts as a net ion source).

4.2.2 Vacuum Chamber Description

Experiments were performed at the University of Michigan's Plasmadynamics & Electric Propulsion Laboratory (PEPL) in the Large Vacuum Test Facility (LVTF) vacuum chamber. LVTF is a roughly cylindrical chamber with rounded endcaps as shown in Figure 4.5. It is composed of stainless steel, its largest diameter is 6 m, and it spans 9 m in length. LVTF achieved a base pressure of approximately $5x10^{-7}$ Torr with an operating pressure of approximately $1x10^{-6}$ Torr using seven CVI TM-1200 re-entrant cryopumps during the experiments presented. The background operating pressure of $1x10^{-6}$ Torr can be converted to a mean free path using a Xenon charge exchange cross section of $2x10^{-18}$ m^2 and assuming a neutral temperature of 300 K [150]. The resulting mean free path of 15.5 m is considered conservative with regards to plasma collisionality (charge exchange mean free paths are the shortest for Xenon) and is larger than any chamber dimension.

4.2.3 Plasma Diagnostics

Three cylindrical, Tungsten Langmuir probes, two thoriated Tungsten emissive probes, and a retarding potential analyzer (RPA) were used over the course of these experiments. These diagnostics were located on a diagnostic stand shown in Figure 4.6, with the exception of two Langmuir probes. These two Langmuir probes were placed 96 cm directly behind the hollow cathode and 6 cm from the chamber wall (this probe was 280 cm off the hollow cathode axis and 210 cm downstream). The length of the stand, posterior, and wall Langmuir probes was 5.2 cm, 4.9 cm, and 5.2 cm respectively. The diameter of these probes was 0.0635 cm, 0.08 cm, and 0.0254 cm respectively. The exposed emissive probe tips were 4 cm in length and 0.0254 cm in diameter with a slight bend according to the recommended practice for tenuous plasmas [151]. Probes were electrically and physically isolated and extended (at least 24 cm) from the rotation stage to prevent wake effects and possible arcing to the

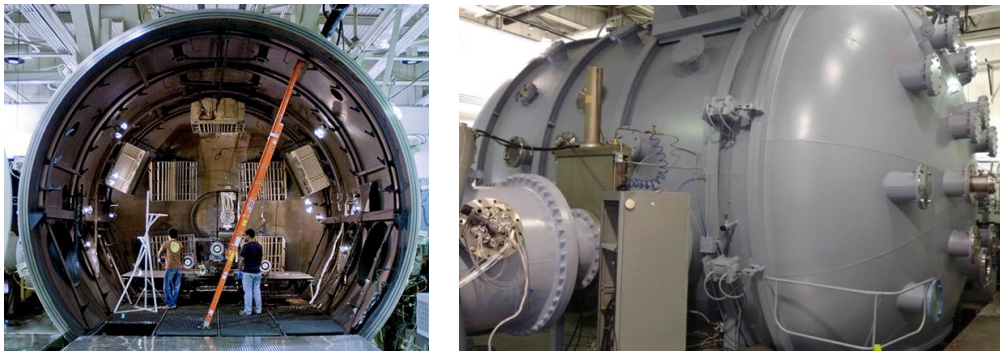

(a) (b)

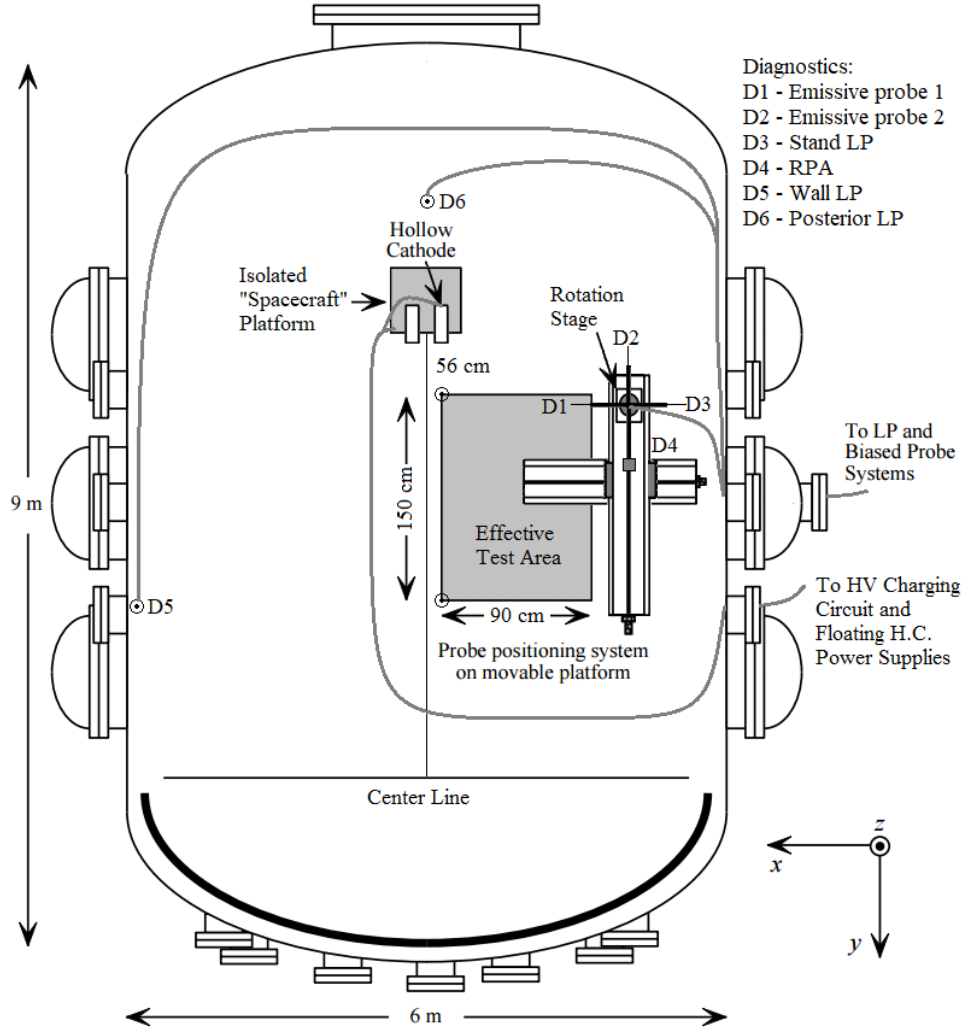

(c)

Figure 4.5: The LVTF interior (a), exterior (b), and an aerial view of the LVTF configuration used during the described experiments (c).

chamber. The diagnostic stand was mounted atop 2 large, linear Velmex motion stages and a rotation stage. This created a large effective testing area and placed probes at approximately the same height as the hollow cathode orifice (174 cm +/- 2 cm above the chamber grates). The testing area and orientation of relevant hardware is presented via aerial view in Figure 4.5 (c).

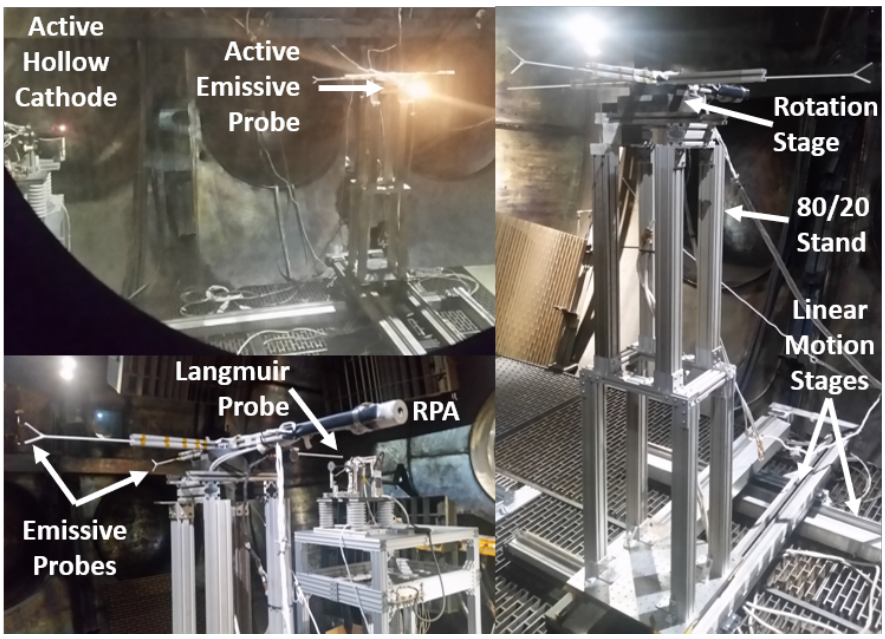

Figure 4.6: Various photos of the 80/20 diagnostic stand, the three motion stages used to position it, and its diagnostic suite consisting of a RPA, Langmuir probe, and two emissive probes.

The primary plasma measurements used in this analysis are those made by an emissive probe 206 cm downstream of the hollow cathode orifice. These plasma potential measurements were made using the floating probe technique in the limit of high emission [151]. In this method, a current is passed through the thin probe filament to heat it to thermionic electron emission temperatures. These thermionic electrons effectively neutralize the sheath around the filament so that the probe floats very close to the plasma potential [151, 152]. Calibration curves were used to ensure the probe was sufficiently hot by increasing the heating current through the filament until the probe floating potential plateaued [151, 152]. An example calibration curve

and the emissive probe measurement circuit can be found in Appendix B.

The other plasma measurements treated in this section are those of the Langmuir probes. However, the typical Langmuir probe I-V sweep was not performed as the long duration of each sweep (on the order of seconds) would invalidate any such measurement taking place during a fast transient. Instead, the Langmuir probe data presented below was obtained by simply biasing the Langmuir probes highly positive or highly negative in order to measure the electron and ion saturation currents in real time. Specifically, the probes were biased at +200 V with respect to the chamber walls to collect electron saturation current and -200 V with respect to the chamber walls to collect ion saturation current. Without any additional information, the saturation currents to a cylindrical Langmuir probe cannot be used to directly calculate electron and ion densities. However, the measurements still provide an indication of density, drift velocity, and plasma potential changes occurring in various regions near the S/C when the "beam" is first emitted.

More plasma measurements were completed and analyzed during this experimental campaign, however these other measurements focused primarily on the steady state contactor plasma properties. The results from these measurements report the same trends examined in more detail during Chapters 5 and 6. Along the same lines, different cathode configurations and simulated electron beam currents were studied during this experimental campaign. The results from these measurements report the same trends addressed specifically in Chapter 7. These additional measurements are not presented for the sake of brevity, but they consistently support the more detailed results and conclusions presented elsewhere (both in this document and in previous publications) [153, 154].

4.3 Experimental Results

4.3.1 Potential Transient Response

A high voltage power supply was used to simulate electron beam ignition once the hollow cathode had reached equilibrium at a Xenon gas flow rate of 7 sccm, keeper current of 5 A, and keeper potential of 26.6 V. Figure 4.7 shows the measured electron "beam" current supplied by the high voltage power supply in order to mimic DC electron beam ignition. The waveform indicates that the power supply reaches its steady state current value in approximately 255 ms. However, this rise time is insignificant in comparison to the time it takes for the S/C and plasma potentials to reach equilibrium. The current was set to 33 mA, but an analysis of Figure 4.7 reveals an average current of 30.6 mA while the "beam" was firing. It is likely that the high voltage power supply was unable to set the current to 33 mA with a high degree of accuracy as it is well below its maximum current setting. Thus this 2.4 mA discrepancy is likely within the uncertainty of the power supply. Before "electron beam" ignition, "beam current" was non-zero as the S/C was partially grounded through the unpowered cathode bias power supply. However, the steady state S/C potential was still negative of the chamber walls when the supply was first powered, mimicking a spacecraft floating negative in a space plasma. There was also a brief "beam" current drop which bottomed out at -4 mA when the cathode bias power supply was turned off. This feature is not particularly relevant to the ability to neutralize active electron beam emission, but likely impacted measurements when the power supply/"electron beam" was turned off. Finally, the current measurement is rather noisy. This is likely because of the current measurement technique used. The cables and current sense resistor were partially unshielded and located in a control room with significant electromagnetic interference (EMI). This EMI could easily couple to the current sensing circuit and induce voltage noise on the order of a few mV (which translates to current

noise on the order of a few mA). Such noise should not alter the current's average (or DC) value.

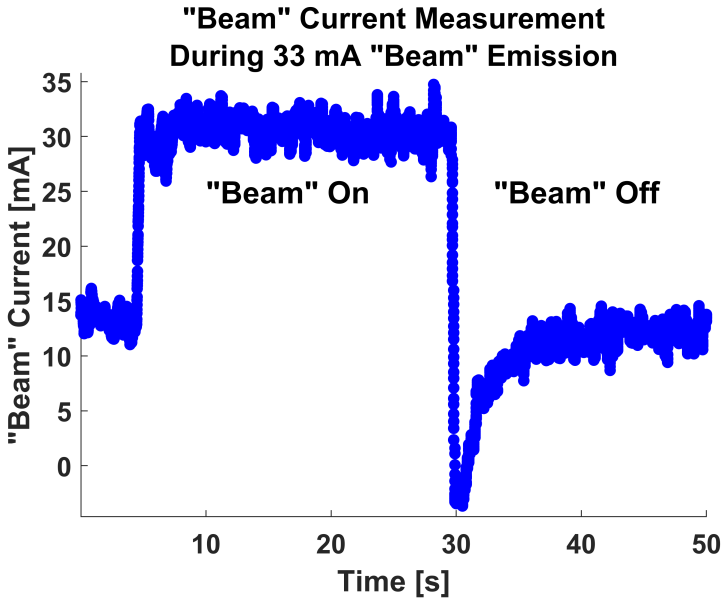

Figure 4.7: "Beam" current from the high voltage power supply during a 33 mA transient testing after being filtered with a 50 point moving average.

Figure 4.8 proves that "spacecraft" neutralization is achievable by operating a plasma contactor in a vacuum chamber. Rather than increasing linearly until the maximum power supply voltage setting is reached, the S/C potential is observed to peak at a manageable 51.7 V and then slowly decrease to an equilibrium value of 34.5 V. To highlight the significance and magnitude of the observed neutralization, an example scenario without neutralization is provided here using Equation (3.2). The capacitance between the S/C and chamber wall (C_{SC}) may be approximated by treating the isolated conducting plates of the S/C and its supporting platform as a parallel plate capacitor whose separation is the isolation ceramic height. This results in a capacitance of 68.1 pF. Solving Equation (3.2) using the measured "beam" current of 30.6 mA and a C_{SC} of 68.1 pF results in a $\frac{\partial V_{SC}}{\partial t}$ of 4.5x10^8 V/s. This predicted $\frac{\partial V_{SC}}{\partial t}$ would lead to the maximum power supply voltage of 20,000 V being exceeded in just 45 μs. For comparison, the highest measured $\frac{\partial V_{SC}}{\partial t}$ was only 1,060 V/s (although

this is likely a gross underestimation of the peak $\frac{\partial V_{SC}}{\partial t}$ given the 5 ms oscilloscope measurement period).

It is also clear from the contemporaneous oscilloscope data presented in Figure 4.8 that it takes the spacecraft and plasma potentials in the system over 15 seconds to reach equilibrium. The S/C potential and plasma potential of Figure 4.8 (as measured using an active emissive probe 206 cm downstream of the hollow cathode orifice) appear to react with no detectable delay between their signals. The rapid initial rise time and lack of delay between potential signatures suggest that the plasma responds quickly to the "beam" current, as one would expect using typical diffusion and plasma frequency time constants [155]. This also makes the long potential equilibrium time exceeding 15 seconds rather mysterious. A likely cause of this phenomenon is presented in Section 4.4.

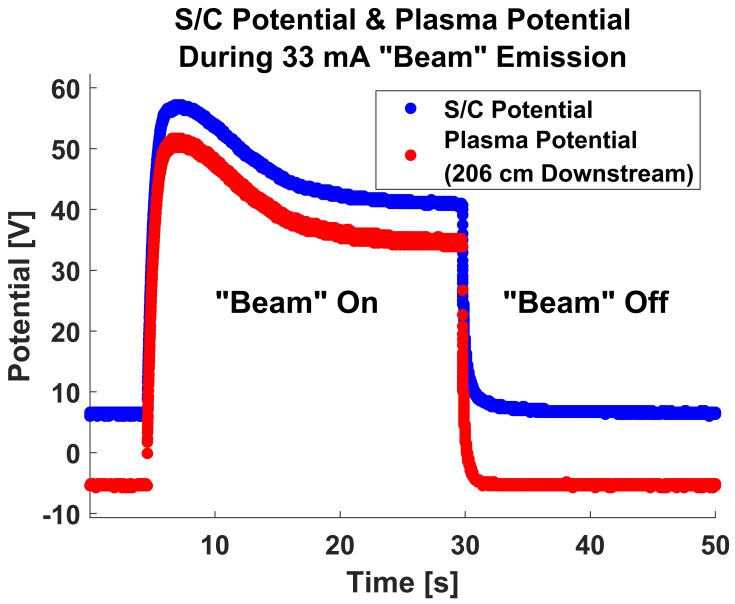

Figure 4.8: "Spacecraft" and plasma potential transients during 33 mA "beam" firing.

4.3.2 Local Saturation Current Transients

Langmuir probe saturation currents during a 33 mA "beam" firing are presented in Figures 4.9, 4.10, 4.11, 4.12. Without any additional information, the saturation

currents to a cylindrical Langmuir probe cannot be used to directly calculate electron and ion densities as previously stated. However, the measurements still provide an indication of density, drift velocity, and plasma potential changes occurring in various regions near the S/C when the "beam" is first emitted. For example, the saturation current is roughly proportional to the local charged density for both ions and electrons.

Figures 4.9 - 4.12 are all taken from an independent "beam" firing with the same "beam" current of 33 mA. On the left plot of these figures, we observe that the electron saturation current consistently dropped as soon as the "beam" was fired. This drop was almost certainly caused by some combination of three dependencies. First, the increase in local plasma potential (see Figure 4.8) and corresponding decrease in the probe bias relative to this local potential acted to decrease the electron saturation current. This is because the electron saturation current scales almost linearly with Langmuir probe bias in our experiments (see Chapter 5, Figure 5.7). Second, the electron saturation current scales linearly with electron density. Finally, the electron saturation current scales as the square root of electron temperature. It is also worth noting that the electron temperature actually increases with S/C potential (as explored in Chapter 5), reducing the impact of a decrease in electron density and/or relative probe bias. The general shape of this drop was typically the inverse of the potential increase observed in Figure 4.8. One exception to this trend is that there appear to be oscillations in the electron saturation current presented in Figure 4.9 when the "beam" is first fired. The exact cause of this low frequency ($\sim$0.25 Hz) behavior near the hollow cathode orifice is unknown. It is possible there is local turbulence near the hollow cathode when the "beam" is fired.

There are also discrepancies in the electron saturation current response when the "beam" is turned off. The current is shown to return to its unbiased, steady state value with different time scales, approximating underdamped, critically damped, and over damped responses. The largest drop in electron saturation current occurred

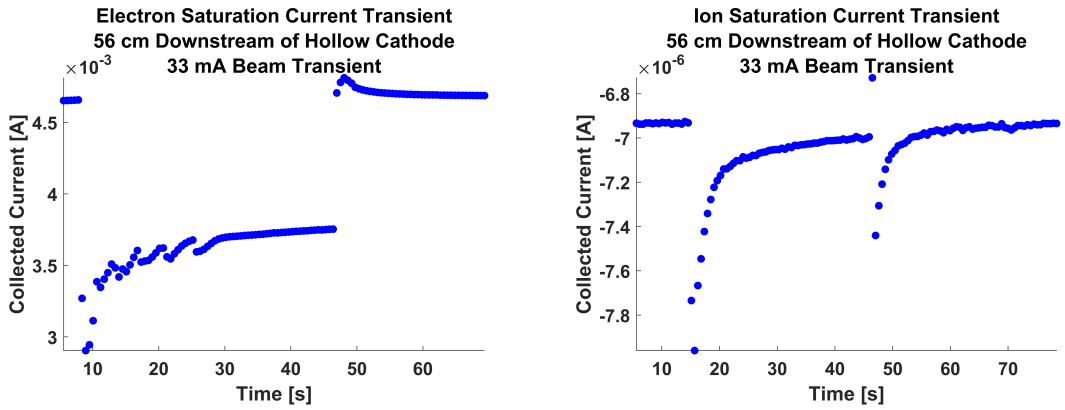

(a) (b)

Figure 4.9: Langmuir probe electron (a) and ion (b) saturation currents 56 cm downstream of the hollow cathode during 33 mA "beam" firings.

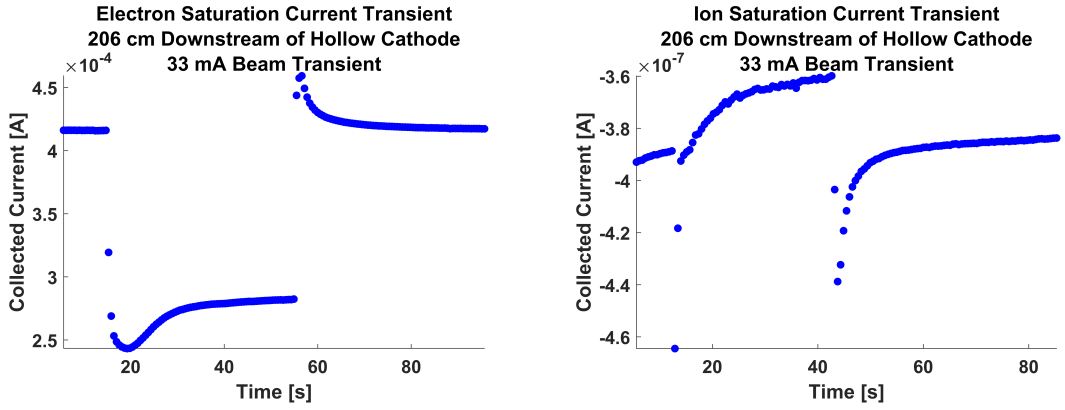

(a) (b)

Figure 4.10: Langmuir probe electron (a) and ion (b) saturation currents 206 cm downstream of the hollow cathode during 33 mA "beam" firings.

near the wall (a 65% drop seen in Figure 4.12) and the smallest drop occurred behind the hollow cathode (a 23% drop seen in Figure 4.11). These are the two lowest plasma density areas so it is interesting that they reacted so differently. The current theory is that relative differences in electron saturation current at different locations is primarily due to electron density changes as the contactor plasma potential increases with the S/C potential (S/C bias). This theory is supported and expanded upon in Chapter 5.

The ion saturation current spikes when the "beam" is first fired as ions are forced

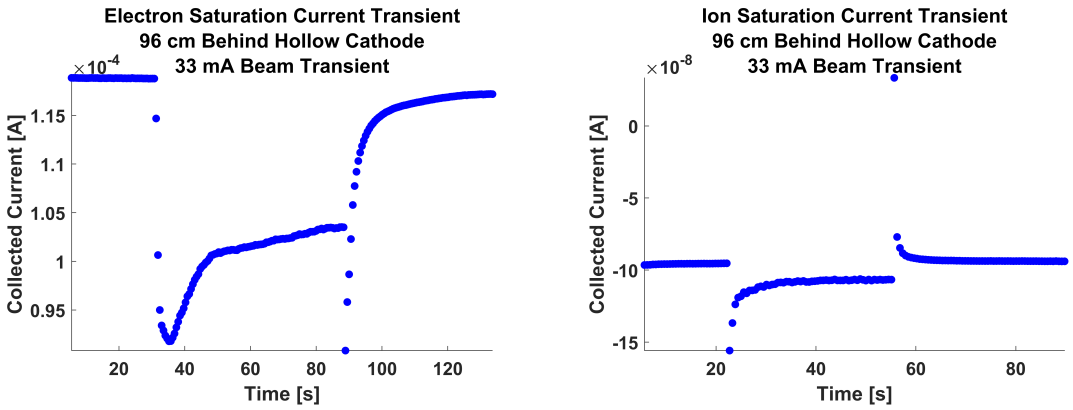

(a) (b)

Figure 4.11: Langmuir probe electron (a) and ion (b) saturation currents 96 cm behind the hollow cathode during 33 mA "beam" firings.

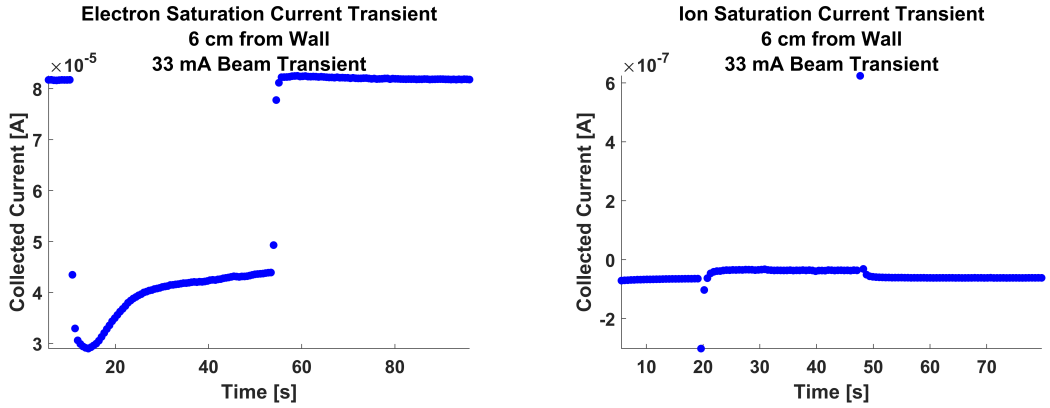

(a) (b)

Figure 4.12: Langmuir probe electron (a) and ion (b) saturation currents 6 from the chamber wall during 33 mA "beam" firings.

out of the plasma to compensate for the electron "beam" current leaving the system. The magnitude of these spikes is highly variable and likely determined by chance as the plasma response and time scales are much faster than could be faithfully recreated given the current measurement frequency (∼2 Hz). The steady state ion saturation current observed while the "beam" is firing generally does not change as much as the electron saturation current. In fact, at three of the Langmuir probe positions these two values varied by less than 13%. This is not all that surprising given that ion saturation current scales as the square root of probe bias relative to the

plasma (whereas this relationship is almost linear for the electron saturation current) [36]. Accounting for this relative change in probe bias adds less than 10% to the ion saturation current in our system. Thus, if there are no ion density changes the ion saturation current will not change much. The exception to this trend of only minor ion saturation current changes is the Langmuir probe near the wall shown in Figure 4.12, which saw a 45% decrease in ion saturation current while the beam was firing. This is likely due to a decrease in ion density, which nominally agrees with our previously proposed theory that the electron density dropped near the chamber wall. The results of Chapter 5 further explore and support this theory.

The ion saturation current reacts rather unpredictably when the "beam" is turned off. The ion saturation current is actually shown to go positive (net electron collection) for the two transient measurements of Figures 4.11 and 4.12 at the moment the "beam" is shut off. It is possible that this occurs in all cases but it was not properly captured due to the current measurement frequency. Either way, it is likely caused by the negative electron "beam" current induced when the high voltage cathode bias power supply is shut down (see Figure 4.7). The ion saturation currents are observed to return to a steady state condition via a damped response.

4.4 A Circuit Model Approach to Potential Transients

The equilibrium times observed in the results above are much longer than one would expect based on plasma time scales (such as the plasma period or particle chamber transit times). To better understand and explain this disconnect, we look to the literature and find similarly long response times have been observed in space for comparable systems. Potential transients of a similar shape and time scale were observed on the geosynchronous ATS-5 and ATS-6 satellites when turning on a plasma contactor in order to neutralize negative spacecraft charging [80]. Replication of the ATS-5 mission in NASCAP (a dedicated spacecraft charging code) revealed that

spacecraft system capacitances and resistances drove long equilibrium times in a surprisingly simple fashion [80]. Here we will use a similar approach to determine if this could be the cause of long equilibrium times in our vacuum chamber experiments.

We can approximate our physical system in Keysight's Advanced Design System (ADS) circuit simulation software by using a simple RC circuit model. The high voltage cathode bias power supply (or "electron beam") is approximated using a 30.6 mA current source with a 255 ms rise time to mimic the current waveform in Figure 4.7. The capacitance between the S/C and chamber wall was approximated by treating the isolated conducting plates of the S/C and its supporting platform as a parallel plate capacitor whose separation is the isolation ceramic height as before. The resulting capacitance of 68.1 pF is actually within a factor of two of the 104 pF ATS-5 spacecraft capacitance found using NASCAP [80]. We can estimate a plasma resistance using Ohm's Law as the "beam" current magnitude is essentially equal to the current flowing from the S/C to the chamber wall. A plasma resistance of roughly 1450 Ω is found by linearizing the relationship between the "beam" current and S/C potential shown in Figure 4.13. These measurements were taken using the same cathode configuration as Figure 4.8. Figure 4.14 summarizes the S/C potential transient simulation results using Keysight's ADS software and shows the representative RC circuit used.

The magnitude and time scale of the predicted S/C potential transient are very similar to those observed in Figure 4.8. The S/C potential first peaks and then drops $\sim$15 V in 25 seconds. The value of the S/C potential peak was $\sim$50 V during experiments and $\sim$45 V as predicted via ADS circuit simulation. One notable difference between the two potential plots of Figure 4.8 and Figure 4.14 is that Figure 4.8 is significantly more rounded. This is likely because the effective plasma resistance is non-linear over S/C potential. For instance, estimating the plasma resistance from Figure 4.13 using the lowest two S/C potentials (rather than the highest four S/C

potentials) produces a much lower resistance of ∼230 Ω. A variable plasma resistance which starts small and increases as the peak potential is approached could explain the S/C potential peak rounding which occurs during electron beam ignition.

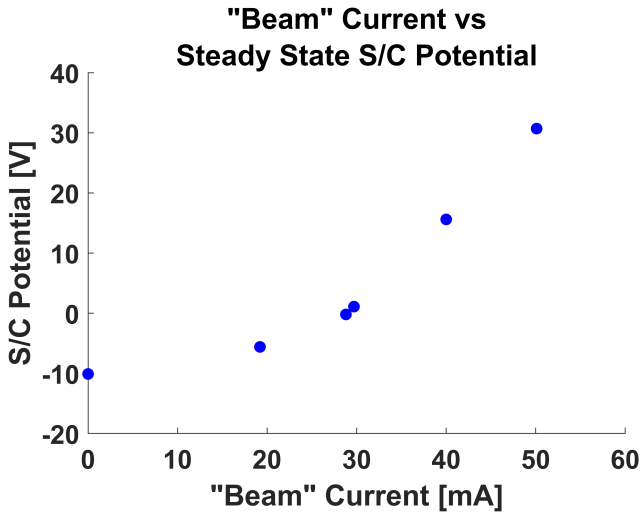

Figure 4.13: "Beam" current versus steady state S/C potential for a keeper current of 5 A and Xenon flowrate of 7 sccm.

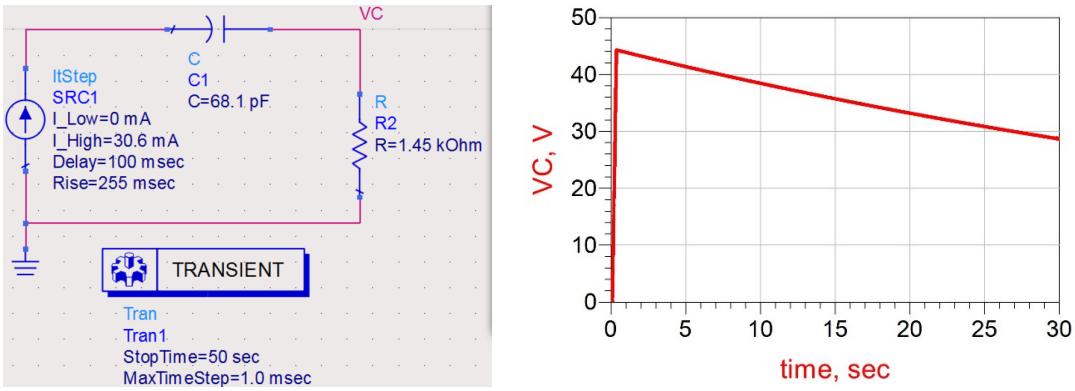

(a) (b)

Figure 4.14: Capacitive charging transient simulation using a basic RC circuit model. The circuit model (a) and resulting S/C potential transient (b) are shown.

4.5 Chamber Microdischarges

The maximum "beam" current and its corresponding equilibrium S/C potential were effectively limited by the onset of microdischarges in the chamber when the S/C potential exceeded 60 V. These microdischarges presented themselves as a small flash of light on a grounded chamber surface (see Figure 4.15) and an immediate reduction of the S/C potential relative to Earth ground. A current burst was also detected by the high voltage cathode bias power supply during microdischarges. Microdischarges occurred sporadically under high S/C potential (> 60 V) conditions, with their frequency increasing for higher S/C potentials. The discharges took place throughout the chamber, but were concentrated near the simulated S/C and on the diagnostic suite when it was brought close to the hollow cathode plasma source. Microdischarge frequency could be reduced by "conditioning", which consisted of raising the S/C potential for extended periods of time to "blast off" impurities and likely discharge points. While conditioning increased the maximum discharge-free S/C potential slightly, this was ultimately the limiting factor on maximum S/C potential during testing.

Microdischarges were observed throughout experiments exploring the ion emission model. The working theory to explain their occurrence is that microdischarges represent a dielectric breakdown in the insulating metal oxide layer coating metal objects in the vacuum chamber. Pure metals are passivated when exposed to air, as oxygen bonds to exposed metal atoms and rapidly forms a metal oxide layer [156]. The thickness, resistivity, and dielectric strength of this layer varies depending on the metal and surface conditions being considered. In addition, many components used in vacuum chambers are purposely anodized to thicken their metal oxide layer for increased durability. One example of an anodized component is the aluminum 80/20 structural support. These 80/20 supports have an Al_2O_3 (aluminum oxide) thickness of roughly 10 μm. Naturally occurring aluminum oxide layers are typically closer to

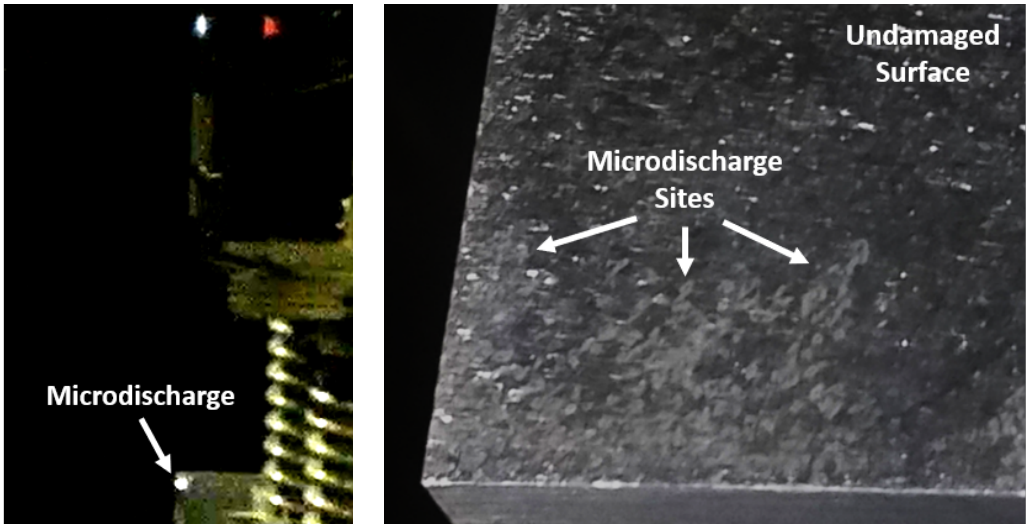

(a) (b)

Figure 4.15: Photos of an active microdischarge site (a) and microdischarge damage incurred by a rough aluminum plate during transient testing (b).

4 nm thick [156]. By assuming perfectly flat layers and an Al_2O_3 dielectric strength of 16.9 V/μm, the estimated dielectric breakdown voltage is then in the range of 0.07 - 170 V [157]. 0.07 V is unrealistically low, so we can state that values in this range were almost certainly experienced by metal oxide layers during the experiments presented here. However, it is difficult to definitively attribute dielectric breakdowns without dedicated experiments. Luckily, emissive probe measurements presented in Chapter 6 demonstrate voltage drops exceeding 10 V just 0.1 mm from the surface of copper planar probes. In addition, these voltage drops increased substantially after the probes were heated by a nearby emissive probe. This observation suggests a metal oxide layer is causing the observed voltage drop, as copper oxide layer thickness increases dramatically at higher temperatures [158, 159]. Indeed, a similar process to the one theorized here is used to grow metal oxide coatings. Plasma electrolytic oxidation (or microarc oxidation) uses large potential differences to exceed the local dielectric breakdown potential of metal oxide layers [160]. The ensuing high temperature plasma discharge grows a thicker oxide coating than more standard anodizing techniques. This process likely occurs during our microdischarges as the discharge

plasma releases a burst of charged particles which quickly reduces the S/C potential, exhausts the ionized material, and extinguishes itself. An example plot of the S/C potential during a microdischarge is shown in Figure 4.16. During this event, the S/C potential drops from 200 V to just 10 V in just 1.1 ms.

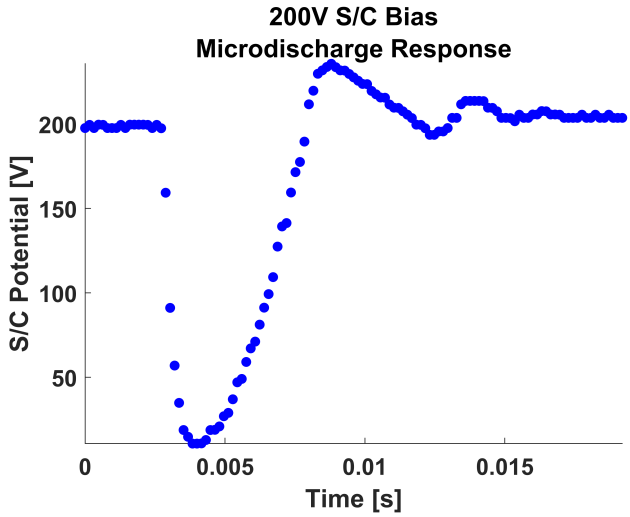

Figure 4.16: Example S/C potential microdischarge response.

4.6 Summary

The results presented above demonstrate that ion emission using a hollow cathode is a viable neutralization technique in an Earth-based vacuum chamber. It successfully prevented the S/C potential from increasing without bound and equilibrium was achieved at relatively small positive potentials. The chamber plasma potential was found to react in unison with the S/C potential, indicating the plasma responds rapidly to any change in S/C potential. Saturation current transients indicated density changes near the chamber wall and the possible presence of turbulence near the hollow cathode orifice. Long potential transient times can be explained using simple RC circuit simulations of the experimental system. Disruptive microdischarges dictated the upper limit on S/C potentials, however it is possible to reduce their severity

by adjusting the experimental setup. The maximum "beam" current and corresponding S/C potential are primarily limited by the onset of these microdischarges in the subsequent steady state experiments.

CHAPTER V

Ion Emission Validation II: Equilibrium Response to Electron Beam Emission

5.1 Motivation

Validating the numerical tools presented in Chapter 3 is a critical step in enabling electron beam emission in tenuous space plasmas. One major step in this validation process is ensuring that the contactor plasma reacts as expected when an electron beam is emitted in space. Observing the same features using numerical tools as those observed in an instrumented vacuum chamber allows one to perform a direct, quantitative validation of the numerical tools and lends credence to the tools' assumptions in the regimes under study. Conversely, unexpected or novel results may expose physical processes which are not yet accounted for in the predictive tools and open new opportunities for model improvement. In this chapter, we first summarize the predicted contactor plasma response to positive spacecraft charging induced by electron beam emission in space. Next, we describe experiments designed to observe these same responses in an earth-based vacuum chamber. Finally, we compare the results of these experiments to the predicted space response and discuss some discrepancies.

Here we detail the predicted sequence of events when firing a constant current electron beam during the steady state operation of a hollow cathode plasma contactor in

space. Predictions were made using the CPIC simulation tool and the semi-analytical ion emission model developed in collaboration with Gian Luca Delzanno and Federico Lucco Castello [14–16]. Prior to electron beam ignition, we expect the hollow cathode contactor plasma to expand in a manner consistent with plasma particle energies, ambipolar diffusion effects, and the local (ambient) magnetic field [17]. Ion density profiles at three distinct points in time after hollow cathode ignition are shown in Figure 5.1 as predicted by CPIC simulation. The input parameters for this simulation are listed in Table 3.2. In this simulation, the hollow cathode contactor plasma was emitted from a small surface area on one side of a spherical spacecraft. It is evident that the contactor plasma expands from the spherical spacecraft in the direction it was emitted.

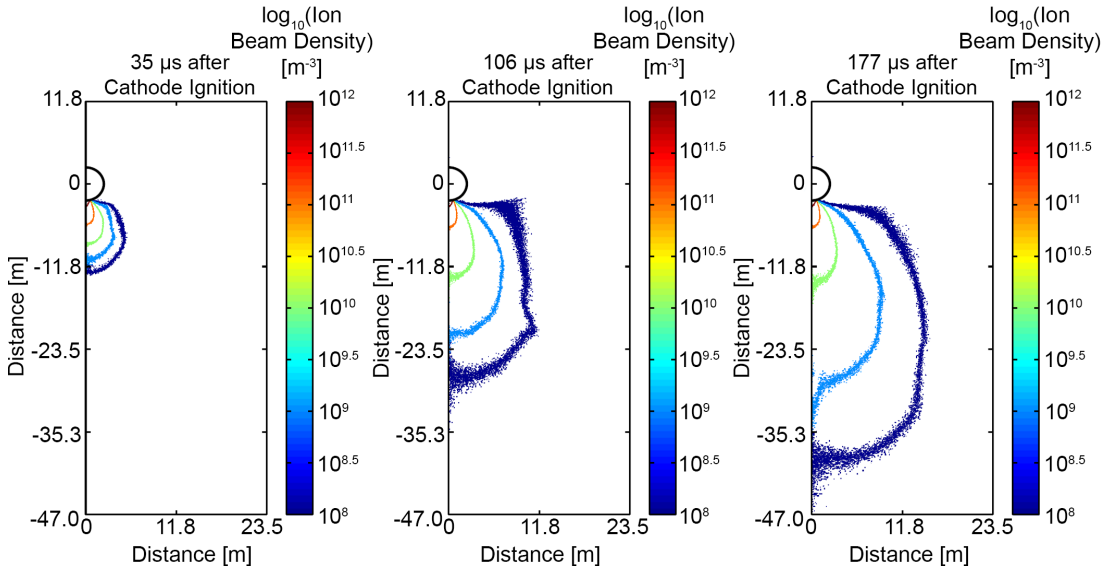

Figure 5.1: Ion density contours at three distinct times after hollow cathode ignition as predicted using the CPIC tool [15].

When a constant current electron beam with beam current equal to the contactor current (the net ion current produced by the plasma contactor) was fired in CPIC simulations, the plasma generally continued to expand away from the spacecraft. However, it was observed that the ion and electron populations no longer expanded at the same rate. Instead, a quasi-neutral region close to the spacecraft could be

discerned from an ion-rich region further from the spacecraft. These regions were formalized when developing the quasi-neutral ion emission model described in Chapter 3. This spherically symmetric model uses the quasi-neutral plasma radius (the quasi-neutral location furthest from the spacecraft), r_{qn}, and ion front radius (the location of the ion furthest from the spacecraft), r_i. The model also uses the spacecraft radius, r_1, and the radius of the grounded boundary, r_2, as shown in Figure 5.2. The observed position of the quasi-neutral boundary, r_{qn}, since igniting the electron beam during a CPIC simulation can be seen in Figure 5.2. The CPIC and ion emission (base) model inputs used in Figure 5.2 are as listed in Table 3.6. While some noise is present, the location of r_{qn} largely remains unchanged once the electron beam is fired. For this reason, the semi-analytical ion emission model (labeled the "Base Model" in Figure 5.2) uses a constant r_{qn}.

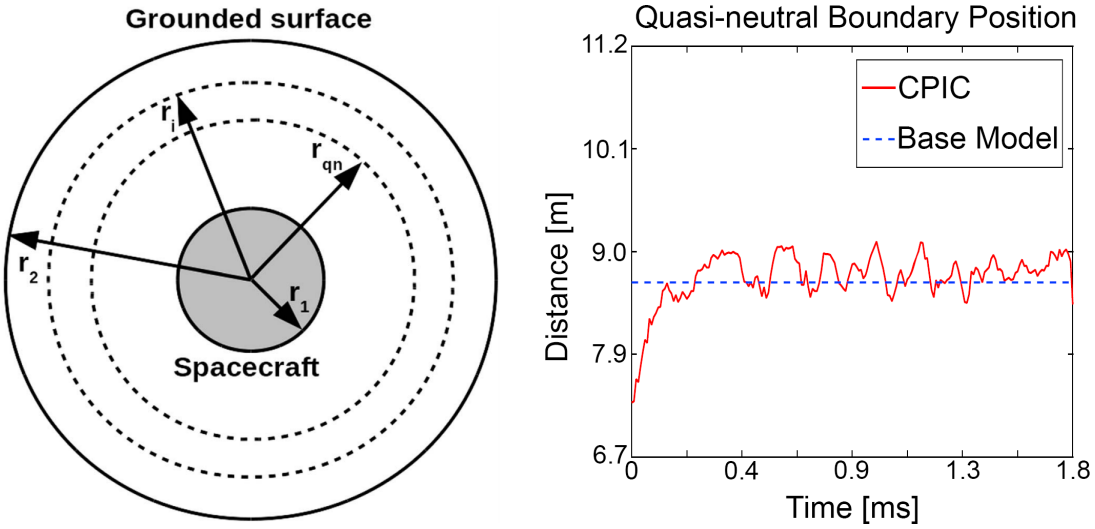

(a) (b)

Figure 5.2: The plasma boundaries defined by the semi-analytical ion emission (a) and the predicted position of the quasi-neutral radius, r_{qn}, during beam emission (b) [16]. Beam emission begins at Time = 0.

The plasma was also allowed to expand until it reached the grounded simulation boundary, which is the configuration which best represents a steady state vacuum chamber experiment. The ion density, electron density, and potential profiles found

using a spherically symmetric CPIC simulation and the ion emission model are shown in Figure 3.8 once the contactor has reached equilibrium with the grounded simulation profiles. Here the boundary between quasi-neutral and ion-rich plasma regions is clearly visible and denoted with a vertical dashed line. Similarly, the position of r_i (the furthest plasma ion) is also denoted with a vertical dashed line. It is evident when examining the potential profile that contactor plasma potentials have increased significantly since the beam was first fired (when the plasma and spacecraft potentials were approximately 0). The quasi-neutral region was found to be at roughly the spacecraft potential, with a small potential drop across it on the order of a few electron temperature [16]. This small dip is pictured in Figure 4.1 to the left of the left-most dashed line. The remaining potential difference between the quasi-neutral plasma and the grounded simulation boundary is then made up for in the ion-rich region (again, see Figure 4.1).

The results detailed above are precisely the focus of the experimental campaign described below. Plasma properties including ion density, electron density, plasma potential, and electron temperature were measured and are reported in locations ranging from the hollow cathode plasma source to the conducting vacuum chamber walls. These results are used to locate the boundary between the quasi-neutral and ion-rich experimental plasma regions. Finally, the observed trends are compared to predicted trends and discrepancies are discussed.

5.2 Experimental Setup

5.2.1 General Experimental Description

Experiments were performed in LVTF using a configuration similar to the one described in Sections 4.2.1 and 4.2.2. Notable differences during these experiments were that the isolated "spacecraft" was limited to just the isolated hollow cathode body

and the high voltage cathode power supply (powered by an isolation transformer) was exchanged for a low voltage power supply powered through a standard outlet. A photo of the exact hollow cathode setup is provided in Figure 5.3. The cathode was operated using an 8 sccm flow of neutral Argon expellant and a keeper (discharge) current of 10 A, which resulted in a keeper (discharge) voltage of 37.0 – 37.9 V. The background operating pressure of $1x10^{-6}$ Torr can be converted to a mean free path using an Argon charge exchange cross section of $4x10^{-19}$ m^2 and assuming a neutral temperature of 300 K [161]. The resulting mean free path of 78 m is considered conservative with regards to plasma collisionality (charge exchange mean free paths are the shortest for Argon) and is larger than any chamber dimension.

The steady state plasma in LVTF was examined using two identical, cylindrical Langmuir probes. The conducting, Tungsten probe tip was supported using an insulating alumina ceramic tube and secured in place using a ceramic paste. The probe tips were 5.1 cm (2 in) in length and 0.51 mm (0.02 in) in diameter and cleaned using electron bombardment prior to beginning a measurement series. One of these probes can be seen in Figure 5.4 (c).

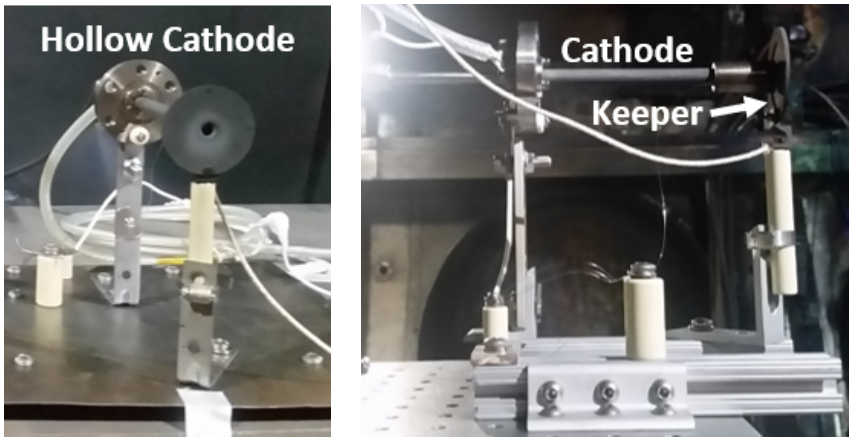

(a) (b)

Figure 5.3: The hollow cathode used during the described experiments.

The Langmuir probes were positioned at the same height as the hollow cathode orifice in LVTF (152 cm above the chamber grates). Two Velmex Linear motion

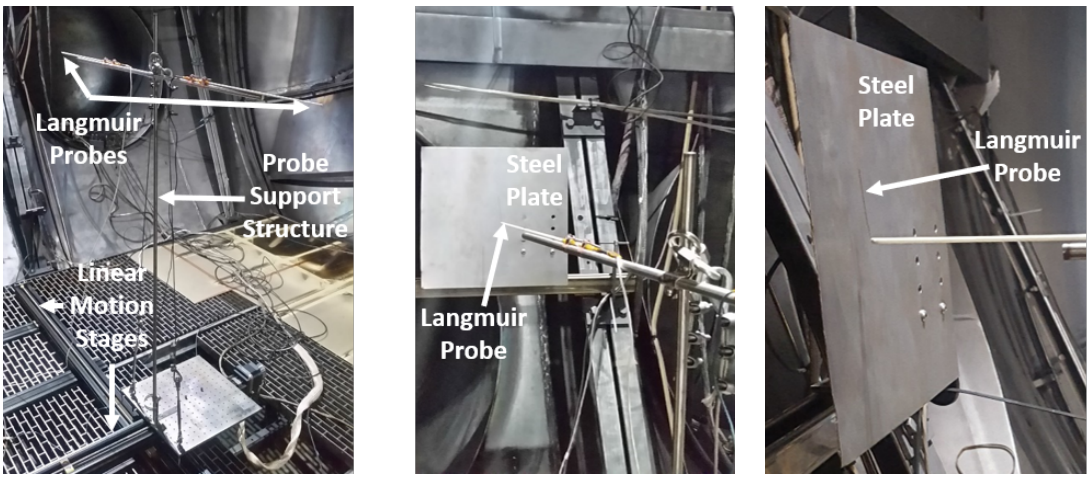

(a) (b) (c)

Figure 5.4: The Langmuir probe support structure mounted on two linear Velmex motion stages (a) and a Langmuir probe approaching the wall-mounted steel plate (b,c) are shown.

stages were used to move these probes in the x-y plane (see Figure 5.4 (a). Two identical Langmuir probes were used to expand the effective testing area along the x-axis (transverse to the plasma flow), as one probe could effectively be used for each half of the testing area. Using this setup, an accessible testing area of 110 cm by 255 cm was achieved. Bulk Langmuir probe sweeps in this area generally had a linear spacing of 20 cm starting 8 cm downstream of the hollow cathode orifice. The measurement locations were at axial distances of 8, 28, 48, 68, 88, and 108 cm downstream of the hollow cathode and transverse distances of 0, 20, 40, 60, 80, 100, 122, 142, 162, 182, 202, and 222 cm left of the hollow cathode orifice for a grand total of 72 positions per set of bulk plasma measurements. These Langmuir probe measurement locations are presented visually in Figure 5.5.

Langmuir probe measurements were made by biasing the probe and measuring the collected current through a Keithley 2400 sourcemeter controlled via LabView. In order to obtain plasma measurements up to the vacuum chamber wall, a steel plate was mounted to the chamber wall in a location bordering the testing area. This conducting plate served to make the "chamber wall" more accessible by bringing it

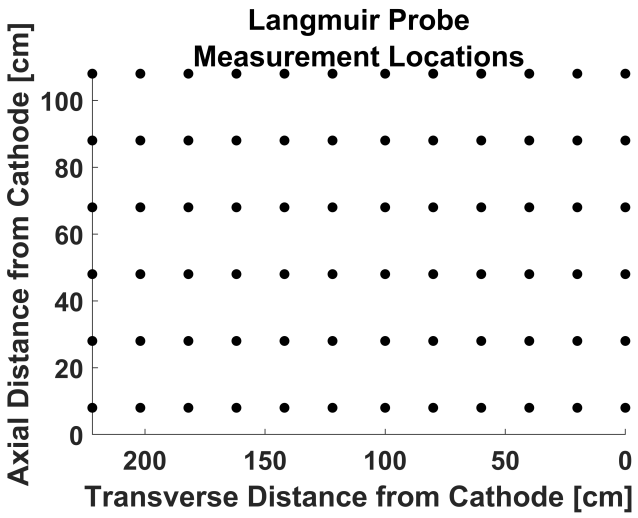

Figure 5.5: Langmuir probe measurement locations used during the described experiments.

within the testing area and simplifying its geometry by flattening the plasma sheath. The conducting plate can be viewed in Figure 5.4 (b) and a graphical representation of the entire vacuum chamber interior is given in Figure 5.6. Sheath measurements were made in several locations between the plate surface and a position 10 cm away from the surface. The spacing in this interval was at most 1 cm and specific positions can be seen on each respective graph in Section 5.3.2.

5.2.2 Langmuir Probe Analysis Techniques

5.2.2.1 Langmuir Probe Analysis Approach

Here we describe the Langmuir probe analysis algorithm developed to reliably compute the ion density, electron density, electron temperature, plasma potential, and floating potential at each measurement location. In order to streamline the analysis process and limit the impact of human error, the same automated procedure is applied to each I-V sweep. The wide range of plasma conditions measured throughout the testing area led to several iterations of the analysis procedure. While many analysis techniques were considered and tested during this iterative process, ultimately the

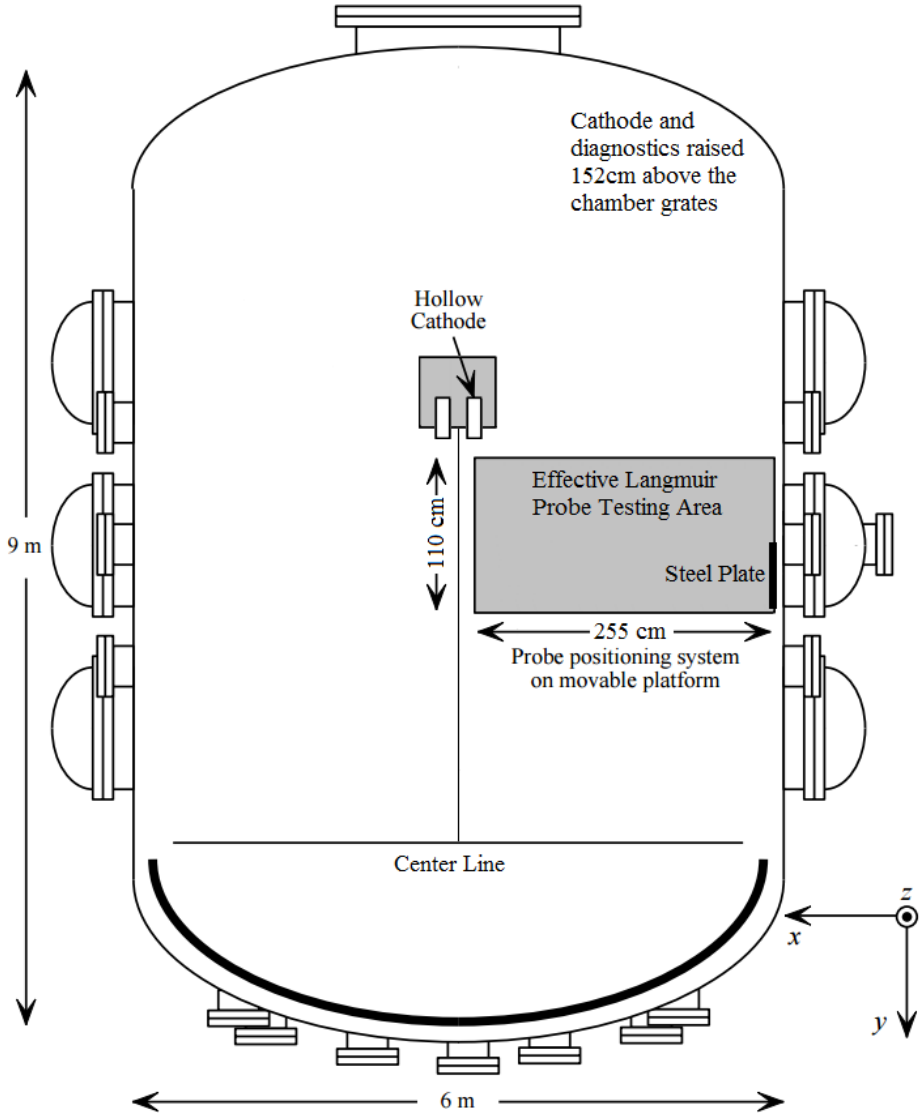

Figure 5.6: An aerial view of the bulk plasma experiment configuration in LVTF.

decision was made to employ the simplest and most widely used techniques appropriate for our plasma conditions with some minor modifications as described below [35, 36, 162–164]. The standard assumption that the cylindrical probe is a finite length section of an infinite cylinder is used with this approach in mind. The length-to-radius ratio of the Langmuir probe used here is 200, which limits the error induced using this assumption substantially when compared to a shorter/wider cylinders [165, 166]. However, the length is not sufficient to be treated as infinite for Debye lengths over $\sim$0.5 cm and more current density is incident on the cylinder ends than predicted by

the most widely used Langmuir probe theories [165, 166]. The empirical and analytical correction procedures developed to account for "end effects" are certainly useful. However, using them for this application would substantially increase analysis complexity and be of questionable accuracy, as they do not represent our physical probe configuration [165, 166]. The final Langmuir probe analysis procedure is very similar to the one recommended by Lobbia and Beal for use with electric propulsion devices [167]. A complete copy of this MATLAB analysis code is provided in Appendix C for reference.

The first step in the analysis procedure is removing the lowest voltage point and the 3 highest voltage points from the total 401 points taken in each sweep. This is simply done to remove any capacitive currents which may be induced by rapidly changing the Langmuir probe potential during initial bias application. The next step in the analysis procedure is smoothing the current data points using a filter to reduce measurement noise. Applying a smoothing algorithm or filter is typical for Langmuir probe measurements [168]. It is especially critical for our measurements, as I-V sweeps in the lowest plasma density locations require current measurement accuracy on the order of nanoamps. The Savitsky-Golay filter was selected as a standard Langmuir probe filter [168]. The Savitsky-Golay filter fits a specified window (number of points) surrounding the point under consideration with a specified order of polynomial using a linear least square fit and changes the point under consideration to the value of the polynomial function at the same location [169]. The filter window is kept small (15 points out of the 397 total points, or about 3.8% of the range) and the polynomial order kept large when possible to reduce any changes to the underlying shape of the I-V curve. Specifically, the polynomial order selected for bulk plasma measurements (where measurement noise was lowest) is 7, the order for grounded (0 V) sheath measurements is 5, and the order for 30 V sheath measurements (where measurement noise was highest) is 1. Examples of some of the noisiest raw and filtered I-V curves

from measurements in the plasma sheath can be seen in Figure 5.7 (a).

5.2.2.2 Floating Potential and Ion Density

Once the current is properly filtered, the desired plasma properties are calculated as follows. The floating potential is found by simply averaging the applied voltages when the smallest positive and negative currents were collected. Voltage steps of roughly 0.1 V ensured that this step does not induce significant error. The ion density is found using Orbit-Motion-Limited (OML) theory [32]. OML theory is the most commonly used analysis technique for plasma conditions in which the Debye length, λ_D, is larger than the Langmuir probe radius, r_p, [36]. For reference, the range of λ_D/r_p presented below is 1.4 – 570. OML uses the conservation of energy and angular momentum to calculate an impact parameter which determines whether an attracted particle (in this case, ions) will strike the probe surface [32, 36]. The development of this theory sets the plasma potential at an infinite distance to a potential value of zero Volts and assumes that the sheath is large and its local potential varies gently [32, 36]. Another assumption required by OML theory is that the background pressure is low enough for the plasma to be considered collisionless (such that energy and momentum are conserved) [32, 36]. The estimated charge exchange mean free path for the plasma presented below is 78 m based on ionization gauge measurements near the chamber walls. This mean free path is much greater than the largest chamber dimension of 9 m, so we consider the plasma conditions appropriate for applying OML theory. For a more complete treatment of competing cylindrical Langmuir probe ion collection theories and their respective assumptions, see the informative summary compiled by Francis Chen [36]. For more information on modern OML modifications, see the recent work by Tang and Delzanno [37].

A least squares linear fit of the ion saturation current squared is performed to calculate the ion density. OML theory dictates that ion density scales with the square

root of this line's slope according to Equation (5.1) [32, 170]. n_i is the ion density, α is the linear fit slope, m_i is the ion mass, A is the Langmuir probe surface area, and q is the elementary charge in Equation (5.1). Examples of this linear fit can be seen in Figure 5.7 (b). The specific fit range is the first 75% of points between the minimum sweep voltage and the floating potential. The last 25% was excluded from the linear fit as the electron current begins to pick up near the floating potential (again, see Figure 5.7 (b)).

$$n_i = \sqrt{\frac{\alpha \pi^2 m_i}{2A^2 q^3}} \quad m^{-3} \tag{5.1}$$

The ion current collected to the Langmuir probe is estimated for each applied voltage using fits and OML theory. By subtracting this calculated ion current from the measured current, an estimate of the collected electron current is produced. The accuracy of this estimate depends on how well ion collection is predicted using OML theory. However, electron current is already much greater than ion current for probe potentials close to the plasma potential. These are the only electron currents used directly in this analysis procedure, so the electron current error induced by OML ion current fitting can be treated as negligible. The estimated electron current is then used to calculate plasma potential, electron density, and electron temperature.

5.2.2.3 Plasma Potential

The plasma potential is found using the peak in the first derivative of the electron current [35, 36, 167]. While this is a standard technique, its implementation proved challenging across large sets of Langmuir probe I-V curves in plasma environments with differing densities. For example, in many low-density cases the derivative plateaued rather than peaking (see Figure 5.7 (c)). To assist the peak finding process,

the first derivative was filtered using the same parameters as described above for the raw current measurement. That way, the filter parameters could be adjusted until a subset of detected peaks aligned with peak locations selected by inspection. Once these universal filter parameters were chosen and applied to the entire dataset, an inspection of the automated plasma potential selections yielded a maximum difference (or error) of +/- 2 V. However, the vast majority of calculated plasma potentials fell within 0.2 V of those selected by hand. The first (lowest voltage) peak in the derivative was found using the MATLAB findpeaks function and a minimum peak height of 0.5.

5.2.2.4 Electron Temperature

The electron temperature is found by taking the natural log of the current between the floating and plasma potentials and fitting it with a line using a least squares fit [35, 36, 167]. Only the center of this range is fit to limit the effect of ion current collection error (at lower voltages) and plasma potential measurement error (at higher voltages). Many different spans in the center of this range were tested to find the best balance between the number of points fit and end effect errors. Ultimately the middle 25% was selected as the most consistent fit range. Example fits of this region are shown in Figure 5.7 (d). Fitting the natural log of the electron retardation regime is a standard technique which only requires that the ambient electron population have a Maxwellian electron energy distribution function (EEDF) [35, 36]. While not all hollow cathode EEDFs match an ideal Maxwellian function, many are quite close [161, 171, 172]. An example EEDF from this set of experiments is given in Figure 5.8 as determined using the Druyvesteyn technique on a Langmuir probe sweep 8 cm from the hollow cathode orifice [161, 173]. It is clear from this example that a Maxwellian function captures the general trends well enough to be used as a simple representation of electron thermal velocities.

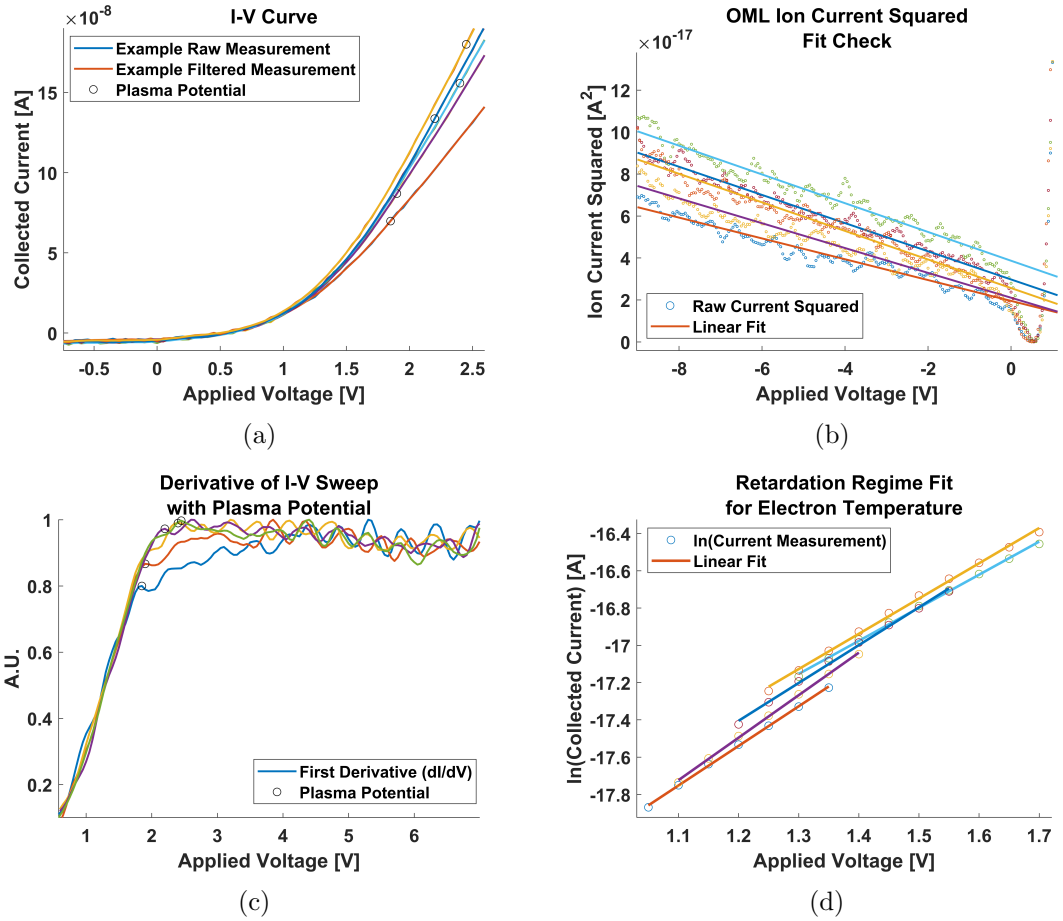

Figure 5.7: Example analyses of challenging I-V sweeps at positions 1, 2, 3, 4, and 5 cm from the grounded steel plate for a cathode bias of 0 V. Shown are the raw and filtered I-V sweeps (a), OML fit of the ion saturation current squared as used for ion density (b), first derivative of the current as used for plasma potential (c), and electron retardation regime fit as used for electron temperature (d). Legends are provided only for the 1 cm position for simplicity.

5.2.2.5 Electron Density

The electron density was found using the electron current at the plasma potential via the electron saturation current technique [35, 36, 167]. This technique exploits the fact that when the Langmuir probe is at the plasma potential, it will simply collect the thermal electron current over its surface. The explicit expression used to calculate electron density is given in Equation (5.2). n_e is electron density, $I_{e,sat}$ is the electron saturation current (electron current at the plasma potential), T_e is the

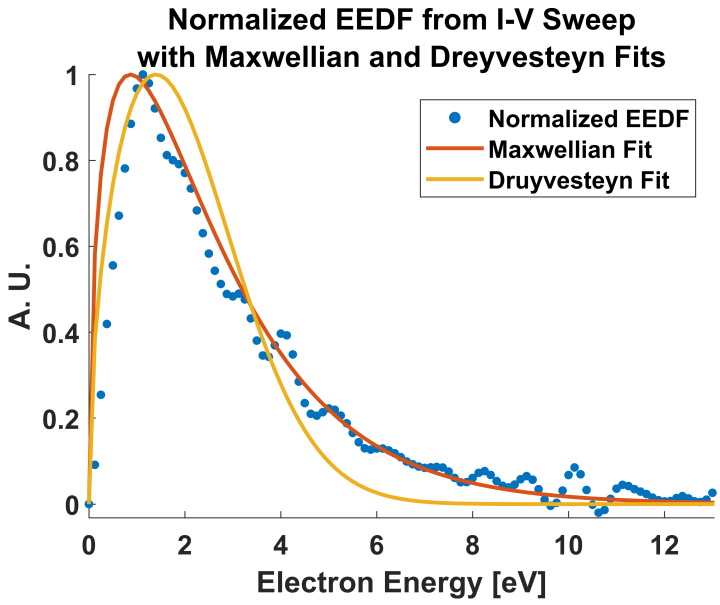

Figure 5.8: Normalized EEDF from a cylindrical Langmuir probe sweep 8 cm downstream of a hollow cathode orifice with a 40 V cathode bias. Maxwellian and Druyvesteyn distribution function fits are shown.

electron temperature, and m_e is the electron mass in Equation (5.2). While there is some minor error in this estimate thanks to the inherent noise of a single current measurement, the dominant error term comes from inaccuracies in the estimate of plasma potential. Personal inspection of plasma potential error yields a resultant maximum error of a factor of 2 in electron density measurements, although the vast majority fell within 20% of what was measured. The maximum errors found when using the analysis procedure developed here align with typical values for a cylindrical Langmuir probe [174].

$$n_e = \frac{I_{e,sat}}{qA\sqrt{\frac{qT_e}{2\pi m_e}}} \quad m^{-3} \tag{5.2}$$

5.3 Experimental Results

5.3.1 Bulk Plasma Results

The bulk plasma properties of two contactor plasma plumes are presented below via contour plot. The only meaningful difference in the experimental conditions between the two plasmas is that the hollow cathode was biased to 0 V relative to the vacuum chamber walls (grounded) for one set of measurements and 40 V for the other set of measurements. The hollow cathode was injected up in the figure reference frame. Its orifice (injection location) was 8 cm below the horizontal axis in the bottom right-hand corner. The floating potential, plasma potential, electron temperature, electron density, ion density, and density ratio (the local ratio of electron density to ion density) are presented in Figures 5.9, 5.10, 5.11, 5.12, 5.13, and 5.14 respectively. Preliminary examination of this data yields results one might expect from a hollow cathode in diode mode, or more generally from a small plasma source with a given flow vector. There are some small features and imperfections which point to measurement error. This is to be expected considering Langmuir probe measurements generally have an error of 10% up to a factor of 2 [170, 174, 175]. A complete treatment of Langmuir probe error estimation can be found in the work of Omar Leon [96]. Trends can still be clearly discerned in most contours despite the presence of these errors due to even larger plasma parameter ranges and the high number of measurements presented. Some of these trends are discussed below and a contrast is drawn between the two plasmas during discussions in Section 5.4.

Floating potential measurements (Figure 5.9) reveal minimal deviations from 0 V for the 0 V bias case. Interestingly, there is a floating potential decrease of roughly 11 Volts as one moves from the hollow cathode to the wall for the 40 V bias case. While interesting, these observations are not particularly revealing about the plasma on their own. More importantly, there is a significant decrease in the plasma potential

when moving away from the plasma source for both the 0 V and 40 V case (see Figure 5.10). The total plasma potential drop was 7.8 V for the 0 V bias case and 14.5 V for the 40 V bias case. These potential drops align with previous numerical predictions, as they are on the order of the electron temperature [16]. For example, the maximum electron temperature of the 0 V bias case was 2.0 eV, meaning that the potential dropped by 3.9 Te over the bulk plasma. Similarly, the maximum electron temperature of the 40 V bias case was 2.3 eV and the potential dropped by 6.3 Te. The maximum electron temperature was found close to the cathode orifice and the local temperature dropped off in a manner similar to the plasma potential (see Figure 5.11). The electron temperature dropped over the testing area by a factor of 7.7 for the 0 V bias case (2.0 eV to 0.26 eV) and a factor of 2.4 for the 40 V bias case (2.3 eV to 0.98 eV). This discrepancy is discussed in Section 5.4.

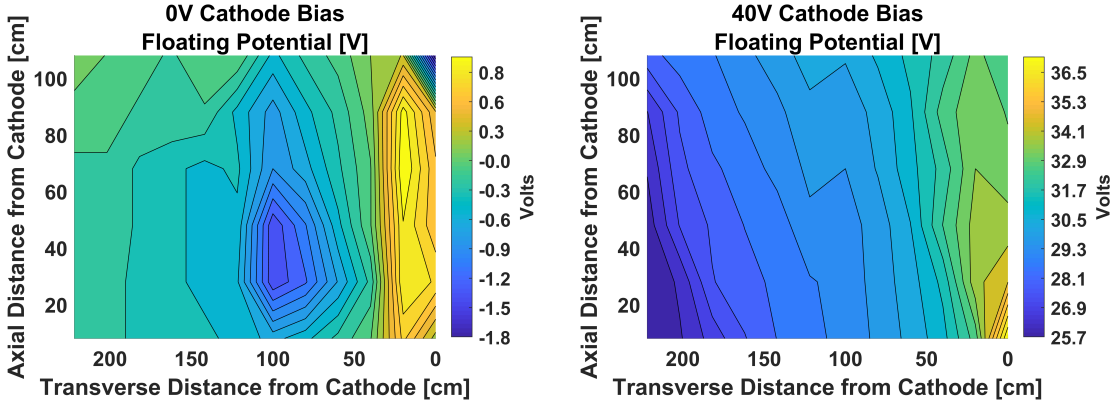

(a) (b)

Figure 5.9: Contour plots of the bulk floating potential for a hollow cathode biased to 0 V (a) and 40 V (b) relative to the chamber walls.

The electron and ion densities presented in Figures 5.12 and 5.13 generally have the same shape and look as one would expect for a hollow cathode plasma source. However, a direct comparison using the ratio of electron density to ion density at each location (as shown in Figure 5.14) reveals a strange region near the cathode orifice of the 0 V bias case with no immediately obvious explanation based on plasma theory.

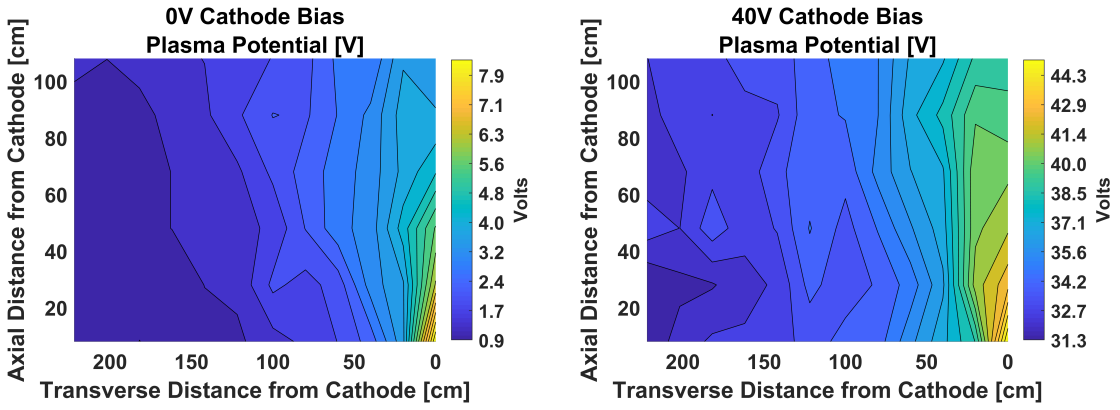

(a) (b)

Figure 5.10: Contour plots of the bulk plasma potential for a hollow cathode biased to 0 V (a) and 40 V (b) relative to the chamber walls.

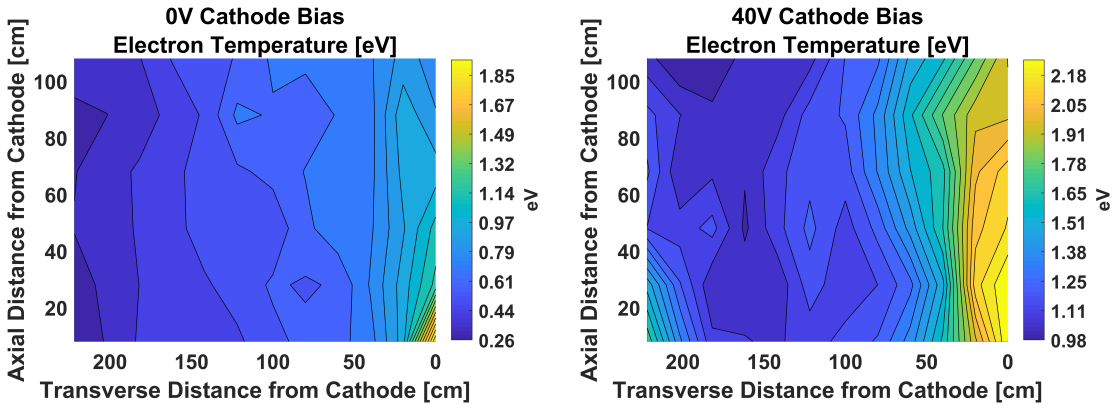

(a) (b)

Figure 5.11: Contour plots of the bulk electron temperature for a hollow cathode biased to 0 V (a) and 40 V (b) relative to the chamber walls.

In addition, ion and electron density measurements differ by up to a factor of 8 in this region, which represents the largest deviation observed. This noteworthy region is examined further in Section 5.5 and found to be unphysical. When ignoring this region, we found that the largest discrepancy between ion and electron densities is a factor of 5.2 in the 0 V bias case. The largest density discrepancy in the 40 V bias case was found to be 3. It is clear from Figure 5.14 that ion density measurements are generally higher than electron density measurements. On average, the measured ion density at a given location was 2.5 times higher than the electron density measured

at the same location. This phenomenon is examined further in Section 5.6. There are also no clearly defined regions which denote the transition from a quasi-neutral plasma to an ion-rich plasma for the 40 V bias case [16]. The search for a transition from a quasi-neutral region to an ion-rich region continues in the next section with the examination of the plasma sheath near the chamber wall.

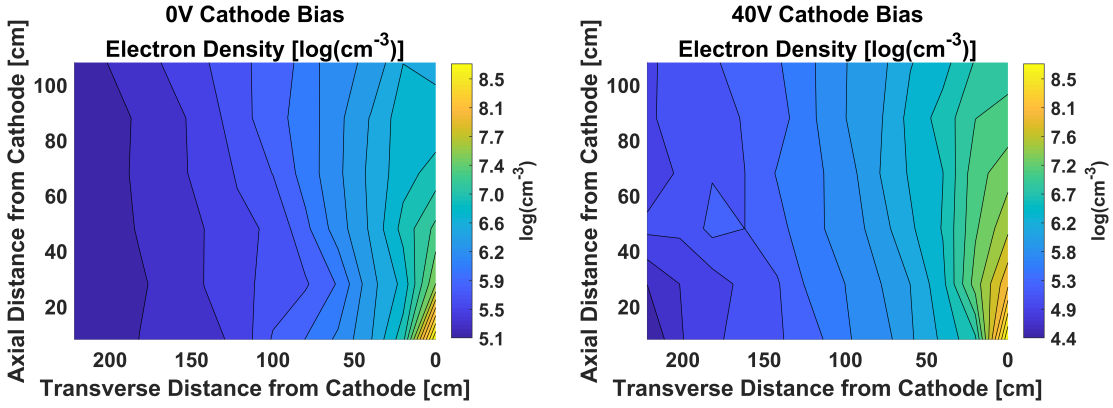

(a) (b)

Figure 5.12: Contour plots of the bulk electron density for a hollow cathode biased to 0 V (a) and 40 V (b) relative to the chamber walls.

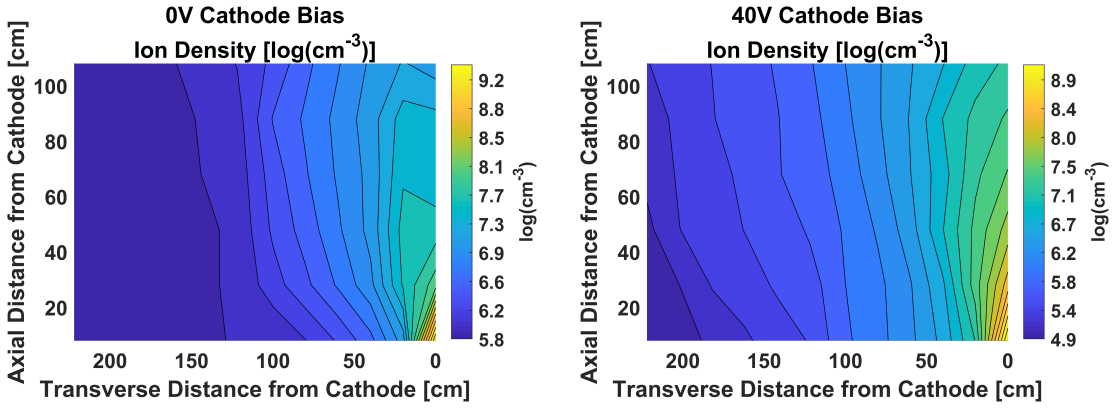

(a) (b)

Figure 5.13: Contour plots of the bulk ion density for a hollow cathode biased to 0 V (a) and 40 V (b) relative to the chamber walls.

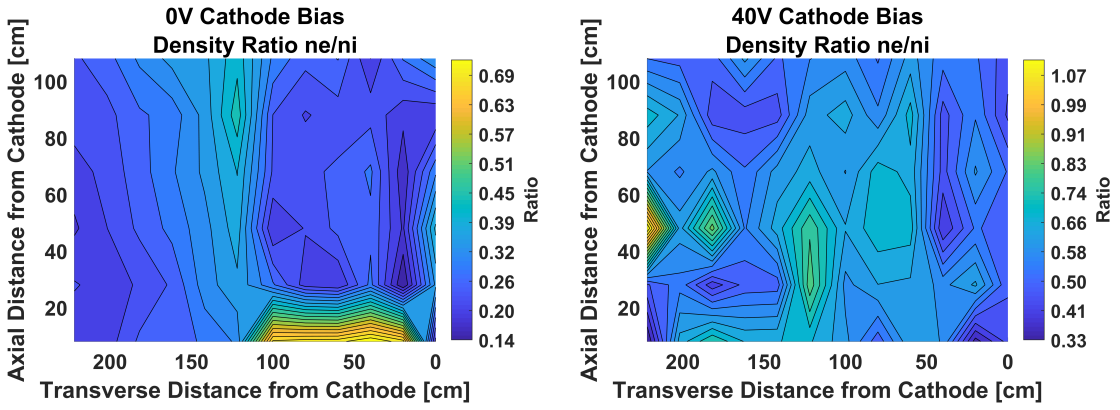

(a) (b)

Figure 5.14: Contour plots of the bulk density ratio (the local ratio of electron density to ion density) for a hollow cathode biased to 0 V (a) and 40 V (b) relative to the chamber walls.

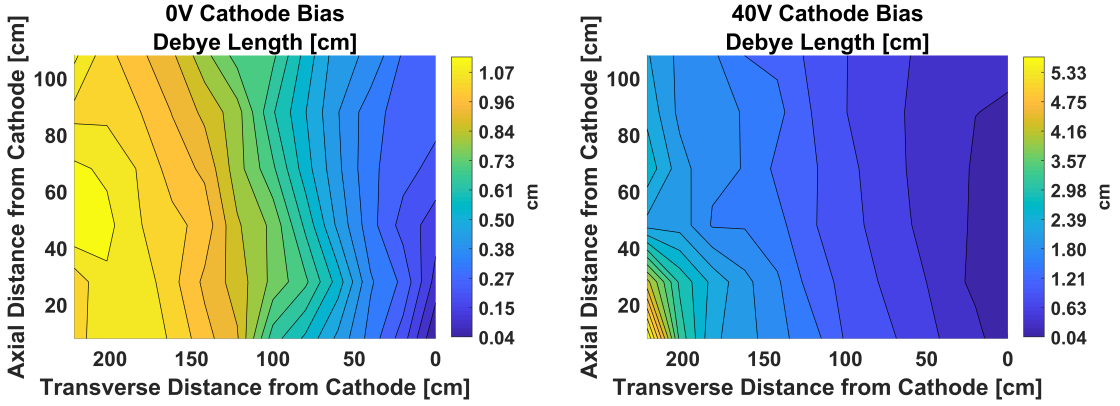

(a) (b)

Figure 5.15: Contour plots of the bulk Debye length for a hollow cathode biased to 0 V (a) and 40 V (b) relative to the chamber walls.

5.3.2 Sheath Plasma Results

The sheath plasma properties of two hollow cathode contactor plasmas are presented below. The only meaningful difference in the experimental conditions between the two plasmas is that the hollow cathode was biased to 0 V relative to the vacuum chamber walls (grounded) for one set of measurements and 30 V for the other set of measurements. The hollow cathode plasma plume was injected parallel to the steel plate's surface (orthogonal to the probe movement) in a location 108 cm upstream

and 249 cm transverse of the plate's surface (see Figure 5.6). The sheath plasma potential, electron temperature, ion density, electron density, and density ratio (the local ratio of electron density to ion density) are shown in Figures 5.16, 5.17, 5.18, 5.19, and 5.20 respectively.

The sheath measurements in this section appear to be rather noisy in comparison to the bulk plasma measurements presented above. This is to be expected as the plasma densities and collected currents in these locations are quite low (see Figure 5.7). In addition, standard Langmuir probe theory is derived assuming the probe is immersed in a fairly quasi-neutral, equi-potential plasma with no significant drift velocity [32, 36, 162, 176]. These assumptions begin to break down in a plasma sheath, making it quite challenging to accurately measure plasma properties in a tenuous sheath such as this [177]. This difficulty is also shared by many other plasma diagnostics, to the point that switching to an alternative diagnostic package may not have aided measurement accuracy. Error bars are not included in the figures below, as previous research failed to quantify the effects of operating a Langmuir probe in a tenuous sheath [177]. A general error of 20 - 50 % is the current best estimate for the plasma measurements in this section. Errors of this magnitude still leave room for useful experimental interpretation with respect to the ion emission model. Qualitative examination of this data also yields results one might expect from the sheath of a plasma close to a grounded, conducting object.

The figures below present a picture consistent with the structure of an ion-rich sheath. To illustrate this point, a least squares fit was performed on the sheath plasma potential assuming the theoretical sheath potential expression of Equation (2.9). Figure 5.16 is thus fit with an exponential function in red. The quality of this fit indicates that plasma potential measurements align with the theoretical ion-rich sheath structure. A rough prediction of the sheath electron density is also included in Figure 5.19 using the Boltzmann relation (or Boltzmann factor) one would expect for

Maxwellian electrons in a sheath [178]. The exact plasma potential fit of Figure 5.16, the average electron temperature measurement, and the maximum measured electron density were all used to produce this predictive electron density profile. The accuracy of this prediction based on the Boltzmann relation suggests agreement between plasma potential and electron density measurements.

Electron temperature and ion density do not appear to change appreciably in the sheath region as all measured values are within a factor of 2. The roughly constant electron temperature for the 30 V bias case was almost 3 times higher than for the 0 V bias case ($\sim$1.4 eV versus $\sim$0.5 eV). Though extreme, this discrepancy is a logical extension of the trend observed in the bulk electron temperature (see Figure 5.11). One would typically expect the ion density to decrease noticeably when approaching the chamber wall/steel plate in order to maintain a constant ion flux in the sheath, however this is only required if the ions pass through an accelerating plasma potential barrier [178]. Examination of Figure 5.16 reveals the sheath potential barrier to be rather small in this case. The sheath potential drops by $\sim$1.4 V for the 0 V bias case and $\sim$2.8 V for the 30 V bias case. Neither of these potential drops represent more than a 10% increase in the ion drift velocity acquired when transiting the bulk plasma (assuming the ions are generated at the plasma potential measured closest to the hollow cathode). This minor drop in the ion drift velocity appears to be mostly obscured by measurement error.

The electron density profile (see Figure 5.19) is found to drop significantly when approaching the chamber wall/steel plate, leading to a corresponding drop in the density ratio. The density drop is spread out over a longer distance for the 30 V bias case, which is perhaps to be expected given this case's larger Debye length ($\sim$2.8 cm versus $\sim$1.6 cm). The electron density drop is more severe for the 30 V bias case as well. While both densities start at $\sim 1.1 \times 10^5$ cm^{-3} for positions 10 cm from the chamber wall/steel plate, the electron density is 4.9×10^4 cm^{-3} and 5.5×10^3 cm^{-3} at

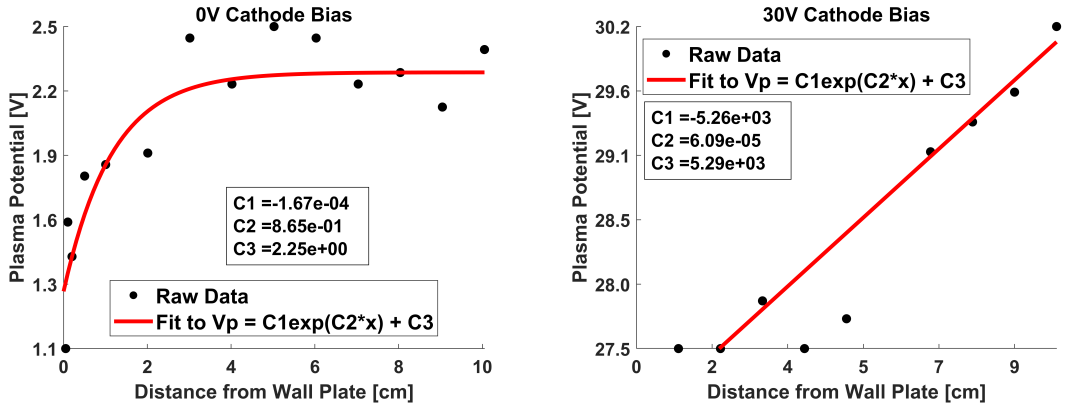

(a) (b)

Figure 5.16: The sheath plasma potential for a hollow cathode biased to 0 V (a) and 30 V (b) relative to the chamber walls. A least squares, theoretical exponential fit is also shown.

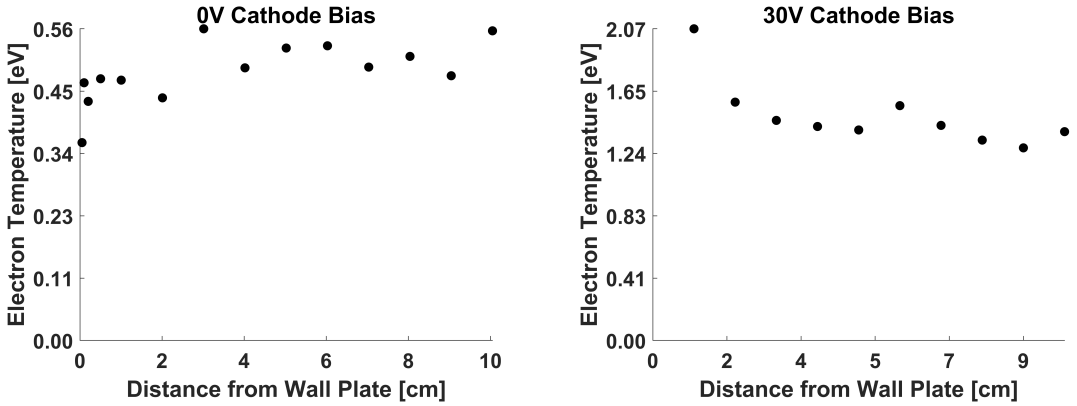

(a) (b)

Figure 5.17: The sheath electron temperature for a hollow cathode biased to 0 V (a) and 30 V (b) relative to the chamber walls.

1 cm for the 0 V and 30 V bias case respectively. Inspection of the density ratios in Figure 5.20 reveals that the plasma is transitioning from a quasi-neutral region to an ion-rich region over a very short distance near the chamber wall, marking it as the location where ion emission occurs for a steady state chamber experiment. This transition is especially clear for the 30 V bias case which represents high-current electron beam emission. For the 30 V bias case, $n_e/n_i = 0.024$ just 1 cm from the chamber wall/steel plate.

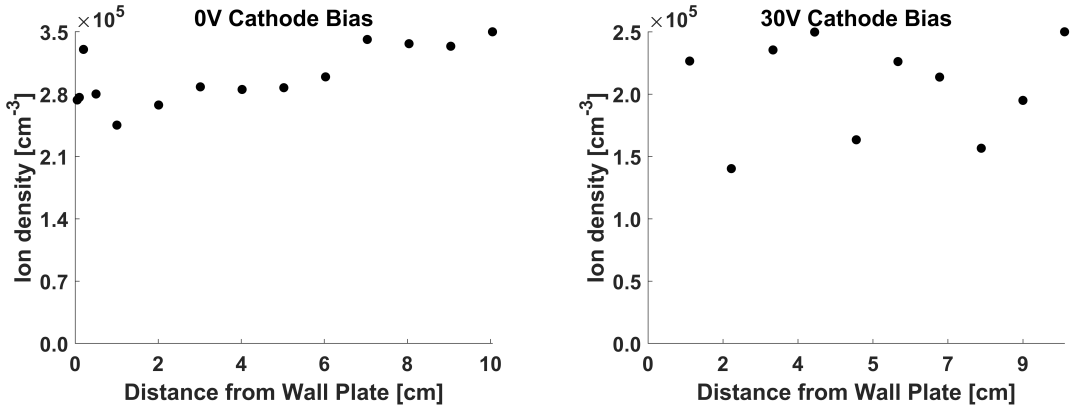

(a) (b)

Figure 5.18: The sheath ion density for a hollow cathode biased to 0 V (a) and 30 V (b) relative to the chamber walls.

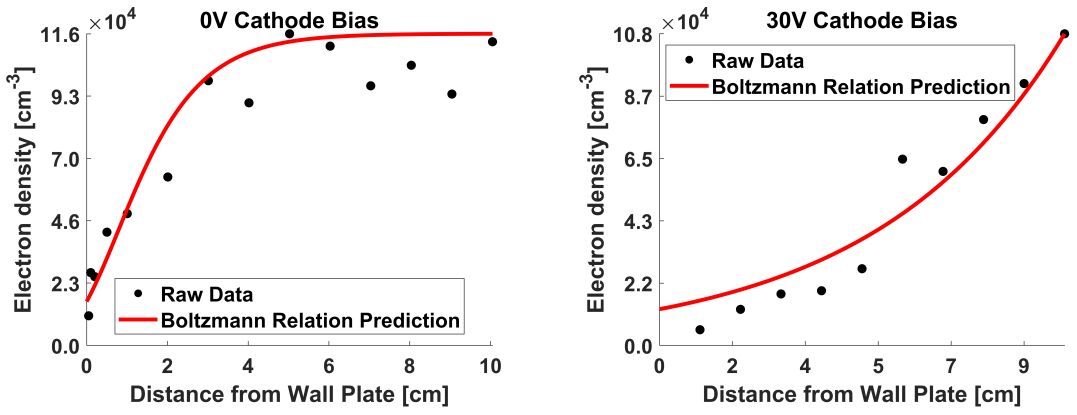

(a) (b)

Figure 5.19: The sheath electron density for a hollow cathode biased to 0 V (a) and 30 V (b) relative to the chamber walls. An electron density profile prediction based on plasma potential measurements and the Boltzmann relation is also shown.

5.4 Bulk Plasma Charging Response

In this analysis, we directly examine changes to the bulk plasma when biasing the hollow cathode (which approximates spacecraft charging during electron beam emission). In Figure 5.21 we see that the floating and plasma potentials both increase significantly when the cathode bias is increased by 40 V. The plasma potential increases by 30 - 37 V throughout the testing area and the floating potential similarly

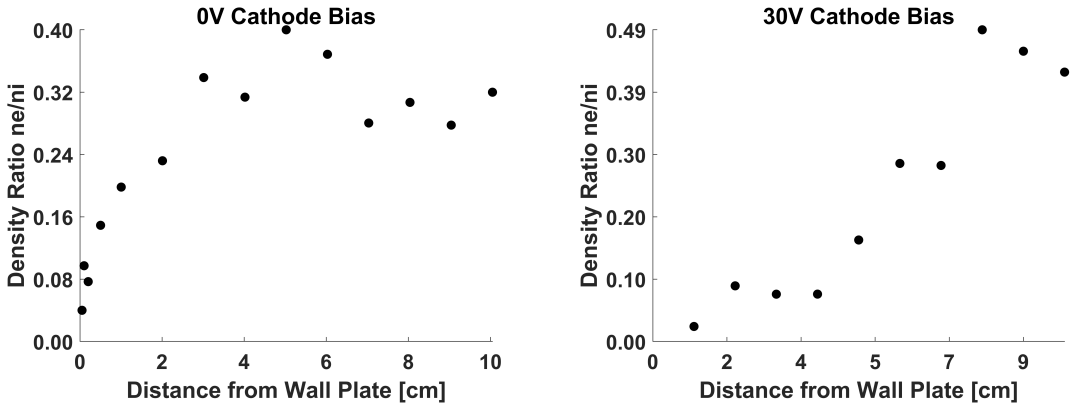

(a) (b)

Figure 5.20: The sheath density ratio (the local ratio of electron density to ion density) for a hollow cathode biased to 0 V (a) and 30 V (b) relative to the chamber walls.

increases by 26 - 37 V. This result is expected based on previous CPIC simulations and semi-analytical modeling, which predicted the quasi-neutral region plasma potential would remain within a few Te of the spacecraft potential (see Figure 3.8) [14–16]. It is evident from Figure 5.21 that the floating and plasma potentials increase the most for locations on-axis with the hollow cathode plasma injection. This is likely caused by the two other bulk plasma changes discussed in this section. The electron temperature and on-axis charged particle densities are both found to increase for the higher bias case.

One unexpected result from the bulk plasma experiments is the universal increase in electron temperature with cathode bias. Figure 5.22 shows changes in electron temperature (and the associated Debye length) by dividing the local value for a cathode bias of 40 V by the value for a lower cathode bias of 0 V. It was found that increasing the cathode bias by 40 V produced electron temperatures that are greater by a factor of 1.1 – 6.6. This discrepancy is even greater when ignoring the most similar measurement (the point closest to the hollow cathode orifice). The electron temperature increased by at least 70% when ignoring this point, signifying that the bulk/distant electron temperature is most effected by cathode potential changes. The

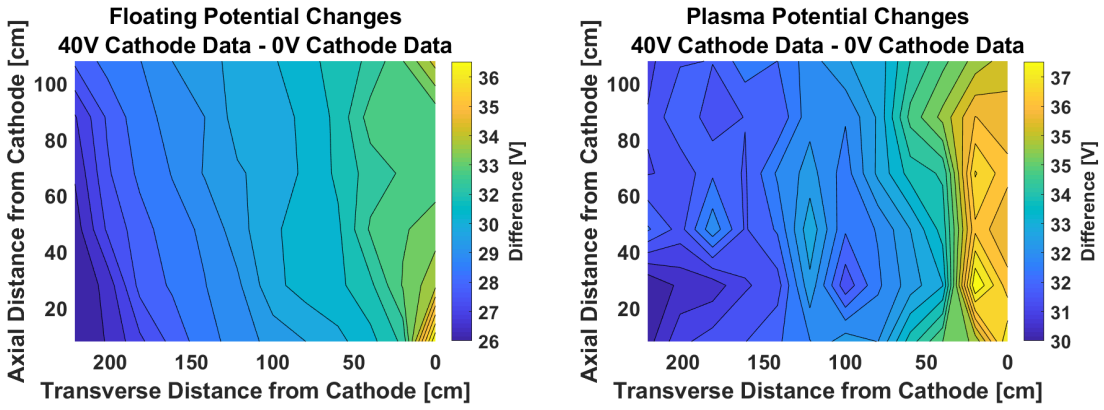

(a) (b)

Figure 5.21: Absolute change to the floating potential (a) and plasma potential (b) when increasing the cathode bias from 0 V to 40 V.

exact cause of this phenonmenon was not studied via simulation or modeling, however a likely explanation is outlined here. Current saturation measurements indicate that very few electrons ($< 10\%$) are emitted to the chamber walls in the 40 V bias case. This is the result of an enlarged potential barrier between the plasma potential where electrons are created (near the hollow cathode orifice) and the grounded chamber walls, as indicated by Figure 5.21 (b). The enlarged potential barrier increases the minimum energy required to reach distant regions of the contactor plasma, with low energy electrons traveling only a short distance before the potential barrier forces them back to the hollow cathode keeper (the highest potential object in the vacuum chamber) where they are collected and measured. Thus only the most energetic electrons making up the high energy tail of the EEDF (see Figure 5.8) are present to be measured in the bulk contactor plasma. This high energy tail of the EEDF presents as a higher electron temperature in our Langmuir probe analysis. This explanation is consistent with Figure 5.22 (a), where the largest increases in electron temperature are furthest from the hollow cathode. The plasma potential is at its lowest in distant plasma regions such as the corner directly perpendicular to the cathode orifice (see Figure 5.10) and thus only the most energetic electrons are present.

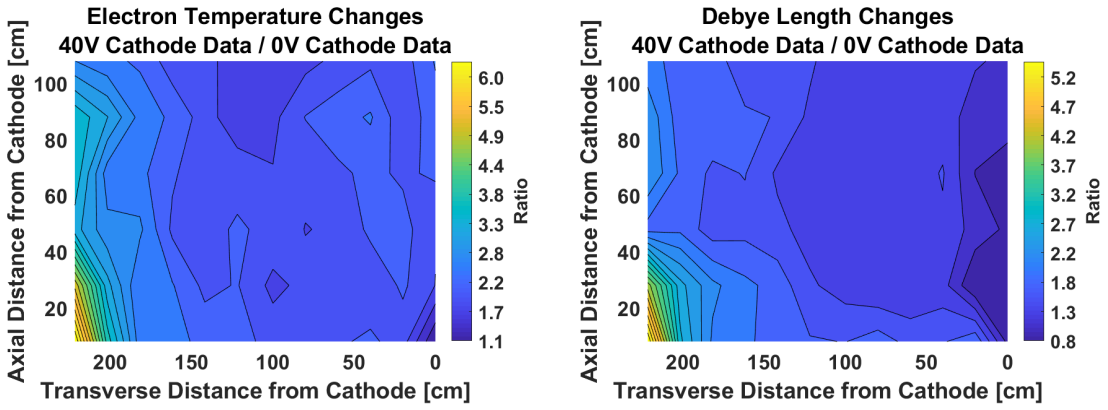

(a) (b)

Figure 5.22: Relative change to the electron temperature (a) and Debye length (b) when increasing the cathode bias from 0 V to 40 V.

Figure 5.23 shows changes in electron and ion densities by dividing the local value for a cathode bias of 40 V by the value for a cathode bias of 0 V. It is clear from this figure that the charged particle densities generally increase on-axis and decrease for positions further afield. This phenomenon was not observed directly during numerical modelling, however a possible explanation is given here. The plasma potential drop increases throughout the contactor plasma for higher cathode biases. For proof of this, observe Figure 5.21 (b) and consider that at no location does the plasma potential increase by the full 40 V that is applied to the cathode. This implies that ion drift velocity increases with cathode bias within the bulk plasma, something that is explored in the subsequent section and confirmed during the experiments presented in Chapter 6. An increased ion drift velocity stemming from a potential drop at the cathode orifice would act to effectively collimate and direct the ion population axially, as the cathode orifice has a divergence half-angle of just 45°. The local ion space-charge is then expected to pull the mobile electrons into this region, similar to the phenomenon observed during ambipolar diffusion [155].

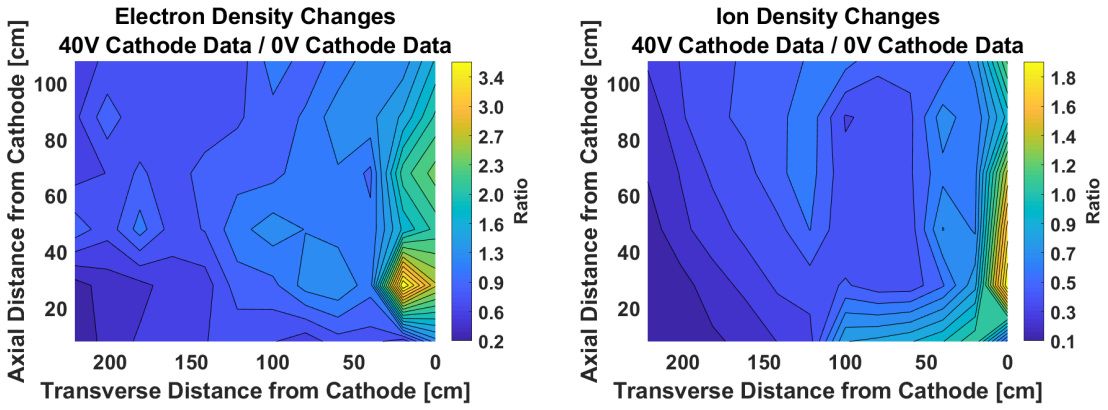

(a) (b)

Figure 5.23: Relative change to the electron density (a) and ion density (b) when increasing the cathode bias from 0 V to 40 V.

5.5 An Estimate of Bulk Ion Drift Velocity

Single, cylindrical Langmuir probes are not known for their ability to measure ion drift velocity. We nonetheless attempt to use established Langmuir probe theory to test our theory on changing ion drift velocities. Hoegy and Wharton laid out an ion collection theory based on OML which individually accounts for the effect of ion drift, ion temperature, and OML ion orbits as shown in Equation (5.3) [170]. I_i is the collected ion current, A is the Langmuir probe surface area, n_i is the ion density, q_i is the ion charge, v_d is the ion drift velocity, k_B is Boltzmann's constant, T_i is the ion temperature, m_i is the ion mass, q is the elementary charge, and V is the probe bias with respect to the plasma in Equation (5.3) [170]. We can estimate the ion current at the plasma potential using the same OML fits described above to remove any functional dependence on probe potential or orbital motion (the third term in parenthesis). By further assuming cold ions (setting term two in the parenthesis to zero) and using the local value of ion density, we are able to estimate vd without any additional information. The cold ion assumption acts to enhance the estimated ion drift velocity, however $T_i < 0.5$ eV as a general rule (as seen in Chapter 6). This indicates that the cold ion assumption generally contributes less error to the ion drift

velocity estimate than the errors incurred in calculating plasma potential and ion density. The resulting plots of ion drift velocity are shown in Figure 5.24.

$$I_i = An_i q_i v_d \pi^{-1} \left(1 + \frac{k_B T_i}{m_i v_d^2} + \frac{2qV}{m_i v_d^2}\right)^{\frac{1}{2}} \quad A \tag{5.3}$$

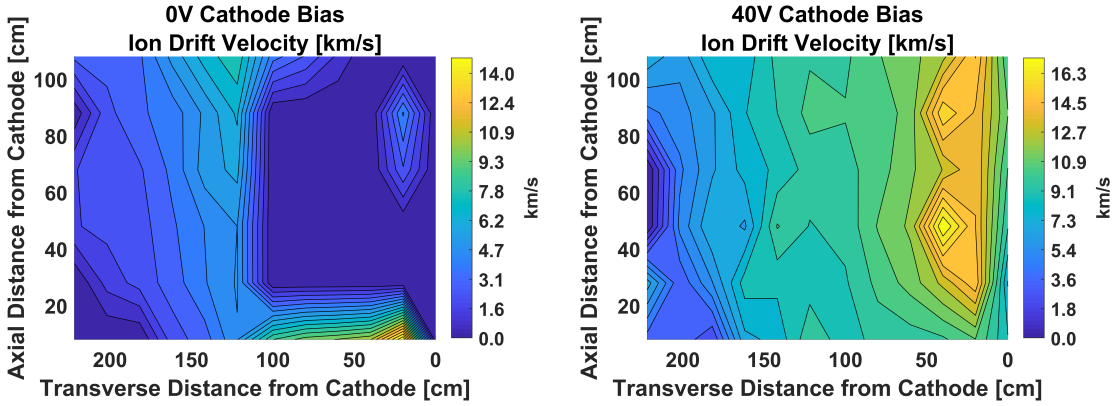

(a) (b)

Figure 5.24: Contour plots of the bulk ion drift velocity for a hollow cathode biased to 0 V (a) and 40 V (b) relative to the chamber walls.

It is difficult to decipher any clear changes in the ion drift velocity between the two sides of Figure 5.24. Instead, we see two clear trends emerge based on the bias. For the 40 V bias case, we see surprisingly clearly that the ion drift velocity decreases when moving away from the hollow cathode axis. This observation lends support to the theory that ions are accelerated roughly in a cone centered on the hollow cathode axis, causing collimation and a corresponding increase in their density when the cathode bias is increased. The ion drift velocity peaks just off-axis are interesting to note and believed to be physical. They are observed again during the experimental campaign presented in Chapter 6. For the 0 V bias case, the ion drift velocity shows the same unexpected feature that was seen for the density ratio (Figure 5.14 (a)). Specifically, Figure 5.24 (a) appears to report zero ion drift velocity for a strangely square section of the test area. An ion drift velocity of zero indicates that the estimated ion current

reaches zero at potentials below the plasma potential, which is an unphysical result in this scenario.

This unphysical result prompted further investigation and revealed a likely cause. The left side of this square section coincides with the dividing line between where measurements were made by the inner Langmuir probe versus the outer Langmuir probe. Timestamps of the bulk Langmuir probe measurements reveal that the inner Langmuir probe started at the testing area's maximum axial position and moved towards the cathode over time. As a result, the measurement closest to the hollow cathode took place right before it moved left for a final 5 I-V sweeps. It is at these last few locations that we observe the density ratio and ion drift velocity measurements suddenly change significantly. Based on this evidence, we can conclude that I-V sweeps in close proximity to the hollow cathode appear to have altered the Langmuir probe's current collection properties, likely by cleaning the biased probe surface via electron or ion bombardment [179]. This theory is in line with previous measurements which indicate a "dirty" probe artificially increases ion density measurements but have a negligible effect on electron temperature [179]. We can thus conclude that the inner Langmuir probe was not cleaned sufficiently prior to the start of the 0 V bias case, resulting in somewhat off density measurements and unphysical estimates of ion drift velocity for a defined plasma region. The density ratios in this defined plasma region are some of the lowest observed in either bulk plasma. However, the trend of ion densities being higher than electron densities persists even when ignoring this region.

5.6 A Discussion of the Bulk Plasma Density Ratio

The range of density ratios (local electron density divided by the local ion density) outside of the region discussed in the preceding section (see Figure 5.14 (a)) is 0.19 - 0.75 for the 0 V bias case. The range of bulk density ratios for the 40 V bias case is 0.33 - 1.15. The density ratio spread can easily be explained by measurement error,

however the range not being centered around one demands further discussion. Taking this trend at face value suggests that the electron density is lower than the ion density in both bias cases. However, it is far more likely that the electron density measurement using the electron saturation current is correct and the OML theory used to estimate ion density is to blame for this discrepancy. OML analyses have been shown to overpredict ion density by a factor of 2-10 when compared to a quorum of alternate density measurement methods including microwave interferometry, hairpin resonance probes, and various other Langmuir probe techniques [162, 176]. An overestimation of the ion density by 2.5 times (as one would expect based on previous experimental measurements) exactly matches the deviation from quasi-neutrality observed here [162, 176]. Different theories exist to explain this discrepancy, with some listing ion collisions in the probe sheath and others listing the dependence on the unknown value of plasma potential [162, 176]. Ion collisions in the probe sheath are highly unlikely to be the culprit in this case as the background pressure is just $1x10^{-6}$ Torr (with a corresponding charge exchange mean free path of 78 m). The dependence on the plasma potential is related to the ion drift velocity and likely played a role here. Consideration of Equation (5.3) reveals that non-zero ion drift velocity and temperature both act to increase the collected ion current and, thus, the calculated ion density. In Chapter 6 we study the ion drift velocity and temperature of a similar contactor plasma and find the ion drift velocity to be non-negligible.

5.7 Summary

The primary experimental goals were achieved during this experimental campaign by observing the plasma response predicted by previous numerical modeling efforts. The bulk plasma potential increases with hollow cathode bias (i.e. when the "beam" is fired). There is a gradual drop in the plasma potential when moving away from the plasma source on the order of a few electron temperature. The bulk, quasi-

neutral region transitions to an ion-rich region at the chamber wall, where the plasma potential and electron density drop off rapidly. This configuration is as expected based on previous modeling efforts. It is also representative of a space-based system in which the electron beam current equals the contactor current (ion current generated by the hollow cathode), with the exception that the transition between quasi-neutral and ion-rich regions is defined by the chamber walls rather than the plasma size prior to electron beam ignition.

Additional, unpredicted phenonmena were observed which promise to aid our understanding of similar physical systems and further increase the fidelity of our modeling efforts. The plasma electron temperature increases significantly when increasing the hollow cathode bias. This observation is explained as a byproduct of the low energy electron population being reabsorbed by a higher potential cathode rather than traversing the quasi-neutral plasma to be measured at large distances. The charged particle populations appear to concentrate on the hollow cathode axis when the cathode potential is increased. This appears to be the result of an increase in the axial ion drift velocity brought about by larger potential drops near the hollow cathode orifice. Plasma ion energetics in similar systems is the topic of research in the subsequent chapter (Chapter 6).

CHAPTER VI

Ion Emission Validation III: Ion Emission Region Characterization

6.1 Motivation

Validating the CPIC simulation and ion emission model results discussed in Chapter 3 is a critical step in enabling spacecraft charge neutralization during high-current electron beam emission in space. The CPIC simulations demonstrate space-charge limited (SCL) ion emission from the surface of a quasi-neutral contactor plasma that can balance electron beam emission. A semi-analytical model was developed to corroborate these CPIC simulation results and the physical processes underlying ion emission. The work presented in previous chapters focuses on how the spacecraft potential and hollow cathode contactor plasma react to firing a simulated electron beam. In contrast, this chapter focuses on a quantitative comparison between the actual ion emission current and those predicted using the space-charge limit and semi-analytical ion emission model. In order to generate current emission predictions, various aspects of the chamber plasma must be measured and provided as model inputs. The semi-analytical model's physical inputs and outputs are summarized graphically in Figure 6.1.

A campaign of ground-based experiments is described below which seeks to val-

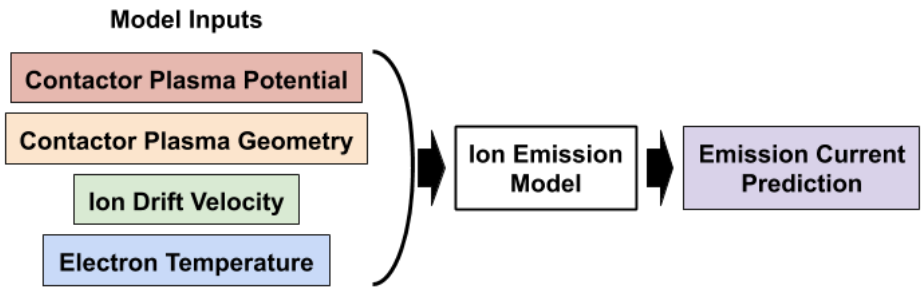

Figure 6.1: A summary of the inputs and output of the ion emission model.

idate the ion emission model using a hollow cathode plasma contactor in an instrumented vacuum chamber. While these experiments are in conditions that are notably different than those of a space experiment, our goal is to validate the physics of ion emission and its respective model in a controlled setting so that we can build confidence for model predictions in other regimes. The experiments in this chapter are broken down into "emitted ion" and "sheath region" experiments. The emitted ion experiments focus solely on the ion energetics at the chamber wall for different hollow cathode potential biases (a laboratory proxy for a changing spacecraft potential during electron beam emission in space). The sheath region experiments focus on characterizing the plasma regions near the chamber wall where the quasi-neutral contactor plasma transitions to an ion-rich sheath region (see Figure 6.2) in order to validate the ion emission model quantitatively. Using plasma potential profile and ion energy distribution function measurements, we can provide the contactor plasma potential, contactor plasma geometry, and ion drift velocity (inputs 1-3) to the semi-analytical ion emission model summarized in Figure 6.1. The final model input of electron temperature (input 4) is approximated for all positions in the chamber using a measurement near the plasma source. A complete set of model inputs is obtained and analyzed in multiple locations near the vacuum chamber wall as part of the sheath region experiments. This process is also completed for two discrete chamber sizes. All measurements using the large chamber size will be input into the semi-analytical

ion emission model and all measurements using the small chamber size will be input into a simple expression for the space-charge limited current. Finally, the ion emission current predicted using these measurements will be compared to the actual ion emission current measured at the chamber wall.

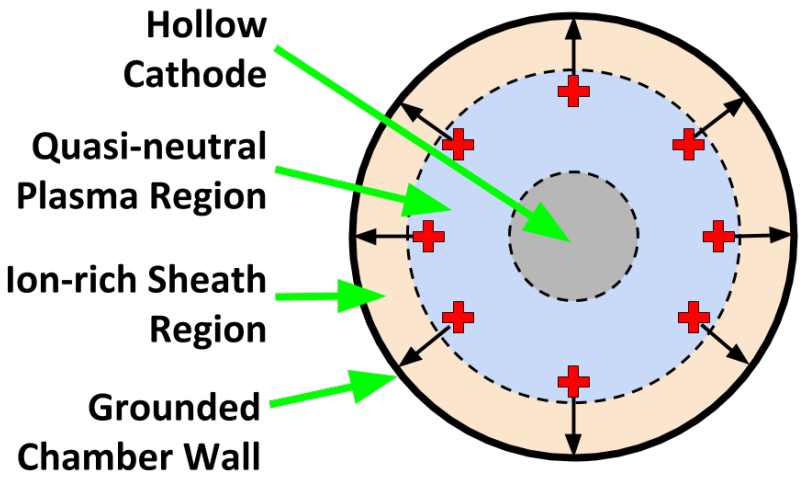

Figure 6.2: Basic experimental plasma regions according to the spherical ion emission model.

6.2 Experimental Setup

6.2.1 Hollow Cathode Plasma Contactor Overview

The hollow cathode used in the described experiments is shown in Figure 6.3 (a). It was selected for its appropriate size, ease of use, and lack of a magnetic field. This heaterless hollow cathode features an enclosed keeper electrode, a 1/4" orifice diameter, and is operated on Xenon gas. A quasi-neutral plasma is produced as keeper current flows between the cathode and keeper electrodes, ionizing neutral Xenon gas in the process [27]. The keeper current was set to 1.0 A for the emitted ion experiments and 1.3 A for the sheath region experiments. The typical neutral Xenon flow rate was 1 standard cubic centimeter per minute (sccm) and about 1% of neutral Xenon propellant was ionized (predominately singly ionized). The resulting plasma had a

density on the order of 10^8 cm^{-3}, an electron temperature of about 2.2 eV, and an ion temperature on the order of 0.1 eV when measured 10 cm directly downsteam from the hollow cathode orifice. Langmuir probe measurements were made at this location to be as close to the plasma source as possible without altering the hollow cathode's performance. The hollow cathode was designed by Plasma Controls, LLC using a proprietary low work function insert. During steady state operation this heaterless cathode produced a plasma representative of space-based plasma contactors.

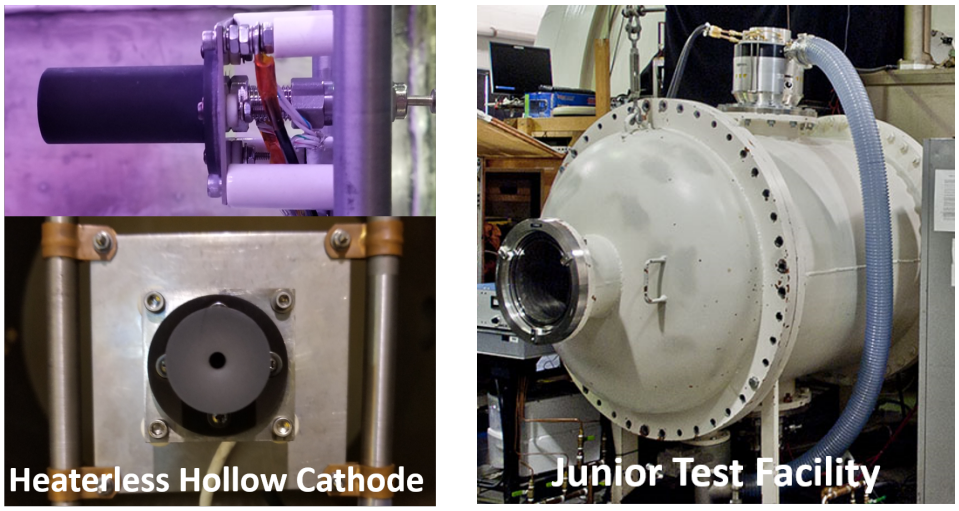

(a) (b)

Figure 6.3: The heaterless hollow cathode with graphite enclosed keeper (a) and Junior Test Facility vacuum chamber (b) used in the described experiments.

6.2.2 General Experimental Description

Experiments were performed at the University of Michigan's Plasmadynamics & Electric Propulsion Laboratory (PEPL) in the Junior Test Facility vacuum chamber. Junior is a roughly cylindrical chamber with rounded endcaps as shown in Figure 6.3 (b). It is composed of stainless steel, its largest diameter is 120 cm, and its center spans 120 cm in length. Large conducting plates were installed in the chamber to simplify its geometry and better approximate a cylinder. These plates were grounded to the chamber walls to more closely mimic previous simulation and model configu-

rations. This simplified cylindrical geometry had a diameter of 120 cm and a length of 38 cm for the emitted ion experiments, 52 cm for the SCL sheath region experiments (small chamber configuration), and 64 cm for the ion emission model sheath region experiments (large chamber configuration). The hollow cathode was inserted into a 3" circular cutout in the center of one plate such that the two were electrically isolated. The hollow cathode was biased positive with respect to the grounded, conductive chamber walls/plates to mimic the equivalent space system's response to electron beam emission according to the circuit diagram in Figure 6.4. The hollow cathode potential can also be thought of as the spacecraft potential with respect to the ambient space plasma, as hollow cathodes are typically tied to spacecraft common.

Junior achieved an operating pressure of $3x10^{-6}$ Torr using a Leybold MAG2000 turbopump. This pressure can be converted to a mean free path using a Xenon charge exchange cross section of $2x10^{-18}$ m^2 and assuming a neutral temperature of 300 K [150]. The resulting mean free path of 5.2 m is considered conservative with regards to plasma collisionality (charge exchange mean free paths are the shortest for Xenon) and is larger than any chamber dimension.

The net current emitted from the plasma to the chamber walls was determined by measuring the net current collected by the hollow cathode as the two values are equal in magnitude. This was done for practical reasons as Junior's chamber walls are grounded via conducting rods driven into the Earth. These rods could not feasibly be removed to measure net current to the chamber walls directly. However, charge conservation in this system dictates that the current collected by the hollow cathode is equal and opposite the current emitted to the chamber walls. This assumption was validated experimentally by simultaneously measuring currents to the hollow cathode and chamber walls in a smaller chamber which could be isolated from Earth ground. The experiments presented in this paper focus on a steady state Xenon plasma with background neutral pressures on the order of 10^{-6} Torr.

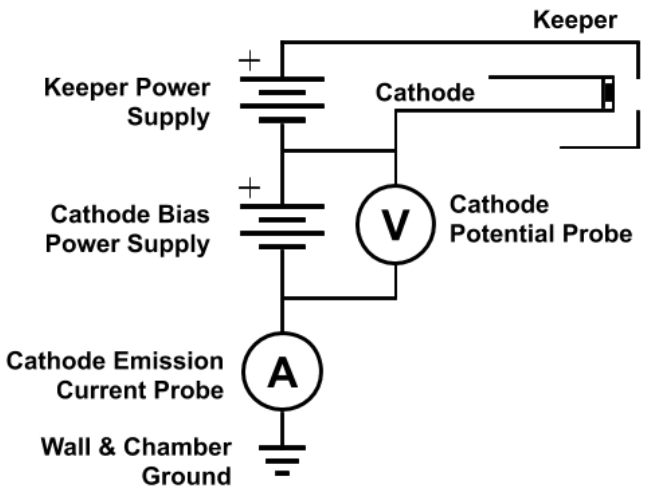

Figure 6.4: Basic testing circuit diagram.

6.2.3 Probe Analysis Techniques

Measurements from the four probe types shown in Figure 6.5 are presented in Sections 6.3 and 6.4 below. Ion energy distribution functions (IEDFs) were obtained from the Retarding Potential Analyzer (RPA) using the first derivative technique described in [180]. A Savitsky-Golay filter was used to remove the noise introduced when taking the derivative and the local plasma potential was determined using a nearby emissive probe [169]. Care was taken to ensure filtering did not significantly alter the nature of the IEDF. This was accomplished using a small (21 point) filter window, third order polynomial fit, and comparing the filtered IEDF to the unfiltered IEDF. A drifting Maxwellian distribution was then fit to the measured IEDFs to obtain their approximate ion temperature and drift velocity. The first step of the fit was to use the peak of the IEDF to set the ion drift energy as this is the most important parameter obtained from the IEDF with regard to the ion emission model. Next, the ion temperature was obtained when the drifting Maxwellian distribution best matched the filtered IEDF according to a least squares fit [181]. Using this modified fit, the ion drift velocity is captured more consistently and accurately than when using a least squares fit without matching the IEDF peak first.

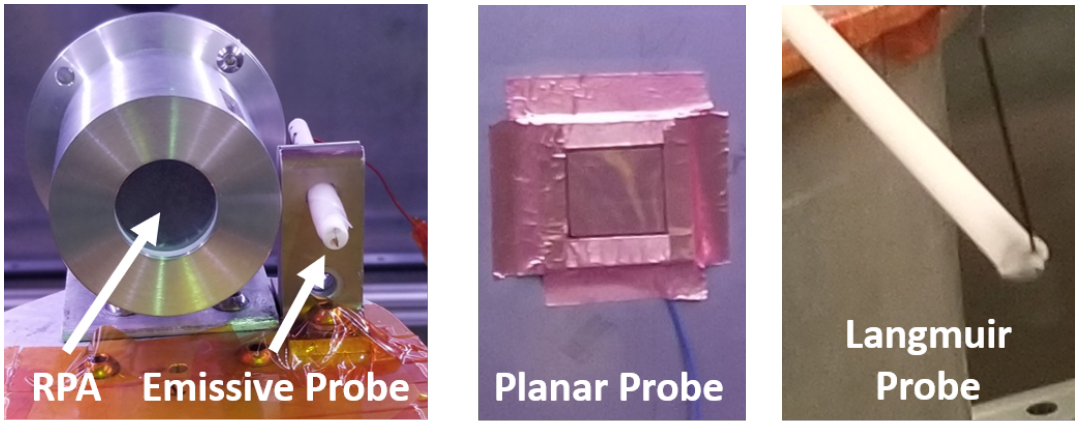

(a) (b) (c)

Figure 6.5: Plasma probes included a retarding potential analyzer (a), thoriated Tungsten emissive probe (a), Copper planar probe (b), and cylindrical, Tungsten Langmuir probe (c).

A thoriated, Tungsten emissive probe was used to measure plasma potential using the floating probe technique in the limit of high emission [151]. A calibration curve is required to determine the optimal emissive probe heating current [151]. An example calibration curve and the emissive probe circuit are included in Appendix B. A least squares fit was used to match the measured plasma potential profile in the sheath with the theoretical exponential potential profile (provided in Equation (2.9)) [34]. A cylindrical, Tungsten Langmuir probe was used to obtain the electron temperature 10 cm downstream from the cathode orifice. The probe measured 0.051 cm (0.02 in) in diameter and 5.1 cm (2 in) in length and Langmuir probe sweeps were analyzed using the same general procedure outlined in Chapter 5 (Section 5.2.2). A Savitsky-Golay filter was used to reduce noise in the Langmuir probe data [169]. This is a standard filter often used for Langmuir probe data [168]. The electron temperature was determined using the standard Langmuir probe technique of an exponential fit of the electron retardation current [36]. The electron density was determined using the electron thermal current when the probe is biased to the plasma potential [36]. Planar probes were constructed from square copper plates and guarded using copper tape to

expose an area of 10 cm^2 with the lowest profile possible. These probes were mounted on the chamber wall and electrically grounded, with their current collection measured via Keithley 6485 picoammeter. These copper planar probes measure the net emission current density without distinguishing between ion and electron contributions.

6.2.4 Emitted Ion Experiments

The first experimental campaign focused on ions emitted from the quasi-neutral contactor plasma. A RPA was embedded in a conducting plate grounded to the chamber wall directly downstream of the hollow cathode as seen in Figure 6.6. A fine, grounded steel mesh was placed in front of the RPA aperture and the first grid of the RPA was also grounded to the chamber wall. This setup measured IEDFs at the chamber walls. The cathode potential was varied parametrically from 0 V to 30 V in steps of 10 Volts and its effect on downstream IEDFs observed. Because the potential of the chamber walls are defined as the ambient space plasma potential in these experiments, these IEDFs approximate the energies of ions emitted from a quasi-neutral plasma in space.

6.2.5 Sheath Region Experiments

The second experimental campaign focused on validating the ion emission model by directly applying it to a fully characterized sheath region near the chamber wall. Specific measurements were made using the techniques described in Section 6.2.3. The spatial plasma potential profile was measured starting 10 cm from the wall and continuing up to the wall surface to characterize the contactor plasma geometry and potential. In our experiments, the system quickly reaches a steady-state in which the geometry of the contactor plasma is characterized by this sheath region. This is unlike a true experiment in space (which is essentially unbounded), but provides a great opportunity to validate the ion emission model in a simpler setting. IEDFs

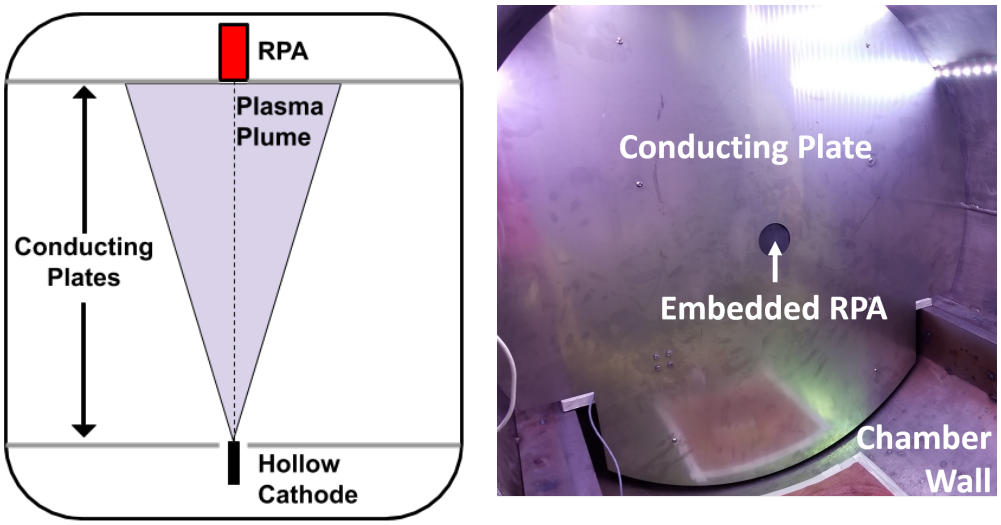

(a) (b)

Figure 6.6: Emitted ion experiment configuration. A RPA was embedded in a grounded, conducting plate directly opposite the hollow cathode to measure ion energies at the wall surface.

near the edge of the sheath region were used to characterize the ion drift velocity out of the quasi-neutral contactor plasma. Electron temperature was measured using a Langmuir probe 10 cm downstream of the hollow cathode and the local emission current density at the chamber wall was measured using planar probes. These local emission current density measurements will be compared with the theoretical current emission predictions made using the ion emission model and an analytical SCL expression. Measurements were taken in the independent positions shown in Figure 6.7 to provide a more complete picture of any geometric effects which may alter the contactor plasma ion emission process. These positions were all located along the vertical centerline of the chamber (at the same height as the hollow cathode). Photos of the two motion stage diagnostic loadouts (Langmuir probe with emissive probe and RPA with emissive probe) are provided in Figure 6.8. Large and small chamber configurations were used for comparison with ion emission model and SCL expression predictions respectively.

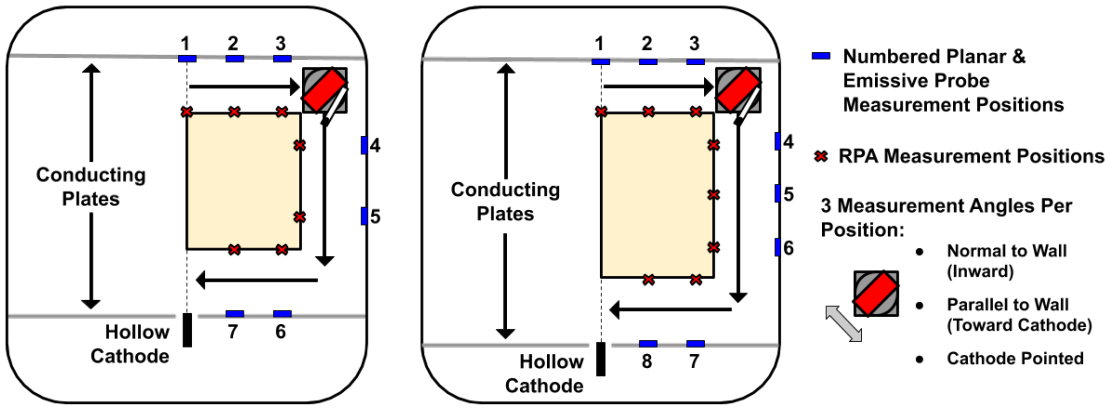

(a) (b)

Figure 6.7: Sheath region experimental configurations. Positions spread throughout the chamber were tested to understand the ion-rich region between the quasi-neutral plasma and chamber wall. The small configuration (a) used for simple SCL comparison featured 7 positions and the large configuration (b) used for ion emission model comparison featured 8 positions.

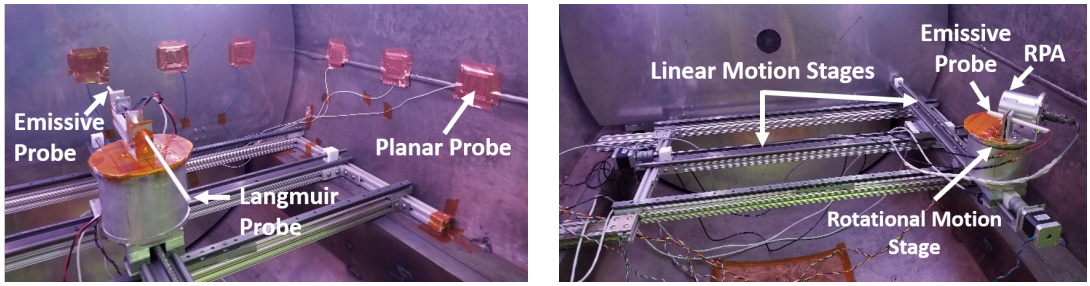

(a) (b)

Figure 6.8: The Junior vacuum chamber interior as instrumented for sheath region experiments. Pictured features include the wall-mounted Copper planar probes at positions 1-6 of the large configuration (a), the Langmuir probe with emissive probe loadout (a), and the RPA with emissive probe loadout (b).

6.3 Experimental Results

6.3.1 Emitted Ion Experiments: Emitted Ion Response to Charging

Two representative IEDFs for the axially emitted ions (see Figure 6.6) at different Xenon flow rates are shown in Figure 6.9. Deviations from an ideal drifting Maxwellian IEDF are evident, but these is fairly common and can be explained by plasma formation occurring in a finite volume with non-uniform potential, as well

as various plasma waves and instabilities [182, 183]. The small, low energy peak in the 5 sccm flow rate IEDF is characteristic of charge exchange ions [182]. Charge exchange ions are produced when "fast" ions exchange their charge with "cold" neutrals [27, 182]. The mean free path of this process is inversely proportional to the background neutral gas density, which in turn scales approximately linearly with the gas flow rate [27, 182]. The notion that this small peak corresponds to charge exchange ions is supported by the lack of an equivalent peak in the IEDF shown in Figure 6.9 (a), where the flow rate was just 1 sccm. These IEDFs feature a significant drift energy of ∼25 eV (∼6 km/s drift velocity), which greatly exceeds their temperature of ∼0.15 eV. This inequality is what produces a wide IEDF peak despite a comparatively low ion temperature. Minor thermal velocity modifications to the ion drift velocity translate to much larger changes in units of energy.

Figure 6.10 examines the effect of positive cathode potential on emitted IEDFs. The left plot of the figure shows a one-to-one, linear relationship between cathode potential and emitted ion drift energy. In other words, for every volt that the spacecraft charges positive, ions are emitted with one eV more drift energy. There is also a ∼14 - 18 eV offset between ion drift energy and cathode potential, which suggests a significant emission velocity even without positive charging. Figure 6.10 (b) shows that the emitted ion temperature decreases by about 40 - 45% with increasing cathode potential and varies with neutral gas flow rate. Although accounting for this effect is not required to validate the ion emission model (which assumes cold, drifting ions), one likely explanation for the temperature decrease is outlined here. It is possible the hollow cathode operated at cooler temperatures when biased more positively. The primary heating mechanism for our cathode is ion bombardment of the insert located in the cathode's interior [27]. This process is likely inhibited by positive cathode biases, as the reabsorbed electron population and changing electric field act to reduce the ion-accelerating sheath voltage near the insert [27].

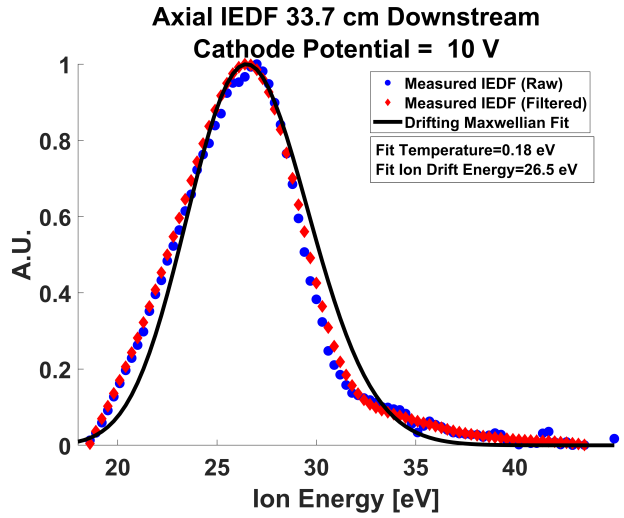

(a)

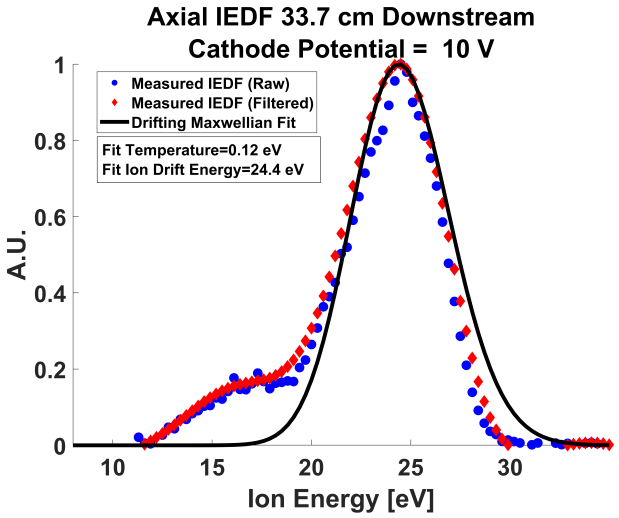

(b)

Figure 6.9: Emitted IEDFs at a cathode potential of 10 V. Flow rates of 1 sccm (a) and 5 sccm (b) were tested. Raw data, filtered data, and the drifting Maxwellian fits are shown.

6.3.2 Sheath Region Experiments: Large Chamber Configuration Measurements for Validating the Ion Emission Model

Sheath region experiments focused on validating the ion emission model, which is simplest when only ions are emitted. This condition occurs when the contactor current (ion generation) equals the electron beam current [16]. Under these conditions, contactor plasma electrons exist only in the quasi-neutral contactor plasma region

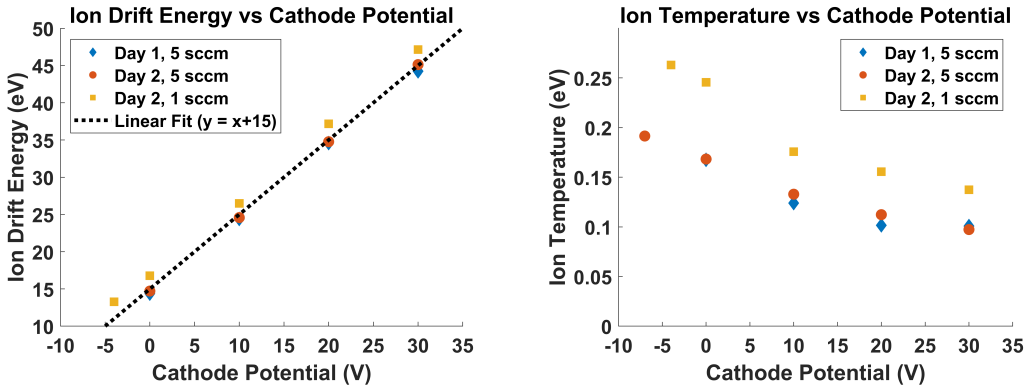

(a) (b)

Figure 6.10: Emitted ion drift energy (a) and temperature (b) versus cathode potential using two different flow rates and test days.

and the wall sheath is free of electrons. This regime is also the target of the experiments discussed in this paper. To mimic this condition, the hollow cathode potential was increased until the ion emission current saturated. An arbitrarily high cathode potential is desired to ensure strictly ion emission, however in practice small variations in plasma production and microdischarges (oxide layer breakdown) on chamber surfaces limit the maximum cathode potential. A 30 V cathode potential was ultimately selected for all sheath region experiments presented below. Exponential fitting of emission current measurements according to the procedure discussed in Chapter 7 (Section 7.4) indicates that less than 9% of the total electron population is emitted using this potential. The bulk plasma electron temperature was measured 10 cm from the cathode orifice using a Langmuir probe and found to be 2.2 eV +/- 0.2 eV, so it is not surprising that most electrons were collected by the positive cathode rather than the chamber wall. This 2.2 eV electron temperature was used for each position when applying the ion emission model, the accuracy of which will be addressed in Section 6.4.8.

IEDFs similar to the example shown in Figure 6.11 were used to determine the ion drift velocity into the sheath from the quasi-neutral plasma at each of the positions shown in Figure 6.7. Measurements were made in each position with the RPA

aperture pointed normal to (away from) the chamber wall, parallel to the chamber wall, and at the hollow cathode orifice. Only a tenuous, background ion population was detected when the RPA aperture was not aimed at the hollow cathode orifice. This indicates that ions streamed directly from the hollow cathode orifice, as expected considering the initial potential drop near the cathode's keeper (referred to as a source sheath in the work of Schwager and Birdsall) [184]. The RPA measurements pointed at the cathode orifice thus were used to obtain the drift velocity of the primary ion population. A simple cosine law was then used to determine the drift velocity component into the sheath at the chamber wall.

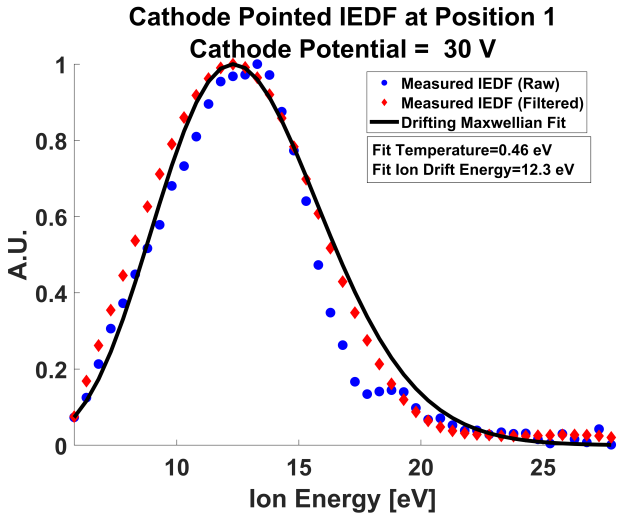

Figure 6.11: Example IEDF with raw data, filtered data, and the drifting Maxwellian fits shown. This example is from position 1 with the cathode potential at 30 V.

In this section, we present results from the large chamber configuration in order to apply the semi-analytical ion emission model directly. Drift velocities from the large configuration are summarized in Table 6.1 below. Table 6.1 and Figure 6.11 confirm that the ion emission model assumption of cold, drifting ions is valid for our experiments. Negative drift velocity values at positions 7 and 8 indicate that ions were primarily flowing out of the sheath rather than into the sheath from the perspective of the quasi-neutral plasma. This is a result of the ions streaming from

hollow cathode orifice and the unique sheath orientation at positions 7 and 8 (see Table 6.1 and Figure 6.7).

Position	1	2	3	4	5	6	7	8
Ion Drift Velocity Pointed at Cathode (km/s)	4.3	4.8	5.2	4.3	3.9	4.6	4.6	3.6
Calculated Ion Drift Velocity into the Sheath (km/s)	4.3	4.6	4.5	2.4	2.7	4.0	-1.9	-2.5

Table 6.1: Measured ion drift velocity when cathode pointed and calculated component into the sheath for the large chamber configuration at a cathode potential of 30 V.

Emissive probe measurements of the sheath plasma potential profile were taken to study the non-neutral sheath thickness and potential drop. Figure 6.12 features a representative potential profile from the large chamber configuration, as well as a fit to the theoretical sheath profile. The theoretical sheath potential profile for planar geometries is defined by an exponential change in potential with position [34]. The exponential constant C2 from this fit can also be used to estimate the Debye length. The Debye length is roughly the inverse of C2 in our (high ion Mach number) experimental regime [34]. Debye length estimates using this approximation fall between 2.2 and 5 cm for positions 1 - 6. It is interesting to note that the measured plasma potential was $\sim$6 V above the chamber reference potential just 0.1 cm from the grounded planar probe mounted to the chamber wall. This was a ubiquitous phenomenon which is discussed further in Section 6.6.2.

Planar probe measurements of the net positive emission current from the large chamber configuration (shown in Figure 6.7 (b)) are summarized in Table 6.2 below (again noting that the probe does not distinguish between electron and ion currents and a small fraction of electrons below 9% are still emitted). One interesting feature of these measurements is that the minimum ion emission current occurred directly downstream of the hollow cathode orifice at position 1. The same phenomena was observed in the small chamber configuration and during a previous experimental cam-

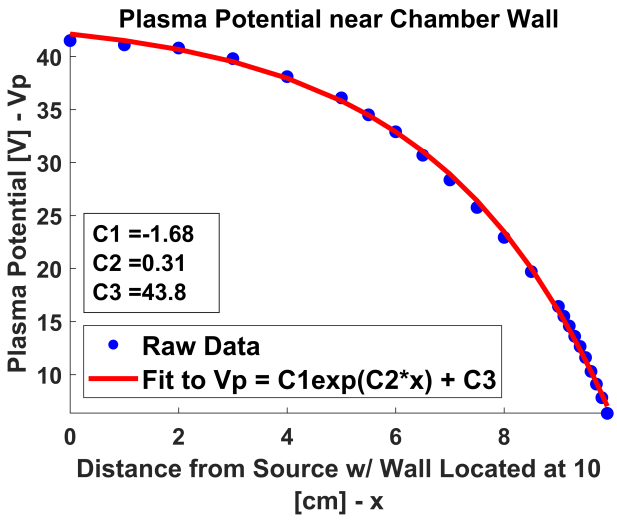

Figure 6.12: Emissive probe plasma potential measurements approaching the chamber wall. This example is from position 1 of the large chamber configuration with the cathode potential at 30 V.

paign in a different vacuum chamber [185]. Thus, the fact that position 1 recorded the lowest ion emission current is consistent with other experimental measurements. Reduced axial ion emission can be attributed to the highest contactor plasma potentials being on-axis (see Chapter 5) and the presence of a tenuous, high speed electron population (as will be discussed for the small chamber configuration in Section 6.5.2). These observations both suggest that electron emission primarily occurs axially, reducing the net ion emission current measured at position 1. Adding a tenuous, drifting electron population to the ion emission model was considered beyond the scope of this work due its negligible impact on an in-space system. Nonetheless, a test of this electron emission theory is performed in Section 6.5.2 using a simple electron emission approximation which produces good agreement for the small chamber configuration. In addition to increased axial electron emission, ion drift velocities were actually measured at their highest slightly off-axis, which should lead directly to increased ion emission currents. This ion drift velocity trend was first observed in Chapter 5 (see Figure 5.24). It is confirmed both in Table 6.1 and Section 6.3.3.

Position	1	2	3	4	5	6	7	8
Emission Current (nA)	90	560	330	310	200	140	270	390

Table 6.2: Net emission current from the large chamber configuration at a cathode potential of 30 V.

6.3.3 Sheath Region Experiments: Small Chamber Configuration Measurements for Comparison with the Space-Charge Limit

The results and insights discussed in the preceding section also apply to this section, in which we present some of the results from the small chamber configuration. The bulk plasma electron temperature was again measured using a Langmuir probe 10 cm from the cathode orifice and found to be 2.4 eV +/- 0.2 eV in this configuration. Exponential fitting of emission current measurements again indicates that less than 9% of the total electron population is emitted using a 30 V cathode potential. This indicates the small chamber configuration experiments also feature an ion emission current (or "beam" current) roughly equal to the contactor current.

An example potential profile from the small chamber configuration is shown in Figure 6.13. It is interesting to note that the potential drop near the chamber wall is even more exaggerated for this example than the one shown for the large configuration (Figure 6.12). This discrepancy between chamber configurations is addressed in Section 6.6.2. Measured ion drift velocities for the small chamber configuration are given in Table 6.3. Cathode stability was highly suspect in the small chamber configuration for the measurements at positions 5 - 7 and so no ion drift velocity estimates are listed for these positions. The net ion emission currents at each position are summarized in Table 6.4.

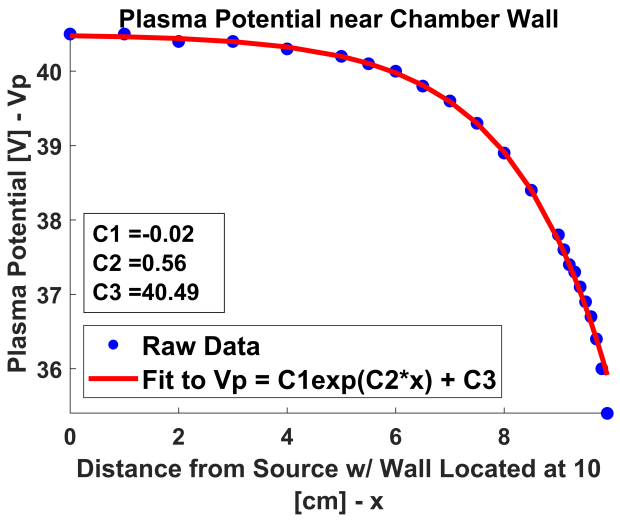

Figure 6.13: Emissive probe plasma potential measurements approaching the chamber wall. This example is from position 1 of the small chamber configuration with the cathode potential at 30 V.

Position	1	2	3	4	5	6	7
Ion Drift Velocity Pointed at Cathode (km/s)	3.9	4.4	4.1	4.3	N/A	N/A	N/A
Calculated Ion Drift Velocity into the Sheath (km/s)	3.9	4.1	3.4	2.8	N/A	N/A	N/A

Table 6.3: Measured ion drift velocity when cathode pointed and calculated component into the sheath for the small chamber configuration at a cathode potential of 30 V.

6.4 Comparison of Experimental Results with the Ion Emission Model

6.4.1 Interpreting Probe Measurements via Modeling

In this section we briefly review the semi-analytical ion emission model and use two unique techniques (potential point selection and current density iteration) to apply

Position	1	2	3	4	5	6	7
Emission Current (nA)	50	210	270	430	290	240	320

Table 6.4: Net emission current from the small chamber configuration at a cathode potential of 30 V.

it to the large chamber configuration sheath region results described above. A planar approximation using the Cartesian coordinate system is selected for this application rather than the previously reported spherical coordinate system of Chapter 3 for simplicity. The use of a planar, one-dimensional model is valid for this application as the planar probe and sheath dimensions (a few cm) are much smaller than the chamber diameter (120 cm) in this system. The planar, one-dimensional ion emission model consists of the solution to Poisson's equation (Equation (6.1)). ϕ is the electrostatic (plasma) potential, x is the distance measured from the "sheath edge", e is the elementary charge, ϵ_0 is the permittivity of free space, n_e is the electron density, and n_i is the ion density in Equation (6.1). Note that the term sheath edge is defined as a plane 10 cm from the chamber wall in this context. This definition is required to standardize comparisons between model and measurement by providing a domain in which the model can be applied without violating any of its assumptions.

$$\frac{\partial^2 \phi}{\partial x^2} = \frac{e}{\epsilon_0}(n_e - n_i) \quad V/m^2 \tag{6.1}$$

By assuming cold, drifting ions (i.e. ion temperature $T_i = 0$) and combining the steady-state continuity and momentum equations, the ion density is obtained according to Equation (6.2). v_{0d} is the ion drift velocity at the sheath edge, J_{0i} is the ion current density at the sheath edge, m_i is the ion mass, and ϕ_S is the potential at the sheath edge ($\phi_S = \phi(0)$) in Equation (6.2).

$$n_i = \frac{J_{0i}}{e\sqrt{v_{0d}^2 + \frac{2e}{m_i}[\phi_S - \phi(x)]}} \quad m^{-3} \tag{6.2}$$

The electron density is obtained using steady-state kinetic theory assuming a non-drifting Maxwellian electron distribution at the sheath edge. By assuming that the

potential is positive and monotonically decreasing from the sheath edge to the wall we obtain Equation (6.3). $v_{th,e}$ is the thermal electron velocity ($v_{th,e} = \sqrt{\frac{T_e}{m_e}}$), J_{0e} is the electron current density at the sheath edge, and T_e is the electron temperature in the electron density expression (Equation (6.3)) below.

$$n_e = \frac{J_{0e}}{2ev_{th,e}} exp\left(-\frac{e\left(\phi_S - \phi(x)\right)}{T_e}\right)\left[1 + erf\sqrt{\frac{e\phi(x)}{T_e}}\right] \quad m^{-3} \tag{6.3}$$

Using the equations listed above, the emitted current densities at the wall are as described in Equation (6.4). These current densities are then converted to emitted currents using the probe surface area ($A_{probe} = 10^{-3}$ m^2).

$$J_e = J_{0e} exp\left(-\frac{e\left(\phi_S - \phi(L)\right)}{T_e}\right) \quad J_i = J_{0i} \quad A/m^2 \tag{6.4}$$

Solving this set of equations requires specifying ion mass (m_i), ion drift velocity (v_{0d}), ion current density at the sheath edge (J_{0i}), electron temperature (T_e), and electron current density at the sheath edge (J_{0e}). In addition, two boundary conditions are required by Equation 6.1 as it is a second order differential equation. Of these seven required unknowns, three (ion mass, ion drift velocity, and electron temperature) were measured during the experimental campaign. Two of the remaining four unknowns are obtained using the potential data at the sheath edge ($\phi^{data}(0)$) and at the wall ($\phi^{data}(L)$ where $L = 10$ cm). The final two unknowns are specified differently in the two techniques described in the proceeding sections. Using these parameters as input, the ion emission model yields an electrostatic potential profile, the local ion and electron densities, and the emitted ion and electron currents. The potential profile produced by the model can be compared to the data quantitatively using the L_2-norm of the error provided in Equation (6.5) [186].

$$L_2\ Error = \sqrt{\frac{\int_0^L \left[\phi(x) - \phi^{data}(x)\right]^2 dx}{\int_0^L \left[\phi^{data}(x)\right]^2 dx}} \tag{6.5}$$

The model described can return solutions where the potential is in good agreement with the data. However there are two additional constraints that must be applied to ensure that model solutions are physically meaningful. First, we note that the electron density at the sheath edge may be sizably larger than the ion density for some model solutions. Such solutions contrast with Particle-In-Cell simulations and the experimental campaign discussed in Chapter 5, which featured a quasi-neutral region (where $n_e \sim n_i$) surrounded by an ion-rich region when the contactor current equaled the electron beam current [14, 15]. Thus, we expect solutions in which $n_i \geq n_e$ are the only physically meaningful solutions and apply it as a model constraint. The second constraint is that the potential profile must be monotonic, as expected from Particle-In-Cell simulations, previous experiments, and relevant sheath theory [14, 15, 34, 184]. These constraints ensure that only physically meaningful solutions to the ion emission model are considered.

6.4.2 Potential Profile Fitting for Model Application

At some positions, the model can be applied directly to the measured potential profile. At other positions the hollow cathode was less stable during the measurement period, making the potential profile noisier (as seen in Figure 6.14). At these positions the measured potential profile was not necessarily monotonic (which is a constraint of the model) and a numerical fit is used when applying the ion emission model. A simple least-squares exponential fitting like the one shown in Figure 6.14 is used for probe positions 4 - 6 of the large chamber configuration.

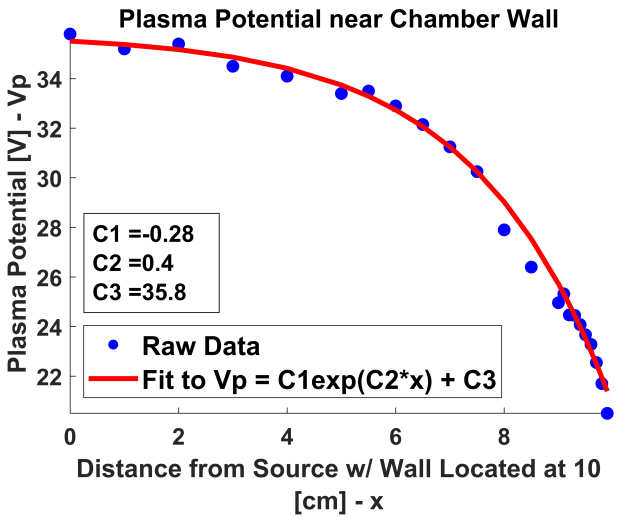

Figure 6.14: Emissive probe plasma potential measurements approaching the chamber wall. This example is from position 6 of the large chamber configuration with the cathode potential at 30 V.

6.4.3 Description of the Potential Point Selection Technique

When using the potential point selection technique, we select two internal potential points from $\phi^{data}(x)$ as the final two model inputs. This technique produces a large set of possible solutions by iteratively selecting the two unique potential points from a region of the measured potential profile. By performing many numerical experiments, we determined selecting points further from the sheath edge yielded primarily solutions with $n_e > n_i$ in part of the domain. Instead, acceptable solutions are typically obtained for points within 5 cm of the sheath edge. Unfortunately, there are only a few raw measurement points to select from in this region (where measurement spacing was 1 cm). A shape-preserving, piecewise, cubic interpolation was added between raw measurements to reduce potential spacing to 0.1 cm. This addition enhances the number of possible solutions available for analysis.

More explicitly, when using this technique we select points by iterating through N_j (typically $N_j = 21$) potential points (x_j and x_k) between x_{in} and x_{out} from the sheath edge. We then loop over these points as $j = 1, ..., N_j - 1$, and $k = j + 1, ..., N_j$

and choose $\phi^{data}(x_j)$ and $\phi^{data}(x_k)$ as the last two inputs for Poisson's equation. We solve the non-linear system for every combination of x_j and x_k points and retain only solutions with monotonic potential profiles that satisfy $n_i \geq n_e$. This provides a distribution of predicted emission currents whose mean is compared against the data.

6.4.4 Example Analysis Using Potential Point Selection

In order to illustrate the potential point selection technique, we turn to the analysis of position 2. For position 2, we analyze 210 configurations generated using points spaced 0.1 cm apart in the region of $x_{in} = 1$ cm and $x_{out} = 5$ cm. Of these 210 tested configurations, Figure 6.15 shows the electron and ion densities for all 39 solutions that satisfy the two model constraints. Each solution uses a unique set of internal potential points as inputs. Figure 6.16 shows the corresponding potential profiles. All configurations produce potential profiles very similar to the data, indicating that potential is not a good indicator for which solutions are meaningful and which are not when using the potential point selection technique.

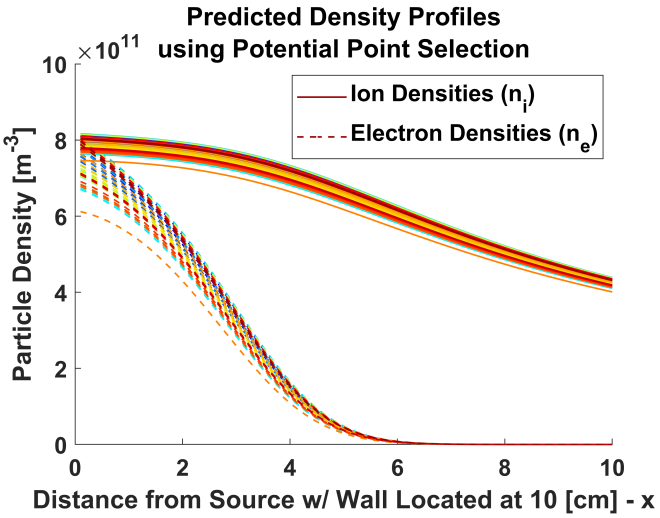

Figure 6.15: Electron and ion densities approaching the chamber wall as produced by the potential point selection technique and ion emission model at position 2. All 39 viable solutions are shown.

At position 2, solutions meeting both model constraints corresponded to potential

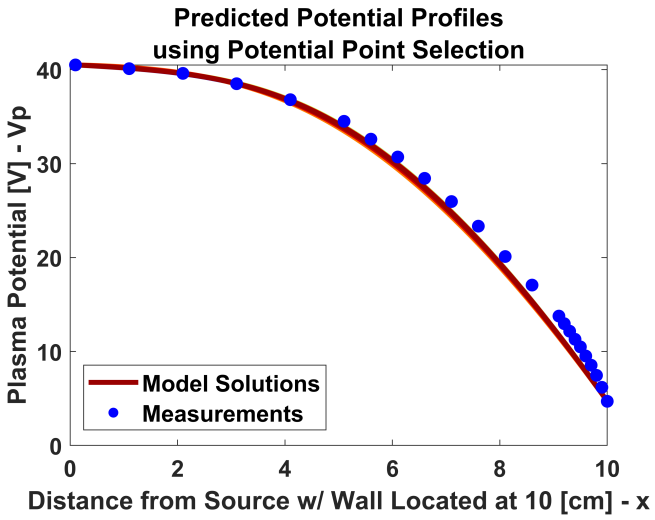

Figure 6.16: Potential profile approaching the chamber wall as produced by the potential point selection technique and ion emission model at position 2. All 39 viable solutions are shown.

points sampled within $x_j \epsilon$ [1.8, 2.8] cm and $x_k \epsilon$ [2.4, 4.0] cm. One can see the discrepancy between the model and potential measurements are more pronounced for $x > 4$ cm in Figure 6.16 as a result. Figure 6.17 (a) shows a histogram of the net emission current predicted at the wall ($I_{net} = I_i + I_e$) for all 39 viable configurations. In this case the electron current is practically zero and so Figure 6.17 essentially shows the ion current. The maximum emitted current is 602 nA, while the minimum is 550 nA. The mean current is 582 nA, agreeing within 4% of the 560 nA measured at position 2. The L_2-norm of the error associated with the potential profile is also shown in Figure 6.17 and varies modestly between 2.7% and 3.6%.

6.4.5 Description of the Current Density Iteration Technique

When using the current density iteration technique, we select values for J_{0e} and J_{0i} as the final two model inputs and define the L_2-norm of the error (see (6.5)) as a cost function to minimize the difference between the model and measured potential profiles. Because the true values of J_{0e} and J_{0i} are unknown, we iterate over an appropriate range of values using the SCL current density (J_{SCL}) as a starting point

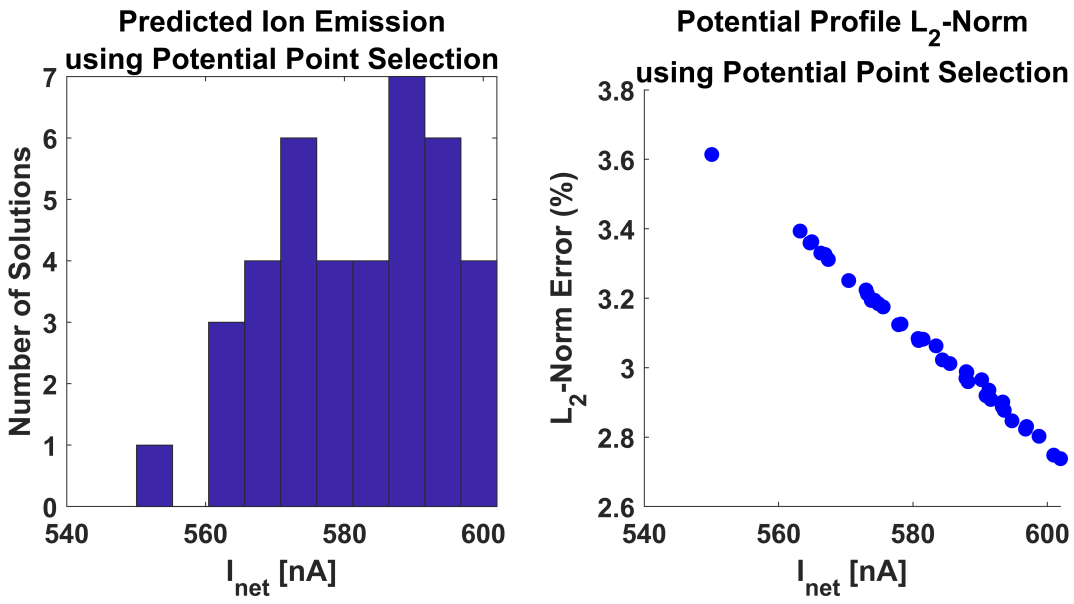

(a) (b)

Figure 6.17: Histogram of emitted currents predicted by the potential point selection technique and ion emission model at position 2 (a). L_2-norm of the potential profile error using the potential point selection technique and ion emission model at position 2 (b). All 39 viable solutions are shown.

for the ion current density. Only those model solutions that satisfy $n_i \geq n_e$ and have monotonic potential profiles are retained as physically meaningful. Model potential profiles corresponding to each remaining pair of J_{0e} and J_{0i} are then compared to the measured potential profile using the L_2-norm of the error as a cost function. The pair of J_{0e} and J_{0i} values which produces the lowest L_2-norm of the error is selected as the optimal input to the model.

6.4.6 Example Analysis Using Current Density Iteration

In order to illustrate the current density iteration technique, we again turn to the analysis of position 2. Figure 6.18 (a) shows the potential profiles for each pair of J_{0e} and J_{0i} considered. It is evident that the potential at the wall and sheath edge are constant (as discussed previously) and some non-monotonic profiles are visible. Special attention is paid to the potential profile that best matches the chamber

measurements on Figure 6.18 (b). It indicates that the current density iteration technique slightly overpredicts the potential near the sheath edge and underpredicts the potential near the wall. This was a common result and primarily stems from treating all potential points equally rather than paying special attention to critical potentials near the sheath edge.

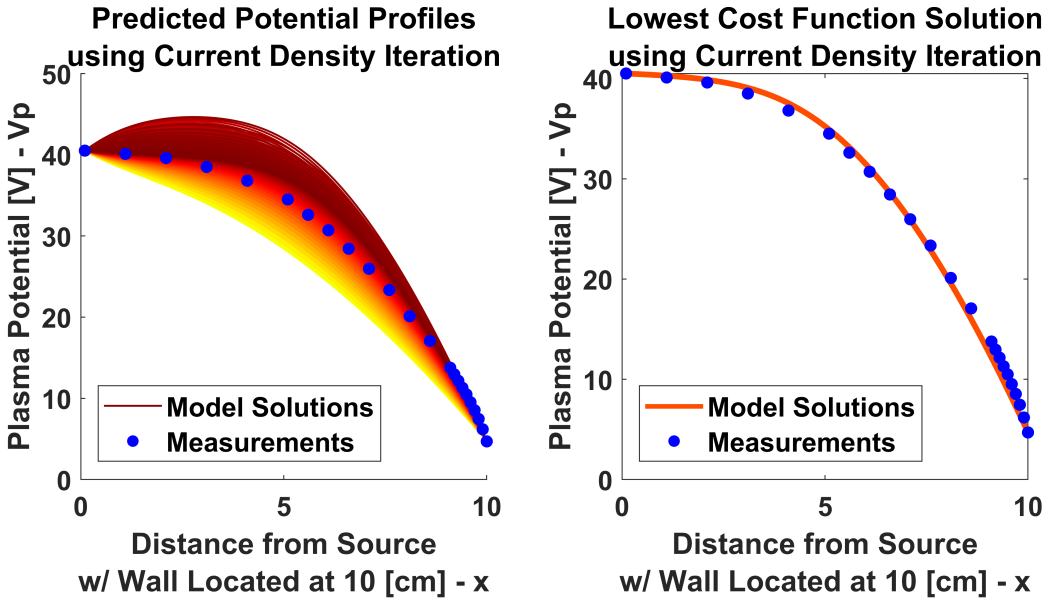

(a) (b)

Figure 6.18: Potential profile output for each set of J_{0e} and J_{0i} using the current density iteration technique at position 2 (a). Potential profile output corresponding to the cost function minimum at position 2 (b).

Figure 6.19 shows the L_2-norm of error over the entire range of physically meaningful J_{0e} and J_{0i} values. The range of J_{0e}/J_{SCL} was 10 - 100 and the range of J_{0i}/J_{SCL} was 0.5 - 1.5. The minimum L_2-norm of 3% corresponded to $J_{0e}/J_{SCL} = 57.4$ and $J_{0i}/J_{SCL} = 1.08$. The ion emission model predicts a net emission current of 679 nA at this minimum, in good agreement with the 560 nA measured at position 2. The white/empty cells in Figure 6.19 indicate current densities that do not meet all ion emission model constraints. Specifically, the upper band is a region in which $n_e < n_i$ and the lower band is a region in which the potential profile is non-monotonic.

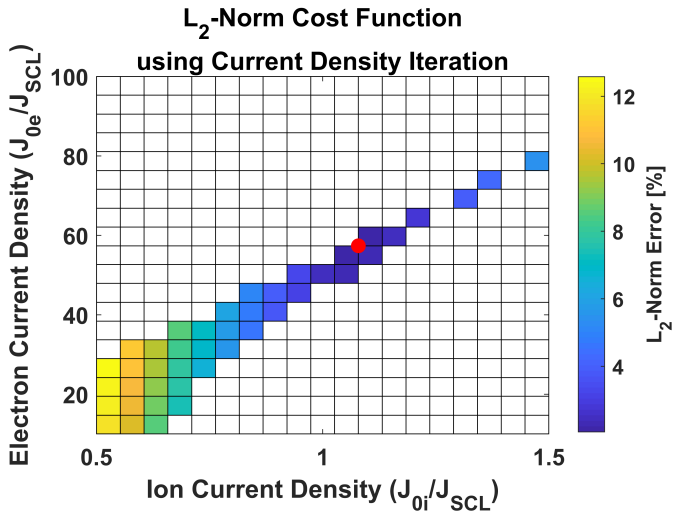

Figure 6.19: Electron and ion current densities input into the current density iteration technique as normalized by the SCL current density at position 2. The potential profile L_2-norm of error cost function is shown for each set of J_{0e} and J_{0i} and the cost function minimum is indicated with a red dot.

6.4.7 Ion Emission Model Results

The ion emission model was applied to positions 1 - 6 of the large chamber configuration in order to test its validity using a range of plasma conditions. The model is not applied to positions 7 and 8, as one of its assumptions is not valid in these locations. Specifically, the model assumes that drifting Maxwellian ions are flowing from the sheath edge to the wall. However, because ions stream directly from the hollow cathode in these experiments, the main ion population at positions 7 and 8 is flowing away from the wall rather than towards it (see Figure 6.7 and Table 6.1). While there is still net ion emission at these locations, developing a new physics model to approximate it is considered beyond the scope of this work.

The results of applying the ion emission model are given in the tables below. Table 6.5 summarizes the many viable solutions obtained when using the potential point selection technique. Table 6.6 summarizes the solutions obtained when using the current density iteration technique. Table 6.7 summarizes emission current predictions made using the potential point selection technique. Table 6.8 summarizes

emission current predictions made using the current density iteration technique. The ion emission model predictions are compared to the measured emission current and the associated error between the two values is listed.

Position	Fit Used	First Potential Point Range, x_j(cm)	Second Potential Point Range, x_k(cm)	Viable $n_i \geq n_e$ Solutions	Potential Profile L_2 Error Range (%)
1	None	1.8-3.6	2.4-4.6	70	3.7-5.1
2	None	1.8-2.8	2.4-4.0	39	2.7-3.6
3	None	1.0-1.8	1.2-2.4	16	4.3-4.9
4	Exponential	1.0-1.3	1.2-1.4	9	6.0-6.8
5	Exponential	1.0-2.2	1.2-3.8	53	1.5-2.1
6	Exponential	1.0-2.2	1.2-3.8	57	1.6-2.1

Table 6.5: Summary of model solutions for each position using the potential point selection technique.

Position	Fit Used	J_e/J_{SCL} Range	J_i/J_{SCL} Range	Optimal J_e/J_{SCL} & J_i/J_{SCL}	Potential Profile L_2 Error (%)
1	None	10-100	0.5-1.5	72 & 1.3	2.9%
2	None	10-100	0.5-1.5	57 & 1.1	2.1%
3	None	10-100	0.5-1.5	38 & 0.71	3.3%
4	Exponential	100-200	1-1.8	170 & 1.6	3.2%
5	Exponential	80-200	1-2.3	190 & 1.6	0.9%
6	Exponential	10-100	0.5-1.5	76 & 1.2	1.0%

Table 6.6: Summary of model solutions for each position using the current density iteration technique.

6.4.8 Ion Emission Model Result Discussion

Figures 6.15, 6.16, 6.17, 6.18, and 6.19 show the differences between the potential point selection and the current density iteration techniques when applying the semi-analytical ion emission model to the large chamber configuration results. The current density iteration technique tends to overestimate the potential profile near the sheath edge and underestimate it at the wall such that the model solution and data agree in

Position	Measured Emission Current (nA)	Fit Used	Emission Current Prediction Range (nA)	Average Emission Current Prediction (nA)	% Error
1	90	None	534-617	572	540%
2	560	None	550-602	582	3.9%
3	330	None	326-353	342	3.6%
4	310	Exponential	267-289	282	9.0%
5	200	Exponential	177-201	189	5.8%
6	140	Exponential	243-271	256	83%

Table 6.7: Comparison of measured emission current and ion emission model prediction using the potential point selection technique at a cathode potential of 30 V.

Position	Measured Emission Current (nA)	Fit Used	Emission Current Prediction (nA)	% Error
1	90	None	718	700%
2	560	None	679	21%
3	330	None	410	24%
4	310	Exponential	400	29%
5	200	Exponential	248	24%
6	140	Exponential	320	130%

Table 6.8: Comparison of measured emission current and ion emission model prediction using the current density iteration technique at a cathode potential of 30 V.

three points (one interior point in addition to the sheath edge and wall potentials) as seen in the right plot of Figure 6.18. For the potential point selection technique, the modeled potential profile agrees with the data at two interior points by design and the two model constraints (that the potential be monotonic and that $n_e < n_i$) tend to place these interior points near the sheath edge. As a result, the potential point selection technique represents the potential near the sheath edge more accurately than the current density iteration technique and features a larger error near the wall. This is a likely explanation for why the potential point selection technique produces a more accurate prediction, suggesting the importance of accurately capturing the electric field near the sheath edge. Regardless, both techniques produce good agreement in terms of the emitted current at the wall for probes 2 - 5 of the large configuration (see Tables 6.7 and 6.8).

The good agreement at positions 2 - 5 of the large configuration offers strong experimental support for the ion emission model. Indeed, the agreement is within 10% using potential point selection and within 30% using current density iteration for these 4 positions. Given that each individual plasma measurement has a respective error term on the order of 20% (which can be amplified by the model), 30% agreement is very good. For example, the error associated with measuring the electron temperature with a Langmuir probe is at least 10% [170, 174]. In addition, the bulk electron temperature was only measured 10 cm from the hollow cathode orifice and used for all positions. The experiments presented in Chapter 5 indicate that the electron temperature can vary fairly substantially (over 50%) in a chamber contactor plasma of this size. Another notable error term comes from the floating probe technique used to measure plasma potential. This technique tends to create a space-charge barrier and underestimate the plasma potential by 1.5 - 2 times T_e [151]. This error propagates directly to the measured IEDFs, resulting in higher ion drift velocities. It is likely that a combination of these errors, a noisier potential profile, and a highly

radial position led position 6 predictions to have an error of 83% and 130%. To test this hypothesis, more realistic values of electron temperature (1.5 eV) and ion drift velocity (3.6 km/s) were used to reanalyze position 6 by accounting for electron temperature drop in the contactor plasma and an emissive probe space-charge barrier. This new analysis predicted 210 nA of ion emission, decreasing the potential point selection prediction error from 83% to 50%. The remaining 50% error at position 6 is likely due to a relatively noisy potential profile (compare Figure 6.12 and Figure 6.14) and highly radial position (see Figure 6.7).

We would also like to emphasize that the model is very sensitive to the electric field at the sheath edge (edge of the quasi-neutral plasma). Experiences using the potential point selection technique indicate that potentials near the sheath edge determine whether the $n_e < n_i$ condition is met and have the biggest impact on the ion emission current prediction. It should be noted that multiple fit techniques were explored to best represent noisy potential profiles and agreement between different fits was quite good as long as the $n_e < n_i$ condition was met. This again suggests that the electric field at the sheath edge is critical and the model is fairly insensitive to other aspects of the potential profile (including the fit technique). This sensitivity is likely why the current density iteration technique tended to overpredict ion emission current, as the potential near the sheath edge was consistently underestimated.

Interestingly, the emission current measured at position 1 is significantly below the ion emission model's prediction. The likeliest explanation for the discrepancy between prediction and measurement in the axial position of the large chamber configuration is that probe obscuration altered measurements near position 1. Streaming plasmas are known to produce an extended wake region with altered plasma properties in regions where the flow is obstructed [187, 188]. Probe-supporting hardware partially obstructed the plasma flow during potential measurements at position 1 (as seen in Figure 6.20) and may have produced a significant wake. This effect could explain

why emission at probe 1 of the large configuration was not as predicted, although the prediction was still within an order of magnitude of what was measured.

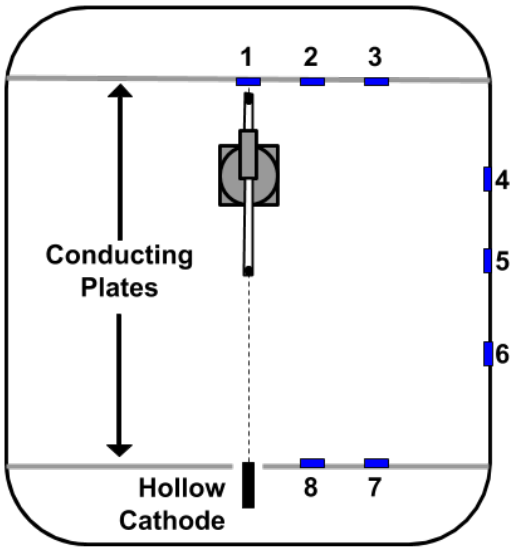

Figure 6.20: Chamber configuration when measuring the plasma potential profile at position 1.

6.5 Comparison of Experimental Results with the Space-Charge Limit

6.5.1 Defining the Space-Charge Limited Region

For the purposes of this analysis, the theoretical space-charge limited current is calculated according to Equation (6.6) below [189].

$$J_{SCL} = \frac{4\epsilon_0}{9d^2}\sqrt{\frac{2e}{m_i}}V^{\frac{3}{2}}\left(\sqrt{1+\frac{E_{drift}}{V}}+\sqrt{\frac{E_{drift}}{V}}\right)^3 \quad A/m^2 \tag{6.6}$$

Here J_{SCL} is the SCL emission current density, ϵ_0 is the permittivity of free space, d is the distance between equipotential surfaces, e is the elementary charge, m_i is the ion mass, V is the voltage difference, and E_{drift} is the ion drift energy. Equation

(6.6) is derived assuming a planar geometry and a cold, drifting ion population in the absence of electrons. These assumptions are the same as those used by the ion emission model described above in Section 6.4.1, which is to be expected as the ion emission model is based on space-charge limited physics. With that being said, there are many benefits to the full ion emission model when compared to the simple analytical expression found in Equation (6.6). For example, the ion emission model is able to produce plasma potential, ion density, and electron density profiles at different points in time (after either plasma emission or electron "beam" ignition) as shown in Chapter 3. One other benefit of the full ion emission model is that it does not require a defined boundary between the quasi-neutral and ion-rich plasma as is required for Equation (6.6). This requirement is discussed further below.

We can solve Equation (6.6) for J_{SCL} using the measured plasma potential profile and ion drift energy in each position. The final requirement is a criterion which defines the boundary between the quasi-neutral and ion-rich plasma to compute the variable d. Defining the boundary between the quasi-neutral plasma and ion-rich sheath has historically been a contentious and/or subjective process [36, 178]. Classical sheath formation theory assumes a non-drifting Maxwellian plasma and defines the boundary between quasi-neutral pre-sheath and ion-rich sheath using the Bohm criterion [178]. We make these same assumptions at positions 5 - 7, where we invoke the Bohm criterion by assuming $n_e = n_i$ when the Bohm speed is reached. However, a substantial ion drift velocity was observed at positions 1 - 4. Thus we select the ratio of electron density to ion density as a simple quasi-neutrality criterion and equate these two densities at the start of the potential profile (10 cm from the chamber wall). Normalized sheath electron density (n_e) is calculated from that point according to the Boltzmann relation (or Boltzmann factor) and ion density (n_i) is calculated according to flux conservation as described in Riemann [178]. The parameter d then corresponds to the location at which the ratio of electron density to ion density equals

a specific value. Previous analytical modeling suggests that $n_e/n_i = 0.85$ is the ideal quasi-neutrality criterion for the ion emission model [190]. However, multiple similar values of n_e/n_i were used to define the quasi-neutral boundary for completeness. Table 6.9 summarizes how the calculated space-charge limited ion emission current using these criteria compares to the measured ion emission current.

	Quasi-neutrality defined as n_e/n_i ratio:			
	0.8	0.85	0.9	0.95
Position	Theoretical Emission Current / Measured Emission Current			
1	32	24	17	11
2	6.8	5.3	3.9	2.6
3	3.1	2.5	2.0	1.4
4	1.2	1.0	0.93	0.82
5	2.0	1.8	1.5	1.3
6	1.2	1.1	1.0	0.90
7	1.6	1.4	1.2	1.0

Table 6.9: Comparison of measured emission current and theoretical space-charge limited current at a cathode potential of 30 V.

Ion emission current measurements at positions 4-7 show surprisingly good agreement with the theoretical space-charge-limit expression considering its simplicity. However, positions 1 - 3 are significantly below this theoretical limit. One explanation for this discrepancy is that significant electron emission occurred in these locations. Deviation from the space-charge limit is consistently higher for positions directly downstream of the cathode orifice, suggesting a substantial electron flow straight from the cathode itself. This theory is supported by the Langmuir probe sweep shown in Figure 6.21, which suggests a tenuous population of drifting electrons was present directly downstream of the hollow cathode orifice.

6.5.2 Accounting for Drifting Electron Populations

A simple analysis was completed to determine whether electron emission can account for the discrepancies at positions 1 - 3. The drifting electron population's density, temperature, and drift energy were obtained using the same general Langmuir

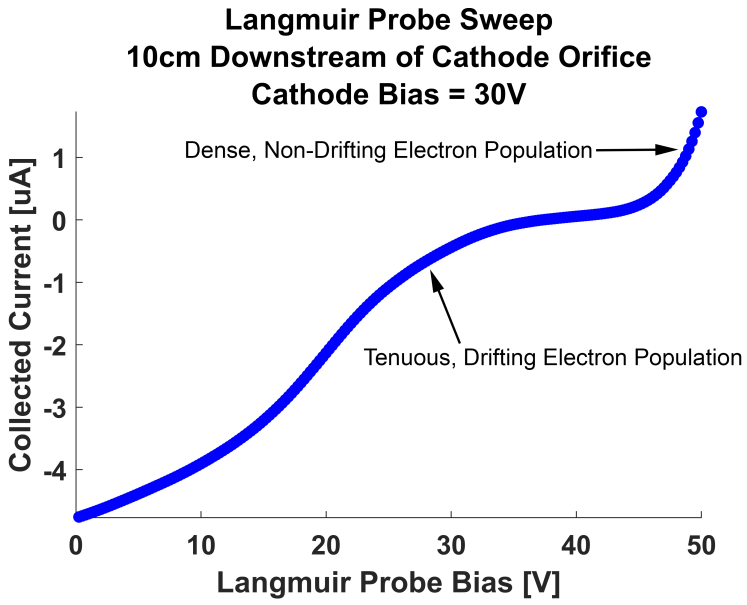

Figure 6.21: Langmuir probe sweep 10 cm downstream of the hollow cathode orifice showing a "bump" before the start of the electron retardation regime. This "bump" represents a drifting electron population.

probe analysis as was discussed in Chapter 5 (note that the appropriate adjustments were made to remove the collected ion current and isolate the electron "bump"). The calculated electron density was 6.1×10^5 cm^{-3}, the electron temperature was 2.8 eV, and the electron drift energy was 20 eV. For comparison, the main electron population had an electron density of 3.4×10^8 cm^{-3}, electron temperature of 2.4 eV, and electron drift energy of 0 eV. The exact origin of this tenuous, drifting electron population is not required for the purposes of this analysis; however it is likely that these are "primary" electrons which were thermionically emitted from the hollow cathode interior and never underwent a collision before leaving the high density region near the cathode orifice [27]. Indeed, a population of fast, drifting electrons has been observed in various Langmuir probe applications [36, 174]. The drifting electron population was propagated to each planar probe location assuming spherical expansion from the hollow cathode orifice ($1/r^2$ expansion). The effective probe surface area was also adjusted to be the relative area of each probe from the perspective of the hollow cathode

orifice. The classic planar probe current collection theory derived by Mott-Smith and Langmuir was used to predict the electron emission current at each position, which was then used to adjust the ratios shown in Table 6.9 [32]. The results of this analysis are shown in Table 6.10. This simple analysis removes most of the discrepancies at positions 1-3. In fact, for the most effective quasi-neutrality definition (a n_e/n_i ratio of 0.9), the agreement between prediction and measurement is within 50% for all positions. This is well within experimental error, suggesting that the space-charge limited emission is occurring at all measured positions in accordance with the ion emission model.

	Quasi-neutrality defined as n_e/n_i ratio:			
	0.8	0.85	0.9	0.95
Position	Theoretical Emission Current / Measured Emission Current			
1	2.7	2.0	1.4	0.93
2	2.0	1.6	1.2	0.79
3	1.3	1.1	0.85	0.61
4	1.2	1.0	0.92	0.81
5	1.9	1.7	1.5	1.2
6	1.2	1.1	1.0	0.90
7	1.6	1.4	1.2	1.0

Table 6.10: Comparison of measured emission current and theoretical space-charge limited current when accounting for electron emission at a cathode potential of 30 V.

6.6 Additional Insights

6.6.1 The Effect of Cathode Bias on Contactor Plasma Ion Drift Velocity

The experiments described above were performed for floating and 0 V bias cases in addition to the 30 V bias case reported. These other bias cases do not directly validate the ion emission model (as they still allow for significant electron emission) and so have not been addressed until now. However, these bias cases are still useful for complementing the experiments in Chapter 5 which focused on the contactor plasma

charging response. For example, potential profiles for the 0 V and 30 V bias cases at position 1 are shown in Figure 6.22. It is evident that increasing the cathode bias has the same effect on bulk plasma potential and Debye length (as indicated by the reduction in C2, which is inversely proportional to Debye length) in this set of experiments that it had in Chapter 5.

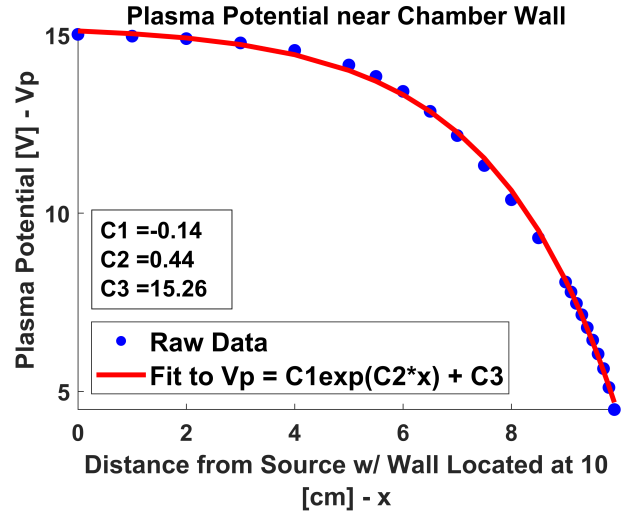

(a)

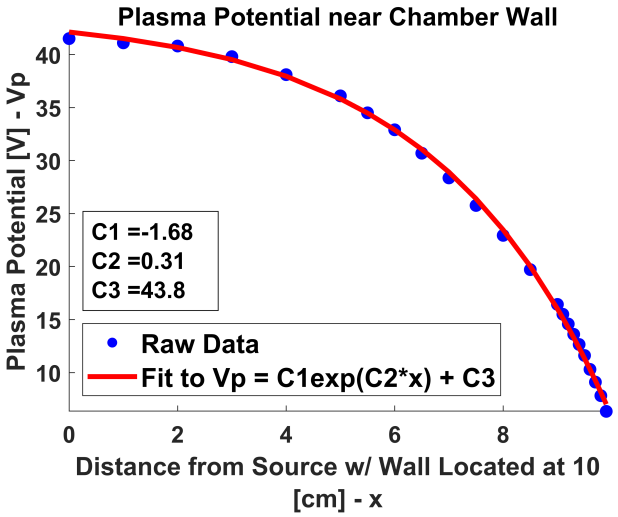

(b)

Figure 6.22: Emissive probe plasma potential measurements approaching the chamber wall. This example is from position 1 of the large chamber configuration with the cathode potential at 0 V (a) and 30 V (b).

Of particular interest is the ability to see changes in the bulk ion drift velocity

using RPA measurements, which are much more accurate than the Langmuir probe estimates utilized in Chapter 5. Table 6.11 summarizes the RPA ion drift velocity measurements for each bias case in the large chamber configuration. It is interesting to note that the contactor plasma ion drift velocity did not necessarily increase substantially with cathode bias. For example, the largest drift velocity increase was only 21%. The highest velocities and velocity increases with bias were measured slightly off-axis for half angles of about 10° - 50°. This interesting feature was also observed in both the small chamber configuration and the Langmuir probe ion drift velocity estimates of Chapter 5 (see Figure 5.24). The precise cause of this novel phenomenon is unknown and not required for this work. However, it is possible that local ion acceleration due to the recently uncovered hollow cathode ion acoustic wave activity is to blame [191, 192].

Position	Floating Potential (V)	Ion Drift Velocity (km/s)		
⇓	⇓	Floating Bias	0 V Bias	30 V Bias
1	-11.5	4.0	4.1	4.3
2	-9.4	3.9	4.0	4.8
3	-9.6	4.3	4.4	5.2
4	-9.0	3.8	3.7	4.3
5	-7.5	3.8	3.5	3.9
6	-7.7	3.9	3.9	4.6
7	-8.0	3.9	3.8	4.6
8	-6.8	3.6	3.5	3.6

Table 6.11: Cathode-pointed ion drift velocities as measured using a RPA in the large chamber configuration for various cathode biases.

6.6.2 Potential Drops Near the Planar Probe Surface

The cause of large plasma potentials close to the chamber wall is still unknown. It is possible that an ultra-thin region of space-charge resembling a Child-Langmuir sheath was pressed up against the chamber wall [27]. This type of sheath often forms for large potential differences between a conductor and the bulk plasma, but there is

no other direct evidence to suggest this or guarantee of its presence in such a thin layer. It is also possible that the emissive probe circuit was not able to accurately measure the plasma potential in such a low density and space-charge limited region. The floating point with large emission technique is argued to be viable for densities between 10^5 and 10^{12} cm^{-3} [152, 193]. The lower density limit is defined by the onset of significant space charge effects [152, 193]. Fujita and Yagura have also shown that an emissive probe ceases to float near the plasma potential if the ion density and/or the potential measurement resistance is too low [193, 194]. While this scenario is theoretically possible, it must be said that the measured potential profiles do not support this claim. The plasma potentials measured by Fujita and Yagura became non-monotonic when approaching a negatively charged grid in a low density sheath similar to the configuration under consideration [194]. More information on the specific emissive probe measurement circuit and calibration procedure are provided in Appendix B.

There is one other likely explanation which has been identified: the presence of a thin, oxide layer on the planar probe's copper surface which induces a significant voltage drop according to Ohm's law. An extremely resistive copper oxide layer quickly forms on the surface of copper when it is exposed to air (such as during instrument installation) [195]. Current passing through this resistive layer could induce a voltage drop such as those observed. This theory is supported by the fact that the potential drop near the chamber wall increased significantly between the large and small experimental configurations. The large configuration experiments were completed first, allowing the copper oxide layer to thicken before the small configuration was used. Furthermore, the high temperature emissive probe ($>$ 2,000K) was moved into contact with the planar probe's copper surface during testing for calibration purposes as the filament expands during operation. Copper oxide thickness, composition, and grain structure is known to be highly dependent on temperature [196]. The oxida-

tion caused by emissive probe heating was visible after testing completed and could explain the increase in potential drops near the planar probe surface.

6.7 Summary

Much insight has been gained on ion emission from a positively biased hollow cathode plasma contactor through carefully planned experiment and complementary predictive modeling. Experiments confirmed that ion drift energy after emission varies linearly with positive cathode potential as expected. Ion temperature after emission is found to be small when compared to the ion drift and less sensitive to cathode potential. Measured ion emission characteristics for a highly positive hollow cathode match the ion emission model and space-charge limited current predictions quite well. This is especially true for four out of six measurements using the large chamber configuration, i.e. positions 2 - 5. The large discrepancy at position 1 of the large configuration has been attributed to probe obscuration, while accounting for some of the measurement errors at position 6 brings the agreement between modeling and data to within 50%. Ion emission predictions using a simple space-charge limit expression were found to be accurate (within 50%) at positions 4 - 7 of the small chamber configuration. Positions 1 - 3 of the small configuration also agreed with SCL predictions within 50% when accounting for an observed drifting electron population using simple spherical expansion. These results represent the first direct experimental validation of the ion emission model and reveal new insights to improve experimental and modeling efforts moving forward. In doing so, this work adds to the understanding of ion emission as it may occur in tenuous space plasmas (such as those in the Earth's magnetosphere).

CHAPTER VII

Ion Emission Validation IV: Scaling Law Experiments to Guide Future Mission Design

7.1 Motivation

Even when accepting the validity of the ion emission model, there remain questions which must be answered before completing a set of space mission requirements. For example, Chapters 3 - 6 all indicate that the spacecraft potential will increase when emitting an electron "beam" during plasma contactor operation. This increase in spacecraft potential slows the escaping electrons as they are electrostatically pulled back by the positive potential. This process can lead to the spacecraft charging safety concerns discussed in Chapter 3. In a real-world system which prevents beam return using a sufficiently high electron beam energy, this slowing still represents an energy loss and loss of power efficiency on the system. If the escaping electrons are slowed significantly, then the electron beam hardware may have to be modified or redesigned to achieve the required electron beam energy and current if feasible. Because of these effects, electron-emitting space missions must include a requirement that spacecraft potential not exceed a certain value during electron beam operation. Understanding and predicting how spacecraft design and plasma contactor operation will impact this peak spacecraft potential is critical when designing space missions.

In this chapter, we show how specifications of the electron beam and plasma contactor subsystems impact spacecraft charging during beam operation. The design specifications under consideration here are the electron beam current, contactor current (the plasma current generated), and contactor ion mass. All of these parameters have been studied using CPIC simulation and/or the semi-analytical ion emission model. Additional scaling parameters such as the contactor plasma expansion time, beam emission time, and plasma contactor injection surface area were also studied using these numerical methods. However, the effect of these parameters could not be evaluated reliably in a steady state vacuum chamber experiment. Instead, we have proposed the B-SPICE mission to directly study the spacecraft potential scaling with plasma expansion and beam emission times in space [112]. Vacuum chamber experiments which directly study the spacecraft potential scaling with ambient magnetic field strength are also under development. These ongoing efforts are discussed further in the Chapter 8. Other design considerations, such as the spacecraft geometry and ambient plasma conditions, are not addressed here as they are typically less flexible than specifications on the electron beam and plasma contactor subsystems for a given mission.

A base case CPIC configuration was selected to isolate the effects of just the respective input (scaling) parameter being studied during previous numerical research. These base case parameters were used except for the scaling parameter being studied, which was varied in deliberate steps. A slightly different, but self-consistent base case was used during ion emission model studies. Again, only the scaling parameter being studied was varied during predictive ion emission model studies. To limit run time, two to three values of each scaling parameter were evaluated and the peak spacecraft potential during beam emission was recorded. To understand how the peak spacecraft potential scales with these parameters using only 2 - 3 operating points, a simple power law fit was performed which defines how the spacecraft potential scales when

changing a specific scaling parameter. A summary of the results of these studies is given in Table 7.1 below.

Scaling Parameter	Beam Current	Contactor Current	Ion Mass	Ion Mass
Prediction Source	CPIC [14]	Ion Emission Model [16]	CPIC [14]	Ion Emission Model [16]
I_{beam} Values (Normalized by $I_{contactor}$)	0.25, 0.5, 1	1	0.5	1
m_i (Ion Mass) Values [amu]	1	4, 40	0.5, 1, 2	4, 40
$I_{contactor}$ Values [uA]	22,000	100, 5000	22,000	100, 1,000, 5,000
Power Law Exponent	1.17 - 1.21	0.76 - 0.77	0.40 - 0.57	0.34 - 0.37

Table 7.1: CPIC and ion emission model predictions summary.

The positive power law exponents listed in Table 7.1 signify that the peak spacecraft potential is predicted to increase with increasing beam current, contactor current, and ion mass. The result that increasing the electron beam current increases the spacecraft potential is not altogether surprising. Removing more negative charge from the conductive spacecraft in a set amount of time should result in more positive charge accumulation. It is interesting to note that the predicted power law exponent is greater than one when varying the electron beam current, implying that doubling the electron beam current will more than double the peak spacecraft potential.

The predication that spacecraft potential will increase with increasing contactor current is slightly more nuanced. Numerical predictions were made by normalizing the electron beam current to the contactor current and during these studies the two values were equal. Based on this information, we can infer that the peak spacecraft potential will decrease when increasing the contactor current and holding beam current constant, as the contactor current exponent ($\sim$0.76) is less than the beam current exponent ($\sim$1.2). This makes sense physically, as increasing the plasma available will

make spacecraft neutralization occur at lower spacecraft potentials. However, increasing both beam current and contactor current proportionally increases charged particle fluxes and system space charges which must be overcome. A simplistic application of the Child-Langmuir law suggests that the spacecraft potential will scale as the contactor current to the 0.67 if currents in this configuration are space-charge limited, which is fairly close to the predicted exponent of $\sim$0.76 [149].

Spacecraft potential is also shown to increase slightly with ion mass, as a power law fit exponent in the range of 0.34 - 0.57 is predicted. The ion drift energy is kept constant while ion mass is changed in these predictive studies, meaning that the contactor plasma ion drift velocity decreases for increasing ion mass, resulting in smaller contactor plasmas. Smaller contactor plasmas and lower ion drift velocities both increase the peak spacecraft potential during beam emission. These independent effects can be isolated by comparing the CPIC and ion emission model predictions. CPIC simulations allowed the plasma to expand for the same amount of time before electron beam emission, leading to significantly different contactor plasma volumes. In contrast, the ion emission model set the ion radius at electron beam ignition to be approximately the same. This is why the ion mass scaling in CPIC (with an exponent range of $0.40 - 0.57$) is greater than in the ion emission model (with an exponent range of $0.34 - 0.37$). The range of exponents predicted by the ion emission model also has physical significance assuming space-charge limited ion emission. Another simplistic application of the Child-Langmuir law suggests that the spacecraft potential will scale as the ion mass to the 0.33, which is quite close to the predicted exponent range of 0.34 – 0.37 [149]. These predictions are discussed further and compared to experimental measurements throughout the present chapter.

In this chapter, we describe the experimental setup, summarize the raw measurements, refine the analysis to maximize the information gained and reduce the impact of covarying parameters, and compare the revealed trends to the predicted

scaling laws. Particular attention is paid to any discrepancies between numerical prediction and experimental results, as they may reveal shortcomings in the numerical simulations and model or their respective inputs. These potential shortcomings are important to uncover, as they prevent the accurate completion of substantive contactor and electron beam subsystem trade studies when designing future electron beam missions.

7.2 Experimental Setup

7.2.1 General Experimental Description

Experiments were performed in the ElectroDynamic Applications (EDA) Inc. vacuum chamber. The EDA chamber is a roughly cylindrical with a hinged endcap as shown in Figure 7.1 (a). It is composed of stainless steel and achieved a base pressure of $5\text{x}10^{-7}$ – $2\text{x}10^{-6}$ Torr with an operating pressure in the range of $4.7\text{x}10^{-6}$ – $5.4\text{x}10^{-4}$ Torr using a CTI Cryo-Torr cryopump during the experiments presented. The corresponding range of mean free paths for these pressures is treated explicitly in Section 7.6.2. The EDA chamber's largest diameter is 0.91 m and it spans 1.42 m in length. An electrically isolated hollow cathode plasma contactor was placed in the center of this chamber to represent a conducting "spacecraft".

A heaterless hollow cathode with an enclosed keeper electrode was used to produce a steady state plasma representative of a space-based contactor plasma. The hollow cathode was provided by Plasma Controls, LLC. It uses a low work function insert fabricated from tungsten and barium-calcium aluminate powders, a 1/8" orifice diameter, and is shown in Figure 7.1 (b). The hollow cathode was operated in the "diode mode" configuration. In the diode mode, a steady state plasma discharge is maintained by forcing a constant discharge current to flow between the cathode and keeper electrodes. The diode mode was used as it best represents the expected

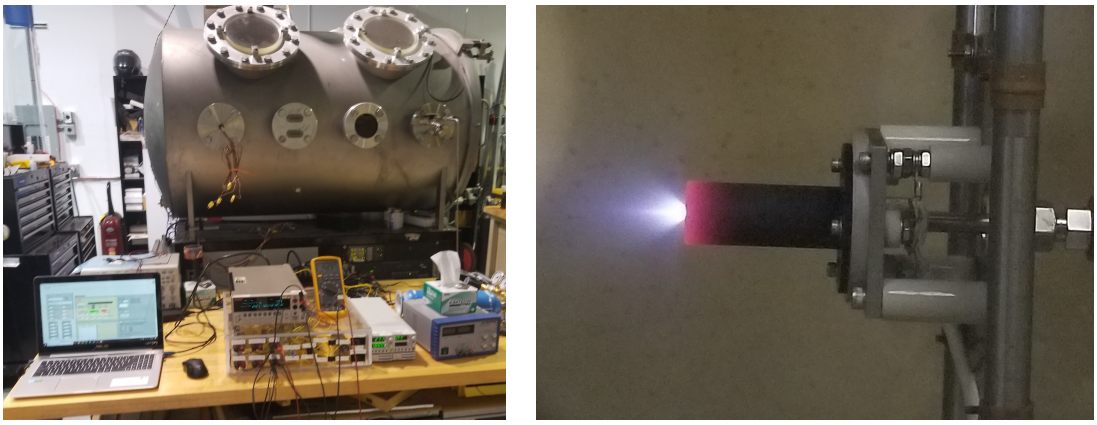

(a) (b)

Figure 7.1: The EDA chamber exterior (a) and hollow cathode (b) used during the described experiments.

in-space use case during electron beam emission (when the spacecraft is positive and the hollow cathode acts as a net ion source). The hollow cathode was biased positive with respect to the grounded, conductive chamber walls to mimic the equivalent space system's response to electron beam emission according to the circuit diagram in Figure 6.4. This positive, constant bias applied by the cathode bias power supply is maintained by removing a constant electron current from the hollow cathode, establishing a steady state plasma under conditions similar to those which produced the predictions summarized in Table 7.1. The hollow cathode potential established using this power supply can also be thought of as the equivalent of a spacecraft potential with respect to the ambient space plasma, as hollow cathodes are typically tied to spacecraft common (the spacecraft frame potential).

7.2.2 Varying Key Scaling Parameters

The scaling parameters examined in this chapter are beam current, ion mass, and contactor current. Two of these values are varied directly during the experiments. The electron beam current was varied directly by using a Keithley 2400 Sourcemeter to change the cathode (spacecraft) potential while simultaneously measuring the net

current to the biased hollow cathode. The atomic mass of the neutral expellant gas (and corresponding ion mass) could be varied directly by changing the neutral gas species flowing to the hollow cathode. The contactor current (or plasma current produced by the hollow cathode plasma contactor) could not be varied directly, nor could it be varied without changing other physical properties of the experimental system. To vary the contactor current, the keeper (discharge) current and neutral gas flow rate were both varied over as large a range as possible. These two physical inputs control the neutral gas density and ionizing discharge current flowing between the cathode and keeper electrodes and were expected to alter contactor current over a large range.

An ideal experimental campaign would vary the scaling parameters under consideration over an infinite range, however in reality there are physical limitations that determine the parameter range achieved. The range of beam currents was effectively limited by microdischarges in the chamber. High beam currents and their associated large cathode bias voltages caused microdischarges (such as those treated in Chapter 4). Microdischarges were both dangerous to the measurement circuit and disrupted measurements enough to make them unusable. The range of contactor currents was limited by keeper current and gas flow rate settings which, if set outside of certain ranges, resulted in unstable hollow cathode operation. The keeper current was limited at the lower end by cathode stability. If the keeper current is too low, then the cathode cannot maintain a high enough temperature for thermionic emission and stable operation. The keeper current was limited at the higher end by the maximum current setting on the keeper power supply (in this case 1.3 A). The neutral gas flow rate was limited on the lower end by cathode stability in a manner similar to the keeper current. If the neutral gas flow rate is too low then there is not sufficient neutral gas present to be ionized and maintain a continuous plasma discharge (similar to the left hand side of a Paschen curve) [197]. At high flow rates, the chamber neutral density

causes plasma interactions to be dominated by particle collisions and a host of unmodeled processes may occur. The contactor expellant was limited to noble gases to make measurement comparisons as cleanly as possible (without molecular chemistry and to help with cathode stability). Thus the ion mass upper limit was achieved using Xenon, with an atomic mass of 131.29 amu (the next heaviest noble gas is the rather rare and dangerous Radon) [198]. The ion mass lower limit was Argon (39.95 amu) [199]. The next lightest noble gas, Neon, could not be pumped from the chamber as it condenses at approximately 9 K and the cryosurface operates at approximately 19 K [200]. A test matrix of cathode configurations was developed based on these physical limitations and is presented in Table 7.2. Not all configurations in the test matrix resulted in stable hollow cathode operation. A total of 170 acceptable operating conditions were found, with the beam current range selected to strike a balance between small voltage steps and the maximum current without inducing microdischarges.

	Gas Flow Rate [sccm]						
Keeper Current [A] ⇓	0.2	0.5	1	2	5	10	20
0.3			K			K	AK
0.4	K	K	K	A		AK	AK
0.5	KX	KX	AK	A		AK	AK
0.6	KX	KX	AK	AK	A	AK	AK
0.7	KX	KX	AK	AK	AK	AK	AK
0.8	KX	AKX	AK	AK	AKX	AKX	AKX
0.9	KX	AKX	AKX	AKX	AKX	AKX	AKX
1.0	KX	AKX	AKX	AKX	AKX	AKX	AKX
1.1	KX	AKX	AKX	AKX	AKX	AKX	AKX
1.2	KX	AKX	AKX	AKX	AKX	AKX	AKX
1.3	KX	AKX	AKX	AKX	AKX	AKX	AKX

Table 7.2: The 170 stable plasma contactor flow configurations under study. The letter A represents Argon expellant use, K represents Krypton, and X represents Xenon.

7.2.3 Data Collection and Analysis

The cathode (or "spacecraft") potential was swept by the sourcemeter and the cathode current collection recorded. Each sweep had 101 points and the cathode potential range was adjusted to produce both net ion emission and net electron emission from the hollow cathode. The keeper voltage, keeper current, neutral gas flow rate, and chamber pressure were also recorded for each sweep. The floating potential is determined by finding the point at which the "beam" current (which is equal to the net ion emission current from the hollow cathode) is closest to zero. The cathode potential is then defined relative to this floating potential and the "beam" current is defined relative to the current at this point. This regime of positive cathode potential with respect to the floating potential is termed the fit region. It is this fit region data set that is analyzed during the majority of this chapter. The fit region plots are presented in terms of the "beam" current versus cathode potential. An example sweep is shown in Figure 7.2.

To make the most direct comparison between experimental sweeps and numerical predictions, the cathode potential must be determined when the "beam" current is some fraction of the contactor current. To do this, the contactor current must first be determined. However, there was no accessible technique which could be used to measure the contactor current precisely (as measuring it directly would perturb the plasma generation process itself). In theory, the contactor current should equal the ion emission current for an infinitely large cathode potential. In practice the maximum cathode potential is limited by chamber microdischarges. Given these considerations, the contactor current is set to the maximum ion emission/"beam" current in each sweep's fit region to start. In Section 7.4, functional fitting is introduced to calculate a more accurate value for the contactor current. These practical difficulties with measuring contactor current also make the cathode potential when "beam" current equals the contactor current a nonsensical value as this value is simply equal to the

maximum sweep voltage applied. Instead, the cases in which "beam" current is 0.25 and 0.5 times the contactor current are treated by selecting the closest experimental points and assigning the corresponding cathode potential relative to the floating potential. This process is visualized in Figure 7.2. The MATLAB code which automates this process is included in the two scripts found in Appendices C and D.

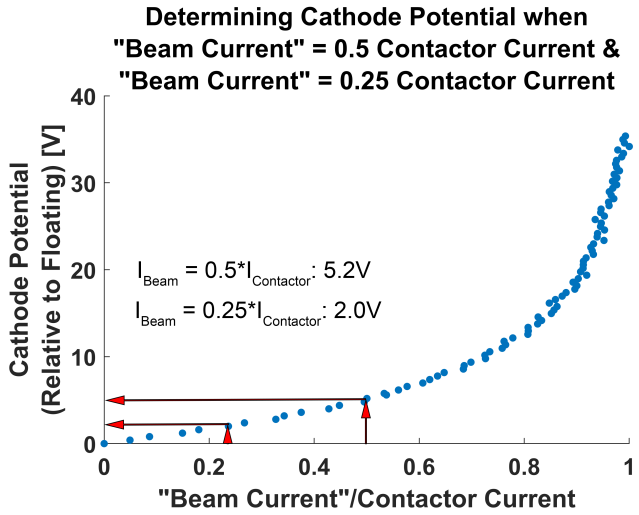

Figure 7.2: An example potential sweep visualizing determination of the spacecraft potential when the "beam" current is 0.25 and 0.5 times the contactor current.

7.3 Initial Experimental Results

7.3.1 Spacecraft Potential Scaling with Electron Beam Current

Beam current scaling predictions were made by comparing the peak spacecraft potential for discrete cases in which the beam current was 0.25 and 0.5 times the contactor current. The sweep point closest to these theoretical "beam" current values is selected during the initial analysis. The same simple power law fit used during numerical predictions was performed by taking the log of the ratio of scaling parameter values and dividing it by the corresponding log of the ratio of peak cathode/"spacecraft" potentials. This procedure was applied to each of the 170 individual experimental

sweeps. A histogram of the resulting power law exponent for each sweep is given in Figure 7.3.

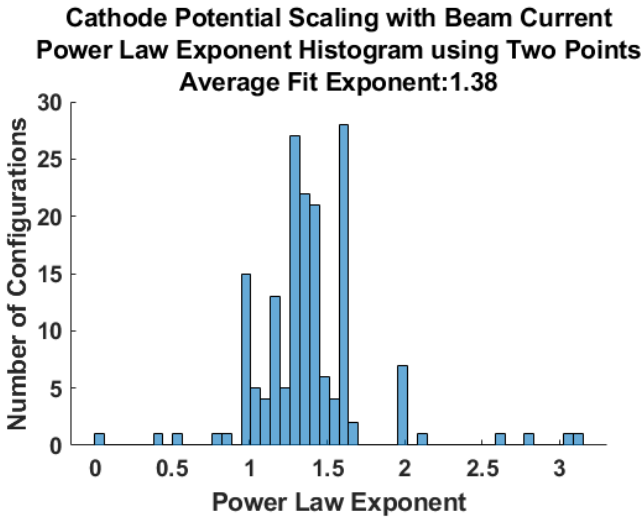

Figure 7.3: An example potential sweep visualizing determination of the spacecraft potential when the "beam" current is 0.25 and 0.5 times the contactor current.

The histogram shown in Figure 7.3 is similar to what was predicted. The average fit exponent of 1.38 is close to the range of 1.17 – 1.21 which was predicted during CPIC simulations using monoatomic Hydrogen and 3 experimental configurations fell into that exact range. With that being said, there is clear spread present and large values ($\sim$2 – 3) appear to skew the average upward. The noise in the histogram here is indicative that there is fairly large variance amongst sweeps. For example, configuration 99 (shown in Figure 7.4 (a)) was the single configuration with an exponent of zero. This is because the "beam" current = 0.25 contactor current point and "beam" current = 0.5 contactor current point are actually the same for this sweep. Sweep 99 clearly represents a case in which the "beam" or ion emission current changed significantly for small cathode potential changes near the floating potential, but there also is a continuous increase in "beam" current at higher voltages. Configuration 159 represents the polar opposite case in terms of power law exponent at 3.12 and is presented in Figure 7.4 (b). Interestingly, sweep 159 exhibits rapid changes near the

floating potential and a clear change in concavity. In addition, the gas flow rate for both configuration 99 and configuration 159 was 20 sccm. Irregular configurations such as these are explored in more detail in Section 7.4. It is also worth noting that the histogram only reports 169 configurations rather than 170. This is because the cathode potential for "beam" current = 0.25 contactor current was actually zero for configuration 143 (10 sccm Xenon with 0.8 A keeper current). This point led to an infinite power law exponent which was excluded.

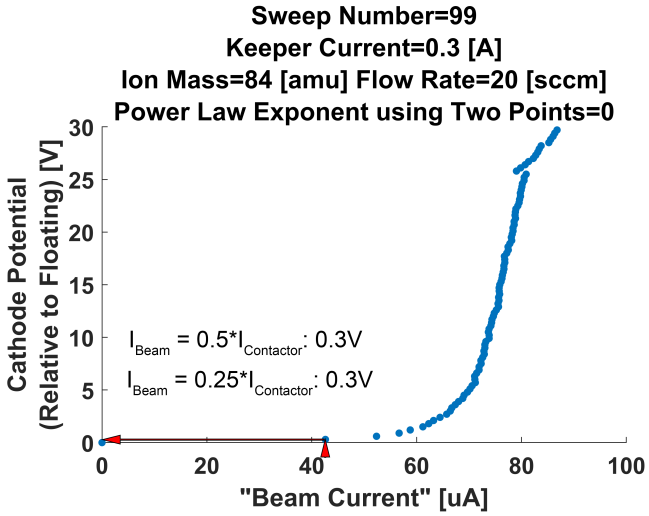

(a)

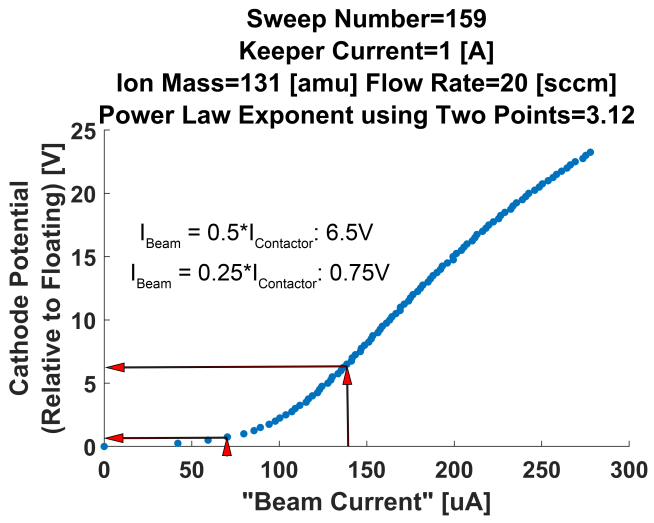

(b)

Figure 7.4: Example sweeps 99 (a) and 159 (b). These sweeps produced the most extreme power law exponents using two points.

7.3.2 Spacecraft Potential Scaling with Contactor Current

Each configuration has one contactor current value and requires a corresponding value for the peak spacecraft potential. The peak spacecraft potential when "beam" current = contactor current was used by the ion emission model. However, this is not possible for experimental measurements as previously discussed. Instead the spacecraft potential when "beam" current = 0.5 times the contactor current is used. A scatter plot of these values for all 170 configurations is provided in Figure 7.5 with a least squares power law fit.

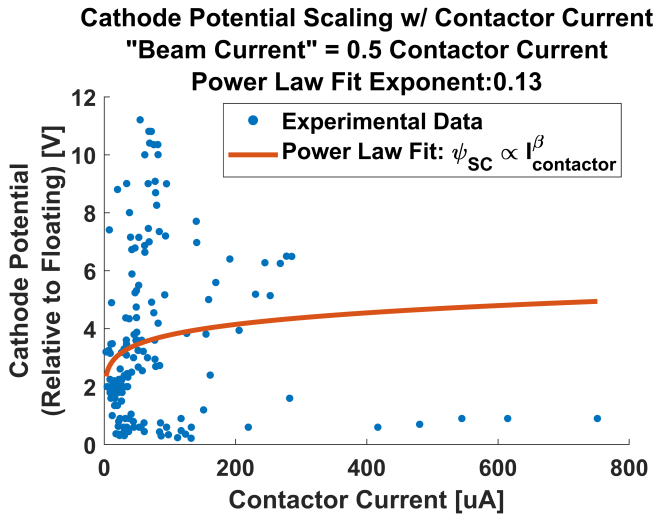

Figure 7.5: Plot of contactor current versus cathode potential for each test configuration including a least squares power law fit.

It is apparent from Figure 7.5 that either the contactor current has no effect on the peak spacecraft potential or other factors are obscuring its effect. In fact, the correlation coefficient between these data sets is a mere 0.0045 and the least squares fit power law exponent is 0.13. This differs fairly substantially from the predicted power law exponent of 0.76 - 0.77. To explore whether other physical factors may be obscuring the effect of contactor current, an attempt is made to remove the impact of changing ion mass and neutral gas flow rate by breaking up the 170 configurations into groups which have both of these values in common. In effect this means the only

physical parameter being purposely varied in a group is the keeper current. A least squares power law fit is performed on each group as shown for two example groups in Figure 7.6. A histogram of the power law exponent calculated for each group is provided in Figure 7.7.

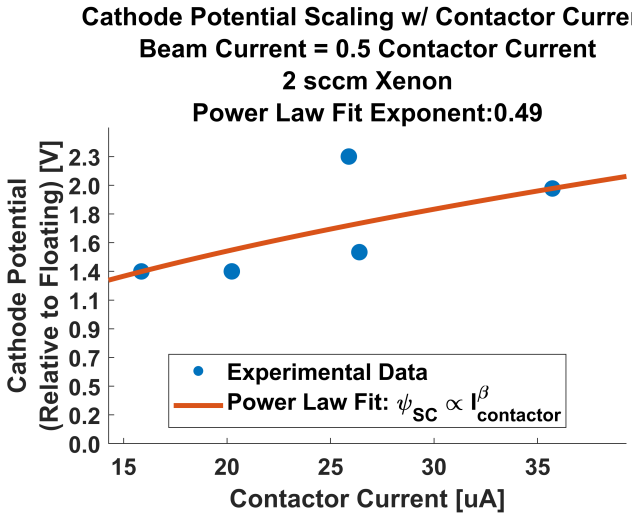

(a)

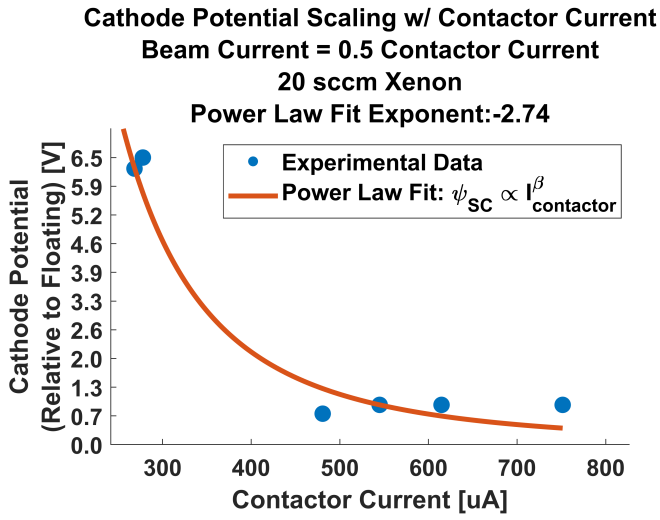

(b)

Figure 7.6: Power law fits of cathode potential (when "beam" current = 0.5 x contactor current) versus contactor current. Configurations were limited to Xenon ions with a 2 sccm (a) and 20 sccm (b) flow rate.

Breaking the data set up into 20 groups with consistent ion mass and neutral gas flow rates indicates that ion mass and neutral gas flow rate are correlated with the

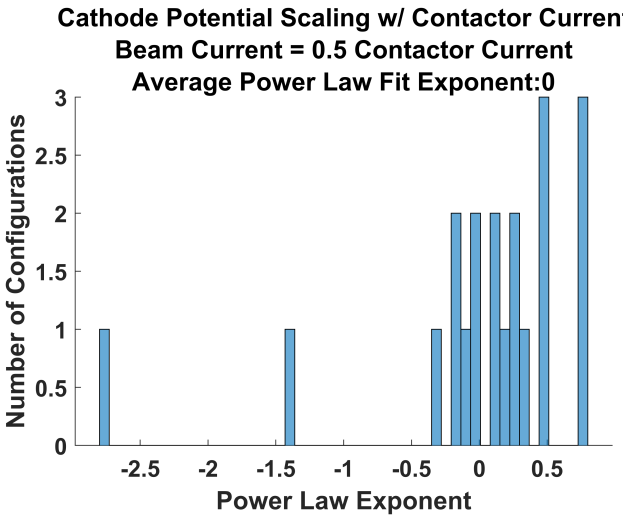

Figure 7.7: A histogram of power law fit exponents for cathode potential (when "beam" current = 0.5 x contactor current) versus contactor current. 20 groups with consistent ion species and gas flow rate are represented.

peak cathode potential. For example, the correlation coefficient between contactor current scaling exponent and neutral gas flow rate is -0.48. The correlation coefficient between contactor current scaling exponent and ion mass is -0.33. These trends indicate that heavier ions and higher gas flow rates both cause spacecraft charging to decrease with increasing contactor current rather than increase as predicted. In fact, 3 out of the 4 lowest power law exponents are found using the 3 highest Xenon flow rates (5, 10, and 20 sccm correspond to exponents of -0.19, -1.4, and -2.7 respectively). This phenomenon is explored in more detail in Section 7.6.2.

7.3.3 Spacecraft Potential Scaling with Ion Mass

Each configuration has one ion mass value and requires a corresponding value for the peak spacecraft potential. As with the contactor current, the peak spacecraft potential when "beam" current = contactor current was used by the ion emission model. However, this is not possible for experimental data. Instead, we again use the spacecraft potential when "beam" current = 0.5 times the contactor current as this exact potential was studied directly via CPIC simulation. Also, where the contactor

current value was unique for each of the 170 configurations, the ion mass falls into just 3 discrete values. Because of this, we can simply present the average "spacecraft" or cathode potential when "beam" current = 0.5 times the contactor current for each ion mass and perform a power law fit. This is done in Figure 7.8.

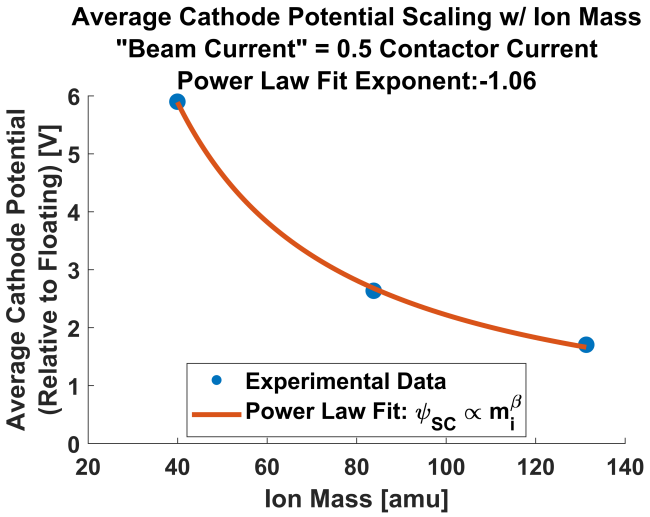

Figure 7.8: Average cathode potential when "beam" current = 0.5 x contactor current for each ion species considered with a least squares power law fit.

The experimental data summarized in Figure 7.8 strongly suggests that spacecraft charging is reduced by increasing contactor ion mass. This qualitative trend and the power law fit exponent of -1.1 differs significantly from the predicted trend, with an exponent of 0.34 – 0.57. One tempting conjecture based on this result is that the numerical models are missing some crucial physical process related to ion species. One major difference between the numerical model used for ion mass scaling predictions and the experiments presented here is that the contactor plasma is allowed to expand into vacuum in the numerical models (plasma emission is initiated shortly before beam emission). In the experiments, the system is in equilibrium when measurements are made. Thus the contactor plasma size does not vary substantially when changing experimental ion masses. This critical difference likely plays a role in arriving at such a confounding result and could potentially explain an experimental result in which

the ion mass had no effect, however system equilibrium conditions do not explain the dramatic potential decrease for higher ion masses. One possible explanation for this dramatic decrease is given in Section 7.7.3 below.

7.4 Functional Fitting of Electron Beam Current versus Cathode Potential

Only three points derived from CPIC simulation were used to predict the beam current scaling with spacecraft potential. As a result, there was very little information to indicate what functional form this scaling would take and a power law was initially assumed. This initial assumption was not based on any physical understanding, but with the addition of experimental data in which the "beam" current is swept in small increments, we are now able to determine the true functional form of this scaling law. Exploratory work was completed to determine this function and it was found that an exponential function was the optimal fit. To illustrate this point, a power law fit and exponential fit of the same example sweep are provided in Figure 7.9. We find that the average least squares R^2 value using a power law is 0.509 whereas the average R^2 value using an exponential function is 0.998.

Exponential fits are effective in recreating the relationship between "beam" current and cathode potential. Their asymptotic limit agrees with our understanding that the amount of ion current one can extract from the contactor plasma is finite and limited to the contactor current and that an infinitely large cathode potential is required to achieve this theoretical value. It also agrees with our understanding of the ion emission process. For example, we assume that equal numbers of ion and electrons are generated during the hollow cathode ionization process and ions are emitted such that they do not return to the hollow cathode (or spacecraft) for positive potentials. Instead some fraction of the plasma electrons are reabsorbed after failing

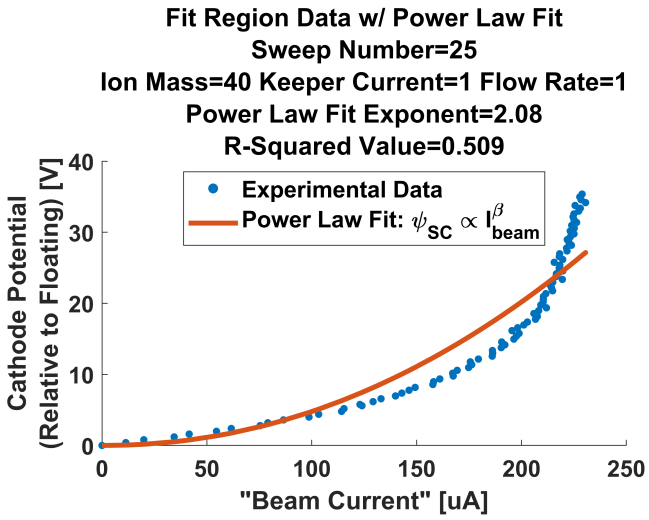

(a)

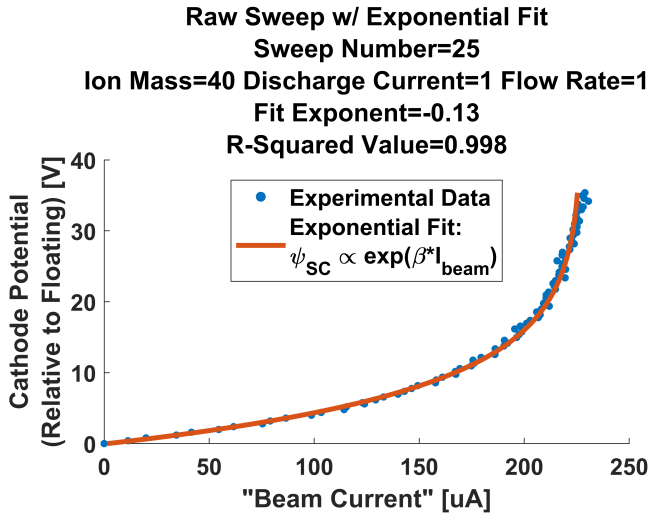

(b)

Figure 7.9: An example sweep showing both power law (a) and exponential (b) least squares fits.

to overcome the potential barrier required to escape the spacecraft-plasma system. As the cathode potential is increased, fewer electrons have sufficient energy to escape and are reabsorbed instead. This reduction in emitted electron current increases the net ion emission current from the system.

Based on this understanding, the determining factor in whether an electron is emitted or reabsorbed is its initial kinetic energy. The EEDF which defines the electron kinetic energy in our plasma is discussed in Section 5.2.2.4 and a Maxwellian

distribution is a fairly good approximation for the plasma as it expands from the collisional volume of the cathode orifice. When a conductor is immersed in a Maxwellian plasma, the collected current to it increases exponentially as its potential is initially increased from the floating potential, as is seen with a Langmuir probe [32]. An exponential fit of this region can be used to estimate the Maxwellian electron temperature using a Langmuir probe, as was done in Chapter 5 [32]. Theoretically electron temperature can be determined in this way regardless of the Langmuir probe (or conductor) geometry [32, 36]. Given these facts, it is not altogether surprising that our isolated, conducting spacecraft reabsorbs electrons according to an exponential function. In fact, we can use the exponential fit of each experimental I-V sweep to approximate its electron temperature using $T_e[eV] = -1/\beta$. A histogram of these electron temperatures approximations (or pseudo electron temperatures) is provided in Figure 7.10.

Most pseudo electron temperatures seem reasonable and the most likely value being in the 2 - 3 eV range matches with results previously treated in this dissertation. However, there are also a few pseudo electron temperatures that are quite large. These outliers above about 20 eV are probably not physical based on the distribution in Figure 7.10 (a). To understand what conditions may be causing these outlier pseudo electron temperatures, we break the values apart by ion species in Figure 7.11. We can see in this figure that the main population of pseudo electron temperatures is widest and highest for Argon and the opposite is true for Xenon. This result shows that psuedo electron temperature decreases for increasing ion mass and suggests the true electron temperature does the same. The outliers also appear to be mainly found using Krypton and Xenon. Upon further investigation, it is clear that high gas flow rates are the cause of these outliers. For example, all Krypton configurations with a pseudo electron temperature above 15 eV used the maximum flow rate of 20 sccm. The same is true for Xenon and any values above 10 eV. An example using the

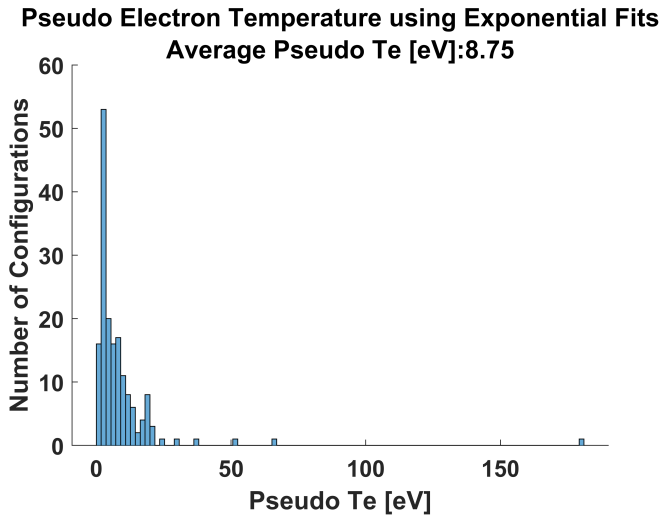

(a)

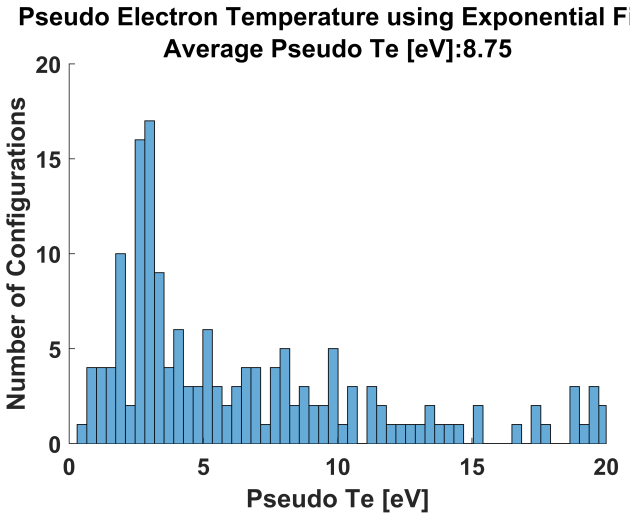

(b)

Figure 7.10: A histogram of the pseudo electron temperatures derived via exponential fitting for 170 configurations (a). A zoomed view is shown in (b).

configuration with the highest pseudo electron temperature is shown in Figure 7.12, which we believe gives some insight into what is happening for these high flow rate configurations.

Findings show that configuration 159 is the most extreme outlying value just as it was for the spacecraft potential scaling with contactor current. Once again, it is the sweep shape and concavity change which is the source of the problem. The exponential region at low cathode potentials is not fit accurately as most sweep points actually

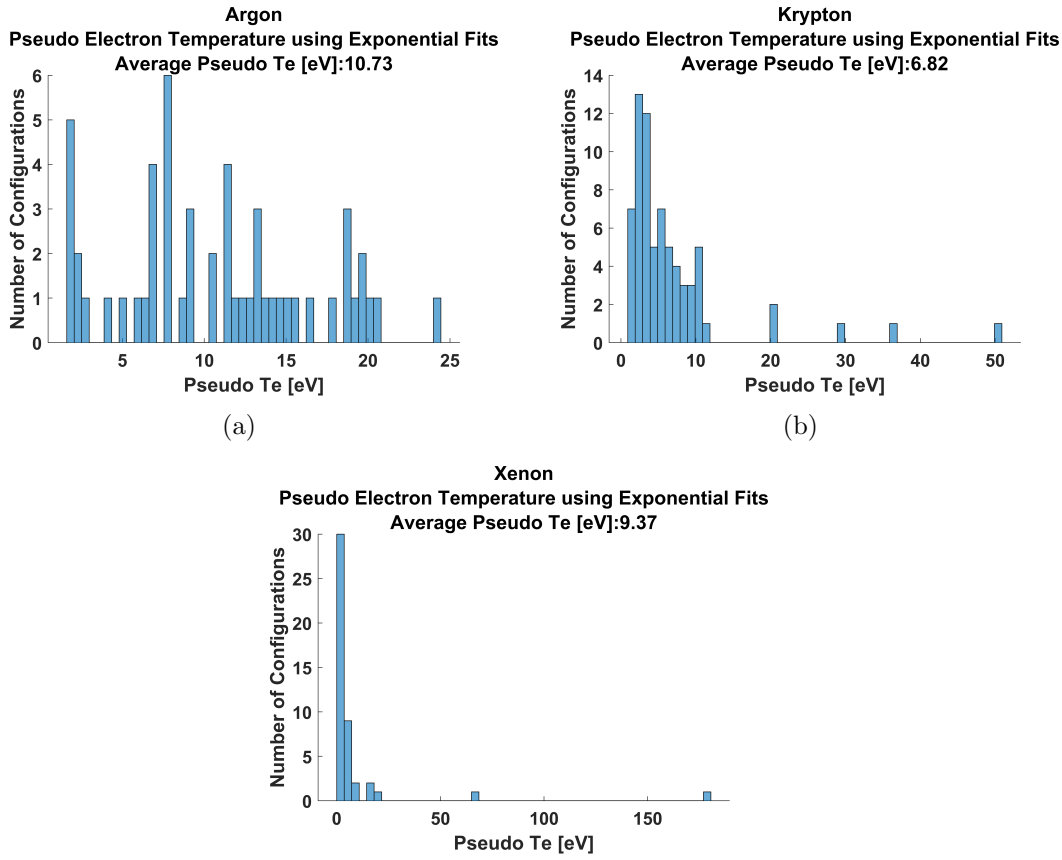

Figure 7.11: Histograms of the Pseudo electron temperatures derived via exponential fitting for Argon (a), Krypton (b), and Xenon (c).

deviate from the trend in this region such that a least squares fit is almost linear and not representative of the electron kinetic energies. While configuration 159 is an extreme example, the deviation from an exponential fit at higher cathode potentials is seen to increase steadily with ion mass and gas flow rate. The 0.2 sccm and 2 sccm counterparts to configuration 159 are shown in Figure 7.13. They demonstrate that deviation from an exponential function increases as the flow rate is increased. The proposed reason for this trend is that there are increased ionizing collisions taking place in the chamber plasma for higher gas flow rates. Higher gas flow rates increase the chamber operating pressure, which decreases neutral collision mean free paths and increases collision frequency. The fact that the concavity change in sweep 159 occurs

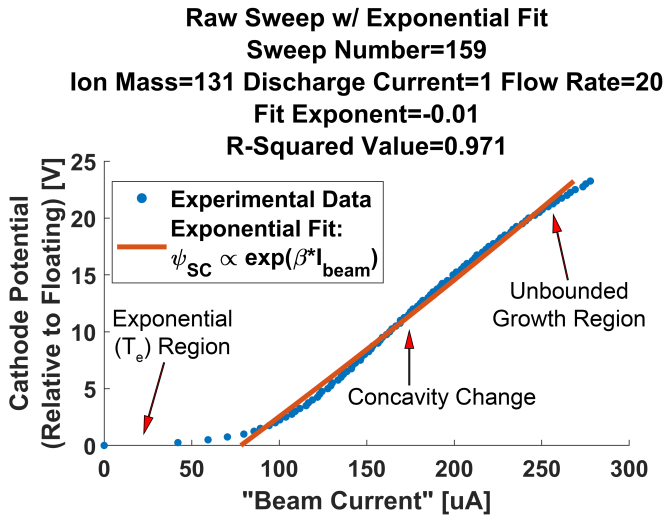

Figure 7.12: An example configuration with an unusually high pseudo electron temperature. An exponential fit is shown to be a poor fit overall as sweep concavity changes at higher cathode potentials.

at approximately the ionization energy of Xenon (12.13 eV) supports this theory [198]. Ionizing collisions are also the most probable cause of increasing deviation with ion mass. These theories will be explored in more detail in Section 7.6.2.

7.5 Covarying Parameters to Consider

There are many physical processes and associated, quantifiable parameters in complex systems such as the one currently considered. The relationship and correlation between each of these parameters could stand alone as its own study. However, doing so is beyond the scope of this dissertation. Instead, all the measured physical parameters deemed relevant to future mission design are outlined and the correlation coefficients amongst them listed. This is done by listing and describing each physical parameter in Table 7.3 and then listing the correlation coefficients in Table 7.4. Yellow boxes are used in Table 7.4 to denote moderate correlations (in which the magnitude of the correlation coefficient is between 0.5 and 0.7). Green boxes are used to denote strong correlations (in which the magnitude of the correlation coefficient is greater

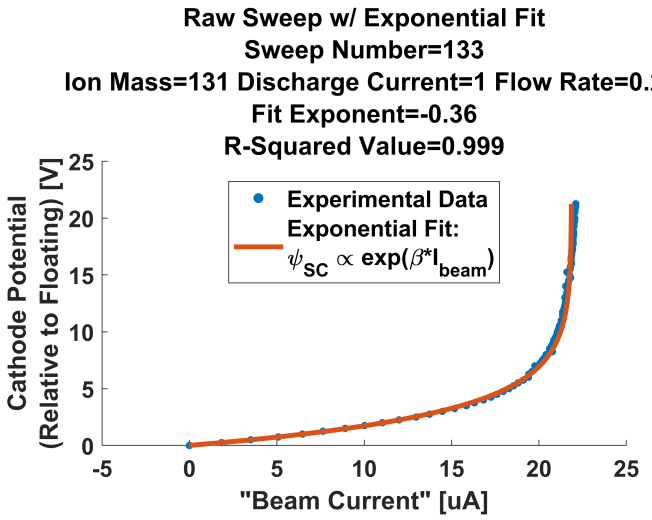

(a)

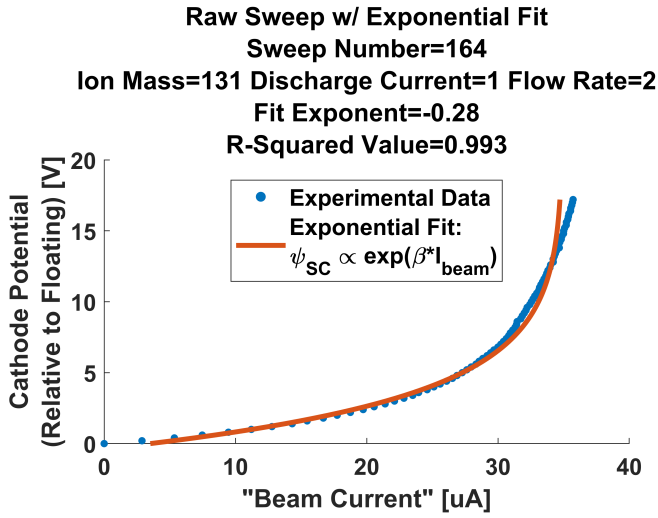

(b)

Figure 7.13: Two example sweeps with a least squares exponential fit. Deviation from an exponential function is shown to increase with flow rate when going from 0.2 sccm (a) to 2 sccm (b).

than 0.7). Negative correlation coefficients indicate an inverse relation between the two parameters (one increases as the other decreases). The closer the magnitude of the correlation coefficient is to one, the more the two parameters are correlated and the relationship between them resembles a straight line. Physical parameters which were not measured directly include the plasma properties of ion drift velocity, electron temperature, electron density, ion density, and plasma potential.

Parameter	Description
Ion Mass (m_i)	The mass of the expellant ionized by the hollow cathode to form the contactor plasma
Gas Flow Rate	The standard volume of gas expelled through the hollow cathode in a set amount of time
Keeper Current	The plasma-generating current flowing between the cathode and keeper electrodes
Expellant Utilization	The percentage of neutral expellant atoms ionized by the hollow cathode
Contactor Current ($I_{contactor}$)	The total plasma current generated by the hollow cathode
Floating Potential	The potential at which the cathode/SC collects zero net current
Keeper Voltage	The keeper voltage relative to the cathode electrode required to maintain the keeper current
Keeper Power	The power consumed by the hollow cathode (keeper current times keeper voltage)
Potential @ Ibeam = 0.25x$I_{contactor}$	The cathode potential at which the "beam" current is one quarter the contactor current
Potential @ Ibeam = 0.5x$I_{contactor}$	The cathode potential at which the "beam" current is half the contactor current
Chamber Pressure	The background neutral pressure in the vacuum chamber

Table 7.3: Physical parameters associated with each sweep.

	Expellant Utilization	Contactor Current	Floating Potential	Keeper Voltage	Keeper Power	SC Potential @ I_{beam} = 0.25 $I_{contactor}$	SC Potential @ I_{beam} = 0.5 $I_{contactor}$	Chamber Pressure
Ion Mass	-0.17	0.02	-0.31	-0.31	-0.06	-0.57	-0.58	0.26
Gas Flow Rate	-0.34	0.45	-0.30	-0.31	-0.35	-0.31	-0.23	0.76
Keeper Current	0.19	0.19	-0.01	-0.61	0.75	-0.10	-0.06	0.07
Expellant Utilization		0.24	-0.03	0.35	0.59	0.11	0.12	-0.28
Contactor Current			-0.35	-0.12	0.13	-0.07	0.00	0.66
Floating Potential				0.21	0.22	0.59	0.53	-0.35
Keeper Voltage					0.03	0.32	0.29	-0.41
Keeper Power						0.16	0.19	-0.25
SC Potential @ I_{beam} = 0.25 $I_{contactor}$							0.95	-0.37
SC Potential @ I_{beam} = 0.5 $I_{contactor}$								-0.28

Table 7.4: Correlation coefficients between experimental parameters of interest.

Of the moderate and strong correlations in Table 7.4, there are not many which demand further analysis here. The decrease in spacecraft charging for heavier ions is treated elsewhere in this chapter and likely due to electron temperature changes. The strong positive correlation between gas flow rate and chamber pressure is to be expected, as is the strong positive correlation between potential for a beam current of one quarter and one half of the contactor current. The keeper power is the product of keeper current and keeper voltage so the correlations amongst these parameters are also to be expected. The moderate positive correlation between keeper power and expellant utilization is interesting to see, but not unexpected. Keeper power is required to ionize the neutral expellant gas and an increase in this power increases the fraction of neutral gas ionized. The moderate correlation between chamber pressure and contactor current suggests that increasing the gas flow rate increases the plasma current generated by the hollow cathode and/or the chamber pressure is sufficiently high for ionization in the bulk plasma to be non-negligible. Ionization in the bulk plasma is treated in more detail in Section 7.6.2. Finally, the floating potential is shown to be moderately correlated with spacecraft charging. This makes sense, as significant ion emission current increases would be particularly difficult when starting at a raised floating potential. Figure 7.14 below shows a scatter plot of floating potential versus cathode potential when the beam current is half the contactor current to give a sense of the floating potential distribution and how it impacts spacecraft charging during these experiments.

7.6 Defining a Common Data Set

7.6.1 Comparable Experimental Configurations

While it is useful to have as much data as possible in a general analysis, isolating the effects of one parameter often requires constructing a common data set in

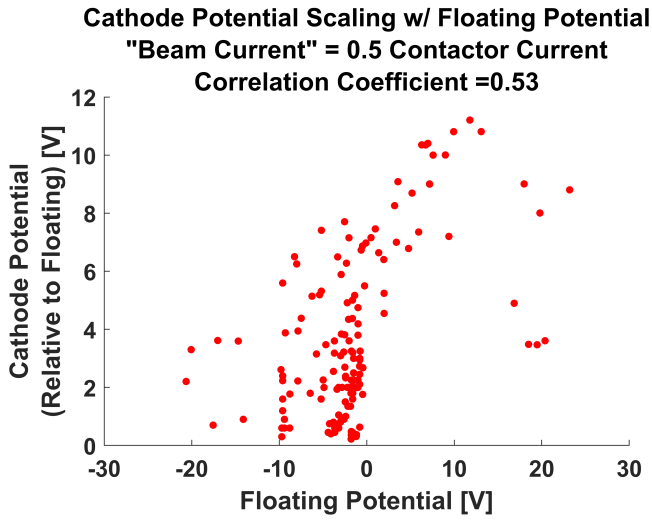

Figure 7.14: Cathode potential when beam current is half the contactor current generally increases with increasing floating potential.

which no other parameters change. In this section, we construct one such common data set to make more accurate assessments than was possible previously using the raw experimental data alone. The first step in this process is limiting the number of configurations to only those which were achieved using all three gas species (namely Argon, Krypton, and Xenon). That way studies can be performed by isolating each parameter and categorical results are not skewed by configurations using different conditions. For example, Xenon has the fewest number of configurations and its average may be skewed because it does not have any configurations with a keeper current below 0.5 A. Selecting a common data set in which configurations are consistent results in Table 7.5 and leaves 90 configurations for comparison. The keeper current values for this common data set are [0.9, 1.0, 1.1, 1.2, 1.3] A. The gas flow rate values for the common data set are [0.5 1 2 5 10 20] sccm.

7.6.2 Removing Collisional Effects

We have already theorized that collisions and, more specifically, ionization in the bulk chamber plasma play a significant role in the measured I-V sweep for large gas

	Gas Flow Rate [sccm]						
Keeper Current [A] ⇓	0.2	0.5	1	2	5	10	20
0.3			K			K	AK
0.4	K	K	K	A		AK	AK
0.5	KX	KX	AK	A		AK	AK
0.6	KX	KX	AK	AK	A	AK	AK
0.7	KX	KX	AK	AK	AK	AK	AK
0.8	KX	AKX	AK	AK	AKX	AKX	AKX
0.9	KX	AKX	AKX	AKX	AKX	AKX	AKX
1.0	KX	AKX	AKX	AKX	AKX	AKX	AKX
1.1	KX	AKX	AKX	AKX	AKX	AKX	AKX
1.2	KX	AKX	AKX	AKX	AKX	AKX	AKX
1.3	KX	AKX	AKX	AKX	AKX	AKX	AKX

Table 7.5: The 90 plasma contactor flow configurations with common keeper current and gas flow rates for each ion species. 80 configurations are greyed out as they do not fall into this category and are henceforth ignored. The letter A represents Argon expellant use, K represents Krypton, and X represents Xenon.

flow rates and ion masses. To confidently remove these effects from our analysis, we must first show numerically when the onset of collisions occurs in the bulk chamber plasma. Charge exchange, impact ionization, and electron-neutral scattering collisions will be considered as the most frequent collisions in our plasma system. We will calculate the mean free path of these processes using Equation (7.1), in which $\lambda_{collision}$ is the collision mean free path, n_n is the neutral gas particle density, and $\sigma_{collision}$ is the collisional cross section [27]. We assume that the relative particle velocity is equal to that of the (much faster) charged particle and ignore the neutral gas velocity in order to make use of Equation (7.1). This is a very safe assumption for electrons (with temperatures in excess of 20,000 K) and the work in Chapter 6 shows that it is also safe for ions.

$$\lambda_{collision} = \frac{1}{n_n \sigma_{collision}} \quad m \tag{7.1}$$

The collisional cross sections used will be a single value to start since we do not have detailed particle energy measurements of this system. The peak collisional cross section is used to consistently produce the shortest mean free paths as a conservative estimate in terms of collisionality. This approximation is accurate enough for our purposes for the charge exchange cross section (it is within a factor of 3 for all energies relevant to this system). However, the impact ionization and electron-neutral scattering cross sections vary significantly over energy. The charge exchange cross sections used for Argon, Krypton, and Xenon are $4x10^{-19}$ m^2, $1x10^{-18}$ m^2, and $2x10^{-18}$ m^2 respectively [150, 161, 201]. The impact ionization cross sections used for Argon, Krypton, and Xenon are $3x10^{-20}$ m^2, $2x10^{-20}$ m^2, and $4x10^{-20}$ m^2 respectively [27, 202, 203]. The electron-neutral scattering cross sections used for Argon, Krypton, and Xenon are $1.2x10^{-19}$ m^2, $1.6x10^{-19}$ m^2, and $3.0x10^{-19}$ m^2 respectively [204, 205]. The neutral particle density is calculated using the ideal gas law assuming a neutral gas temperature of 300 K. The chamber operating pressure is measured by an ionization gauge recessed in the chamber wall and so the local neutral gas density in the bulk contactor plasma is likely somewhat higher. This analysis generates a mean free path estimate for each of the three collision types considered for each configuration. The minimum and maximum mean free paths of each collision are summarized in Table 6.

It is clear from Table 7.6 that only a few collisions occur in the chamber. The average distance from the hollow cathode orifice to the vacuum chamber wall (or some other grounded surface) is on the order of 0.5 m. Mean free paths of that same order represent a regime transition from collisions occurring rarely to typically occurring before particles reach the chamber wall. The minimum mean free path for charge exchange is below 1.0 m even at the lowest flow rate of 0.5 sccm, signifying that these collisions are present for all common configurations. This is not all that surprising given that Figure 6.9 of Chapter 6 contains a low energy peak representative of charge

	Charge Exchange Mean Free Path [m]		Impact Ionization Mean Free Path [m]		Elastic Electron-Neutral Mean Free Path [m]	
Gas Flow Rate [sccm] ⇓	Minimum	Maximum	Minimum	Maximum	Minimum	Maximum
0.5	0.91	14	46	180	6.1	45
1	0.46	7.8	23	100	3.0	10
2	0.24	4.1	12	55	1.6	14
5	0.16	3.9	7.8	52	1.0	13
10	0.054	0.91	2.7	12	0.36	3.0
20	0.029	0.52	1.4	10	0.19	1.7

Table 7.6: The minimum and maximum mean free path estimates for all common configurations.

exchange ions for a 5 sccm flow rate. Given the relatively large cross section of this process and the correspondingly short mean free paths, it seems it is not possible to select common data such that this process is negligible. The same can be said for elastic electron-neutral scattering collisions. The minimum mean free path for this process ranges from 0.19 m to 6.1 m. This range essentially spans the transition between this type of collision being ubiquitous and negligible. However, these elastic scattering collisions do not alter the electron or neutral particle kinetic energies and instead modify their propagation direction. Because the electron energy distribution function is already assumed to be isotropic and Maxwellian, these collisions are expected to have little impact on the contactor plasma.

Impact ionization mean free paths are the largest under consideration, however they are still small enough that ionization in the bulk plasma will play a notable role at high flow rates by assuming the cross section maximum. Impact ionization should have a much greater impact on the I-V sweep shape per collision, as it generates additional plasma rather than effectively slowing ions or redirecting electrons. As a result, it would be prudent to ignore flow rates which produce impact ionization mean free paths close to 0.5 m. To demonstrate this, we provide an example using

estimated values here. By assuming an electron travel distance of 0.5 m, uniform neutral pressure equal to the value measured by the ionization gauge, electron kinetic energy above the ionization threshold, and the minimum impact ionization mean free path of 1.4 m at 20 sccm, we are able to estimate the fraction of plasma electrons which trigger an ionizing collision using the Beer-Lambert law. The Beer-Lambert law is summarized in Equation (7.2), where T is the transmission (or fraction of particles which have not experienced a collision) and d is the distance traveled [48]. The resulting prediction is that 30% of electrons will trigger an ionizing collision. This would cause the effective contactor current to increase 30% as the contactor potential is increased and electrons are able to acquire the ionization energy.

$$T = exp\left(-d/\lambda_{collision}\right) \tag{7.2}$$

The above analysis is unrealistic when considering a Maxwellian EEDF with a temperature of just a few eV such as the one expected for the bulk chamber plasma. Indeed, the proper treatment of integrating the product of cross section and EEDF over all possible energies will yield a negligible number of impact ionization collisions in this case. Figure 7.15 features both the Xenon impact ionization cross section according to energy and the bulk plasma EEDF presented in Chapter 5 in order to visualize why this is the case. Very few electrons in the bulk plasma should have the energy required to ionize Xenon (which has the lowest ionization energy at 12.13 eV) [198]. However, there are also two chamber regions which feature strong electric fields. One sheath region near the vacuum chamber wall was treated in Chapter 6. Electrons originating from the chamber wall (such as secondary electrons kicked off by ion impact) may enter the bulk plasma region with kinetic energy exceeding the ionization energy due to the presence of this electric field [206]. The other region featuring a

strong electric field is near the hollow cathode itself. Using the measurements of Chapter 5, we can say that the potential of the exposed keeper electrode is ∼30 V higher than the plasma potential 8 cm downstream. This potential difference acts to accelerate bulk plasma electrons to high velocities as they approach the hollow cathode keeper. The keeper region also features some of the highest neutral gas densities in the vacuum chamber. Both of these regions have demonstrated an electric field sufficient to ionize Argon, Krypton, and Xenon for cathode biases used during the experiments treated in this chapter.

Impact ionization appears to be the cause of deviations from an exponential function for high flow rates, ion masses, and cathode potentials. For further evidence of this conclusion, we turn to the exponential fit R^2 values representing how well an exponential function matches the sweep data. The R^2 values are averaged according to flow rate and the results summarized in Table 7.7. R^2 values, also known as the coefficient of determination, quantify how well a model or fit represents the variation observed in a dataset by taking the difference between the fit and data (termed the residual) and normalizing it [207]. An R^2 value of one represents a perfect fit and an R^2 value of zero represents essentially no correlation (R^2 can also be calculated using the square of the correlation coefficient). The values in Table 7.7 match the qualitative trend previously discussed, as an exponential fit is less representative of configurations with higher flow rates.

Flow Rate [sccm]	0.5	1	2	5	10	20
Average R^2 Value of Exponential Fit	0.991	0.988	0.994	0.985	0.946	0.894

Table 7.7: Average R^2 of a least squares exponential sweep fit versus neutral gas flow rate.

Configurations with high gas flow rates should be removed from the common data set based on the findings outlined in this section. Doing so ensures that particle collisions in the bulk contactor plasma do not skew the experimental results. Deter-

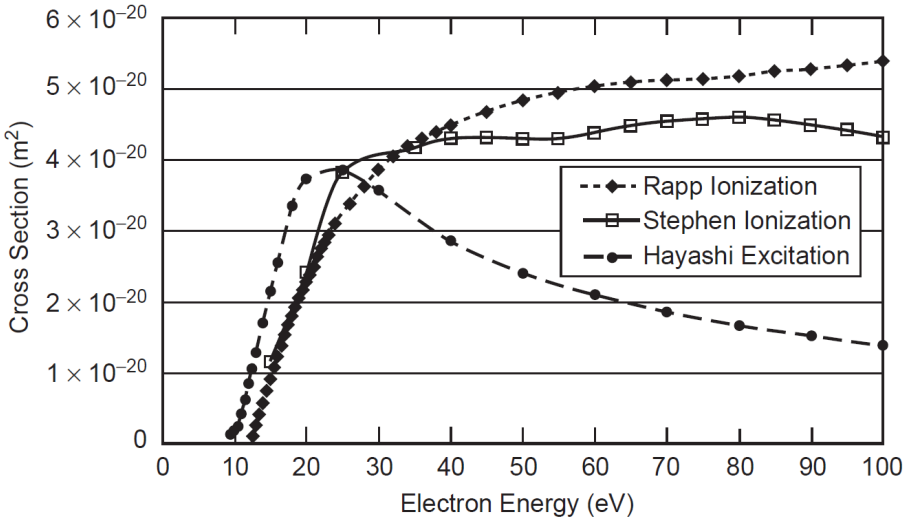

(a)

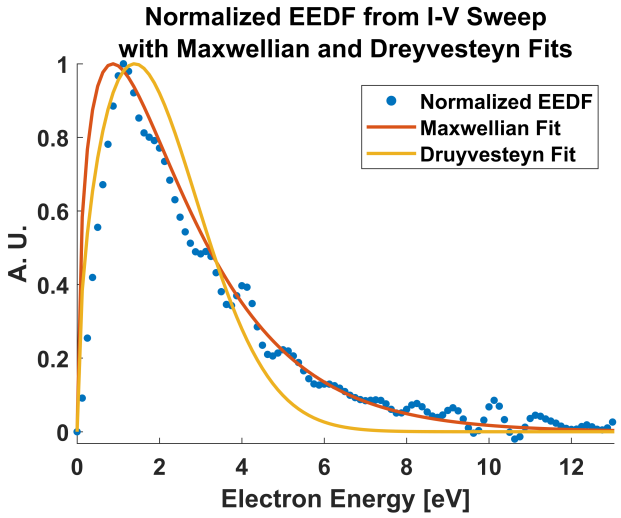

(b)

Figure 7.15: Xenon impact ionization cross sections (a) and an example EEDF for the bulk contactor plasma (b) [27].

mining the optimal flow rate cutoff is less straightforward. For the purposes of this dissertation, configurations with flow rates above 2 sccm are removed from the common data set. This value marks a transition in R^2 values and allows the claim to be made that $< 5\%$ of electrons undergo impact ionization per the earlier Beer-Lambert analysis. This decision leaves a common data set with 45 configurations and a gas flow rate which varies by a factor of 4 (the ion mass varies by a factor of 3.3). The final common data set is shown in Table 7.8 below.

	Gas Flow Rate [sccm]						
Keeper Current [A] ⇓	0.2	0.5	1	2	5	10	20
0.3			K			K	AK
0.4	K	K	K	A		AK	AK
0.5	KX	KX	AK	A		AK	AK
0.6	KX	KX	AK	AK	A	AK	AK
0.7	KX	KX	AK	AK	AK	AK	AK
0.8	KX	AKX	AK	AK	AKX	AKX	AKX
0.9	KX	AKX	AKX	AKX	AKX	AKX	AKX
1.0	KX	AKX	AKX	AKX	AKX	AKX	AKX
1.1	KX	AKX	AKX	AKX	AKX	AKX	AKX
1.2	KX	AKX	AKX	AKX	AKX	AKX	AKX
1.3	KX	AKX	AKX	AKX	AKX	AKX	AKX

Table 7.8: The 45 plasma contactor flow configurations in the common data set. 125 configurations are greyed out because they do not fall into this category and are henceforth ignored. The letter A represents Argon expellant use, K represents Krypton, and X represents Xenon.

7.6.3 Exponential Fitting to Remove Sweep Range Effects

The last remaining concern with the raw data set is the noise introduced by insufficient sampling in the exponential fit region. This concern is addressed here by using values from the exponential fit rather than the raw data points. This is possible only because the exponential fits are so good (their average R^2 value is 0.996) and eliminates any issues with rapid current changes near the floating potential. The contactor current can now be approximated more accurately as the exponential fit's predicted current for a cathode potential of infinity. The floating potential, potential at which the beam current is a quarter of the contactor current, and potential at which the beam current is a half of the contactor current are also redefined according to the fit function. Defining a common data set as described here provides a much clearer picture of the scaling laws which are the subject of this investigation.

7.7 Comparison of Refined Experimental Results with Numerical Predictions

7.7.1 Refined Spacecraft Potential Scaling with Electron Beam Current

Using the same two potentials to represent spacecraft charging as before (cathode potential when the beam current is one quarter and one half the contactor current) results in a power law exponent of 1.27 for every configuration under consideration. This is because representing an exponential function as a power law function using just two points produces the same power law exponent regardless of the constants involved. An exponent of 1.27 is within 9% of all values in the 1.17 – 1.21 range predicted via CPIC simulation [14]. In addition to comparing favorably with previous predictions, we now understand that cathode potential scales exponentially with "beam" current when using a hollow cathode plasma contactor on Earth.

We have outlined how potentials scale when only changing the ratio of beam current to contactor current. Based on this information, we suggest that plasma contactor I-V sweeps such as the ones presented in this chapter be used when predicting the peak spacecraft potential for electron emitting space missions using the ion emission technique. Experiments are required to provide data such as the contactor current of the relevant plasma contactor and initial potential scaling. Without this information, accurate predictions derived from comparison with space-based numerical modeling will not be possible.

7.7.2 Refined Spacecraft Potential Scaling with Contactor Current

The semi-analytical ion emission model predicts that cathode and spacecraft potential will scale as the contactor current to the 0.76 – 0.77 power when the beam current equals the contactor current [16]. The contactor current and corresponding cathode potentials of each of the 45 common configurations are shown in Figure 7.16.

A least squares power law fit is shown, as well as a least squares power law fit using a set power law exponent of 0.76. It is clear from Figure 7.16 that the cathode ("spacecraft") potential increases for higher beam and contactor currents. These two parameters are moderately correlated with a correlation coefficient of 0.56.

The ideal power law exponent is less clear for these parameters. There is still a fair amount of variability that may be due to covarying parameters in Figure 7.16. These covarying parameters also have an effect on cathode potential, leading data points to be spread vertically (over a larger cathode potential range). A vertical spread forces the least squares fit to be more horizontal such that it is centered in the spread and closer to more points overall. A least squares power law fit of this data set produces an exponent of 0.40 and R^2 value of 0.45. An exponent of 0.40 is not quite the 0.76 that was predicted, however it is within a factor of 2 and clearly has the same sign. The R^2 value associated with the fit being rather low is not surprising given the covarying parameters and spread discussed previously. These considerations leave room for doubt in the calculated 0.4 power law fit constant such that a second power law fit with a set exponent of 0.76 is also shown for comparison. This second fit has an R^2 value of 0.37 and is also shown in Figure 7.16. The vertical point spread brought on by covarying parameters is again significant for this fit (note the large impact of the 6 points over 150 uA contactor current). It is interesting to note that this fit does not seem significantly worse than the least squares fit in which the exponent was calculated. This conclusion suggests the predicted scaling law shows the correct trend and may yet be accurate, but that in ground-based experiments this scaling law may not be the most clear or important effect as it is tied to several covarying parameters and other potential experimental effects which have yet to be determined. Controlling for ion mass by evaluating each individually also gave no clearer power law relationship than what is shown in Figure 7.16.

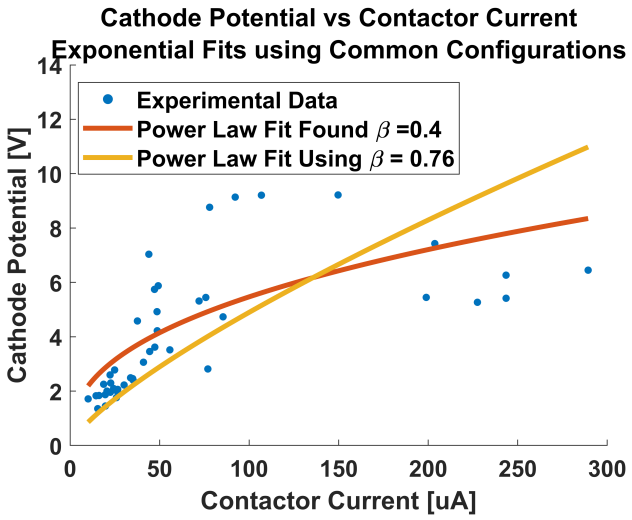

Figure 7.16: Cathode potential versus contactor current for common configurations. A least squares power law fit with variable exponent and 0.76 exponent are shown. Cathode potential is measured relative to floating potential at an ion emission (or beam) current equal to 0.5 times the contactor current.

7.7.3 Refined Spacecraft Potential Scaling with Ion Mass

The semi-analytical ion emission model and CPIC tool predict that cathode and spacecraft potential will scale as the ion mass to the 0.34 – 0.37 and 0.40 – 0.57 power, respectively. The average cathode potential when the beam current is half of the contactor current is shown for each ion mass in Figure 7.17. A least squares power law fit is performed on these three points for comparison with numerical prediction, however it is readily apparent from the -0.88 exponent that the observed trend is not as predicted. One factor which likely plays a role in this discrepancy is the constant contactor plasma size as discussed in Section 7.3. In this section we argue that the dramatic decrease in cathode/spacecraft potential is due to electron temperature changes with ion mass.

The average pseudo electron temperature for each ion mass is also shown in Figure 7.17. We note that the cathode potential and pseudo electron temperature are simply related by a constant value of 1.45 when using exponential fitting. Perhaps the most

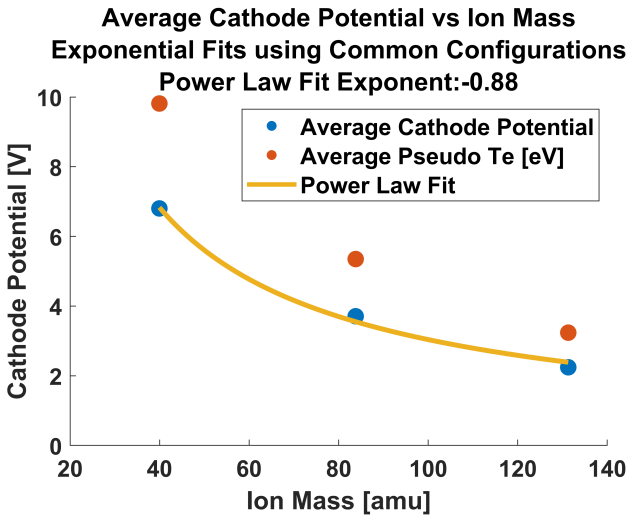

Figure 7.17: Average cathode potential for each ion species in the common data set with a least squares power law fit. Cathode potential is measured relative to floating potential at an ion emission (or beam) current equal to 0.5 times the contactor current.

interesting feature of Figure 7.17 is the significant decrease in cathode potential and pseudo electron temperature with mass. A power law exponent of -0.88 is a far cry from the predicted 0.34 – 0.57. One likely explanation for this discrepancy is that changes in contactor plasma electron temperature were not properly accounted for during predictive numerical studies. These studies kept electron temperature constant in order to remove its effects on spacecraft charging. However, the results treated here strongly suggest that electron temperature decreases with increasing ion mass. To understand how this may impact the cathode potential required to emit half the contactor current as a net ion current, we explore two possible explanations below. One of these explanations is based on the electron kinetic energy while the other is based on the ion-rich region thickness and its electron temperature dependence.

A zeroth order treatment of Maxwellian electrons expanding from the cathode orifice indicates that those with the lowest kinetic energy will return to the cathode for the smallest cathode potentials. Using this conceptual framework, we can imagine that some fraction of electrons with low kinetic energies return to the cathode and

the rest are emitted. This fraction is determined by the cathode potential and should scale according to the electron temperature. Indeed, the 1.45 factor relating cathode potential and pseudo electron temperatures in Figure 7.17 is also the value at which half the electrons are reabsorbed and half are emitted according to the Beer-Lambert law (0.5 = exp(-1/1.45)) [48]. The decreased electron temperature with increasing ion mass should thus force the same fraction of electrons to be recollected at lower cathode potentials as observed above.

Ignoring electron dynamics and solely considering the ion-rich sheath thickness also supports the theory that electron temperature effects dominate ion mass effects in the presented experiments. Assuming SCL ion emission suggests that the voltage required to emit a given ion current from the plasma scales as the ion-rich region thickness to the 4/3 power. As the electron temperature decreases with increasing ion mass, the Debye length will also decrease as it proportional to the square root of the electron temperature. The ion-rich region thickness is proportional to the Debye length in turn. Thus the predicted 0.34 – 0.57 power law exponents may be obscured solely considering these effects.

In a standard hollow cathode configuration, one does not have independent control of plasma electron temperature. Electron temperature decreasing with increasing ion mass has been observed previously using Argon, Krypton, and Xenon [208]. A full treatment of chamber plasma dynamics is required to produce an accurate model of the bulk contactor plasma electron temperature. Developing such a model is considered beyond the scope of this work given the experimental measurements directly reporting this trend. However, it is expected that the external plasma electron temperature is positively correlated with internal electron temperature, allowing us to leverage a basic internal hollow cathode model in support of these experimental results. To gain a basic theoretical understanding why electron temperature decreases with ion mass, we utilize a steady state balance between plasma ion generation and

diffusion inside the hollow cathode volume. Equation (7.3) sets the ion generation rate via impact ionization inside the hollow cathode ($I_{generation}$). This value equals the ion loss rate via diffusion to the hollow cathode walls (I_{loss} of Equation (7.4)) in general terms [27, 209]. q is the elementary ion charge, n_n is the neutral gas density, $\sigma_{ionization}$ is the impact ionization cross section, $v_{th,e}$ is the electron thermal velocity, V is the hollow cathode interior volume, k_B is Boltzmann's constant, T_e is the electron temperature, m_e is the electron mass, Γ_i is the ion flux to the hollow cathode interior, A is the hollow cathode interior surface area, n_i is the ion density, and v_i is the average ion velocity to the hollow cathode interior wall in Equations (7.3) and (7.4). By combining Equations (7.3) and (7.4), assuming plasma quasi-neutrality (setting $n_e = n_i$), and removing constant values, we recover Equation (7.5).

$$I_{generation} = q n_e n_n \sigma_{ionization} v_{th,e} V = q n_e n_n \sigma_{ionization}(T_e) \sqrt{\frac{8 k_B T_e}{\pi m_e}} V \quad A \tag{7.3}$$

$$I_{loss} = q \Gamma_i A = q n_i v_i A \quad A \tag{7.4}$$

$$T_e \quad \propto \quad \left(\frac{v_i}{n_n \sigma_{ionization}(T_e)} \right)^2 \quad K \tag{7.5}$$

The right hand side of Equation (7.5) leaves little room for doubt that electron temperature should decrease with increasing ion mass. Ion velocity, v_i, should be lower for higher ion masses as it is inversely proportional to the square root of ion mass for a set ion energy. Higher masses also have larger cross sections and so accounting for slowing collisional processes would only decrease v_i further for heavier ions. Along the

same lines, the ionization cross section, $\sigma_{ionization}$, increases dramatically for higher mass noble gases at a given electron temperature. Finally, the neutral gas density, n_n, isn't expected to change much with ion mass. In fact, the common data set correlation coefficient between ion mass and chamber neutral gas density is 0.62. This indicates that in practice the neutral gas density does increase with ion mass. All of these factors reduce the value of Equation (7.5) and point to the same conclusion: the electron temperature decreases for higher ion mass.

7.8 Summary

The experiments presented in this chapter focus on how spacecraft design choices affect spacecraft charging during electron beam emission when utilizing the ion emission technique. In doing so, these experiments generate practical knowledge for future mission design. They also advance our understanding of ion emission and what physical processes are required to enable numerical modeling of the upmost accuracy. The spacecraft (cathode) potential scaling with electron "beam" current was found to follow an exponential function closely. Selecting points from these exponential fits resulted in a power law exponent within 9% of what was initially predicted. The contactor current scaling law was difficult to isolate as other covarying parameters must change to physically produce more or less plasma. The spacecraft/cathode charging was generally found to increase slightly with contactor current overall as predicted. The ion mass scaling is actually the opposite of what was previously predicted. Increasing the ion mass in an earth-based vacuum chamber decreases the cathode potential required to emit half the contactor current as a net ion current. This appears to be tied to changes in contactor plasma electron temperature with ion mass. It is advised that future mission designers perform I-V sweeps similar to those shown here using their respective hollow cathode plasma contactor subsystem. Doing so will allow for more accurate prediction and control of spacecraft charging during

electron beam emission in space.

CHAPTER VIII

Conclusion

8.1 Progress Made

Much progress has been made in enabling spacecraft charge neutralization during active electron emission. CPIC simulations first replicated electron beam return in the magnetosphere due to spacecraft charging and space-charged limited ion emission as shown in Chapter 3. Effective spacecraft neutralization during electron beam emission was observed when emitting a larger contactor (plasma) current. It was theorized that ion emission from the quasi-neutral contactor plasma is space-charge limited based on these results. The input parameters of electron beam current and ion mass were varied to predict scaling laws for space applications.

Semi-analytical models were developed to supplement the CPIC tool. The most complete and accurate model replicates important CPIC outputs within a few percent, confirming our theoretical understanding of the ion emission process. These models run on a personal laptop in a reasonable amount of time and are used to test new configurations not accessible to CPIC. These models also predict increasing spacecraft potentials for increased electron beam current, contactor current, simulation size, and decreased plasma injection area. Notable progress was also made in predicting plasma expansion in the absence of CPIC simulations.

Multiple experimental campaigns were completed to examine critical aspects of

the prospective ion-emitting system. Transient experiments confirm that "spacecraft" neutralization is possible in the laboratory. The observed plasma transient is mostly as expected except for long equilibrium times. These equilibrium times can be explained by a simple capacitive circuit model. Steady state plasma experiments also confirm CPIC results. These experiments produced new information on plasma electron temperature changes with "spacecraft" potential and the ion emission location in the chamber. Measured emission currents match the ion emission model and space-charge limit within 50%. This result effectively validates CPIC and the ion emission model for laboratory conditions. Scaling law experiments recreate the predicted beam current scaling. The effects of contactor current are less clear due to covarying parameters. Ion mass has an effect opposite of what was predicted, which is likely due to unmodeled electron temperature changes. In total, the work presented in this dissertation provides all the necessary tools to propose an in-space demonstration.

8.2 Future Work

Many of the questions which can be answered on Earth have been addressed during the course of the work presented in this dissertation. However, there remain a few specific questions which have yet to be answered. One question is if the spacecraft potential scaling with beam current and ion mass is truly electron temperature dependent as expected from Chapter 7. Probing the bulk chamber electron temperature using different expellant gases and then comparing it with the results of Chapter 7 could answer this question. A more difficult question to answer is the effect of a magnetic field on ion emission. CPIC simulations with a magnetospheric field were almost identical to those performed with zero magnetic field. However, a larger magnetic field should play a significant role in shaping the plasma contactor and ion emission process. Understanding the impact of a stronger magnetic field

could extend previous research to more magnetized regions, including LEO and the Jovian magnetosphere.

Numerous questions remain to be answered by in-space experiments. For one, simultaneous electron beam and plasma emission has yet to be reported in tenuous space plasmas. Whether this configuration will effectively neutralize the spacecraft with certainty is the largest remaining question. It would also be beneficial to test related configurations, such as pulsed plasma and RF electron beam emission. Other questions address scaling laws which enable effective spacecraft system design. Many of these remaining questions could be answered with a single in-space demonstration.

8.2.1 Magnetic Field Scaling Studies

8.2.1.1 Vacuum Chamber Experiments

Ion emission experiments with a varying magnetic field are currently underway. A solenoid was constructed with the capability of producing a uniform 5 mT magnetic field. Images of the final solenoid design are provided in Figure 8.1. A maximum 5 mT solenoid field strength was selected to be approximately 100 times stronger than the ambient field on the Earth's surface in order to reduce its effects. The magnetic field strength can be controlled directly via the coil current. The solenoid field in the active test volume was mapped in the absence of a plasma and the magnitude was found to be uniform within 10%. This map can be found in Figure 8.2. The hollow cathode I-V sweep procedure outlined in Chapter 7 can be repeated using this solenoid and a variable magnetic field strength. The results should elucidate the impact of a magnetic field on ion emission for Earth-based experiments.

8.2.1.2 Magnetic Model Development

An analytical model must be developed to explain magnetic field scaling experiments and extend them to space. This model should account for the contactor plasma

(a) (b) (c)

Figure 8.1: Experimental solenoid SOLIDWORKS model (a), standing upright (b), and during magnetic field mapping (c).

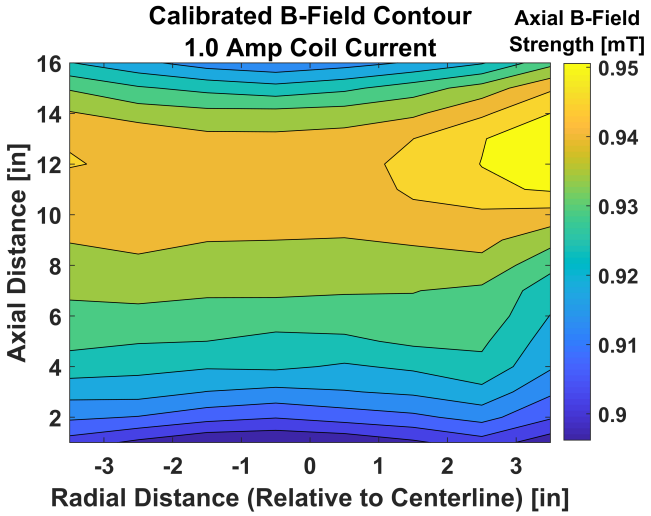

Figure 8.2: Experimental solenoid magnetic field contour featuring the active test volume in the absence of a plasma.

expansion due to magnetic field effects. For example, plasmas are typically locked to magnetic fields if they are sufficiently strong in comparison with cross-field diffusion due to turbulence and collisions (see Chapter 2). We can therefore imagine the plasma expands as an elongated cylinder such that its long axis is aligned with the ambient magnetic field. The length of the cylinder will primarily be defined by non-magnetic conditions including the plasma expansion time, ion drift velocity, and

electron temperature (through ambipolar diffusion). The cylinder radius should depend strongly on the magnetic field strength. We anticipate here that this radius is equal to a multiple of the electron (or possibly the ion) gyroradius as summarized in Equation (8.1). α represents the particle species, r_g is the particle gyroradius, m is the particle mass, v_{perp} is the particle velocity perpendicular to the ambient magnetic field, q is the particle charge, and B is the ambient magnetic field in Equation (8.1). The ion-emitting surface area of an elongated cylinder scales linearly with the radius according to Equation (8.2), as the ends may be ignored for a sufficiently long cylinder. $A_{emission}$ is the ion-emitting surface area, β is an unknown constant defining the contactor plasma radius relative to the charged particle gyroradii, and L is the length of the contactor plasma in Equation (8.2). The ion emission current density is determined by the space-charge limit given in Equation 3, which in this case should not feature a substantial ion drift. In Equation (8.3), J_{SCL} is the space-charge-limited current, ϵ_0 is the permittivity of free space, V_{SC} is the spacecraft potential (which in this case is approximately equal to the plasma potential), and d is the physical separation between the two potential regions. By combining the gyroradius, cylinder surface area, and space-charge limit expressions and assuming a constant ion emission current equal to the electron beam current (as is the case in equilibrium), we arrive at Equation (8.4). Equation (8.4) defines how the peak spacecraft potential scales with the magnetic field strength for a given electron beam current (I_{beam}) using a constant multiplier of C. Future work should include comparing this prediction with experimental results and determining the appropriate constant term (which in this case dictates if the plasma is confined according to the electron or ion gyroradius).

$$r_{g,\alpha} = \frac{m_\alpha v_{perp}}{q_\alpha B} \quad m \tag{8.1}$$

$$A_{emission} \approx 2\pi\beta r_{g,\alpha} L + 2\pi\beta {r_{g,\alpha}}^2 \approx 2\pi\beta r_{g,\alpha} L \quad m^2 \tag{8.2}$$

$$J_{SCL,\alpha} = \frac{4\epsilon_0}{9}\sqrt{\frac{2q_\alpha}{m_\alpha}}\frac{V_{SC}^{3/2}}{d^2} \quad A/m^2 \tag{8.3}$$

$$V_{SC} = \left[\sqrt{\frac{m_\alpha}{2q_\alpha}}\frac{9d^2 I_{beam}}{4\epsilon_0 A_{emission}}\right]^{\frac{2}{3}} \approx \left[\sqrt{\frac{m_\alpha}{2q_\alpha}}\frac{9q_\alpha d^2 B I_{beam}}{8\pi\epsilon_0\beta m_\alpha v_{perp} L}\right]^{\frac{2}{3}} \alpha \quad CB^{\frac{2}{3}} \quad V \tag{8.4}$$

8.2.2 In-Space Demonstrations

Missions demonstrating the ion emission technique are in development. Significant efforts have been made to advance the CONNEX mission concept. A suborbital sounding rocket proposal was also submitted to the NASA Heliophysics Science Mission Directorate in 2019. This proposal was part of the H-FORT Low Cost Access to Space program and is titled the Beam-Spacecraft Plasma Interaction and Charging Experiment (B-SPICE). B-SPICE is expressly designed to validate the ion emission model and explore critical scaling laws in space. B-SPICE explores the effect of contactor expansion time, beam current, and expellant utilization (the percentage of ionized neutral gas). It features a high current (150 mA) electron beam, 500 mA plasma contactor, and spacecraft potential monitor in the form of a tethered child payload. Additional diagnostics include a Langmuir probe to measure the ambient plasma and photometers to observe emissions generated in the electron beam and contactor plasma. A block diagram showing B-SPICE subsystems can be found in Figure 8.3. A 2022 launch reaching an altitude of ∼260 km was proposed.

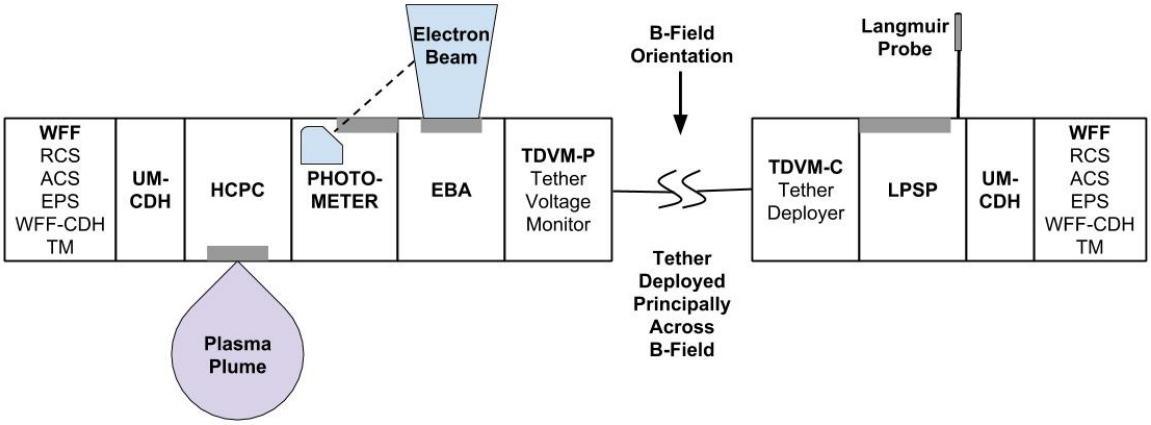

Figure 8.3: A block diagram sketch of the B-SPICE rocket configuration.

8.3 A Look Forward

Much of our research on the ion emission model approaches completion as outlined in this chapter. Our research collaborations have grown stronger and more efficient over the course of this research. We now look forward to tackling spin-off projects born from this close collaboration and supporting future missions which use the ion emission technique. We believe these projects show great promise for furthering space exploration and, more broadly, the scientific body of knowledge. While the ultimate outcome of these efforts is still unknown, our work continues.

APPENDICES

APPENDIX A

Simple Capacitor Model

A simple, spherical capacitor model for spacecraft charging using a plasma contactor during electron beam emission is developed below. To begin, the assumption is made that all charge removed by the beam is stored in the conducting plasma-spacecraft system. This system thus acts like a capacitor storing charge. However, the system is also expanding and increasing its capacitance over time. In steady state, an ideal, conducting spherical capacitor stores all of its charge on its surface. This is similar to what is seen in CPIC simulations, with the subtle difference that charge originates in the center of the sphere and must travel to the plasma front. This interpretation seems to explain the simulation results qualitatively, but a numerical model is needed to explore it further.

A spherical capacitor model was briefly discussed in Gian Luca Delzanno's 2015 JGR paper and this will be the start of our development [14]. It used a perfect spherical capacitor in space, but neglected the continued expansion of the plasma plume while the electron beam was fired. We will define an effective system radius which accounts for the spacecraft radius and plasma expansion as below:

$$r_{effective} = r_{SC} + v_{exp}(\tau_0 + \tau) \tag{A.1}$$

In Equation (A.1), $r_{effective}$ is an effective conducting (plasma) radius, r_{SC} is the spacecraft radius, v_{exp} is the plasma expansion velocity, τ_0 is the time the contactor was operating before the beam was fired, and τ is the time since the beam began firing continuously. Using this effective radius assumes spherical plasma expansion and a constant plasma expansion velocity. Simulations predict a relatively constant plasma expansion velocity. Perfect spherical plasma expansion is not expected in practice or seen in simulations, but is a decent approximation for the purposes of this model. All other geometries produce smaller capacitances, which should produce slightly larger spacecraft potentials than those predicted by this model. A graphical representation of this first model is provided in Figure A.1. To calculate the spacecraft potential, V_{SC}, of this configuration, we invoke the capacitance of an isolated sphere and accumulate charge to this capacitor using the expressions below:

$$C = Q/V_{SC} = 4\pi\epsilon_0 r_{effective} \tag{A.2}$$

$$Q = I_{beam}\tau + Q_0 \tag{A.3}$$

In (A.2), C is the total system capacitance, Q is the total system charge, and ϵ_0 is the permittivity of free space. I_{beam} is the electron beam current and Q_0 is the initial system charge (at the time of electron beam ignition) in Equation (A.3). Combining Equations (A.1), (A.2), and (A.3) yields Equation (A.4):

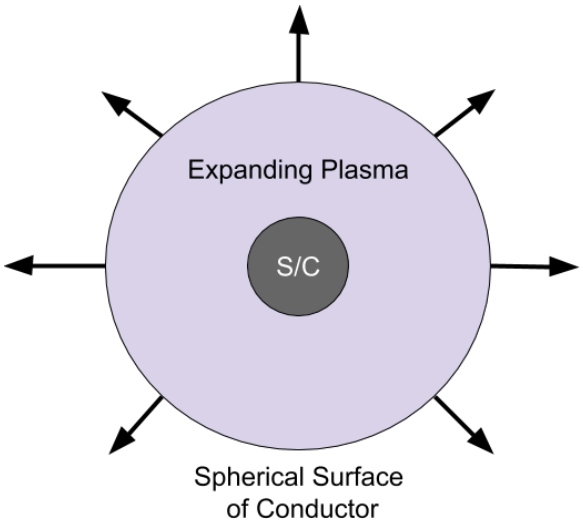

Figure A.1: A graphical representation of the expanding spherical capacitor model.

$$V_{SC} = \frac{Q_0 + I_{beam}\tau}{4\pi\epsilon_0 \left(r_{SC} + v_{exp}(\tau_0 + \tau)\right)} \tag{A.4}$$

Setting $\tau_0 = r_{SC} = 0$ yields the maximum potential the spacecraft can reach while the contactor and beam fire simultaneously. We can also input previous simulation parameters into this simple capacitive model for comparison. Figure A.2 (a) was generated using the C1 parameter set (the ion drift speed, v_d, was used for v_{exp}) and appears similar in magnitude to the corresponding simulation results in Figure A.2 (b) [14]. However, the capacitor model increases monotonically and does not account for the grounded simulation boundaries. It is encouraging to note that the shape of this transient is very similar to results obtained using the full ion emission model with the simulation boundary placed infinitely far away (see Figure A.3) [16].

This model's ability to predict simulation results can be improved by accounting for walls with a concentric spherical capacitance. This configuration is more representative of the simulations presented here and its capacitance is defined in Equation (A.5) below:

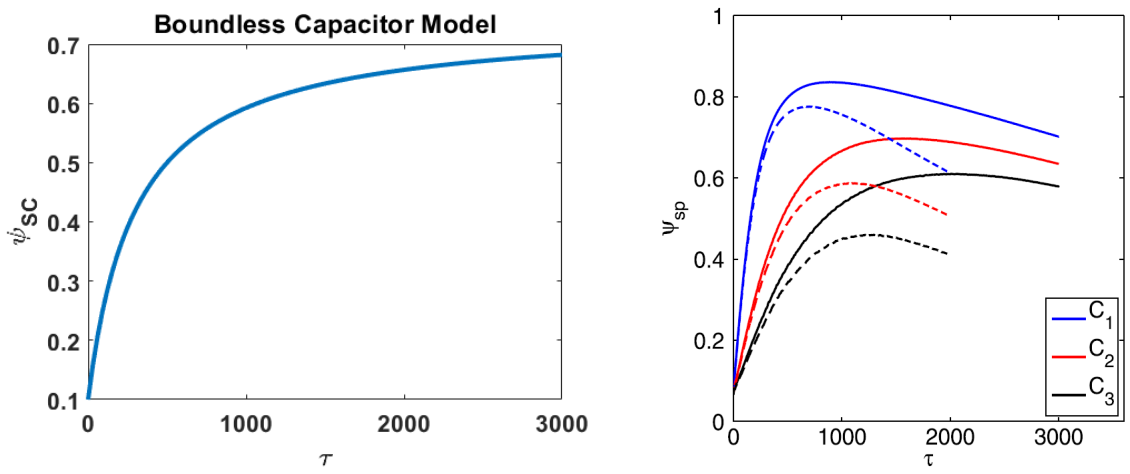

(a) (b)

Figure A.2: Normalized spacecraft potential over normalized time using the capacitive model with no walls and C1 simulation parameters (a). CPIC simulation spacecraft potential over time when changing the time between plasma release and beam firing (colors) and simulation domain size (solid lines use $r_{wall} = 100$ and dashed lines use $r_{wall} = 50$) (b) [14].

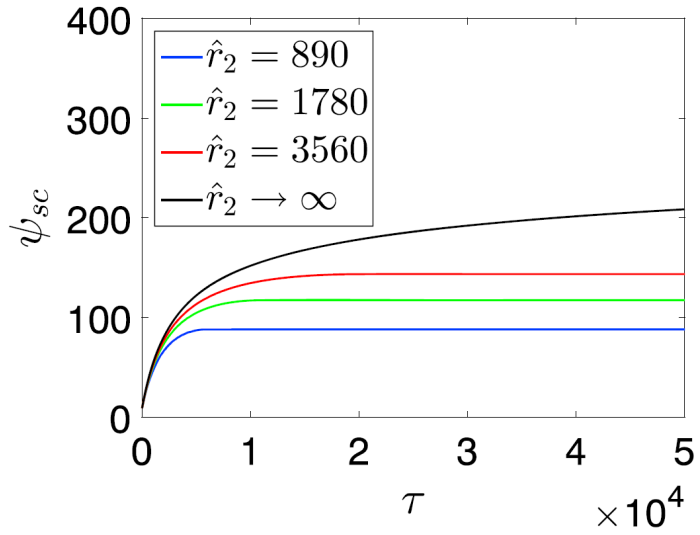

Figure A.3: Normalized semi-analytical ion emission model spacecraft potential transients using various domain boundary radii and a different set of model inputs than those used in Figure A.2 [16].

$$C = \frac{4\pi\epsilon_0}{\frac{1}{r_{effective}} - \frac{1}{r_{wall}}} \tag{A.5}$$

r_{wall} is the radius of the grounded wall (or 0 V simulation boundary) in the equation above. This concentric capacitance model's physical configuration is shown in Figure A.4. The same parameters used in previous CPIC simulations were input into this model. The resulting predictions are plotted side-by-side in Figure A.5. It is clear that the capacitance model does a remarkably good job of predicting the PIC results and their dependence on chamber size. Indeed, it can be argued that the differences between the two graphs are readily explained by previously discussed assumptions of the capacitor model (such as deviations from spherical plasma expansion and constant expansion velocity).

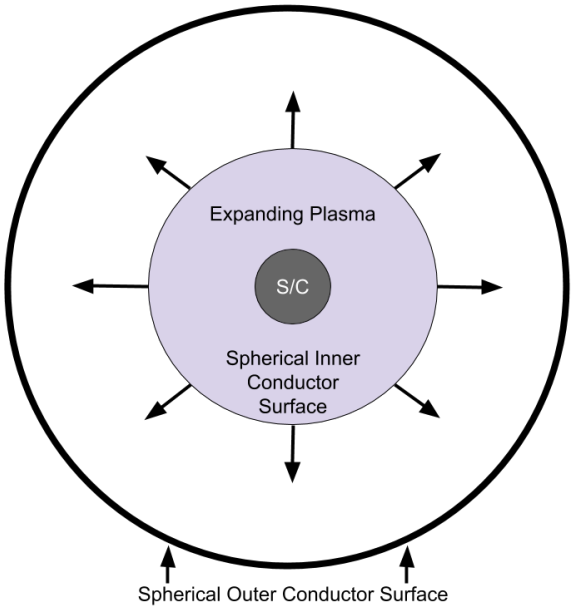

Figure A.4: A graphical representation of the spherical capacitor model with grounded exterior boundaries.

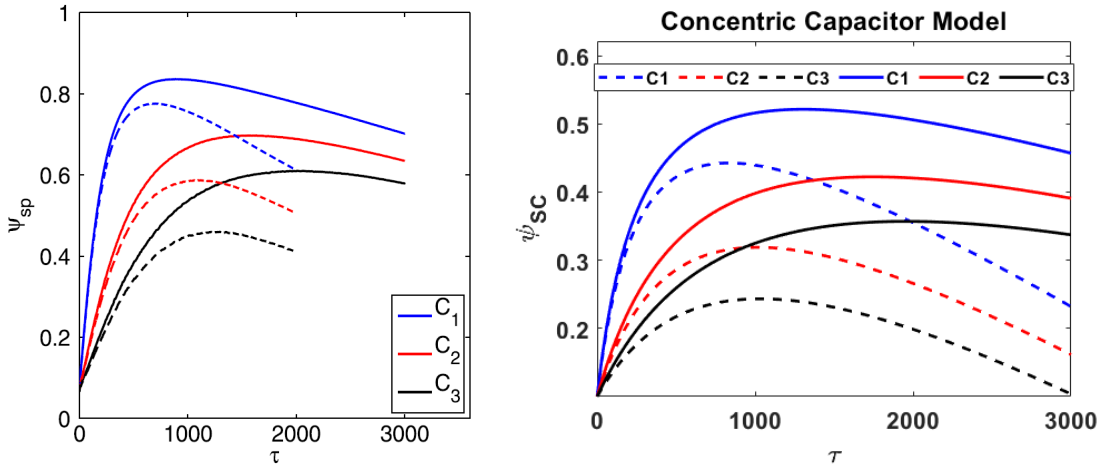

(a) (b)

Figure A.5: Normalized CPIC simulation spacecraft potential over normalized time when changing the time between plasma release and beam firing (colors) and simulation domain size (solid lines use $r_{wall} = 100$ and dashed lines use $r_{wall} = 50$) (a) [14]. On the right is the concentric capacitor model prediction using the same input parameters (b).

APPENDIX B

Emissive Probe Calibration

The emissive probe measurement circuit and an example heating calibration curve are presented below in Figures B.1 and B.2 respectively. Both are standard operating procedure for emissive probes using the floating point with large emission technique as described in [152, 193]. Joule heating is used to heat the probe to electron emitting temperatures via a heating power supply. 10 kΩ resistors are used to account for the resistive voltage drop across the probe itself. These resistors allow a voltmeter to measure the voltage at the center of the emitting probe, which floats closest to the actual plasma potential. The Fluke handheld voltmeter used to measure the probe's floating potential has an internal measurement resistance of 10 MΩ. This large resistance allows the emissive probe to float unperturbed at the plasma potential for plasma densities above 10^5 cm^{-3}, below which space-charge effects become significant [152, 193].

The emissive probe temperature is adjusted to an appropriate value using a calibration curve. The floating potential begins to rise rapidly as the probe temperature is increased via the heating current and significant thermionic electron emission begins. Eventually the floating potential plateaus at the plasma potential as seen in Figure B.2. At this point, the net electron current to the emissive probe surface should be

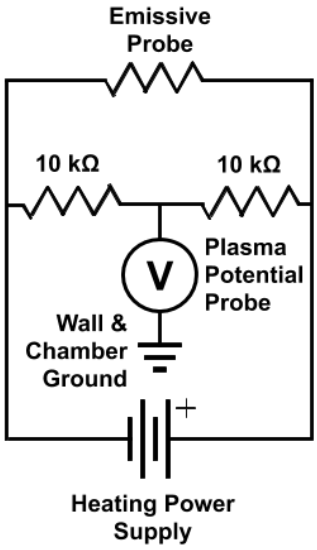

Figure B.1: The emissive probe measurement circuit.

precisely balanced by thermionic emission current such that the emissive probe floats at the plasma potential and there is no sheath. After this point, increasing the emission only slightly changes the floating potential due to space-charge effects [210]. It is also worth noting that the heating current cannot increase indefinitely as the probe itself will melt at some finite temperature. A historical calibration curve has been included for comparison with the example calibration curve in Figure B.3 [152].

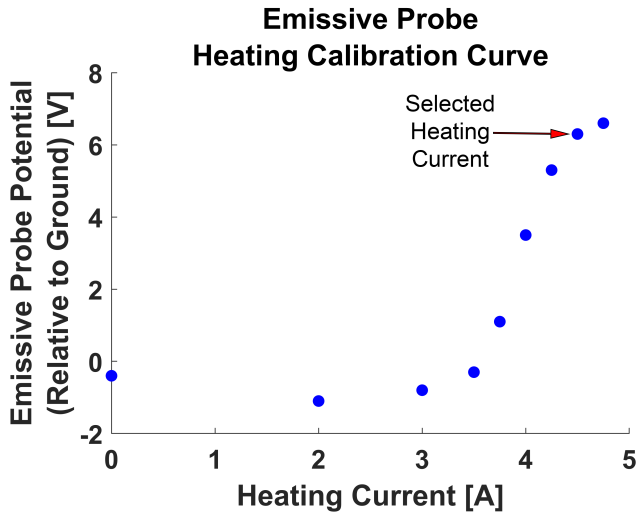

Figure B.2: An example emissive probe heating calibration curve showing the "knee", where sufficient thermionic electron emission is emitted to balance plasma electron collection.

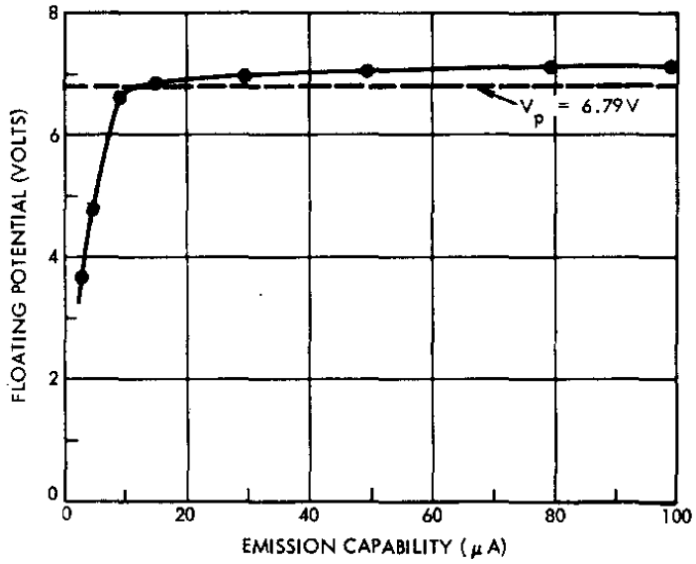

Figure B.3: A historical emissive probe heating calibration curve showing the "knee", where sufficient thermionic electron emission is emitted to balance plasma electron collection. The plasma potential as obtained using the Langmuir probe "intersection" technique is also shown [152].

APPENDIX C

MATLAB Langmuir Probe Analysis Procedure

```
function [Floating_Potential, Plasma_Potential, Ion_Density, Ion_Density_3,
↪  Electron_Density, Electron_Temperature, Electron_Temperature_2,
↪  Ion_Drift_Velocity]=...
LP_Analysis_Package_Cleaned_v5(file,Fast_analysis,filter_polynomial,filter_window
↪  ,Max_Vfloat_to_Vplasma,Min_Peak_Height)

% Grant Miars and Omar Leon

%% The general flow of this analysis is as follows:
    % Define constants and parameters

    % Enter Langmuir probe dimensions

    % Read files

    % Filter the current using a Savitzky-Golay filter

    % Truncate the ends of the data to remove power supply transients

    % Calculate floating potential by averaging the highest negative and
    % lowest positive current values

    % Fit the ion saturation regime and use this fit to estimate the ion
    % current and isolate the electron current

    % Calculate plasma potential using the peak in the electron current
    % derivative

    % Calculate electron temperature using a fit of the center of the
    % electron retardation regime

    % Calculate electron density using electron thermal current at the
    % plasma potential

    % Calculate ion density with a linear fit of the square of the current
    % in the ion saturation region (OML)
```

```
    % Calculate the ion drift velocity using the intercept of a linear fit
    % of the square of the current in the ion saturation region (Brace and
    % Hoegy)

%% Define constants and parameters
u = 1.66e-27; % amu to kg
ion_mass = 40*u; % Mass of Argon in kg
electron_mass = 9.10938e-31; % Mass of electron in kg
ec = 1.6e-19; % Elementary charge
e0 = 8.85e-12; % Permittivity of free Space

% Enter Langmuir probe dimensions
LP_L = 2*2.54e-2; % Length in m
LP_D = 20e-3*2.54e-2; % Diameter in m
AreaLP = pi*LP_L*LP_D; % m^2

% Read text files
% data = read_file(file);
% tempvolt = values(data,{'Voltage'});
% voltage(:,1) = tempvolt{1,1}(:,1);
% tempcurrent = values(data,{'Current'});
% current(:,1) = tempcurrent{1,1}(:,1);

% Read xls files
pos_file = strsplit(file,'\');
disp(pos_file(end))
data = xlsread(file);
voltage(:,1) = data(:,1);
current(:,1) = data(:,2);

% Filter the current
current_filtered = sgolayfilt(current,filter_polynomial,filter_window);

%% Truncate the first few and final volts to remove power supply transients
low_volts_removed = 1;
high_volts_removed = 3;
current = mean(current((voltage(end)-high_volts_removed>=voltage) &
↪  (voltage>=voltage(1)+low_volts_removed)),2);
current_filtered =
↪  mean(current_filtered((voltage(end)-high_volts_removed>=voltage) &
↪  (voltage>=voltage(1)+low_volts_removed)),2);
voltage = mean(voltage((voltage(end)-high_volts_removed>=voltage) &
↪  (voltage>=voltage(1)+low_volts_removed)),2);

%% FLOATING POTENTIAL------------------------------------------------------

% Calculate floating potential by averaging the highest negative and lowest
% positive current values
negative_current_voltages =  voltage(current_filtered<0);
positive_current_voltages =  voltage(current_filtered>0);

Floating_Potential =
↪  mean([negative_current_voltages(end),positive_current_voltages(1)]);
```

```
%% Fit the ion saturation regime and substract it out if you so choose

% Truncate to just include the ion saturation region (first ?% of points)
min_index_for_fit = 1;
max_index_for_fit = 0.75*(Floating_Potential-min(voltage))*length(voltage)/(max(v
↪  oltage)-min(voltage));
voltage_truncated = voltage((min_index_for_fit:max_index_for_fit),1);

% Square the current for fitting and truncate to fit region
current_filtered_squared = current_filtered.^(2);
current_filtered_squared_truncated =
↪  current_filtered_squared((min_index_for_fit:max_index_for_fit),1);

% Define a linear function for fitting
fit_parameters_ID = [1e-10 1e-10];
linear_function_ID = @(fit_parameters_ID,voltage)-fit_parameters_ID(1)*voltage +
↪  fit_parameters_ID(2);

% Linear fit of current squared
options = optimoptions('lsqcurvefit','TolFun',1e-30,'TolX',1e-30,'MaxFunEvals',10
↪  000,'Display','off');
fit_parameters_ID = lsqcurvefit(linear_function_ID,fit_parameters_ID,voltage_trun
↪  cated,-current_filtered_squared_truncated,[],[],options);

% Raise the current to the 4/3 for fitting and truncate to fit region
current_filtered_43 = real(current_filtered.^(4/3));
current_filtered_43_truncated =
↪  current_filtered_43((min_index_for_fit:max_index_for_fit),1);

% Define a linear function for fitting
fit_parameters_ID_2 = [1e-10 1e-10];
linear_function_ID_2 =
↪  @(fit_parameters_ID_2,voltage)-fit_parameters_ID_2(1)*voltage +
↪  fit_parameters_ID_2(2);

% Linear fit of current to the 4/3
fit_parameters_ID_2 = lsqcurvefit(linear_function_ID_2,fit_parameters_ID_2,voltag
↪  e_truncated,-current_filtered_43_truncated,[],[],options);

% Subtract out the ion current to just work with the electron current
Ion_current = -real((linear_function_ID(fit_parameters_ID,voltage).^(1/2)) -
↪  (-linear_function_ID(fit_parameters_ID,voltage)).^(1/2));
Ion_current(Ion_current < 0) = 0;
Electron_current = current_filtered + Ion_current;

%% PLASMA POTENTIAL-------------------------------------------------------

% Take derivatives of the current and filter them
dIdV = derivative(Electron_current,voltage);
dIdV_filtered = sgolayfilt(dIdV,filter_polynomial,filter_window);
dIdV2 = derivative(dIdV_filtered,voltage);
dIdV2_filtered = sgolayfilt(dIdV2,filter_polynomial,filter_window);
```

```
% Produce a range of voltages from the floating potential to the maximum
% possible plasma potential.
Range = and((Floating_Potential<=voltage),(voltage<=Floating_Potential+Max_Vfloat
↪  _to_Vplasma));
Zoomed_dIdV_filtered = dIdV_filtered(Range);
Zoomed_dIdV2_filtered = dIdV2_filtered(Range);

% Divide the derivative array values by the maximum value in this array.
% This makes it possible to determine a sensible minimum peak height.
Norm_Zoomed_dIdV_filtered = Zoomed_dIdV_filtered./max(abs(Zoomed_dIdV_filtered));
Norm_Zoomed_dIdV2_filtered =
↪  Zoomed_dIdV2_filtered./max(abs(Zoomed_dIdV2_filtered));

% Find the peak in the first derivative
[~,Loc] = findpeaks(Norm_Zoomed_dIdV_filtered,'MinPeakHeight',Min_Peak_Height);

% Set the plasma potential to the first peak in the first derivative
Plasma_Potential = voltage(dIdV_filtered==Zoomed_dIdV_filtered(Loc(1)));

%% ELECTRON TEMPERATURE----------------------------------------------------

% Limit the bounds between the floating and plasma potential and ignore the
% extreme Percent_Ignored of this region
Percent_Ignored = 0.75;
bounds = and(((Floating_Potential+Percent_Ignored/2*(Plasma_Potential-Floating_Po
↪  tential))<=voltage),(voltage<=Plasma_Potential-Percent_Ignored/2*(Plasma_Pote
↪  ntial-Floating_Potential))
↪  );
Retardation_current = Electron_current(bounds);
Retardation_voltage = voltage(bounds);

% Find the electron temperature current using a linear fit of the natural
% log of the electron retardation regime

% Define a linear function
fit_parameters_Te = [1e-10 1e-10];
linear_function_Te = @(fit_parameters_Te,Retardation_voltage)fit_parameters_Te(1)
↪  *Retardation_voltage +
↪  fit_parameters_Te(2);

% Linear fit of the log of the electron retardation regime
options = optimoptions('lsqcurvefit','TolFun',1e-30,'TolX',1e-30,'MaxFunEvals',10
↪  000,'Display','off');
fit_parameters_Te = lsqcurvefit(linear_function_Te,fit_parameters_Te,Retardation_
↪  voltage,log(Retardation_current),[],[],options);

% Find the electron saturation current
Electron_sat_current = Electron_current(voltage==Plasma_Potential);

% Calculate electron temperature from a linear fit of the natural log of
% the electron retardation regime
Electron_Temperature = 1/real(fit_parameters_Te(1));
```

```
% Calculate electron temperature from the difference between the floating and
↪  plasma potentials
Electron_Temperature_2 = (Plasma_Potential-Floating_Potential)/5.2;

% Tntegrate the EEDF for the electron temperature
% Electron_Temperature_3 =
↪  trapz(Retardation_voltage,Retardation_current)./Electron_sat_current;

%% ELECTRON DENSITY------------------------------------------------------

% Use equation 3 of [Langmuir Probe Measurements in the Ionosphere] and the
% electron saturation current
C1 = AreaLP*ec;
C2 = sqrt(ec*Electron_Temperature/(2*pi*electron_mass));
Electron_Density = Electron_sat_current/(C1*C2)*1.e-6;

%% ION DENSITY-----------------------------------------------------------

% Calculate ion density using OML [equation 2 of Langmuir Probe Measurements in
↪  the Ionosphere]
% [A study of the accuracy of various Langmuir probe theories] and [Comparative
↪  analyses of plasma probe diagnostic techniques]
% point to ion densities being over estimated.
Ion_Density = (abs(fit_parameters_ID(1))*power(pi,2)*ion_mass/(2*power(AreaLP,2)*
↪  power(ec,3))).^0.5*1.e-6;

% Calculate ion density according to [Evaluation of Langmuir probe ion
% density measurement in weakly ionized discharges using plasma oscillation
↪  probes and microwave interferometry]
% & [A floating potential method for measuring ion density]
% A = LP_D./2;
% nf = (Plasma_Potential-Floating_Potential)./(Electron_Temperature);
% B = nf.^(3/4).*sqrt(e0.*Electron_Temperature./ec);
% cs = sqrt(ec.*Electron_Temperature./ion_mass);
% IiVf =
↪  real((linear_function_ID_2(fit_parameters_ID_2,Floating_Potential)).^(3/4));
% C = IiVf./(2.*pi.*LP_L.*0.5.*cs);
% Ion_Density_2 = ((-B - sqrt(B.^2 - 4.*A.*C))./(2.*A)).^2*1.e-6;

% Grant's Equation derived using the Child-Langmuir Sheath Above
Ion_Density_3 = (abs(fit_parameters_ID_2(1))).^(3/4)./(1.12.*pi.*LP_L.*ec.*Electr
↪  on_Temperature.*sqrt(e0./(Electron_Density.*ion_mass)));

% Ion Density from ABR
% IiVf =
↪  real((linear_function_ID_2(fit_parameters_ID_2,Floating_Potential)).^(3/4));
% cs = sqrt(ec.*Electron_Temperature./ion_mass);
% DBL = sqrt(e0.*Electron_Temperature./(Electron_Density.*ec));
% Ep = LP_D./(2.*DBL);
% a = 0.607 + 2432./exp(7.01.*Ep.^0.096);
% Ion_Density_4 = abs(real(IiVf./(2.*pi.*cs.*a)))*1.e-6;

%% ION DRIFT VELOCITY----------------------------------------------------
% Calculated using equation 2 of [Langmuir Probe Measurements in the Ionosphere]
```

```
Ion_Current_at_Vp = Ion_current(dIdV_filtered==Zoomed_dIdV_filtered(Loc(1)));
Ion_Drift_Velocity = Ion_Current_at_Vp.*pi./(AreaLP.*Ion_Density.*ec.*10.^6);

%% Is fast analysis mode is off, compute the EEDF and plot relevant information
if (Fast_analysis == false)

    %% EEDF-----------------------------------------------------------------
    % Use the second derivative of the electron retardation regime to
    % create an EEDF using the Druyvesteyn technique
    EEDF_voltage = flip(Plasma_Potential - voltage);
    EEDF = flip(dIdV2_filtered);
    EEDF = EEDF(EEDF_voltage >= 0);
    EEDF_voltage = EEDF_voltage(EEDF_voltage >= 0);
    EEDF = (electron_mass.*EEDF_voltage./(2.*ec)).^0.5.*EEDF;
    EEDF = EEDF./max(EEDF);

    % Fit the EEDF with a Maxwellian [Electron Energy Distribution
    % Measurements in the Plume Region of a Low Current Hollow Cathode]
    fit_parameters_Maxwellian_init = 1;
    Maxwellian_Function = @(fit_parameters_Maxwellian,EEDF_voltage) sqrt(EEDF_vol
    ↪  tage)./(fit_parameters_Maxwellian(1)).^(-3./2).*exp(-EEDF_voltage./fit_pa
    ↪  rameters_Maxwellian(1))./max(sqrt(EEDF_voltage)./(fit_parameters_Maxwelli
    ↪  an(1)).^(-3./2).*exp(-EEDF_voltage./fit_parameters_Maxwellian(1)));
    fit_parameters_Maxwellian = lsqcurvefit(Maxwellian_Function,fit_parameters_Ma
    ↪  xwellian_init,EEDF_voltage,EEDF,[],[],options);

    % Fit the EEDF with a Druyvesteyn [Electron Energy Distribution
    % Measurements in the Plume Region of a Low Current Hollow Cathode]
    fit_parameters_Druyvesteyn_init = 1;
    Druyvesteyn_Function = @(fit_parameters_Druyvesteyn,EEDF_voltage)
    ↪  sqrt(EEDF_voltage)./(fit_parameters_Druyvesteyn(1)).^(-3./2).*exp(-0.243.
    ↪  *(EEDF_voltage./fit_parameters_Druyvesteyn(1)).^2)./max(sqrt(EEDF_voltage
    ↪  )./(fit_parameters_Druyvesteyn(1)).^(-3./2).*exp(-0.243.*(EEDF_voltage./f
    ↪  it_parameters_Druyvesteyn(1)).^2));
    fit_parameters_Druyvesteyn = lsqcurvefit(Druyvesteyn_Function,fit_parameters_
    ↪  Druyvesteyn_init,EEDF_voltage,EEDF,[],[],options);

    %% Plot all figures
    % Plot Raw and Filtered Data
    figure(2)
    hold on;
    plot(voltage,current,voltage,current_filtered,'Linewidth',1.5);
    current_temp = current_filtered(Range);
    plot(Plasma_Potential,current_temp(Loc(1)),'Ok')
    title('I-V Curve');
    xlabel('Applied Voltage (V)');
    ylabel('Collected Current (A)');
    legend({'Example Raw Measurement','Example Filtered Measurement','Plasma
    ↪  Potential'},'Location','best')
    set(gca,'fontsize',14,'fontweight','bold');
    hold off;

    % Plot of I^2 vs V and fits
    figure(3)
```

```
hold on;
scatter(voltage,current_filtered.^(2),3);
plot(voltage,-linear_function_ID(fit_parameters_ID,voltage),'LineWidth',1.5);
title({'OML Ion Current Squared','Fit Check'});
xlabel('Applied Voltage (V)');
ylabel('Ion Current Squared (A^2)');
legend({'Raw Current Squared','Linear Fit'},'Location','best')
set(gca,'fontsize',14,'fontweight','bold');
hold off;

% Plot of I^4/3 vs V and fits
figure(4)
hold on;
plot(voltage,-current_filtered.^(4/3),voltage,linear_function_ID_2(fit_parame
↪  ters_ID_2,voltage),'LineWidth',1.5);
title({'SCL Sheath Linear','Fit Check'});
xlabel('Applied Voltage (V)');
ylabel('Ion Current to the 4/3 (A)');
legend({'Raw','Fit'},'Location','best')
set(gca,'fontsize',14,'fontweight','bold');
hold off;

% Plot of Electron Current
figure(5)
hold on
plot(voltage,current_filtered,voltage,Electron_current,voltage,Ion_current,'L
↪  ineWidth',1.5);
title('Electron Current')
xlabel('Applied Voltage (V)');
ylabel('Collected Current (A)');
legend({'Filtered Current','Calculated Electron Current','Calculated Ion
↪  Current'},'Location','best')
set(gca,'fontsize',14,'fontweight','bold');
hold off

%Plot Electron Temperature Fit Region
figure(6)
hold on;
scatter(Retardation_voltage,log(Retardation_current));
plot(Retardation_voltage,linear_function_Te(fit_parameters_Te,Retardation_vol
↪  tage),'LineWidth',2);
title({'Retardation Regime Fit','for Electron Temperature'});
xlabel('Applied Voltage (V)');
ylabel('ln(Collected Current) (A)');
legend({'ln(Current Measurement)','Linear Fit'},'Location','best')
set(gca,'fontsize',14,'fontweight','bold');
hold off;

% Plotting the plasma potential on dIdV
figure(7)
hold on;
plot(voltage(Range),Norm_Zoomed_dIdV_filtered,'LineWidth',1.5);
plot(Plasma_Potential,Norm_Zoomed_dIdV_filtered(Loc(1)),'Ok')
title({'Derivative of I-V Sweep','with Plasma Potential'});
```

```
    xlabel('Applied Voltage (V)');
    ylabel('A.U.');
    legend({'First Derivative (dI/dV)','Plasma Potential'},'Location','best')
    set(gca,'fontsize',14,'fontweight','bold');
    hold off;

    % Plot all EEDFs in one figure
    figure(8)
    hold on;
    scatter(EEDF_voltage,EEDF,20,'filled');
    plot(EEDF_voltage,real(Maxwellian_Function(fit_parameters_Maxwellian,EEDF_vol
    ↪ tage)),'LineWidth',2);
    plot(EEDF_voltage,real(Druyvesteyn_Function(fit_parameters_Druyvesteyn,EEDF_v
    ↪ oltage)),'LineWidth',2);
    title({'Normalized EEDF from I-V Sweep','with Maxwellian and Dreyvesteyn
    ↪ Fits'});
    xlabel('Electron Energy (eV)');
    ylabel('A. U.');
    legend({'Normalized EEDF','Maxwellian Fit','Druyvesteyn
    ↪ Fit'},'Location','best')
    set(gca,'fontsize',14,'fontweight','bold');
    hold off;
end
end
```

APPENDIX D

MATLAB Raw Scaling Law Analysis Procedure

```
% Grant Miars
clear all;
close all;

%% Define Constants
u = 1.66e-27; % amu to kg
me = 9.10938e-31; % Mass of electron in kg
ec = 1.6e-19; % Elementary charge
kb = 1.38e-23; % Boltzmann constant

%% Enter Parameters

% Define the initial number of points in the sweep
num_points = 101;

% Enter keeper currents and gas flow rates we are interested in comparing
keeper_current_array = [0.9 1 1.1 1.2 1.3];
flow_rate_array = [0.5 1 2];
mi_array = [39.95*u 83.8*u 131.29*u];

% Plots for specific sweep number
sweep_num = 100;

%% Choosing File and Figure Location
data_directory = 'C:\Users\Owner\Google Drive\CONNEX Experiments\Data\Fall 2018
↪  EDA Testing\';

file_name1 = 'Argon_*'; % The asterisk is very important!
file_name2 = 'Krypton_*'; % The asterisk is very important!
file_name3 = 'Xenon_*'; % The asterisk is very important!
files1 = dir(horzcat(data_directory,file_name1));
files2 = dir(horzcat(data_directory,file_name2));
files3 = dir(horzcat(data_directory,file_name3));
num_files1 = length(files1);
num_files2 = length(files2);
num_files3 = length(files3);
```

```
total_num_files = num_files1 + num_files2 + num_files3;

%% Parse initial data

% Parse data from Argon files
for i=1:num_files1
    % Reading the files
    full_directory1 = horzcat(data_directory,files1(i).name);
    data1 = read_file(full_directory1);

    % Get universal data for each sweep
    keeper_voltage(i,1) = data1('Discharge_voltage');
    keeper_current(i,1) = data1('Discharge_current');
    flow_rate(i,1) = data1('Flow_rate');
    pressure(i,1) = data1('Pressure');

    % Get voltage and current data for each sweep
    tempvolt = values(data1,{'Voltage'});
    voltage(:,i) = linspace(0,0,length(tempvolt{1,1}(:,1)));
    voltage(:,i) = voltage(:,i) + tempvolt{1,1}(:,1);
    tempcurrent = values(data1,{'Current'});
    current(:,i) = linspace(0,0,length(tempcurrent{1,1}(:,1)));
    current(:,i) = current(:,i) + tempcurrent{1,1}(:,1);

    % Mass of Argon in kg
    mi(i,1) = 39.95*u;
end

% Parse data from Krypton files
for i=1:num_files2
    % Reading the files
    full_directory2 = horzcat(data_directory,files2(i).name);
    data2 = read_file(full_directory2);

    % Get universal data for each sweep
    keeper_voltage(i+num_files1,1) = data2('Discharge_voltage');
    keeper_current(i+num_files1,1) = data2('Discharge_current');
    flow_rate(i+num_files1,1) = data2('Flow_rate');
    pressure(i+num_files1,1) = data2('Pressure');

    % Get voltage and current data for each sweep
    tempvolt = values(data2,{'Voltage'});
    voltage(:,i+num_files1) = linspace(0,0,length(tempvolt{1,1}(:,1)));
    voltage(:,i+num_files1) = voltage(:,i+num_files1) + tempvolt{1,1}(:,1);
    tempcurrent = values(data2,{'Current'});
    current(:,i+num_files1) = linspace(0,0,length(tempcurrent{1,1}(:,1)));
    current(:,i+num_files1) = current(:,i+num_files1) + tempcurrent{1,1}(:,1);

    % Mass of Krypton in kg
    mi(i+num_files1,1) = 83.8*u;
end

% Parse data from Xenon files
for i=1:num_files3
```

```
    % Reading the files
    full_directory3 = horzcat(data_directory,files3(i).name);
    data3 = read_file(full_directory3);

    % Get universal data for each sweep
    keeper_voltage(i+num_files1+num_files2,1) = data3('Discharge_voltage');
    keeper_current(i+num_files1+num_files2,1) = data3('Discharge_current');
    flow_rate(i+num_files1+num_files2,1) = data3('Flow_rate');
    pressure(i+num_files1+num_files2,1) = data3('Pressure');

    % Get voltage and current data for each sweep
    tempvolt = values(data3,{'Voltage'});
    voltage(:,i+num_files1+num_files2) = linspace(0,0,length(tempvolt{1,1}(:,1)));
    voltage(:,i+num_files1+num_files2) = voltage(:,i+num_files1+num_files2) +
    ↪  tempvolt{1,1}(:,1);
    tempcurrent = values(data3,{'Current'});
    current(:,i+num_files1+num_files2) =
    ↪  linspace(0,0,length(tempcurrent{1,1}(:,1)));
    current(:,i+num_files1+num_files2) = current(:,i+num_files1+num_files2) +
    ↪  tempcurrent{1,1}(:,1);

    % Mass of Xenon in kg
    mi(i+num_files1+num_files2,1) = 131.29*u;
end

% Find the discharge power of each sweep
keeper_power = keeper_current.*keeper_voltage;

%% Do data analysis common to all files
for i=1:total_num_files
    %% Remove range finding points introduced by Keithley 2400
    % Identify the points to ignore based on when the voltage is decreasing
    for j=1:num_points
        if(j<15)
            valid_point_array(j,i) = voltage(j+1,i) > voltage(j,i);
        else
            valid_point_array(j,i) = 1;
        end
    end

    % Delete low current points from both voltage and current arrays
    current(:,i) = current(:,i).*valid_point_array(:,i);
    voltage(:,i) = voltage(:,i).*valid_point_array(:,i);
    current(current == 0) = NaN;
    voltage(voltage == 0) = NaN;

    %% Find specific points in the parsed data for each sweep in order to define
    ↪  a power law fit region

    % Find the maximum Beam Current measured
    max_current(i,1) = max(current(:,i));

    % Find the expellant utilization using the maximum Beam Current
    expellant_utilization(i,1) = 100*max_current(i,1)./(0.071745*flow_rate(i,1));
```

```
% Find the approximate floating potential index
[~,floating_potential_index(i,1)] = min(abs(current(:,i)));

% Find the floating potential
floating_potential(i,1) = voltage(floating_potential_index(i,1),i);

%% Set the sweep fit voltage range minimum and maximums to go from the
↪  floating potential to the maximum voltage
fit_min(i,1) = floating_potential_index(i,1);%min(find(valid_point_array(:,i)
↪  == 1));
fit_max(i,1) = num_points;

% Truncate to just include this fit region
fit_voltage(1:fit_max(i,1) - fit_min(i,1) + 1,i) =
↪  voltage((fit_min(i,1):fit_max(i,1)),i);
fit_current(1:fit_max(i,1) - fit_min(i,1) + 1,i) =
↪  current((fit_min(i,1):fit_max(i,1)),i);

% Shift voltages and currents to start at zero
fit_voltage(1:fit_max(i,1) - fit_min(i,1) + 1,i) = fit_voltage(1:fit_max(i,1)
↪  - fit_min(i,1) + 1,i) - min(fit_voltage(1:fit_max(i,1) - fit_min(i,1) +
↪  1,i));
fit_current(1:fit_max(i,1) - fit_min(i,1) + 1,i) = fit_current(1:fit_max(i,1)
↪  - fit_min(i,1) + 1,i) - min(fit_current(1:fit_max(i,1) - fit_min(i,1) +
↪  1,i));

% Remove the NaN values
x = rmmissing(fit_current(1:fit_max(i,1) - fit_min(i,1) + 1,i));
y = rmmissing(fit_voltage(1:fit_max(i,1) - fit_min(i,1) + 1,i));

%% Find relevant points in the fit data set
% Define the contactor current as the maximum of these fit currents
contactor_current(i,1) = max(fit_current(:,i));

% Find the approximate voltage for Ibeam = 0.25*Icontactor
[~,quarter_current_index(i,1)] =
↪  min(abs(fit_current(:,i)./contactor_current(i,1)-0.25));
quarter_current_voltage(i,1) = fit_voltage(quarter_current_index(i,1),i);

% Find the approximate voltage for Ibeam = 0.5*Icontactor
[~,half_current_index(i,1)] =
↪  min(abs(fit_current(:,i)./contactor_current(i,1)-0.5));
half_current_voltage(i,1) = fit_voltage(half_current_index(i,1),i);

%% Define and perform an power law fit of the prepared sweep data
% Define the custom equation we are fitting to
power_eqn = fittype('a.*x.^b');

% Select boundaries for fitting parameters
warning off;
options = fitoptions(power_eqn);
options.Lower = [1000000 0];
options.Upper = [1000000000 3];
```

```
options.TolFun = 1e-30;

% Use these options for even more accurate (and slow) fits
options.Robust = 'LAR';
options.TolX = 10^-30;
options.MaxFunEvals = 1000;
options.MaxIter = 1000;

% Perform the fit and save relevant values
[f,gof] = fit(x,y,power_eqn,options);
ion_emit_multiplier(i,1) = f.a;
ion_emit_power(i,1) = f.b;
corrcoef_array = corrcoef(rmmissing(fit_current(:,i)),rmmissing(ion_emit_mult
↪  iplier(i,1).*(fit_voltage(:,i).^ion_emit_exponent(i,1))));
rsquared(i,1) = corrcoef_array(2,1).^2;

%% Generate an array of ion emit powers and R-squared values when using
↪  different keeper current and gas flow rate values
% Argon matrix
if((0 < i) && (i < 55))
   Argon_ion_emit_power(find(keeper_current(i,1) ==
   ↪  keeper_current_array),find(flow_rate(i,1) == flow_rate_array)) =
   ↪  ion_emit_power(i,1);
   Argon_rsquared(find(keeper_current(i,1) ==
   ↪  keeper_current_array),find(flow_rate(i,1) == flow_rate_array)) =
   ↪  rsquared(i,1);
   Argon_contactor_current(find(keeper_current(i,1) ==
   ↪  keeper_current_array),find(flow_rate(i,1) == flow_rate_array)) =
   ↪  contactor_current(i,1);
   Argon_half_current_voltage(find(keeper_current(i,1) ==
   ↪  keeper_current_array),find(flow_rate(i,1) == flow_rate_array)) =
   ↪  half_current_voltage(i,1);
% Krypton matrix
elseif((54 < i) && (i < 128))
   Krypton_ion_emit_power(find(keeper_current(i,1) ==
   ↪  keeper_current_array),find(flow_rate(i,1) == flow_rate_array)) =
   ↪  ion_emit_power(i,1);
   Krypton_rsquared(find(keeper_current(i,1) ==
   ↪  keeper_current_array),find(flow_rate(i,1) == flow_rate_array)) =
   ↪  rsquared(i,1);
   Krypton_contactor_current(find(keeper_current(i,1) ==
   ↪  keeper_current_array),find(flow_rate(i,1) == flow_rate_array)) =
   ↪  contactor_current(i,1);
   Krypton_half_current_voltage(find(keeper_current(i,1) ==
   ↪  keeper_current_array),find(flow_rate(i,1) == flow_rate_array)) =
   ↪  half_current_voltage(i,1);
% Xenon matrix
else
   Xenon_ion_emit_power(find(keeper_current(i,1) ==
   ↪  keeper_current_array),find(flow_rate(i,1) == flow_rate_array)) =
   ↪  ion_emit_power(i,1);
   Xenon_rsquared(find(keeper_current(i,1) ==
   ↪  keeper_current_array),find(flow_rate(i,1) == flow_rate_array)) =
   ↪  rsquared(i,1);
```

```
   Xenon_contactor_current(find(keeper_current(i,1) ==
   ↪  keeper_current_array),find(flow_rate(i,1) == flow_rate_array)) =
   ↪  contactor_current(i,1);
   Xenon_half_current_voltage(find(keeper_current(i,1) ==
   ↪  keeper_current_array),find(flow_rate(i,1) == flow_rate_array)) =
   ↪  half_current_voltage(i,1);
end

%% Generate vectors of data with only common configuration keeper current and
↪  gas flow rate values
if(ismember(keeper_current(i,1),keeper_current_array) &&
↪  ismember(flow_rate(i,1),flow_rate_array))
    common_ion_emit_power(i,1) = ion_emit_power(i,1);
    common_rsquared(i,1) = rsquared(i,1);
    common_contactor_current(i,1) = contactor_current(i,1);
    common_half_current_voltage(i,1) = half_current_voltage(i,1);
    common_pressure(i,1) = pressure(i,1);
    common_floating_potential(i,1) = floating_potential(i,1);
    common_expellant_utilization(i,1) = expellant_utilization(i,1);
    common_keeper_current(i,1) = keeper_current(i,1);
    common_keeper_voltage(i,1) = keeper_voltage(i,1);
    common_keeper_power(i,1) = keeper_power(i,1);
    common_flow_rate(i,1) = flow_rate(i,1);
else
    common_ion_emit_power(i,1) = NaN;
    common_rsquared(i,1) = NaN;
    common_contactor_current(i,1) = NaN;
    common_half_current_voltage(i,1) = NaN;
    common_pressure(i,1) = NaN;
    common_floating_potential(i,1) = NaN;
    common_expellant_utilization(i,1) = NaN;
    common_keeper_current(i,1) = NaN;
    common_keeper_voltage(i,1) = NaN;
    common_keeper_power(i,1) = NaN;
    common_flow_rate(i,1) = NaN;
end

%% Generate mass specific arrays of data with only common configuration
↪  keeper current and gas flow rate values
% Argon matrix
if((0 < i) && (i < num_files1 + 1))
   common_Argon_ion_emit_power(find(keeper_current(i,1) ==
   ↪  keeper_current_array),find(flow_rate(i,1) == flow_rate_array)) =
   ↪  ion_emit_power(i,1);
   common_Argon_rsquared(find(keeper_current(i,1) ==
   ↪  keeper_current_array),find(flow_rate(i,1) == flow_rate_array)) =
   ↪  rsquared(i,1);
   common_Argon_contactor_current(find(keeper_current(i,1) ==
   ↪  keeper_current_array),find(flow_rate(i,1) == flow_rate_array)) =
   ↪  contactor_current(i,1);
   common_Argon_half_current_voltage(find(keeper_current(i,1) ==
   ↪  keeper_current_array),find(flow_rate(i,1) == flow_rate_array)) =
   ↪  half_current_voltage(i,1);
% Krypton matrix
```

```
    elseif((num_files1 < i) && (i < num_files1 + num_files2 + 1))
       common_Krypton_ion_emit_power(find(keeper_current(i,1) ==
       ↪  keeper_current_array),find(flow_rate(i,1) == flow_rate_array)) =
       ↪  ion_emit_power(i,1);
       common_Krypton_rsquared(find(keeper_current(i,1) ==
       ↪  keeper_current_array),find(flow_rate(i,1) == flow_rate_array)) =
       ↪  rsquared(i,1);
       common_Krypton_contactor_current(find(keeper_current(i,1) ==
       ↪  keeper_current_array),find(flow_rate(i,1) == flow_rate_array)) =
       ↪  contactor_current(i,1);
       common_Krypton_half_current_voltage(find(keeper_current(i,1) ==
       ↪  keeper_current_array),find(flow_rate(i,1) == flow_rate_array)) =
       ↪  half_current_voltage(i,1);
    % Xenon matrix
    else
       common_Xenon_ion_emit_power(find(keeper_current(i,1) ==
       ↪  keeper_current_array),find(flow_rate(i,1) == flow_rate_array)) =
       ↪  ion_emit_power(i,1);
       common_Xenon_rsquared(find(keeper_current(i,1) ==
       ↪  keeper_current_array),find(flow_rate(i,1) == flow_rate_array)) =
       ↪  rsquared(i,1);
       common_Xenon_contactor_current(find(keeper_current(i,1) ==
       ↪  keeper_current_array),find(flow_rate(i,1) == flow_rate_array)) =
       ↪  contactor_current(i,1);
       common_Xenon_half_current_voltage(find(keeper_current(i,1) ==
       ↪  keeper_current_array),find(flow_rate(i,1) == flow_rate_array)) =
       ↪  half_current_voltage(i,1);
    end

end

%% Remove nonsensical values from the power law goodness of fit arrays
cleaned_rsquared = rsquared;
cleaned_rsquared(abs(rsquared) > 1) = NaN;
nanmean(cleaned_rsquared)

cleaned_Argon_rsquared =  Argon_rsquared;
cleaned_Argon_rsquared(abs(cleaned_Argon_rsquared) > 1) = NaN;

cleaned_Krypton_rsquared =  Krypton_rsquared;
cleaned_Krypton_rsquared(abs(cleaned_Krypton_rsquared) > 1) = NaN;

cleaned_Xenon_rsquared =  Xenon_rsquared;
cleaned_Xenon_rsquared(abs(cleaned_Xenon_rsquared) > 1) = NaN;

%% Create an array of average ion emit powers and electron temperatures varying
↪  just ion mass and flow rate
for i=1:length(flow_rate_array)
    avg_ion_emit_power(1,i) = nanmean(Argon_ion_emit_power(:,i));
    avg_ion_emit_power(2,i) = nanmean(Krypton_ion_emit_power(:,i));
    avg_ion_emit_power(3,i) = nanmean(Xenon_ion_emit_power(:,i));

    avg_rsquared(1,i) = nanmean(cleaned_Argon_rsquared(:,i));
    avg_rsquared(2,i) = nanmean(cleaned_Krypton_rsquared(:,i));
```

```
    avg_rsquared(3,i) = nanmean(cleaned_Xenon_rsquared(:,i));

    avg_contactor_current(1,i) = nanmean(Argon_contactor_current(:,i));
    avg_contactor_current(2,i) = nanmean(Krypton_contactor_current(:,i));
    avg_contactor_current(3,i) = nanmean(Xenon_contactor_current(:,i));

    avg_half_voltage_current(1,i) = nanmean(Argon_half_current_voltage(:,i));
    avg_half_voltage_current(2,i) = nanmean(Krypton_half_current_voltage(:,i));
    avg_half_voltage_current(3,i) = nanmean(Xenon_half_current_voltage(:,i));
end

%% Average parameters according to ion mass
% Average half current voltages for each unique mass type
avg_Argon_half_current_voltage = nanmean(half_current_voltage(1:num_files1,1));
avg_Krypton_half_current_voltage =
↪  nanmean(half_current_voltage(num_files1+1:num_files1+num_files2,1));
avg_Xenon_half_current_voltage = nanmean(half_current_voltage(num_files1+num_file⌋
↪  s2+1:num_files1+num_files2+num_files3,1));

% Average Keeper Voltage for each unique mass type
avg_Argon_keeper_voltage = nanmean(keeper_voltage(1:num_files1,1));
avg_Krypton_keeper_voltage =
↪  nanmean(keeper_voltage(num_files1+1:num_files1+num_files2,1));
avg_Xenon_keeper_voltage = nanmean(keeper_voltage(num_files1+num_files2+1:num_fil⌋
↪  es1+num_files2+num_files3,1));

% Average the floating potential for each unique mass type
avg_Argon_floating_potential = nanmean(floating_potential(1:num_files1,1));
avg_Krypton_floating_potential =
↪  nanmean(floating_potential(num_files1+1:num_files1+num_files2,1));
avg_Xenon_floating_potential = nanmean(floating_potential(num_files1+num_files2+1⌋
↪  :num_files1+num_files2+num_files3,1));

% Average contactor currents for each unique mass type
avg_Argon_contactor_current = nanmean(contactor_current(1:num_files1,1));
avg_Krypton_contactor_current =
↪  nanmean(contactor_current(num_files1+1:num_files1+num_files2,1));
avg_Xenon_contactor_current = nanmean(contactor_current(num_files1+num_files2+1:n⌋
↪  um_files1+num_files2+num_files3,1));

% Average power law exponent for each unique mass type
avg_Argon_ion_emit_power = nanmean(ion_emit_power(1:num_files1,1));
avg_Krypton_ion_emit_power =
↪  nanmean(ion_emit_power(num_files1+1:num_files1+num_files2,1));
avg_Xenon_ion_emit_power = nanmean(ion_emit_power(num_files1+num_files2+1:num_fil⌋
↪  es1+num_files2+num_files3,1));

% Average the floating potential for each unique mass type using common
% configurations
avg_common_Argon_half_current_voltage =
↪  nanmean(nanmean(Argon_half_current_voltage));
avg_common_Krypton_half_current_voltage =
↪  nanmean(nanmean(Krypton_half_current_voltage));
```

```
avg_common_Xenon_half_current_voltage =
↪  nanmean(nanmean(Xenon_half_current_voltage));

%% Perform a power fit of contactor current versus half current voltage and ion
↪  mass versus half current voltage
% Define the custom equation we are fitting to
power_eqn = fittype('a.*x.^b+c');

% Select boundaries for fitting parameters
warning off;
options = fitoptions(power_eqn);
options.Lower = [0 -10 0];
options.Upper = [1000 10 0];
options.TolFun = 1e-30;

% Fit the Cathode Potential scaling with contactor current
f = fit(contactor_current,half_current_voltage,power_eqn,options);

% Fit the Cathode Potential scaling with ion mass
g = fit((mi_array'./u),[avg_Argon_half_current_voltage;avg_Krypton_half_current_v
↪  oltage;avg_Xenon_half_current_voltage],power_eqn,options);

%% Calculate the ion emit power array using values and division
ion_emit_power_2 = log(half_current_voltage./quarter_current_voltage)./log(2);

% Remove values from the ion emit power array if they don't have enough
% points in the fit region or create infinities
ion_emit_power_2((quarter_current_voltage == 0)) = NaN; % | (half_current_index -
↪  floating_potential_index < min_fit_points)) = NaN;

%% Create arrays for smooth plotting
continuous_mi_array = linspace(min(mi_array),max(mi_array),1000)./u;
continuous_contactor_current_array =
↪  linspace(min(contactor_current),max(contactor_current),1000);

%% Plot Data

close all;

figure();
hold on;

scatter([39.95 83.8 131.29],[avg_Argon_half_current_voltage
↪  avg_Krypton_half_current_voltage
↪  avg_Xenon_half_current_voltage],100,'filled');
plot(continuous_mi_array,g.a.*(continuous_mi_array).^g.b+g.c,'LineWidth',3);

str = strcat('Power Law Fit Exponent: ',num2str(round(g.b,2)));
title({'Average Cathode Potential Scaling w/ Ion Mass','Beam Current =
↪  0.5*Contactor Current',str});
xlabel('Ion Mass [amu]');
ylabel({'Average Cathode Potential','(Relative to Floating) [V]'});
set(gca,'fontsize',14,'fontweight','bold');
```

```
h_legend = legend('Experimental Data','Power Law Fit: \psi_{SC} \alpha
↪  m_{i}^{\beta}','Location','best','Interpreter','tex');
set(h_legend,'fontweight','bold','fontsize',14);
hold off;

figure()
hold on;

scatter(contactor_current.*10^6,half_current_voltage,20,'filled');
plot(continuous_contactor_current_array.*10^6,f.a.*(continuous_contactor_current_
↪  array).^f.b+f.c,'LineWidth',3);

str = strcat('Power Law Fit Exponent: ',num2str(round(f.b,2)));
title({'Cathode Potential Scaling w/ Contactor Current','Beam Current =
↪  0.5*Contactor Current',str});
xlabel('Contactor Current [uA]');
ylabel({'Cathode Potential','(Relative to Floating) [V]'});
%axis([0 1 0 30]);
h_legend = legend('Experimental Data','Power Law Fit: \psi_{SC} \alpha
↪  I_{contactor}^{\beta}','Location','best','Interpreter','tex');
set(h_legend,'fontweight','bold','fontsize',14);
set(gca,'fontsize',14,'fontweight','bold');
hold off;

figure();
hold on;
histogram(ion_emit_power,50);
str = strcat('Average Fit Exponent:',num2str(round(nanmean(ion_emit_power),2)));
title({'Cathode Potential Scaling','with Beam Current','Exponent Histogram using
↪  Fits',str});
xlabel('Power Law Fit Exponent');
ylabel('Number of Sweeps');
set(gca,'fontsize',14,'fontweight','bold');
hold off;

figure();
hold on;
histogram(ion_emit_power_2,50);
str = strcat('Average Fit Exponent:',num2str(round(nanmean(ion_emit_power_2),2)));
title({'Cathode Potential Scaling with Beam Current','Power Law Exponent
↪  Histogram using Two Points',str});
xlabel('Power Law Exponent');
ylabel('Number of Configurations');
set(gca,'fontsize',14,'fontweight','bold');
hold off;

% sweep_num = 143;
%
% figure()
% hold on;
%
% scatter((fit_current(1:fit_max(sweep_num,1) - fit_min(sweep_num,1) + 1,sweep_nu
↪  m))./contactor_current(sweep_num,1),fit_voltage(1:fit_max(sweep_num,1) -
↪  fit_min(sweep_num,1) + 1,sweep_num),20,'filled');
```

```
% title({'Determining Cathode Potential when','Beam Current = 0.5 Contactor
↪  Current &','Beam Current = 0.25 Contactor Current'});
% xlabel('Beam Current/Contactor Current');
% ylabel({'Cathode Potential','(Relative to Floating) [V]'});
% ax = gca;
% set(gca,'fontsize',14,'fontweight','bold');
% hold off;

% %% Plot all raw common configuration sweeps
% for k = 1:total_num_files %num_sweep_range_min:sweep_range_max
%
%     if(~isnan(common_keeper_current(k,1)))
%         %k = 159;
%         figure
%         hold on;
%         scatter(10.^6.*(fit_current(1:fit_max(k,1) - fit_min(k,1) +
↪  1,k)),fit_voltage(1:fit_max(k,1) - fit_min(k,1) + 1,k),20,'filled');
%         str = strcat('Sweep Number=',num2str(k));
%         str2 = strcat('Ion Mass= ',num2str(round(mi(k,1)./u,0)),' Keeper
↪  Current= ',num2str(round(keeper_current(k,1),1)),' Flow Rate=
↪  ',num2str(round(flow_rate(k,1),2)));
%         str3 = strcat('Power Law Exponent using Two
↪  Points=',num2str(round(ion_emit_power_2(k,1),2)));
%         title({'Fit Region Data',str,str2,str3});
%         xlabel('Beam Current [uA]');
%         ylabel({'Cathode Potential','(Relative to Floating) [V]'});
%         set(gca,'fontsize',14,'fontweight','bold');
%         hold off;
%     end
% end

%% Plot all raw common configuration sweeps with power law fit
for k = 1:total_num_files %num_sweep_range_min:sweep_range_max

    if(~isnan(common_keeper_current(k,1)))

        % Compute the power law voltage for a specific sweep
        voltage_fit = ion_emit_multiplier(k,1).*fit_current(1:fit_max(k,1) -
        ↪  fit_min(k,1) + 1,k).^ion_emit_power(k,1);

        figure
        hold on;
        scatter(10.^6.*(fit_current(1:fit_max(k,1) - fit_min(k,1) +
        ↪  1,k)),fit_voltage(1:fit_max(k,1) - fit_min(k,1) + 1,k),20,'filled');
        plot(10.^6.*(fit_current(1:fit_max(k,1) - fit_min(k,1) +
        ↪  1,k)),voltage_fit,'LineWidth',3);
        str = strcat('Sweep Number=',num2str(k));
        str2 = strcat('Ion Mass= ',num2str(round(mi(k,1)./u,0)),' Keeper Current=
        ↪  ',num2str(round(keeper_current(k,1),1)),' Flow Rate=
        ↪  ',num2str(round(flow_rate(k,1),2)));
        str3 = strcat('Power Law Fit
        ↪  Exponent=',num2str(round(ion_emit_power(k,1),2)));
        str4 = strcat('R-Squared Value=',num2str(round(rsquared(k,1),3)));
        title({'Fit Region Data w/ Power Law Fit',str,str2,str3,str4});
```

```
        xlabel('Beam Current [uA]');
        ylabel({'Cathode Potential','(Relative to Floating) [V]'});
        %axis([0 1.1.*10.^6.*max(current_fit_shifted(:,1)) 0 20]);
        h_legend = legend('Experimental Data','Power Law Fit: \psi_{SC} \alpha
        ↪  I_{beam}^{\beta}','Location','best','Interpreter','tex');
        set(h_legend,'fontweight','bold','fontsize',14);
        set(gca,'fontsize',14,'fontweight','bold');
        hold off;
    end
end

figure()
hold on;

scatter(voltage(:,sweep_num),current(:,sweep_num),20,'filled','r');

title({'Beam Current Measurement'});
xlabel('Cathode Bias w.r.t. Chamber Wall [V]');
ylabel({'Emitted Ion Current [mA]'});
%axis([0 700 3 18]);
ax = gca;
set(gca,'fontsize',14,'fontweight','bold');
hold off;


figure()
hold on;

scatter(pressure,half_current_voltage,20,'filled','r');

str = strcat('Correlation Coefficient =
↪  ',num2str(round(min(min(corrcoef(pressure,half_current_voltage))),2)));
title({'Cathode Potential Scaling w/ Chamber Pressure','Beam Current = 0.5
↪  Contactor Current',str});
xlabel('Pressure [uTorr]');
ylabel({'Cathode Potential','(Relative to Floating) [V]'});
%axis([0 700 3 18]);
ax = gca;
set(gca,'fontsize',14,'fontweight','bold');
hold off;

figure()
hold on;

scatter(floating_potential,half_current_voltage,20,'filled','r');

str = strcat('Correlation Coefficient = ',num2str(round(min(min(corrcoef(floating⌋
↪  _potential,half_current_voltage))),2)));
title({'Cathode Potential Scaling w/ Floating Potential','Beam Current = 0.5
↪  Contactor Current',str});
xlabel('Floating Potential [V]');
ylabel({'Cathode Potential','(Relative to Floating) [V]'});
%axis([0 700 3 18]);
ax = gca;
```

```
set(gca,'fontsize',14,'fontweight','bold');
hold off;

% figure()
% hold on;
%
% scatter(expellant_utilization,half_current_voltage,20,'filled','r');
%
% str = strcat('Correlation Coefficient = ',num2str(round(min(min(corrcoef(expell
↪  ant_utilization,half_current_voltage))),2)));
% title({'Cathode Potential Scaling w/ Expellant Utilization','Beam Current = 0.5
↪  Contactor Current',str});
% xlabel('Expellant Utilization [%]');
% ylabel({'Cathode Potential','(Relative to Floating) [V]'});
% %axis([0 700 3 18]);
% ax = gca;
% set(gca,'fontsize',14,'fontweight','bold');
% hold off;

figure()
hold on;

scatter(flow_rate,pressure,20,'filled','r');

str = strcat('Correlation Coefficient =
↪  ',num2str(round(min(min(corrcoef(flow_rate,pressure))),2)));
title({'Chamber Pressure Scaling w/ Flow Rate',str});
xlabel('Flow Rate [sccm]');
ylabel({'Chamber Pressure [uTorr]'});
%axis([0 700 3 18]);
ax = gca;
set(gca,'fontsize',14,'fontweight','bold');
hold off;
```

APPENDIX E

MATLAB Scaling Law Analysis Procedure with Exponential Fitting

```
% Grant Miars
clear all;

%% Enter Parameters

% Define the initial number of points in the sweep
num_points = 101;

% Enter keeper currents and gas flow rates we are interested in comparing
discharge_current_array = [0.9 1 1.1 1.2 1.3];
flow_rate_array = [0.5 1 2];

% Plots for specific sweep number
sweep_num = 1;
sweep_range_min = 1;
sweep_range_max = 0;

%% Define Constants
u = 1.66e-27; % amu to kg
me = 9.10938e-31; % Mass of electron in kg
ec = 1.6e-19; % Elementary charge
kb = 1.38e-23; % Boltzmann constant
mi_array = [39.95*u 83.8*u 131.29*u]; % Ion masses
Ei_array = [15.76 14.00 12.13]; % Ionization Energies

% Charge Exchange Cross Sections from:
% Electron Energy Distribution Measurements in the Plume Region of a Low Current
↪  Hollow Cathode (Argon)
% Krypton charge exchange cross sections for Hall effect thruster models (Krypton)
% Xenon charge exchange cross sections for electrostatic thruster models (Xenon)
CEX_cross_section_array = [4.*10^-19 10^-18 2.*10^-18];

% Impact Ionization Mean Free Paths
% Peak used for consistency
```

```
% An update of argon inelastic cross sections for plasma discharges (Argon)
% Electron-impact ionization of all ionization stages of krypton (Krypton)
% Fundamentals of Electric Propulsion (Xenon)
Ionization_cross_section_array = [3.*10.^-20 2.*10.^-20 4.*10^-20];

% Electron-Neutral Mean Free Paths
% Peak used for consistency
% Comparisons of sets of electron-neutral scattering cross sections and swarm
↪  parameters in noble gases Argon
% Comparisons of sets of electron-neutral scattering cross sections and swarm
↪  parameters in noble gases Krypton and Xenon
EN_cross_section_array = [1.2.*10.^-19 1.6.*10.^-19 3.*10.^-19];

%% Choosing File and Figure Location
data_directory = 'C:\Users\Owner\Google Drive\CONNEX Experiments\Data\Fall 2018
↪  EDA Testing\';

file_name1 = 'Argon_*'; % The asterisk is very important!
file_name2 = 'Krypton_*'; % The asterisk is very important!
file_name3 = 'Xenon_*'; % The asterisk is very important!
files1 = dir(horzcat(data_directory,file_name1));
files2 = dir(horzcat(data_directory,file_name2));
files3 = dir(horzcat(data_directory,file_name3));
num_files1 = length(files1);
num_files2 = length(files2);
num_files3 = length(files3);
total_num_files = num_files1 + num_files2 + num_files3;

%% Initialize arrays to have the correct length (for speed)
rmse = zeros(1,total_num_files)';
CEX_mean_free_path = zeros(1,total_num_files)';
Ionization_mean_free_path = zeros(1,total_num_files)';
EN_mean_free_path = zeros(1,total_num_files)';
discharge_voltage = zeros(1,total_num_files)';
discharge_current = zeros(1,total_num_files)';
discharge_power = zeros(1,total_num_files)';
background_density = zeros(1,total_num_files)';
flow_rate = zeros(1,total_num_files)';
pressure = zeros(1,total_num_files)';
voltage = zeros(num_points,total_num_files);
current = zeros(num_points,total_num_files);
mi = zeros(1,total_num_files)';
valid_point_array = zeros(num_points,total_num_files);
max_current = zeros(1,total_num_files)';
floating_potential_index = zeros(1,total_num_files)';
floating_potential = zeros(1,total_num_files)';
fit_min = zeros(1,total_num_files)';
fit_max = zeros(1,total_num_files)';
fit_voltage = NaN(num_points,total_num_files);
fit_current = NaN(num_points,total_num_files);
%fit_voltage = zeros(min_fit_points + 1,total_num_files);
%fit_current = zeros(min_fit_points + 1,total_num_files);
ion_emit_multiplier = zeros(1,total_num_files)';
ion_emit_exponent = zeros(1,total_num_files)';
```

```
ion_emit_constant = zeros(1,total_num_files)';
rsquared = zeros(1,total_num_files)';
contactor_current = zeros(1,total_num_files)';
expellant_utilization = zeros(1,total_num_files)';
floating_potential_fit = zeros(1,total_num_files)';
quarter_current_voltage = zeros(1,total_num_files)';
half_current_voltage = zeros(1,total_num_files)';
common_ion_emit_exponent = zeros(1,total_num_files)';
common_rsquared = zeros(1,total_num_files)';
common_contactor_current = zeros(1,total_num_files)';
common_half_current_voltage = zeros(1,total_num_files)';
common_pressure = zeros(1,total_num_files)';
common_floating_potential = zeros(1,total_num_files)';
common_expellant_utilization = zeros(1,total_num_files)';
common_discharge_current = zeros(1,total_num_files)';
common_discharge_voltage = zeros(1,total_num_files)';
common_discharge_power = zeros(1,total_num_files)';
common_flow_rate = zeros(1,total_num_files)';
common_mi = zeros(1,total_num_files)';
residuals = NaN(num_points,total_num_files);

%% Parse initial data

% Parse data from Argon files
for i=1:num_files1
    % Reading the files
    full_directory1 = horzcat(data_directory,files1(i).name);
    data1 = read_file(full_directory1);

    % Get universal data for each sweep
    discharge_voltage(i,1) = data1('Discharge_voltage');
    discharge_current(i,1) = data1('Discharge_current');
    flow_rate(i,1) = data1('Flow_rate');
    pressure(i,1) = data1('Pressure');

    % Get voltage and current data for each sweep
    tempvolt = values(data1,{'Voltage'});
    voltage(:,i) = linspace(0,0,length(tempvolt{1,1}(:,1)));
    voltage(:,i) = voltage(:,i) + tempvolt{1,1}(:,1);
    tempcurrent = values(data1,{'Current'});
    current(:,i) = linspace(0,0,length(tempcurrent{1,1}(:,1)));
    current(:,i) = current(:,i) + tempcurrent{1,1}(:,1);

    % Mass of Argon in kg
    mi(i,1) = 39.95*u;

    % Find the discharge power
    discharge_power(i,1) = discharge_current(i,1).*discharge_voltage(i,1);

    % Find the background density
    background_density(i,1) = 9.65.*10.^24.*pressure(i,1).*10^-6./300;

    % Find the relevant mean free paths
```

```
    CEX_mean_free_path(i,1) =
    ↪  1./(background_density(i,1).*CEX_cross_section_array(1,1));
    Ionization_mean_free_path(i,1) =
    ↪  1./(background_density(i,1).*Ionization_cross_section_array(1,1));
    EN_mean_free_path(i,1) =
    ↪  1./(background_density(i,1).*EN_cross_section_array(1,1));
end

% Parse data from Krypton files
for i=1:num_files2
    % Reading the files
    full_directory2 = horzcat(data_directory,files2(i).name);
    data2 = read_file(full_directory2);

    % Get universal data for each sweep
    discharge_voltage(i+num_files1,1) = data2('Discharge_voltage');
    discharge_current(i+num_files1,1) = data2('Discharge_current');
    flow_rate(i+num_files1,1) = data2('Flow_rate');
    pressure(i+num_files1,1) = data2('Pressure');

    % Get voltage and current data for each sweep
    tempvolt = values(data2,{'Voltage'});
    voltage(:,i+num_files1) = linspace(0,0,length(tempvolt{1,1}(:,1)));
    voltage(:,i+num_files1) = voltage(:,i+num_files1) + tempvolt{1,1}(:,1);
    tempcurrent = values(data2,{'Current'});
    current(:,i+num_files1) = linspace(0,0,length(tempcurrent{1,1}(:,1)));
    current(:,i+num_files1) = current(:,i+num_files1) + tempcurrent{1,1}(:,1);

    % Mass of Krypton in kg
    mi(i+num_files1,1) = 83.8*u;

    % Find the discharge power
    discharge_power(i+num_files1,1) =
    ↪  discharge_current(i+num_files1,1).*discharge_voltage(i+num_files1,1);

    % Find the background density
    background_density(i+num_files1,1) =
    ↪  9.65.*10.^24.*pressure(i+num_files1,1).*10^-6./300;

    % Find the relevant mean free paths
    CEX_mean_free_path(i+num_files1,1) =
    ↪  1./(background_density(i+num_files1,1).*CEX_cross_section_array(1,2));
    Ionization_mean_free_path(i+num_files1,1) = 1./(background_density(i+num_file⌋
    ↪  s1,1).*Ionization_cross_section_array(1,2));
    EN_mean_free_path(i+num_files1,1) =
    ↪  1./(background_density(i+num_files1,1).*EN_cross_section_array(1,2));
end

% Parse data from Xenon files
for i=1:num_files3
    % Reading the files
    full_directory3 = horzcat(data_directory,files3(i).name);
    data3 = read_file(full_directory3);
```

```
    % Get universal data for each sweep
    discharge_voltage(i+num_files1+num_files2,1) = data3('Discharge_voltage');
    discharge_current(i+num_files1+num_files2,1) = data3('Discharge_current');
    flow_rate(i+num_files1+num_files2,1) = data3('Flow_rate');
    pressure(i+num_files1+num_files2,1) = data3('Pressure');

    % Get voltage and current data for each sweep
    tempvolt = values(data3,{'Voltage'});
    voltage(:,i+num_files1+num_files2) = linspace(0,0,length(tempvolt{1,1}(:,1)));
    voltage(:,i+num_files1+num_files2) = voltage(:,i+num_files1+num_files2) +
    ↪  tempvolt{1,1}(:,1);
    tempcurrent = values(data3,{'Current'});
    current(:,i+num_files1+num_files2) =
    ↪  linspace(0,0,length(tempcurrent{1,1}(:,1)));
    current(:,i+num_files1+num_files2) = current(:,i+num_files1+num_files2) +
    ↪  tempcurrent{1,1}(:,1);

    % Mass of Xenon in kg
    mi(i+num_files1+num_files2,1) = 131.29*u;

    % Find the discharge power
    discharge_power(i+num_files1+num_files2,1) = discharge_current(i+num_files1+n⌋
    ↪  um_files2,1).*discharge_voltage(i+num_files1+num_files2,1);

    % Find the background density
    background_density(i+num_files1+num_files2,1) =
    ↪  9.65.*10.^24.*pressure(i+num_files1+num_files2,1).*10^-6./300;

    % Find the relevant mean free paths
    CEX_mean_free_path(i+num_files1+num_files2,1) = 1./(background_density(i+num_⌋
    ↪  files1+num_files2,1).*CEX_cross_section_array(1,3));
    Ionization_mean_free_path(i+num_files1+num_files2,1) = 1./(background_density⌋
    ↪  (i+num_files1+num_files2,1).*Ionization_cross_section_array(1,3));
    EN_mean_free_path(i+num_files1+num_files2,1) = 1./(background_density(i+num_f⌋
    ↪  iles1+num_files2,1).*EN_cross_section_array(1,3));
end

%% Do data analysis common to all files
for i=1:total_num_files
    %% Remove range finding points introduced by Keithley 2400
    % Identify the points to ignore based on when the voltage is decreasing
    for j=1:num_points
        if(j<15)
            valid_point_array(j,i) = voltage(j+1,i) > voltage(j,i);
        else
            valid_point_array(j,i) = 1;
        end
    end

    % Delete low current points from both voltage and current arrays
    current(:,i) = current(:,i).*valid_point_array(:,i);
    voltage(:,i) = voltage(:,i).*valid_point_array(:,i);
    current(current == 0) = NaN;
    voltage(voltage == 0) = NaN;
```

```
    %% Find specific points in the parsed data for each sweep in order to perform
    ↪  an exponential fit
    % Find the maximum Beam Current measured
    max_current(i,1) = max(current(:,i));

    % Find the approximate floating potential index
    [~,floating_potential_index(i,1)] = min(abs(current(:,i)));

%     % If the current at the selected floating potential is negative, move
%     % up until it is positive
%     while(current(floating_potential_index(i,1),i) < 0)
%         floating_potential_index(i,1) = floating_potential_index(i,1) + 1;
%     end

    % Find the floating potential value
    floating_potential(i,1) = voltage(floating_potential_index(i,1),i);

    %% Set the sweep fit voltage range minimum and maximums to go from the
    ↪  floating potential up to the ionization energy
    fit_min(i,1) = floating_potential_index(i,1);%min(find(valid_point_array(:,i)
    ↪  == 1));
    fit_max(i,1) = num_points; %floating_potential_index(i,1) + min_fit_points;%+
    ↪  round(0.2 .*(length(current(:,i)) -
    ↪  floating_potential_index(i,1)-20));%floating_potential_index(i,1) +
    ↪  20;%length(current(:,i));

    % Truncate to just include this fit region
    fit_voltage(1:fit_max(i,1) - fit_min(i,1) + 1,i) =
    ↪  voltage((fit_min(i,1):fit_max(i,1)),i);
    fit_current(1:fit_max(i,1) - fit_min(i,1) + 1,i) =
    ↪  current((fit_min(i,1):fit_max(i,1)),i);

    % Shift fitted voltage range to start at zero
    fit_voltage(1:fit_max(i,1) - fit_min(i,1) + 1,i) = fit_voltage(1:fit_max(i,1)
    ↪  - fit_min(i,1) + 1,i) - min(fit_voltage(1:fit_max(i,1) - fit_min(i,1) +
    ↪  1,i));
    fit_current(1:fit_max(i,1) - fit_min(i,1) + 1,i) = fit_current(1:fit_max(i,1)
    ↪  - fit_min(i,1) + 1,i) - min(fit_current(1:fit_max(i,1) - fit_min(i,1) +
    ↪  1,i));

    % Remove the NaN values
    x = rmmissing(fit_voltage(:,i));
    y = rmmissing(fit_current(:,i));

    %% Define and perform an exponential fit of the prepared sweep data
    % Define the custom equation we are fitting to
    exp_eqn = fittype('a.*exp(b.*x)+c');

    % Select boundaries for fitting parameters
    warning off;
    options = fitoptions(exp_eqn);
    options.Lower = [-0.1 -10 -1];
    options.Upper = [0 0 1];
```

```
options.TolFun = 1e-30;

% Use these options for even more accurate (and slow) fits
options.Robust = 'LAR';
options.TolX = 10^-30;
options.MaxFunEvals = 1000;
options.MaxIter = 1000;

% Perform the fit
[f,gof,exp_output] = fit(x,y,exp_eqn,options);

% Save relevant fit values
ion_emit_multiplier(i,1) = f.a;
ion_emit_exponent(i,1) = f.b;
ion_emit_constant(i,1) = f.c;
rmse(i,1) = gof.rmse;
residuals((fit_min(i,1):fit_max(i,1)),i) = exp_output.residuals;
corrcoef_array =
↪  corrcoef(rmmissing(fit_current(:,i)),rmmissing(ion_emit_multiplier(i,1).*
↪  exp(fit_voltage(:,i).*ion_emit_exponent(i,1))+ion_emit_constant(i,1)));
rsquared(i,1) = corrcoef_array(2,1).^2;

%% Calculate new values based on the exponential fit
% Calculate a final contactor current based on the fit
contactor_current(i,1) = f.c;

% Find the expellant utilization using the maximum Beam Current
expellant_utilization(i,1) =
↪  100*contactor_current(i,1)./(0.071745*flow_rate(i,1));

% Find the floating potential
syms x
floating_potential_equation = f.a.*exp(f.b.*x)+f.c == 0;
floating_potential_fit(i,1) =
↪  double(vpasolve(floating_potential_equation,x,3));

% Find the approximate voltage for Ibeam = 0.25*Icontactor
quarter_current_equation = f.a.*exp(f.b.*x)+f.c == contactor_current(i,1)./4;
quarter_current_voltage(i,1) = double(vpasolve(quarter_current_equation,x,3))
↪  - floating_potential_fit(i,1);

% Find the approximate voltage for Ibeam = 0.5*Icontactor
half_current_equation = f.a.*exp(f.b.*x)+f.c == contactor_current(i,1)./2;
half_current_voltage(i,1) = double(vpasolve(half_current_equation,x,3)) -
↪  floating_potential_fit(i,1);

%% Generate vectors of data with only common configuration keeper current and
↪  gas flow rate values
if(ismember(discharge_current(i,1),discharge_current_array) &&
↪  ismember(flow_rate(i,1),flow_rate_array))
    common_ion_emit_exponent(i,1) = ion_emit_exponent(i,1);
    common_rsquared(i,1) = rsquared(i,1);
    common_contactor_current(i,1) = contactor_current(i,1);
    common_half_current_voltage(i,1) = half_current_voltage(i,1);
```

```
    common_pressure(i,1) = pressure(i,1);
    common_floating_potential(i,1) = floating_potential(i,1);
    common_expellant_utilization(i,1) = expellant_utilization(i,1);
    common_discharge_current(i,1) = discharge_current(i,1);
    common_discharge_voltage(i,1) = discharge_voltage(i,1);
    common_discharge_power(i,1) = discharge_power(i,1);
    common_flow_rate(i,1) = flow_rate(i,1);
    common_mi(i,1) = mi(i,1);
else
    common_ion_emit_exponent(i,1) = NaN;
    common_rsquared(i,1) = NaN;
    common_contactor_current(i,1) = NaN;
    common_half_current_voltage(i,1) = NaN;
    common_pressure(i,1) = NaN;
    common_floating_potential(i,1) = NaN;
    common_expellant_utilization(i,1) = NaN;
    common_discharge_current(i,1) = NaN;
    common_discharge_voltage(i,1) = NaN;
    common_discharge_power(i,1) = NaN;
    common_flow_rate(i,1) = NaN;
    common_mi(i,1) = NaN;
end

%% Generate mass specific arrays of data with only common configuration
↪  keeper current and gas flow rate values
% Argon matrix
if((0 < i) && (i < num_files1 + 1))
   common_Argon_ion_emit_exponent(find(discharge_current(i,1) ==
   ↪  discharge_current_array),find(flow_rate(i,1) == flow_rate_array)) =
   ↪  ion_emit_exponent(i,1);
   common_Argon_rsquared(find(discharge_current(i,1) ==
   ↪  discharge_current_array),find(flow_rate(i,1) == flow_rate_array)) =
   ↪  rsquared(i,1);
   common_Argon_contactor_current(find(discharge_current(i,1) ==
   ↪  discharge_current_array),find(flow_rate(i,1) == flow_rate_array)) =
   ↪  contactor_current(i,1);
   common_Argon_half_current_voltage(find(discharge_current(i,1) ==
   ↪  discharge_current_array),find(flow_rate(i,1) == flow_rate_array)) =
   ↪  half_current_voltage(i,1);
% Krypton matrix
elseif((num_files1 < i) && (i < num_files1 + num_files2 + 1))
   common_Krypton_ion_emit_exponent(find(discharge_current(i,1) ==
   ↪  discharge_current_array),find(flow_rate(i,1) == flow_rate_array)) =
   ↪  ion_emit_exponent(i,1);
   common_Krypton_rsquared(find(discharge_current(i,1) ==
   ↪  discharge_current_array),find(flow_rate(i,1) == flow_rate_array)) =
   ↪  rsquared(i,1);
   common_Krypton_contactor_current(find(discharge_current(i,1) ==
   ↪  discharge_current_array),find(flow_rate(i,1) == flow_rate_array)) =
   ↪  contactor_current(i,1);
   common_Krypton_half_current_voltage(find(discharge_current(i,1) ==
   ↪  discharge_current_array),find(flow_rate(i,1) == flow_rate_array)) =
   ↪  half_current_voltage(i,1);
% Xenon matrix
```

```
    else
       common_Xenon_ion_emit_exponent(find(discharge_current(i,1) ==
       ↪  discharge_current_array),find(flow_rate(i,1) == flow_rate_array)) =
       ↪  ion_emit_exponent(i,1);
       common_Xenon_rsquared(find(discharge_current(i,1) ==
       ↪  discharge_current_array),find(flow_rate(i,1) == flow_rate_array)) =
       ↪  rsquared(i,1);
       common_Xenon_contactor_current(find(discharge_current(i,1) ==
       ↪  discharge_current_array),find(flow_rate(i,1) == flow_rate_array)) =
       ↪  contactor_current(i,1);
       common_Xenon_half_current_voltage(find(discharge_current(i,1) ==
       ↪  discharge_current_array),find(flow_rate(i,1) == flow_rate_array)) =
       ↪  half_current_voltage(i,1);
    end

end

%% Calculate a pseudo electron temperatures based on the exponential fits
Te = -1./ion_emit_exponent;
common_Te = -1./common_ion_emit_exponent;

common_Argon_Te = -1./common_Argon_ion_emit_exponent;
common_Krypton_Te = -1./common_Krypton_ion_emit_exponent;
common_Xenon_Te = -1./common_Xenon_ion_emit_exponent;

%% Remove illogically large values from rsquared arrays
cleaned_rsquared = rsquared;
cleaned_rsquared(abs(rsquared) > 1) = NaN;

cleaned_common_Argon_rsquared = common_Argon_rsquared;
cleaned_common_Argon_rsquared(abs(cleaned_common_Argon_rsquared) > 1) = NaN;

cleaned_common_Krypton_rsquared = common_Krypton_rsquared;
cleaned_common_Krypton_rsquared(abs(cleaned_common_Krypton_rsquared) > 1) = NaN;

cleaned_common_Xenon_rsquared = common_Xenon_rsquared;
cleaned_common_Xenon_rsquared(abs(cleaned_common_Xenon_rsquared) > 1) = NaN;

%% Remove NaNs from common configuration arrays
cleaned_common_ion_emit_exponent = rmmissing(common_ion_emit_exponent);
cleaned_common_rsquared = rmmissing(common_rsquared);
cleaned_common_contactor_current = rmmissing(common_contactor_current);
cleaned_common_half_current_voltage = rmmissing(common_half_current_voltage);
cleaned_common_pressure = rmmissing(common_pressure);
cleaned_common_floating_potential = rmmissing(common_floating_potential);
cleaned_common_expellant_utilization = rmmissing(common_expellant_utilization);
cleaned_common_discharge_current = rmmissing(common_discharge_current);
cleaned_common_discharge_voltage = rmmissing(common_discharge_voltage);
cleaned_common_discharge_power = rmmissing(common_discharge_power);
cleaned_common_flow_rate = rmmissing(common_flow_rate);
cleaned_common_Te = rmmissing(common_Te);
cleaned_common_mi = rmmissing(common_mi);

%% Create an array of average values when varying just ion mass and flow rate
```

```
for i=1:length(flow_rate_array)
    avg_common_Te(1,i) = nanmean(-1./common_Argon_ion_emit_exponent(:,i));
    avg_common_Te(2,i) = nanmean(-1./common_Krypton_ion_emit_exponent(:,i));
    avg_common_Te(3,i) = nanmean(-1./common_Xenon_ion_emit_exponent(:,i));

    avg_common_rsquared(1,i) = nanmean(cleaned_common_Argon_rsquared(:,i));
    avg_common_rsquared(2,i) = nanmean(cleaned_common_Krypton_rsquared(:,i));
    avg_common_rsquared(3,i) = nanmean(cleaned_common_Xenon_rsquared(:,i));

    avg_common_contactor_current(1,i) =
    ↪  nanmean(common_Argon_contactor_current(:,i));
    avg_common_contactor_current(2,i) =
    ↪  nanmean(common_Krypton_contactor_current(:,i));
    avg_common_contactor_current(3,i) =
    ↪  nanmean(common_Xenon_contactor_current(:,i));

    avg_common_half_current_voltage(1,i) =
    ↪  nanmean(common_Argon_half_current_voltage(:,i));
    avg_common_half_current_voltage(2,i) =
    ↪  nanmean(common_Krypton_half_current_voltage(:,i));
    avg_common_half_current_voltage(3,i) =
    ↪  nanmean(common_Xenon_half_current_voltage(:,i));
end

%% Average parameters for common configurations according to ion mass
% Average the half current potential for each unique mass type using common
% configurations
avg_common_Argon_half_current_voltage =
↪  nanmean(avg_common_half_current_voltage(1,:));
avg_common_Krypton_half_current_voltage =
↪  nanmean(avg_common_half_current_voltage(2,:));
avg_common_Xenon_half_current_voltage =
↪  nanmean(avg_common_half_current_voltage(3,:));

% Calculate a pseudo electron temperature using average ion emission
% exponents for each unique mass type
avg_common_Argon_Te = nanmean(nanmean(common_Argon_Te));
avg_common_Krypton_Te = nanmean(nanmean(common_Krypton_Te));
avg_common_Xenon_Te = nanmean(nanmean(common_Xenon_Te));

%% Calculate residual statistics
max_residuals = max(abs(residuals))';
normalized_residuals = (residuals'./max_current)';
average_normalized_residuals = mean(abs(rmmissing(normalized_residuals)))';
max_normalized_residuals = max(abs(rmmissing(normalized_residuals)))';

%% Perform a power fit of contactor current versus half current voltage
% Define the custom equation we are fitting to
pow_eqn = fittype('a.*x.^b + c');

% Select boundaries for fitting parameters
warning off;
options = fitoptions(pow_eqn);
options.Lower = [0 0 0];
```

```
options.Upper = [1000 1 0];
options.TolFun = 1e-30;

% Fit the Cathode Potential scaling with contactor current using common
↪  configurations
f = fit(cleaned_common_contactor_current,cleaned_common_half_current_voltage,pow_
↪  eqn,options);

%% Perform a power fit of ion mass versus half current voltage
% Select boundaries for fitting parameters
options.Lower = [0 -10 0];
options.Upper = [10000 10 0];

% Fit the Cathode Potential scaling with ion mass
g = fit((mi_array'./u),[avg_common_Argon_half_current_voltage;avg_common_Krypton_
↪  half_current_voltage;avg_common_Xenon_half_current_voltage],pow_eqn,options);

% Fit the Cathode Potential scaling with contactor current using common
↪  configurations with a power law exponent of 0.76
options.Lower = [0 0.76 0];
options.Upper = [10000 0.76 0];
f2 = fit(cleaned_common_contactor_current,cleaned_common_half_current_voltage,pow
↪  _eqn,options);

%% Create arrays for smooth plotting
continuous_mi_array = linspace(min(mi_array),max(mi_array),1000)./u;
continuous_contactor_current_array = linspace(min(cleaned_common_contactor_curren
↪  t),max(cleaned_common_contactor_current),1000);

%% Plot analysis summary

close all;

figure();
hold on;
scatter([39.95 83.8 131.29],[avg_common_Argon_half_current_voltage
↪  avg_common_Krypton_half_current_voltage
↪  avg_common_Xenon_half_current_voltage],100,'filled');
scatter([39.95 83.8 131.29],[avg_common_Argon_Te avg_common_Krypton_Te
↪  avg_common_Xenon_Te],100,'filled');
plot(continuous_mi_array,g.a.*(continuous_mi_array).^g.b+g.c,'LineWidth',3);
str = strcat('Power Law Fit Exponent: ',num2str(round(g.b,2)));
title({'Average Cathode Potential vs Ion Mass','Exponential Fits using Common
↪  Configurations',str});
xlabel('Ion Mass [amu]');
ylabel({'Cathode Potential [V]'});
set(gca,'fontsize',14,'fontweight','bold');
h_legend = legend('Average Cathode Potential','Average Pseudo Te [eV]','Power Law
↪  Fit','Location','best','Interpreter','none');
set(h_legend,'fontweight','bold','fontsize',14);
hold off;

figure();
hold on;
```

```
scatter(cleaned_common_contactor_current.*10^6,cleaned_common_half_current_voltag
↪  e,20,'filled');
plot(continuous_contactor_current_array.*10^6,f.a.*(continuous_contactor_current_
↪  array).^f.b,'LineWidth',3);
plot(continuous_contactor_current_array.*10^6,f2.a.*(continuous_contactor_current
↪  _array).^f2.b,'LineWidth',3);
str = strcat('Power Law Fit Found \beta = ',num2str(round(f.b,2)));
title({'Cathode Potential vs Contactor Current','Exponential Fits using Common
↪  Configurations'});
xlabel('Contactor Current [uA]');
ylabel({'Cathode Potential [V]'});
h_legend = legend('Experimental Data',str,'Power Law Fit Using \beta =
↪  0.76','Location','best','Interpreter','tex');
set(h_legend,'fontweight','bold','fontsize',14);
set(gca,'fontsize',14,'fontweight','bold');
hold off;

figure();
hold on;
scatter(flow_rate_array,avg_common_Te(1,:),50,'filled')
scatter(flow_rate_array,avg_common_Te(2,:),50,'filled')
scatter(flow_rate_array,avg_common_Te(3,:),50,'filled')
title({'Pseudo Electron Temperature vs Gas Flow Rate','Exponential Fits using
↪  Common Configurations'});
xlabel('Neutral Gas Flow Rate [sccm]');
ylabel({'Pseudo Electron','Temperature [eV]'});
h_legend =
↪  legend('Argon','Krypton','Xenon','Location','best','Interpreter','tex');
set(h_legend,'fontweight','bold','fontsize',14);
set(gca,'fontsize',14,'fontweight','bold');
hold off;

figure();
hold on;
scatter(flow_rate_array,avg_common_rsquared(1,:),50,'filled')
scatter(flow_rate_array,avg_common_rsquared(2,:),50,'filled')
scatter(flow_rate_array,avg_common_rsquared(3,:),50,'filled')
title({'R-Squared Values vs Gas Flow Rate','Exponential Fits using Common
↪  Configurations'});
xlabel('Neutral Gas Flow Rate [sccm]');
ylabel({'R-Squared Value'});
h_legend =
↪  legend('Argon','Krypton','Xenon','Location','best','Interpreter','tex');
set(h_legend,'fontweight','bold','fontsize',14);
set(gca,'fontsize',14,'fontweight','bold');
hold off;

figure();
hold on;
scatter(flow_rate_array,mean(avg_common_rsquared),50,'filled')
title({'R-Squared Values vs Gas Flow Rate','Exponential Fits using Common
↪  Configurations'});
xlabel('Neutral Gas Flow Rate [sccm]');
ylabel({'R-Squared Value'});
```

```
set(gca,'fontsize',14,'fontweight','bold');
hold off;

figure();
hold on;
scatter(flow_rate_array,avg_common_contactor_current(1,:).*10^6,50,'filled')
scatter(flow_rate_array,avg_common_contactor_current(2,:).*10^6,50,'filled')
scatter(flow_rate_array,avg_common_contactor_current(3,:).*10^6,50,'filled')
title({'Contactor Current vs Gas Flow Rate','Exponential Fits using Common
↪  Configurations'});
xlabel('Neutral Gas Flow Rate [sccm]');
ylabel({'Contactor Current [uA]'});
h_legend =
↪  legend('Argon','Krypton','Xenon','Location','best','Interpreter','tex');
set(h_legend,'fontweight','bold','fontsize',14);
set(gca,'fontsize',14,'fontweight','bold');
hold off;

figure();
hold on;
scatter(cleaned_common_floating_potential,cleaned_common_half_current_voltage,20,⌋
↪  'filled','r');
title({'Cathode Potential vs Floating Potential','using Common Configurations'});
xlabel('Floating Potential [V]');
ylabel({'Cathode Potential','when Iemission = 0.5*Icontactor','(Relative to
↪  Floating) [V]'});
%axis([0 700 3 18]);
set(gca,'fontsize',14,'fontweight','bold');
hold off;

figure();
hold on;
scatter(cleaned_common_expellant_utilization,cleaned_common_half_current_voltage,⌋
↪  20,'filled','r');
title({'Cathode Potential vs Expellant Utilization','Exponential Fits using
↪  Common Configurations'});
xlabel('Expellant Utilization [%]');
ylabel({'Cathode Potential','when Iemission = 0.5*Icontactor','(Relative to
↪  Floating) [V]'});
%axis([0 700 3 18]);
ax = gca;
set(gca,'fontsize',14,'fontweight','bold');
hold off;

figure();
hold on;
histogram(Te,500);
str = strcat('Average Pseudo Te [eV]:',num2str(round(nanmean(Te),2)));
title({'Pseudo Electron Temperature using Exponential Fits',str});
xlabel('Pseudo Te [eV]');
ylabel({'Number of Configurations'});
axis([0 20 0 20]);
set(gca,'fontsize',14,'fontweight','bold');
hold off;
```

```
figure();
hold on;
histogram(Te(1:num_files1,1),50);
str = strcat('Average Pseudo Te
↪  [eV]:',num2str(round(nanmean(Te(1:num_files1,1)),2)));
title({'Argon','Pseudo Electron Temperature using Exponential Fits',str});
xlabel('Pseudo Te [eV]');
ylabel({'Number of Configurations'});
set(gca,'fontsize',14,'fontweight','bold');
hold off;

figure();
hold on;
histogram(Te(num_files1+1:num_files1+num_files2,1),50);
str = strcat('Average Pseudo Te
↪  [eV]:',num2str(round(nanmean(Te(num_files1+1:num_files1+num_files2,1)),2)));
title({'Krypton','Pseudo Electron Temperature using Exponential Fits',str});
xlabel('Pseudo Te [eV]');
ylabel({'Number of Configurations'});
set(gca,'fontsize',14,'fontweight','bold');
hold off;

figure();
hold on;
histogram(Te(num_files1+num_files2+1:num_files1+num_files2+num_files3,1),50);
str = strcat('Average Pseudo Te [eV]:',num2str(round(nanmean(Te(num_files1+num_fi⌋
↪  les2+1:num_files1+num_files2+num_files3,1)),2)));
title({'Xenon','Pseudo Electron Temperature using Exponential Fits',str});
xlabel('Pseudo Te [eV]');
ylabel({'Number of Configurations'});
set(gca,'fontsize',14,'fontweight','bold');
hold off;

%% Plot all common configuration sweeps with exponential fit
for k = 1:total_num_files %num_sweep_range_min:sweep_range_max

    if(~isnan(common_discharge_current(k,1)))

        % Compute the fit exponential current fit for a specific sweep
        current_fit = ion_emit_multiplier(k,1).*exp(fit_voltage(:,k).*ion_emit_ex⌋
        ↪  ponent(k,1))+ion_emit_constant(k,1);

        figure
        hold on;
        scatter(10.^6.*(fit_current(:,k)),fit_voltage(:,k),20,'filled');
        plot(10.^6.*current_fit,fit_voltage(:,k),'LineWidth',3);
        str = strcat('Sweep Number=',num2str(k));
        str2 = strcat('Ion Mass= ',num2str(round(mi(k,1)./u,0)),' Discharge
        ↪  Current= ',num2str(round(discharge_current(k,1),1)),' Flow Rate=
        ↪  ',num2str(round(flow_rate(k,1),2)));
        str3 = strcat('Fit Exponent=',num2str(round(ion_emit_exponent(k,1),2)),'
        ↪  Pseudo Te [eV]=',num2str(round(Te(k,1),2)));
        str4 = strcat('R-Squared Value=',num2str(round(rsquared(k,1),3)));
```

```
        title({'Raw Sweep w/ Exponential Fit',str,str2,str3,str4});
        xlabel('Beam Current [uA]');
        ylabel({'Cathode Potential','(Relative to Floating) [V]'});
        %axis([0 1.1.*10.^6.*max(current_fit_shifted(:,1)) 0 20]);
        h_legend = legend('Experimental Data',['Exponential Fit:' newline
        ↪  '\psi_{SC} \alpha
        ↪  exp(\beta*I_{beam})'],'Location','best','Interpreter','tex');
        set(h_legend,'fontweight','bold','fontsize',14);
        set(gca,'fontsize',14,'fontweight','bold');
        hold off;
    end
end
```

BIBLIOGRAPHY

BIBLIOGRAPHY

[1] W. N. Hess, M. C. Trichel, T. N. Davis, William C. Beggs, George E. Kraft, E. Stassinopoulos, and E. J. R. Maier. Artificial Aurora Experiment: Experiment and principal results. *Journal of Geophysical Research*, 76(25):6067–6081, 1971.

[2] R. C. Olsen, L. E. Weddle, and J. L. Roeder. Plasma wave observations during Ion Gun Experiments. *Journal of Geophysical Research: Space Physics*, 95(A6):7759–7771, June 1990.

[3] J. R. Winckler. The application of artificial electron beams to magnetospheric research. *Reviews of Geophysics*, 18(3):659–682, 1980.

[4] R. B. Torbert, H. Vaith, M. Granoff, M. Widholm, J. A. Gaidos, B. H. Briggs, I. G. Dors, M. W. Chutter, J. Macri, M. Argall, D. Bodet, J. Needell, M. B. Steller, W. Baumjohann, R. Nakamura, F. Plaschke, H. Ottacher, J. Hasiba, K. Hofmann, C. A. Kletzing, S. R. Bounds, R. T. Dvorsky, K. Sigsbee, and V. Kooi. The Electron Drift Instrument for MMS. *Space Science Reviews*, 199:283–305, March 2016.

[5] A. C. Barrie, F. Cipriani, C. P. Escoubet, S. Toledo-Redondo, R. Nakamura, K. Torkar, Z. Sternovsky, S. Elkington, D. Gershman, B. Giles, and C. Schiff. Characterizing spacecraft potential effects on measured particle trajectories. *Physics of Plasmas*, 26(10):103504, October 2019.

[6] C. Krafft and A. S. Volokitin. Electron beam interaction with space plasmas. *Plasma Physics and Controlled Fusion*, 41(12B):B305–B315, December 1999.

[7] H. A. Cohen, R. C. Adamo, and et al. P78-2 satellite and payload responses to electron beam operations on March 30, 1979. October 1980.

[8] Joseph E. Borovsky, Gian Luca Delzanno, Eric E. Dors, Michelle F. Thomsen, Ennio R. Sanchez, Michael G. Henderson, Robert A. Marshall, Brian E. Gilchrist, Grant Miars, Bruce E. Carlsten, Steven A. Storms, Michael A. Holloway, and Dinh Nguyen. Solving the auroral-arc-generator question by using an electron beam to unambiguously connect critical magnetospheric measurements to auroral images. *Journal of Atmospheric and Solar-Terrestrial Physics*, page 105310, May 2020.

[9] Gian Luca Delzanno, Joseph E. Borovsky, Michelle F. Thomsen, Brian E. Gilchrist, and Ennio Sanchez. Can an electron gun solve the outstanding problem of magnetosphere-ionosphere connectivity? *Journal of Geophysical Research: Space Physics*, 121(7):6769–6773, July 2016.

[10] Joseph E. Borovsky and Gian Luca Delzanno. Active Experiments in Space: The Future. *Frontiers in Astronomy and Space Sciences*, 6, 2019.

[11] Bruce E. Carlsten, Patrick L. Colestock, Gregory S. Cunningham, Gian Luca Delzanno, Eric E. Dors, Michael A. Holloway, Christopher A. Jeffery, John W. Lewellen, Quinn R. Marksteiner, Dinh C. Nguyen, Geoffrey D. Reeves, and Kevin A. Shipman. Radiation-Belt Remediation Using Space-Based Antennas and Electron Beams. *IEEE Transactions on Plasma Science*, 47(5):2045–2063, May 2019.

[12] Elizabeth A. MacDonald, J. E. Borovsky, Brian Larsen, and Eric Dors. A science mission concept to actively probe magnetosphere-ionosphere coupling. *Decadal Survey in Solar and Space Physics papers*, 2012.

[13] National Research Council, Division on Engineering and Physical Sciences, Aeronautics and Space Engineering Board, Space Studies Board, and Committee on a Decadal Strategy for Solar and Space Physics (Heliophysics). *Solar and Space Physics: A Science for a Technological Society*. National Academies Press, August 2013.

[14] G. L. Delzanno, J. E. Borovsky, M. F. Thomsen, J. D. Moulton, and E. A. MacDonald. Future beam experiments in the magnetosphere with plasma contactors: How do we get the charge off the spacecraft? *Journal of Geophysical Research: Space Physics*, 120(5):3647–3664, 2015.

[15] G. L. Delzanno, J. E. Borovsky, M. F. Thomsen, and J. D. Moulton. Future beam experiments in the magnetosphere with plasma contactors: The electron collection and ion emission routes. *Journal of Geophysical Research: Space Physics*, 120(5):3588–3602, 2015.

[16] F. Lucco Castello, G. L. Delzanno, J. E. Borovsky, G. Miars, O. Leon, and B. E. Gilchrist. Spacecraft-Charging Mitigation of a High-Power Electron Beam Emitted by a Magnetospheric Spacecraft: Simple Theoretical Model for the Transient of the Spacecraft Potential. *Journal of Geophysical Research: Space Physics*, 123(8):6424–6442, 2018.

[17] Claudia Colandrea. *Model to study the expansion of plasma contactor emitted by a magnetospheric spacecraft to mitigate charging effects.* PhD thesis, Politecnico Di Torino, 2018.

[18] J. C. Maxwell M.A. V. Illustrations of the dynamical theory of gases.—Part I. On the motions and collisions of perfectly elastic spheres. *The London, Edinburgh, and Dublin Philosophical Magazine and Journal of Science*, 19(124):19–32, January 1860.

[19] Shu T Lai. *Fundamentals of Spacecraft Charging*. Princeton University Press, November 2011.

[20] Jie Zhu, Aaron J. Ridley, and Yue Deng. Simulating electron and ion temperature in a global ionosphere thermosphere model: Validation and modeling an idealized substorm. *Journal of Atmospheric and Solar-Terrestrial Physics*, 138-139:243–260, February 2016.

[21] R. M. Katus, A. M. Keesee, E. Scime, and M. W. Liemohn. Storm time equatorial magnetospheric ion temperature derived from TWINS ENA flux. *Journal of Geophysical Research: Space Physics*, 122(4):3985–3996, 2017.

[22] Hans-Joachim Kunze. Collisional Processes. In Hans-Joachim Kunze, editor, *Introduction to Plasma Spectroscopy*, Springer Series on Atomic, Optical, and Plasma Physics, pages 115–134. Springer, Berlin, Heidelberg, 2009.

[23] Klaus Bartschat and Mark J. Kushner. Electron collisions with atoms, ions, molecules, and surfaces: Fundamental science empowering advances in technology. *Proceedings of the National Academy of Sciences*, 113(26):7026–7034, June 2016.

[24] Andrew Hurlbatt, Andrew Robert Gibson, Sandra Schröter, Jérôme Bredin, Alexander Paul Stuart Foote, Pascaline Grondein, Deborah O'Connell, and Timo Gans. Concepts, Capabilities, and Limitations of Global Models: A Review. *Plasma Processes and Polymers*, 14(1-2):1600138, 2017.

[25] Rajesh Dorai and Mark J. Kushner. A model for plasma modification of polypropylene using atmospheric pressure discharges. *Journal of Physics D: Applied Physics*, 36(6):666–685, February 2003.

[26] A. V. Phelps. The Diffusion of Charged Particles in Collisional Plasmas: Free and Ambipolar Diffusion at Low and Moderate Pressures. *Journal of Research of the National Institute of Standards and Technology*, 95(4):407–431, 1990.

[27] Dan M. Goebel and Ira Katz. *Fundamentals of Electric Propulsion: Ion and Hall Thrusters*. John Wiley & Sons, December 2008.

[28] Michael A. Lieberman and Allan J. Lichtenberg. Direct Current (DC) Sheaths. In *Principles of Plasma Discharges and Materials Processing*, pages 165–206. John Wiley & Sons, Inc., 2005.

[29] Scott David Baalrud. *Kinetic theory of instability-enhanced collective interactions in plasma*. PhD thesis, University of Wisconsin - Madison, 2010.

[30] Sven Bilen, Matthew Domonkos, and Alec Gallimore. The far-field plasma environment of a hollow cathode assembly. In *35th Joint Propulsion Conference and Exhibit*, Los Angeles,CA,U.S.A., June 1999.

[31] Henry Berry Garrett. The charging of spacecraft surfaces. *Reviews of Geophysics*, 19(4):577–616, November 1981.

[32] H. M. Mott-Smith and Irving Langmuir. The Theory of Collectors in Gaseous Discharges. *Physical Review*, 28(4):727–763, October 1926.

[33] D. Darian, S. Marholm, M. Mortensen, and W. J. Miloch. Theory and simulations of spherical and cylindrical Langmuir probes in non-Maxwellian plasmas. *Plasma Physics and Controlled Fusion*, 61(8):085025, June 2019.

[34] T. E. Sheridan and J. A. Goree. Analytic expression for the electric potential in the plasma sheath. *IEEE Transactions on Plasma Science*, 17(6):884–888, December 1989.

[35] Luís Conde. An introduction to Langmuir probe diagnostics of plasmas. Technical report, Universidad Politécnica de Madrid, Madrid, Spain, May 2011.

[36] Francis Chen. Lecture Notes on Langmuir Probe Diagnostics, June 2003.

[37] Xian-Zhu Tang and Gian Luca Delzanno. Orbital-motion-limited theory of dust charging and plasma response. *Physics of Plasmas*, 21(12):123708, December 2014.

[38] Martin Lampe. Limits of validity for orbital-motion-limited theory for a small floating collector. *Journal of Plasma Physics*, 65(3):171–180, April 2001.

[39] Shu T. Lai. Secondary and Backscattered Electrons. In *Fundamentals of Spacecraft Charging*, Spacecraft Interactions with Space Plasmas, pages 18–24. Princeton University Press, 2012.

[40] Ira Katz, Myron Mandell, Gary Jongeward, and M. S. Gussenhoven. The importance of accurate secondary electron yields in modeling spacecraft charging. *Journal of Geophysical Research: Space Physics*, 91(A12):13739–13744, 1986.

[41] J. R. Dennison, Phil Lundgreen, and Justin Christensen. Parameterization of Secondary and Backscattered Electron Yields for Spacecraft Charging. January 2018.

[42] E. J. Sternglass. Theory of Secondary Electron Emission by High-Speed Ions. *Physical Review*, 108(1):1–12, October 1957.

[43] N. L. Inouye Sanders. Secondary emission effects on spacecraft charging: Energy distribution considerations. January 1979.

[44] Ernest J. Sternglass. Backscattering of Kilovolt Electrons from Solids. *Physical Review*, 95(2):345–358, July 1954.

[45] S. M. L. Prokopenko and J. G. Laframboise. High-voltage differential charging of geostationary spacecraft. *Journal of Geophysical Research: Space Physics*, 85(A8):4125–4131, 1980.

[46] P. Stannard, Israel Katz, Myron Mandell, J. Cassidy, D. Parks, M. Rotenberg, and P. Steen. Analysis of the charging of the SCATHA (P78-2) satellite. January 1981.

[47] S.T. Lai and M.F. Tautz. Aspects of Spacecraft Charging in Sunlight. *IEEE Transactions on Plasma Science*, 34(5):2053–2061, October 2006.

[48] Johann Heinrich Lambert. *I. H. Lambert ... Photometria sive de mensura et gradibus luminis, colorum et umbrae*. Augustae Vindelicorum : sumptibus viduae Eberhardi Klett typis Chistophori Petri Detleffsen, 1760, 1760.

[49] B. Feuerbacher and B. Fitton. Experimental Investigation of Photoemission from Satellite Surface Materials. *Journal of Applied Physics*, 43(4):1563–1572, April 1972.

[50] Réjean J. L. Grard. Properties of the satellite photoelectron sheath derived from photoemission laboratory measurements. *Journal of Geophysical Research (1896-1977)*, 78(16):2885–2906, 1973.

[51] Shu T. Lai and Maurice Tautz. High-level spacecraft charging in eclipse at geosynchronous altitudes: A statistical study. *Journal of Geophysical Research: Space Physics*, 111(A9), 2006.

[52] C. K. Garrett Purvis. Design guidelines for assessing and controlling spacecraft charging effects. Technical report, September 1984.

[53] Joseph I Minow and Linda Neergaard Parker. Spacecraft Charging: Anomaly and Failure Mechanisms, July 2014.

[54] USA. MIL-STD-1541 : Electromagnetic Compatibility Requirements for Space Systems, 1971.

[55] Albert C. Whittlesey and Henry B. Garrett. NASA's Technical Handbook for Avoiding On-Orbit ESD Anomalies Due to Internal Charging Effects. 1998.

[56] Shu T. Lai, Kerri Cahoy, Whitney Lohmeyer, Ashley Carlton, Raichelle Aniceto, and Joseph Minow. Deep Dielectric Charging and Spacecraft Anomalies. In *Extreme Events in Geospace*, pages 419–432. Elsevier, 2018.

[57] Henry B. Garrett and Albert C. Whittlesey. *Guide to Mitigating Spacecraft Charging Effects*. John Wiley & Sons, Inc., 2012.

[58] A.R. Frederickson, E.G. Holeman, and E.G. Mullen. Characteristics of spontaneous electrical discharging of various insulators in space radiations. *IEEE Transactions on Nuclear Science*, 39(6):1773–1782, December 1992.

[59] NASA. NASA-HDBK-4002 Avoiding Problems Caused by Spacecraft On-Orbit Internal Charging Effects. Technical report, NASA, February 1999.

[60] D J Rodgers, L Levy, P M Latham, K A Ryden, J Sørensen, and G L Wrenn. Prediction of Internal Dielectric Charging Using the DICTAT Code. 1998.

[61] H. Koons, J. Mazur, R. Selesnick, J. Blake, J. Fennell, Jim Roeder, and P. Anderson. The Impact of the Space Environment on Space Systems. *paper presented at 6th Spacecraft Charging Technology*, -1:7–11, October 1998.

[62] Satellite anomalies: Benefits of a centralized anomaly database and methods for securely sharing information among satellite operators. Technical report, RAND, Santa Monica, CA, 2014.

[63] Michelle F. Thomsen, Michael G. Henderson, and Vania K. Jordanova. Statistical properties of the surface-charging environment at geosynchronous orbit. *Space Weather*, 11(5):237–244, 2013.

[64] Dale C. Ferguson, Robert V. Hilmer, and Victoria A. Davis. Best Geosynchronous Earth Orbit Daytime Spacecraft Charging Index. *Journal of Spacecraft and Rockets*, 52(2):526–543, 2015.

[65] J.-C. Matéo-Vélez, A. Sicard, D. Payan, N. Ganushkina, N. P. Meredith, and I. Sillanpäa. Spacecraft surface charging induced by severe environments at geosynchronous orbit. *Space Weather*, 16(1):89–106, 2018.

[66] Ho-Sung Choi, Jaejin Lee, Kyung-Suk Cho, Young-Sil Kwak, Il-Hyun Cho, Young-Deuk Park, Yeon-Han Kim, Daniel N. Baker, Geoffrey D. Reeves, and Dong-Kyu Lee. Analysis of GEO spacecraft anomalies: Space weather relationships. *Space Weather*, 9(6), 2011.

[67] Lyman Spitzer, Jr. The Dynamics of the Interstellar Medium. III. Galactic Distribution. *The Astrophysical Journal*, 95:329, May 1942.

[68] B. Lehnert. Electrodynamic Effects connected with the Motion of a Satellite of the Earth. *Tellus*, 8(3):408–409, 1956.

[69] David B. Beard and Francis S. Johnson. Charge and magnetic field interaction with satellites. *Journal of Geophysical Research (1896-1977)*, 65(1):1–8, 1960.

[70] David B. Beard and Francis S. Johnson. Ionospheric limitations on attainable satellite potential. *Journal of Geophysical Research (1896-1977)*, 66(12):4113–4122, 1961.

[71] K. P. Chopra. Interactions of Rapidly Moving Bodies in Terrestrial Atmosphere. *Reviews of Modern Physics*, 33(2):153–189, April 1961.

[72] R. E. Donley Bourdeau. Measurements of Sheath Currents and Equilibrium Potential on the Explorer VIII Satellite (1960 xi). Technical Note D-1064, NASA, July 1961.

[73] Ira B. Bernstein and Irving N. Rabinowitz. Theory of Electrostatic Probes in a Low-Density Plasma. *Physics of Fluids*, 2:112–121, March 1959.

[74] A. H. Davis and I. Harris. Interaction of a Charged Satellite with the Ionosphere. Technical Report TN D 704, NASA, Washington D.C., September 1961.

[75] S. F. Singer. *Interactions of Space Vehicles with an Ionized Atmosphere*. Elsevier, 1965.

[76] E. C. Whipple. The equilibrium electric potential of a body in the upper atmosphere and in interplanetary space. Technical report, June 1965.

[77] H.B. Garrett and A.C. Whittlesey. Spacecraft charging, an update. *IEEE Transactions on Plasma Science*, 28(6):2017–2028, December 2000.

[78] S. E. DeForest and C. E. McIlwain. Plasma clouds in the magnetosphere. *Journal of Geophysical Research (1896-1977)*, 76(16):3587–3611, 1971.

[79] S. E. Deforest. Spacecraft charging at synchronous orbit. *Journal of Geophysical Research*, February 1972.

[80] R. C. Olsen. Experiments in charge control at geosynchronous orbit - ATS-5 and ATS-6. *Journal of Spacecraft and Rockets*, 22(3):254–264, 1985.

[81] M. S. Gussenhoven, E. G. Mullen, and D. A. Hardy. Artificial Charging of Spacecraft Due to Electron Beam Emission. *IEEE Transactions on Nuclear Science*, 34(6):1614–1619, December 1987.

[82] N. H. Stone and C. Bonifazi. The TSS-1R Mission: Overview and scientific context. *Geophysical Research Letters*, 25(4):409–412, 1998.

[83] Mario D. Grossi. Plasma Motor Generator (PMG) Electrodynamic Tether Experiment. Final Report NAG9-643, Smithsonian Institution Astrophysical Observatory , NASA, Cambridge, Mass., 1995.

[84] I. Katz, J. R. Lilley, A. Greb, J. E. McCoy, J. Galofaro, and D. C. Ferguson. Plasma turbulence enhanced current collection: Results from the plasma motor generator electrodynamic tether flight. *Journal of Geophysical Research: Space Physics*, 100(A2):1687–1690, February 1995.

[85] J. R. Dennison. Dynamic Interplay Between Spacecraft Charging, Space Environment Interactions, and Evolving Materials. *IEEE Transactions on Plasma Science*, 43(9):2933–2940, September 2015.

[86] Henry. B. Garrett, Ira Katz, Insoo Jun, Wousik Kim, Albert C. Whittlesey, and Robin W. Evans. The Jovian Charging Environment and Its Effects—A Review. *IEEE Transactions on Plasma Science*, 40(2):144–154, February 2012.

[87] Lois K. Sarno-Smith, Brian A. Larsen, Ruth M. Skoug, Michael W. Liemohn, Aaron Breneman, John R. Wygant, and Michelle F. Thomsen. Spacecraft surface charging within geosynchronous orbit observed by the Van Allen Probes. *Space Weather*, 14(2):151–164, 2016.

[88] Dale C Ferguson. Charging of the International Space Station Due to its High Voltage Solar Arrays. Technical Report 211831, NASA Glenn Research Center, Cleveland, OH, 2002.

[89] Dale C. Ferguson. New Frontiers in Spacecraft Charging. *IEEE Transactions on Plasma Science*, 40(2):139–143, February 2012.

[90] Dan M Goebel, Olya Filimonova, John R Anderson, Ira Katz, Stephanie Leifer, and James E Polk. Definitive High Voltage Solar Array Testing in Space and Thruster Plume Plasma Environments. 2014.

[91] Christian Carpenter. On the Operational Status of the ISS Plasma Contactor Hollow Cathodes. In *40th AIAA/ASME/SAE/ASEE Joint Propulsion Conference and Exhibit*, Fort Lauderdale, Florida, July 2004.

[92] Amri Hernandez-Pellerano, Christopher J Iannello, Henry B Garrett, Andrew T Ging, Ira Katz, R Lloyd Keith, Joseph I Minow, Emily M Willis, Todd A Schneider, Albert C Whittlesey, Edward J Wollack, and Kenneth H Wright. International Space Station (ISS) Plasma Contactor Unit (PCU) Utilization Plan Assessment Update. *International Space Station*, page 300, 2014.

[93] Simon Lee and Alicia Johnstone. CubeSat Design Specification Rev. 14, 2020.

[94] Emily M. Minow Willis. Spacecraft Charging Analysis of a CubeSat. Pasadena, CA, United States, June 2014.

[95] O. Leon, W. Hoegy, J. McTernan, L. Habash Krause, G. Miars, and B. E. Gilchrist. Predicting spacecraft charging effects due to Langmuir probe operation on a CubeSat using analytic equations. *AGU Fall Meeting Abstracts*, 41, December 2018.

[96] Omar Leon. *The Twin-Probe Method: Improving Langmuir Probe Accuracy on Small Spacecraft*. PhD thesis, The University of Michigan, Ann Arbor, MI, 2020.

[97] Jesse Mcternan, Sven Bilén, and L. Krause. Facility for Real-time Test and Verification of LEO Space Plasma Phenomena. Los Angeles, CA, May 2017.

[98] Lee W. Parker and Brian L. Murphy. Potential buildup on an electron-emitting ionospheric satellite. *Journal of Geophysical Research (1896-1977)*, 72(5):1631–1636, 1967.

[99] N. Kawashima, S. Sasaki, K.I. Oyama, K. Hirao, T. Obayashi, W.J. Raitt, A.B. White, P.R. Williamson, P.M. Banks, and W.F. Sharp. Results from a tethered rocket experiment (Charge-2). *Advances in Space Research*, 8(1):197–201, January 1988.

[100] Neil B. Myers, W. John Raitt, A. Brent White, Peter M. Banks, Brian E. Gilchrist, and Susumu Sasaki. Vehicle charging effects during electron beam emission from the CHARGE-2 experiment. *Journal of Spacecraft and Rockets*, 27(1):25–37, 1990.

[101] N. B. Myers, A. B. White, L. Olsen, and W. J. Raitt. CHARGE-2B Electron Gun System. Final Technical Report AD-A231, Air Force Systems Command, Fort Belvoir, VA, November 1990.

[102] Yi Chen, Rui Huang, Xianlin Ren, Liping He, and Ye He. History of the Tether Concept and Tether Missions: A Review. *ISRN Astronomy and Astrophysics*, 2013:1–7, 2013.

[103] Bjorn Grandal and A. North. *Artificial Particle Beams in Space Plasma Studies*. Nato Science Series B:. Springer US, 1982.

[104] Edward P. Szuszczewicz. Controlled electron beam experiments in space and supporting laboratory experiments: a review. *Journal of Atmospheric and Terrestrial Physics*, 47(12):1189–1210, December 1985.

[105] J. R. Winckler, P. R. Malcolm, R. L. Arnoldy, W. J. Burke, K. N. Erickson, J. Ernstmeyer, R. C. Franz, T. J. Hallinan, P. J. Kellogg, S. J. Monson, K. A. Lynch, G. Murphy, and R. J. Nemzek. ECHO 7: An electron beam experiment in the magnetosphere. *Eos, Transactions American Geophysical Union*, 70(25):657–668, 1989.

[106] D. A. Gurnett, W. S. Kurth, J. T. Steinberg, P. M. Banks, R. I. Bush, and W. J. Raitt. Whistler-mode radiation from the Spacelab 2 electron beam. *Geophysical Research Letters*, 13(3):225–228, 1986.

[107] Vladimir S. Aslanov and Alexander S. Ledkov. Space tether systems: review of the problem. In Vladimir S. Aslanov and Alexander S. Ledkov, editors, *Dynamics of Tethered Satellite Systems*, pages 3–104. Woodhead Publishing, January 2012.

[108] Evgeny V. Mishin. Artificial Aurora Experiments and Application to Natural Aurora. *Frontiers in Astronomy and Space Sciences*, 6, 2019.

[109] Andrew Nicholas, Ted Finne, Hollis Jones, Fred Herrero, Bernie Vancil, Dean Aalami, Ivan Galysh, Anthony Mai, and James Yen. Wind Ion-drift Neutral Composition Suite cathode activation procedure and current–voltage characteristics. *Radiation Effects and Defects in Solids*, 168(10):821–832, October 2013.

[110] B E Gilchrist, O Leon, G Miars, I C Bell III, S G Bilén, D Winship, W Faistenhammer, D Yoon, R Barnhart, J Lafayette, Y Liu, G Jenkins, C Wright, H Tang, and C Cooper. Picosat/Femtosatellite Electrodynamic Tether Propulsion. Marid, Spain, 2019.

[111] John W. Lewellen, Cynthia E. Buechler, Bruce E. Carlsten, Gregory E. Dale, Michael A. Holloway, Douglas E. Patrick, Steven A. Storms, and Dinh C. Nguyen. Space-Borne Electron Accelerator Design. *Frontiers in Astronomy and Space Sciences*, 6, 2019.

[112] Grant Miars, Brian E. Gilchrist, Gian Luca Delzanno, Omar Leon, and John D. Williams. B-SPICE: The Beam-Spacecraft Plasma Interaction and Charging Experiment. AGU Fall Meeting 2019, December 2019.

[113] D. F. Hall. Electrostatic propulsion beam divergence effects on spacecraft surfaces, volume 2. Technical report, January 1973.

[114] R. C. Olsen and E. C. Whipple. Active experiments in modifying spacecraft potential: Results from ATS-5 and ATS-6. Technical report, March 1979.

[115] Arthur L. Pavel. *SCATHA Satellite Instrumentation Report*. Air Force Geophysics Laboratories, Air Force Systems Command, United States Air Force, 1976.

[116] Dan M. Goebel, Richard E. Wirz, and Ira Katz. Analytical Ion Thruster Discharge Performance Model. *Journal of Propulsion and Power*, 23(5):1055–1067, 2007.

[117] Daniel George Courtney. *Ionic liquid ion source emitter arrays fabricated on bulk porous substrates for spacecraft propulsion.* Thesis, Massachusetts Institute of Technology, 2011.

[118] L. W. Swanson. Liquid metal ion sources: Mechanism and applications. *Nuclear Instruments and Methods in Physics Research*, 218(1):347–353, December 1983.

[119] Geoffrey Taylor. Disintegration of Water Drops in an Electric Field. *Proceedings of the Royal Society of London. Series A, Mathematical and Physical Sciences*, 280(1382):383–397, 1964.

[120] R. Schmidt, H. Arends, A. Pedersen, F. Rüdenauer, M. Fehringer, B. T. Narheim, R. Svenes, K. Kvernsveen, K. Tsuruda, T. Mukai, H. Hayakawa, and M. Nakamura. Results from active spacecraft potential control on the Geotail spacecraft. *Journal of Geophysical Research: Space Physics*, 100(A9):17253–17259, September 1995.

[121] K. Torkar, W. Riedler, C. P. Escoubet, M. Fehringer, R. Schmidt, R. J. L. Grard, H. Arends, F. Rüdenauer, W. Steiger, B. T. Narheim, K. Svenes, R. Torbert, M. André, A. Fazakerley, R. Goldstein, R. C. Olsen, A. Pedersen, E. Whip-

ple, and H. Zhao. Active spacecraft potential control for Cluster – implementation and first results. *Ann. Geophys.*, 19(10/12):1289–1302, September 2001.

[122] O. W. Richardson. *(Thermionic) Emission From Hot Bodies*. Watchmaker Publishing, March 2003.

[123] H. A. Adamo Cohen, A. L. Chesley, T. Aggson, M. S. Gussenhoven, R. C. Olsen, and E. Whipple. A Comparison of Three Techniques of Discharging Satellites. 1979.

[124] John Nation, Levi Schächter, Rick Mako, L.K. Len, William Peter, Cha-Mei Tang, and Triveni Rao. Advances in cold cathode physics and technology. *Proceedings of the IEEE*, 87:865–889, June 1999.

[125] Ralph Howard Fowler and L. Nordheim. Electron emission in intense electric fields. *Proceedings of the Royal Society of London. Series A, Containing Papers of a Mathematical and Physical Character*, 119(781):173–181, May 1928.

[126] C.M. Marrese. A review of field emission cathode technologies for electric propulsion systems and instruments. In *2000 IEEE Aerospace Conference. Proceedings (Cat. No.00TH8484)*, volume 4, pages 85–98, Big Sky, MT, USA, 2000.

[127] John D. Williams and Paul J. Wilbur. Experimental study of plasma contactor phenomena. *Journal of Spacecraft and Rockets*, 27(6):634–641, 1990.

[128] M. J. Gerver, D. E. Hastings, and M. R. Oberhardt. Theory of plasma contactors in ground-based experiments and low earth orbit. *Journal of Spacecraft and Rockets*, 27(4):391–402, 1990.

[129] S. T. Lai. An overview of electron and ion beam effects in charging and discharging to spacecraft. *IEEE Transactions on Nuclear Science*, 36(6):2027–2032, December 1989.

[130] Michael Patterson. Functional Testing of the Space Station Plasma Contactor. Technical Report AIAA-94-3308, NASA, June 1994.

[131] Lauren P. Rand and John D. Williams. Instant Start Electride Hollow Cathode. 2013.

[132] J. C. Sturman. Development and design of three monitoring instruments for spacecraft charging. Technical report, September 1981.

[133] J. L. Roeder and J. F. Fennell. Differential Charging of Satellite Surface Materials. *IEEE Transactions on Plasma Science*, 37(1):281–289, January 2009.

[134] Robert B. Lobbia and Alec D. Gallimore. Temporal limits of a rapidly swept Langmuir probe. *Physics of Plasmas*, 17(7):073502, July 2010.

[135] Emily Willis, Joseph I. Minow, Linda N. Parker, Maria Z. Pour, Charles Swenson, Ken-ichi Nishikawa, and Linda Habash Krause. Observations of Transient ISS Floating Potential Variations during High Voltage Solar Array Operations. In *AIAA SPACE 2016*, Long Beach, California, September 2016.

[136] M. R. Oberhardt, D. A. Hardy, D. C. Thompson, W. J. Raitt, E. Melchioni, C. Bonifazi, and M. P. Gough. Positive spacecraft charging as measured by the Shuttle potential and Return Electron experiment. *IEEE Transactions on Nuclear Science*, 40(6):1532–1541, December 1993.

[137] Richard Christopher Olsen. Current limiting mechanisms in electron and ion beams experiments. Technical Report, Monterey, California. Naval Postgraduate School, August 1989.

[138] Shu T. Lai. A Critical Overview of Measurement Techniques of Spacecraft Charging in Space Plasma. In Robert F. Pfaff, Josep E. Borovsky, and David T. Young, editors, *Measurement Techniques in Space Plasmas Fields*, pages 217–221. American Geophysical Union, 1998.

[139] I. Katz, J. N. Barfield, J. L. Burch, J. A. Marshall, W. C. Gibson, T. Neubert, W. T. Roberts, W. W. L. Taylor, and J. R. Beattie. Interactions between the space experiments with particle accelerator plasma contactor and the ionosphere. *Journal of Spacecraft and Rockets*, 31(6):1079–1084, 1994.

[140] Dieter Bilitza. IRI the International Standard for the Ionosphere. In *Advances in Radio Science*, volume 16, pages 1–11, September 2018.

[141] A. Collette, D. M. Malaspina, and Z. Sternovsky. Characteristic temperatures of hypervelocity dust impact plasmas. *Journal of Geophysical Research: Space Physics*, 121(9):8182–8187, 2016.

[142] Jakub Vaverka, Asta Pellinen-Wannberg, Johan Kero, Ingrid Mann, Alexandre De Spiegeleer, Maria Hamrin, Carol Norberg, and Timo Pitkänen. Potential of Earth Orbiting Spacecraft Influenced by Meteoroid Hypervelocity Impacts. *IEEE Transactions on Plasma Science*, 45(8):2048–2055, August 2017.

[143] M. W. Evans and F. H. Harlow. The Particle-in-Cell Method for Hydronamic Calculations. Technical Report LA-2139, Los Alamos Scientific Lab., N. Mex., June 1957.

[144] John M. Dawson. Particle simulation of plasmas. *Reviews of Modern Physics*, 55(2):403–447, April 1983.

[145] R. W. Hockney and J. W. Eastwood. *Computer simulation using particles*. Taylor & Francis, Inc., USA, 1988.

[146] Charles K. Birdsall and A. Bruce Langdon. *Plasma Physics Via Computer Simulation*. McGraw-Hill, 1985.

[147] Gian Luca Delzanno, Enrico Camporeale, J. David Moulton, Joseph E. Borovsky, Elizabeth A. MacDonald, and Michelle F. Thomsen. CPIC: a Curvilinear Particle-In-Cell code for plasma-material interaction studies. *IEEE Transactions on Plasma Science*, 41(12):3577–3587, December 2013.

[148] A. A. Vlasov. The Vibrational Properties of an Electron Gas. *Soviet Physics Uspekhi*, 10(6):721, 1968.

[149] C. D. Child. Discharge From Hot CaO. *Physical Review (Series I)*, 32(5):492–511, May 1911.

[150] J. Scott Miller, Steve H. Pullins, Dale J. Levandier, Yu-hui Chiu, and Rainer A. Dressler. Xenon charge exchange cross sections for electrostatic thruster models. *Journal of Applied Physics*, 91(3):984–991, January 2002.

[151] J. P. Sheehan, Yevgeny Raitses, Noah Hershkowitz, and Michael McDonald. Recommended Practice for Use of Emissive Probes in Electric Propulsion Testing. *Journal of Propulsion and Power*, 33(3):614–637, May 2017.

[152] Robert F. Kemp and J. M. Sellen. Plasma Potential Measurements by Electron Emissive Probes. *Review of Scientific Instruments*, 37(4):455–461, April 1966.

[153] Grant Miars, Omar Leon, Brian Gilchrist, Gian Luca Delzanno, and Joe Borovsky. Electrically Isolated System Response to Rapid Charging Events using Hollow Cathode Neutralization. Noordwijk, Netherlands, 2016.

[154] Omar Leon, Grant Miars, Brian Gilchrist, Gian Luca Delzanno, and Joe Borovsky. Plasma Plume Behavior in the Presence of Biased Spacecraft. Noordwijk, Netherlands, 2016.

[155] Michael A. Lieberman and Allan J. Lichtenberg. *Principles of Plasma Discharges and Materials Processing*. John Wiley & Sons, Inc., Hoboken, NJ, USA, April 2005.

[156] Timothy Campbell, Rajiv K. Kalia, Aiichiro Nakano, Priya Vashishta, Shuji Ogata, and Stephen Rodgers. Dynamics of Oxidation of Aluminum Nanoclusters using Variable Charge Molecular-Dynamics Simulations on Parallel Computers. *Physical Review Letters*, 82(24):4866–4869, June 1999.

[157] Accuratus. Aluminum Oxide: Al2O3 Ceramic Properties, 2013.

[158] Shao-Kuan Lee, Hsiu-Ching Hsu, and Wei-Hsing Tuan. Oxidation Behavior of Copper at a Temperature below 300 C and the Methodology for Passivation. *Materials Research*, 19(1):51–56, February 2016.

[159] Jian Li, G. Vizkelethy, P. Revesz, J. W. Mayer, and K. N. Tu. Oxidation and reduction of copper oxide thin films. *Journal of Applied Physics*, 69(2):1020–1029, January 1991.

[160] C.S. Dunleavy, I.O. Golosnoy, J.A. Curran, and T.W. Clyne. Characterisation of discharge events during plasma electrolytic oxidation. *Surface and Coatings Technology*, 203(22):3410–3419, August 2009.

[161] Nicholas James Behlman. *Electron Energy Distribution Measurements in the Plume Region of a Low Current Hollow Cathode*. Worcester Polytechnic Institute, 2009.

[162] V. A. Godyak and B. M. Alexandrovich. Comparative analyses of plasma probe diagnostics techniques. *Journal of Applied Physics*, 118(23):233302, December 2015.

[163] Noah Hershkowitz. How Langmuir Probes Work. In *Plasma Diagnostics: Discharge Parameters and Chemistry*. January 1989.

[164] B. E. Cherrington. The use of electrostatic probes for plasma diagnostics—A review. *Plasma Chemistry and Plasma Processing*, 2(2):113–140, June 1982.

[165] Sigvald Marholm and Richard Marchand. Finite-length effects on cylindrical Langmuir probes. *Physical Review Research*, 2(2):023016, April 2020.

[166] D Johanning, W Seifert, and A Best. Analytical density correction for cylindrical Langmuir probes showing end effects. *Plasma Physics and Controlled Fusion*, 27(2):159–179, February 1985.

[167] Robert B. Lobbia and Brian E. Beal. Recommended Practice for Use of Langmuir Probes in Electric Propulsion Testing. *Journal of Propulsion and Power*, 33(3):566–581, 2017.

[168] F. Magnus and J. T. Gudmundsson. Digital smoothing of the Langmuir probe I-V characteristic. *Review of Scientific Instruments*, 79(7):073503, July 2008.

[169] Abraham. Savitzky and M. J. E. Golay. Smoothing and Differentiation of Data by Simplified Least Squares Procedures. *Analytical Chemistry*, 36(8):1627–1639, July 1964.

[170] Larry H. Brace. Langmuir Probe Measurements in the Ionosphere. In Robert F. Pfaff, Joseph E. Borovsky, and David T. Young, editors, *Measurement Techniques in Space Plasmas:Particles*, pages 23–35. American Geophysical Union, 1998.

[171] Zachary Taillefer and John Joseph Blandino. Characterization of the Near-Plume Region of a Laboratory BaO Hollow Cathode Operating on Xenon and Iodine Propellants. Atlanta, GA, 2017.

[172] K. Dannenmayer, S. Mazouffre, P. Kudrna, and M. Tichý. The time-varying electron energy distribution function in the plume of a Hall thruster. *Plasma Sources Science and Technology*, 23(6):065001, August 2014.

[173] V A Godyak and V I Demidov. Probe measurements of electron-energy distributions in plasmas: what can we measure and how can we achieve reliable results? *Journal of Physics D: Applied Physics*, 44(26):269501, July 2011.

[174] Dan M. Goebel, Kristina K. Jameson, Ron M. Watkins, Ira Katz, and Ioannis G. Mikellides. Hollow cathode theory and experiment. I. Plasma characterization using fast miniature scanning probes. *Journal of Applied Physics*, 98(11):113302, December 2005.

[175] I. H. Hutchinson. *Principles of Plasma Diagnostics*. Cambridge University Press, July 2005.

[176] Isaac D. Sudit and R. Claude Woods. A study of the accuracy of various Langmuir probe theories. *Journal of Applied Physics*, 76(8):4488–4498, October 1994.

[177] J. Olson, N. Brenning, J.-E. Wahlund, and H. Gunell. On the interpretation of Langmuir probe data inside a spacecraft sheath. *The Review of Scientific Instruments*, 81(10):105106, October 2010.

[178] K.-U. Riemann. The Bohm criterion and sheath formation. *Journal of Physics D: Applied Physics*, 24(4):493–518, April 1991.

[179] Koichiro Oyama. DC Langmuir Probe for Measurement of Space Plasma: A Brief Review. *Journal of Astronomy and Space Sciences*, 32(3):167–180, 2015.

[180] Christian Böhm and Jérôme Perrin. Retarding-field analyzer for measurements of ion energy distributions and secondary electron emission coefficients in low-pressure radio frequency discharges. *Review of Scientific Instruments*, 64(1):31–44, January 1993.

[181] H. K. Fang and C. Z. Cheng. Retarding Potential Analyzer (RPA) for Sounding Rocket. In K. Oyama and C. Z. Cheng, editors, *An Introduction to Space Instrumentation*, pages 139–153. TERRAPUB, 2013.

[182] Mark Crofton and Iain Boyd. The T6 Hollow Cathode: Measurements and Modeling. In *34th AIAA Plasmadynamics and Lasers Conference*, Orlando, Florida, June 2003.

[183] John E. Foster and Michael J. Patterson. Downstream Ion Energy Distributions in a Hollow Cathode Ring Cusp Discharge. *Journal of Propulsion and Power*, 21(1):144–151, 2005.

[184] L. A. Schwager and C. K. Birdsall. Collector and source sheaths of a finite ion temperature plasma. *Physics of Fluids B: Plasma Physics*, 2(5):1057–1068, May 1990.

[185] Grant Miars, Omar Leon, Brian Gilchrist, Gian Luca Delzanno, Federico Lucco Castello, and Joseph E. Borovsky. Ion Emission Energetics From a Positively Biased Hollow Cathode Contactor. In *2017 IEEE International Conference on Plasma Science (ICOPS)*, May 2017.

[186] William H. Press, Saul A. Teukolsky, William T. Vetterling, and Brian P. Flannery. *Numerical Recipes 3rd Edition: The Art of Scientific Computing*. Cambridge University Press, USA, 3rd edition, 2007.

[187] Robert Albarran and Aroh Barjatya. Plasma Density Analysis of CubeSat Wakes in the Earth's Ionosphere. *Journal of Spacecraft and Rockets*, 53(3):393–400, January 2016.

[188] Eric Choiniere and Brian E. Gilchrist. Self-Consistent 2-D Kinetic Simulations of High-Voltage Plasma Sheaths Surrounding Ion-Attracting Conductive Cylinders in Flowing Plasmas. *IEEE Transactions on Plasma Science*, 35(1):7–22, February 2007.

[189] Benjamin Ragan-Kelley. *Explorations of Space-Charge Limits in Parallel-Plate Diodes and Associated Techniques for Automation*. PhD thesis, University of California, Berkeley, 2013.

[190] Gian Luca Delzanno and Federico Lucco Castello. Personal Communication, 2017.

[191] Christopher Dodson, Benjamin Jorns, and Richard Wirz. Measurements of ion velocity and wave propagation in a hollow cathode plume. *Plasma Sources Science and Technology*, 28(6):065009, June 2019.

[192] Ioannis G. Mikellides, Alejandro Lopez Ortega, Dan M. Goebel, and Giulia Becatti. Dynamics of a hollow cathode discharge in the frequency range of 1–500 kHz. *Plasma Sources Science and Technology*, 29(3):035003, March 2020.

[193] J. P. Sheehan and N. Hershkowitz. Emissive probes. *Plasma Sources Science and Technology*, 20(6):063001, November 2011.

[194] Hiroharu Fujita and Shinya Yagura. Measurements of Fast Time Evolutions of Plasma Potential Using Emissive Probe. *Japanese Journal of Applied Physics*, 22(Part 1, No. 1):148–151, January 1983.

[195] B. N. Roy and T. Wright. Electrical Conductivity in Polycrystalline Copper Oxide Thin Films. *Crystal Research and Technology*, 31(8):1039–1044, January 1996.

[196] Víctor-Hugo Castrejón-Sánchez, Antonio Coyopol Solís, Roberto López, Cecilia Encarnación-Gomez, Francisco Morales Morales, Orlando Soriano Vargas, Jorge Edmundo Mastache-Mastache, and Gerardo Villa Sánchez. Thermal oxidation of copper over a broad temperature range: towards the formation of cupric oxide (CuO). *Materials Research Express*, 6(7):075909, April 2019.

[197] Friedrich Paschen. Ueber die zum Funkenübergang in Luft, Wasserstoff und Kohlensäure bei verschiedenen Drucken erforderliche Potentialdifferenz. *Annalen der Physik*, 273(5):69–96, 1889.

[198] NIST. Xenon, 2020. Library Catalog: webbook.nist.gov Publisher: National Institute of Standards and Technology.

[199] NIST. Argon, 2020. Library Catalog: webbook.nist.gov Publisher: National Institute of Standards and Technology.

[200] C. Day. Basics and applications of cryopumps. In *Vacuum in Accelerators: Specialized Course of the CERN Accelerator School*, pages 241–274, 2006.

[201] Michael L. Hause, Benjamin D. Prince, and Raymond J. Bemish. Krypton charge exchange cross sections for Hall effect thruster models. *Journal of Applied Physics*, 113(16):163301, April 2013.

[202] Ángel Yanguas-Gil, José Cotrino, and Luís L. Alves. An update of argon inelastic cross sections for plasma discharges. *Journal of Physics D: Applied Physics*, 38(10):1588–1598, May 2005.

[203] S. D. Loch, M. S. Pindzola, C. P. Ballance, D. C. Griffin, D. M. Mitnik, N. R. Badnell, M. G. O'Mullane, H. P. Summers, and A. D. Whiteford. Electron-impact ionization of all ionization stages of krypton. *Physical Review A*, 66(5):052708, November 2002.

[204] L. C. Pitchford, L. L. Alves, K. Bartschat, S. F. Biagi, M. C. Bordage, A. V. Phelps, C. M. Ferreira, G. J. M. Hagelaar, W. L. Morgan, S. Pancheshnyi, V. Puech, A. Stauffer, and O. Zatsarinny. Comparisons of sets of electron–neutral scattering cross sections and swarm parameters in noble gases: I. Argon. *Journal of Physics D: Applied Physics*, 46(33):334001, August 2013.

[205] M. C. Bordage, S. F. Biagi, L. L. Alves, K. Bartschat, S. Chowdhury, L. C. Pitchford, G. J. M. Hagelaar, W. L. Morgan, V. Puech, and O. Zatsarinny. Comparisons of sets of electron–neutral scattering cross sections and swarm parameters in noble gases: III. Krypton and xenon. *Journal of Physics D: Applied Physics*, 46(33):334003, August 2013.

[206] J.W. Murdock and G.H. Miller. Secondary Electron Emission Due to Positive Ion Bombardment. Technical Report ISC-652, 4350066, June 1956.

[207] Robert G. D. Steel, James H. Torrie, and David A. Dickey. *Principles and Procedures of Statistics: A Biometrical Approach*. McGraw-Hill, 1997.

[208] Hyungjoo Shin, Weiye Zhu, Demetre J. Economou, and Vincent M. Donnelly. Ion energy distributions, electron temperatures, and electron densities in Ar, Kr, and Xe pulsed discharges. *Journal of Vacuum Science & Technology A: Vacuum, Surfaces, and Films*, 30(3):031304, May 2012.

[209] Ira Katz, John R. Anderson, James E. Polk, and John R. Brophy. One-Dimensional Hollow Cathode Model. *Journal of Propulsion and Power*, 19(4):595–600, July 2003.

[210] L. Dorf, Y. Raitses, and N. J. Fisch. Electrostatic probe apparatus for measurements in the near-anode region of Hall thrusters. *Review of Scientific Instruments*, 75(5):1255–1260, May 2004.